

Cardiovascular Mechanics: The Biomechanics of Arteries and the Human Heart

Zur Erlangung des akademischen Grades eines
Doktors der Technischen Wissenschaften
ausgeführte Dissertation

eingereicht an der
Fakultät für Elektrotechnik und Informationstechnik
der Technischen Universität Graz



von

Thomas S.E. Eriksson

Betreuer: Univ.-Prof. Dipl.-Ing. Dr. techn. Gerhard A. Holzapfel
Assoz. Prof. Priv.-Doz. Dipl.-Ing. Dr. techn. Gernot Plank

May 24, 2012

Copyright © 2012 Thomas Sven Erik Eriksson. All Rights Reserved.

EIDESSTATTLICHE ERKLÄRUNG

Ich erkläre an Eides statt, dass ich die vorliegende Arbeit selbstständig verfasst, andere als die angegebenen Quellen/Hilfsmittel nicht benutzt und die den benutzten Quellen wörtlich und inhaltlich entnommenen Stellen als solche kenntlich gemacht habe.

Graz, am _____
Datum

Unterschrift

STATUTORY DECLARATION

I declare that I have authored this thesis independently, that I have not used other than the declared sources/resources and that I have explicitly marked all material which has been quoted either literally or by content from the used sources.

Graz, _____
Date

Signature

Abstract

Modeling in biomechanics plays an important role in simulating biological functions and has great potential to aid medical clinicians in determining the cause of a disease, the type of treatment or by aiding in the training of a surgical procedure. Cardiovascular diseases (CVDs) are the leading cause of mortality today. This thesis therefore aims at developing a framework for the modeling CVDs, such as cerebral aneurysms or heart diseases with increased myofiber dispersion as seen in, e.g., hypertrophic cardiomyopathy.

To this end, a three-dimensional growth model of a human saccular cerebral aneurysm is presented that includes the anisotropy of the medial layer. It is shown that including fibers in the media reduces the maximum principal stress, thickness increase and shear stress in the aneurysm wall. It is also shown that the axial pre-stretch has a large impact on the stress levels and thickness increase in the aneurysm wall.

In addition, the constituents needed for the numerical implementation of a structurally based constitutive law describing the behavior of passive myocardium is shown. A comparison is made between this invariant based model and a commonly used Green-Lagrange strain based model and it is shown that using material parameters retrieved when both models is fitted against a simple shear mode experiment, the invariant based model is better suited to predict the stress in the myocardium for other modes of deformation. The passive cardiac model is coupled together with an evolution equation responsible for generating the active stress. A model of the left ventricle (LV) is presented where pressure is calculated as a response to the change in the ventricular volume in order to ensure physiologically realistic pressure-volume loops. The influence of myocardial fiber and sheet distribution is investigated by using two different setups, a generic setup and one based on experiments. The results implies that spacial heterogeneity may play a critical role in mechanical contraction of the LV and that geometrical descriptions of deformation are needed when evaluating the accuracy of a ventricular model.

Further, a novel approach to model the disarray of both the fiber and sheet orientations evident in, especially diseased, myocardium is presented. Analytical and numerical simulations show that the dispersion parameter has great effect on myocardial deformation and stress development. The results also show that the dispersion has a significant impact on pressure-volume loops of an LV, and in future simulations the presented dispersion model for myocardium may advantageously be used together with models of, e.g., growth and remodeling of various cardiac diseases. In cases where fiber-reinforced models are extended to include the effect of distributed fiber orientations, neither the mathematical nor physical motivation for tension-compression fiber switching is clear, and in fact several choices exist for the material modeler. Therefore, methods to study such switching mechanisms is explored by analyzing six potential switching cases. Two different permeations of the dispersed fiber-reinforced model is proposed, depending on whether one can assume that the fibers are (nearly) uncoupled or strongly coupled to the isotropic ground matrix.

Zusammenfassung

Die Modellierung in der Biomechanik spielt eine wichtige Rolle bei der Simulation von biologischen Funktionen und unterstützt Ärzte bei der Diagnose sowie auch bei der weiteren Behandlung von Erkrankungen. Auch im Bereich des Trainings von operativen Eingriffen bietet die Modellierung und Simulation große Möglichkeiten. Kardiovaskuläre Erkrankungen sind die führenden Ursachen von Morbidität und Sterblichkeit in der westlichen Welt. Aus diesem Grund ist das Ziel dieser Dissertation die Entwicklung von Computermodellen für kardiovaskuläre Erkrankungen wie etwa Aneurysmen oder Herzerkrankungen mit erhöhter Muskelfaserdispersion welche zum Beispiel bei der hypertrophen Kardiomyopathie beobachtet werden kann.

Aus diesem Grund wurde ein dreidimensionales Wachstumsmodell eines sackförmigen menschlichen Aneurysmas im Gehirn entwickelt welches die Anisotropie der mittleren Arterien-schicht berücksichtigt. Die Ergebnisse des Modells lassen erkennen, dass die Berücksichtigung der Kollagenfasern in der mittleren Schicht die maximale Hauptnormalspannung, die Zunahme der Dicke und die Scherspannung in der Wand des Aneurysmas verringern. Ferner ist ein erheblicher Einfluss der axialen Vordehnung auf die Spannungsgröße und auf die Zunahme der Wanddicke des Aneurysmas zu beobachten.

Ein strukturbasiertes Materialmodell zur Beschreibung des passiven mechanischen Verhaltens des menschlichen Myokards und die für die numerische Implementierung benötigten Komponenten wird beschrieben. Darauf folgend wird das passive Modell mit den für die Generierung der aktiven Spannungsanteile zuständigen Gleichungen gekoppelt. Die Modellbeschreibung basiert auf den Green-Lagrangischen Verzerrungen. Materialparameter wurden für beide Modelle durch eine Ausgleichsrechnung (curve fitting) eines einfachen Schubversuches gewonnen. Es konnte gezeigt werden, dass das vorgeschlagene Modell die Spannungen im Myokard sehr gut wiedergeben kann. Ein Computermodell des linken Ventrikels (LV) wird präsentiert, bei welchem der Druck als Funktion der Änderung des Ventrikelvolumens berechnet wird um physiologische Druck-Volumen-Kurven zu erhalten. Dabei wird der Einfluss der Muskelfaser- und der Lamellenverteilung auf das biomechanische Verhalten des Myokards durch das Verwenden von zwei unterschiedlichen Konfigurationen untersucht: einer generischen und einer experimentell ermittelten Konfiguration. Das Ergebnis zeigt, dass die räumliche Heterogenität eine entscheidende Rolle in der mechanischen Kontraktion des LV spielt und dass diese räumliche Heterogenität auch gebraucht wird um die Genauigkeit der Analysen am LV zu verbessern.

Ein neuer Ansatz zur Modellierung der Verteilung der Muskelfaser- und der Lamellenorientierung im Myokard, speziell im erkrankten Myokard, wird erörtert. Analytische und numerische Simulationen lassen darauf schließen, dass die Faserverteilung des Myokards einen großen Einfluss auf die Deformation und die Spannungen im Myokard hat. Weiters zeigen Ergebnisse, dass die Faserverteilung erhebliche Veränderungen in den Druck-Volumen-Kurven des LV hervorruft. Für zukünftige Simulationen kann das entwickelte

Modell vorteilhaft mit Modellen für Wachstum und Remodellierung von verschiedenen kardialen Erkrankungen genützt werden. Bei einer Erweiterung von faserverstärkten Materialmodellen um die Verteilung tritt das Problem auf, dass weder eine mathematische, noch eine physikalische Motivation für das Hinzufügen oder das Entfernen des Faseranteils beim Übergang von Zug- auf Druckbeanspruchung klar beschrieben werden kann, da es verschiedenste Möglichkeiten für den Anwender gibt. Aus diesem Grund werden sechs potentielle Möglichkeiten für dieses Problem analysiert und zwei verschiedene Permutationen des faserverstärkten Materialmodells mit Faserverteilung vorgeschlagen, abhängig davon, ob angenommen werden kann, dass eine starke Kopplung zwischen den Fasern und der isotropen Grundsubstanz der extrazellulären Matrix besteht oder diese Kopplung nahezu nicht gegeben ist.

Preface

The work in this PhD thesis was carried out at the Institute of Biomechanics at Graz University of Technology in a collaboration with the Institute of Biophysics at the Medical University of Graz, in Austria. It has been financially supported by the SFB Research Center ‘Mathematical Optimization and Applications in Biomedical Sciences’, project F3210-N18 granted by the Austrian Science Fund. This support is gratefully acknowledged.

I would like to express my sincere and deep gratitude to Prof. Gerhard Holzapfel for your supervision, support and for introducing me to the fascinating field of biomechanics. I would also like to express my deep and genuine gratitude to Prof. Gernot Plank for your constant support and encouragement and for providing me with the opportunity to work in this interesting project. I have learned a lot during these years. Thank you both!

I would like to acknowledge Prof. Nguyen for agreeing to be an examiner of this thesis and I am also grateful to all my colleagues for contributing to a stimulating environment to work in.

I especially want to acknowledge Dr. David Pierce for your guidance and encouragement, both in work related issues as well as in all the fun things we have done on our spare time. To Dr. Anton Prassl, thank you for your technical assistance and for helping me with many administrative details. Furthermore, I want to express my sincere gratitude to Dr. Adam Zdunek for your endless stream of support and your brilliant advice. Many thanks to Dr. Arturo Valentin, for sharing your skills and expertise in programming and to B.Sc. Thomas Fastl, for all the interesting discussions we have had and especially all your help with correcting my German.

Finally, I would like to thank my sister Anna, my father Sven and my grandparents Solbritt, Anna and Ingvar, for your constant support and for believing in me. To the Zdunek family, thank you for your love, trust and encouragement. Also, to my mother Agnetha Öst, your generous love and warmth will always be remembered and never forgotten.

This thesis is dedicated to my fiancée Ania Zdunek. I would not be where I am or do what I do if it were not for you. Thank you for all your love, patience and support in finishing this work. It is pure joy and a wondrous thing to have you in my life.

Thomas Eriksson
Graz, May 24, 2012

CONTENTS

1. Introduction and Motivation	1
1.1. Biomechanical Modeling	1
1.2. Continuum Mechanical Framework	2
1.2.1. Kinematics	2
1.2.2. Stress measures	4
1.2.3. Balance laws	4
1.2.4. Constitutive equations	8
1.2.5. Incompressibility and near incompressibility	9
1.2.6. Invariant formulation	10
1.2.7. Strong and weak form of a boundary-value problem	11
1.3. Cerebral Aneurysms	13
1.3.1. Arterial wall	13
1.3.2. Evolving aneurysm	14
1.4. Cardiac Mechanics	15
1.4.1. Contractile unit	16
1.4.2. Structural organization of the myocardium	17
1.4.3. Modeling cardiac mechanics	18
1.5. Organization of the Thesis	21
2. Influence of Medial Collagen Organization and Axial In Situ Stretch on Saccular Cerebral Aneurysm Growth	25
2.1. Introduction	25
2.2. Growth Model of a Saccular Cerebral Aneurysm	26
2.3. Problem Formulation	28
2.3.1. Model geometry, boundary and loading conditions	28
2.3.2. Stress response	29
2.3.3. Model specification, numerics	32
2.4. Numerical Results	33
2.4.1. Influence of medial collagen organization	33
2.4.2. Influence of axial in situ stretch	35
2.5. Discussion	36
3. Tensors Needed for Finite Element Implementation of an Invariant Based Constitutive Model for Passive Myocardium	41
3.1. Introduction	41

3.2.	Material Model	44
3.2.1.	Volume-preserving continuum mechanical framework	44
3.2.2.	Strain-energy function for the passive mechanical response of the myocardium	45
3.2.3.	Stress tensors	46
3.2.4.	Elasticity tensor in the Lagrangian description	47
3.2.5.	Elasticity tensors in the Eulerian description	49
3.3.	Analytical Expression of the Stress Tensor	50
3.3.1.	General analytical expression for incompressible material	50
3.3.2.	Analytical uniaxial expression	51
3.3.3.	Analytical biaxial expression	51
3.3.4.	Analytical shear expression	52
3.4.	Model Fit to Experimental Data	53
3.4.1.	Fit to a simple shear experiment	53
3.4.2.	Fit to a biaxial experiment	55
3.4.3.	Comparison to available model	57
3.5.	Model Sensitivity	59
3.6.	Ellipsoidal Model	60
3.7.	Concluding Remarks	63
4.	Influence of Spatial Heterogeneity in Tissue Orthotropy upon Mechanical Contraction in the Left Ventricle	67
4.1.	Introduction	67
4.2.	Modeling Framework	69
4.2.1.	Electrophysiological modeling	69
4.2.2.	Active and passive mechanical modeling	70
4.3.	Electro-mechanically Coupled Model of a Rabbit Left Ventricle	73
4.3.1.	Definition of geometry	73
4.3.2.	Material parameters	75
4.3.3.	Initial values and boundary conditions	76
4.3.4.	Transferring data between electrical and mechanical grid	79
4.3.5.	Validation of implementation and passive mechanical properties of LV model	79
4.4.	Results	81
4.4.1.	Model validation	81
4.4.2.	Effect of heterogeneity in orthotropy upon mechanical contraction	81
4.5.	Discussion	83
5.	Modeling the Disarray in Cardiac Fiber and Sheet Orientations	89
5.1.	Introduction	89
5.2.	Modeling Framework	90
5.2.1.	Kinematics	90

5.2.2.	Constitutive relations	92
5.2.3.	Modeling electro-mechanically coupled myocardial tissue	94
5.3.	Representative Examples and Results	95
5.3.1.	Cube with dispersion subjected to active stress	95
5.3.2.	Influence of dispersion on simple shear	97
5.3.3.	Influence of increased myocyte dispersion	98
5.3.4.	Passive inflation of ventricular section	98
5.3.5.	Simulation of an LV with healthy and diseased dispersion parameters	100
5.4.	Discussion	102
6.	On Tension-Compression Switching in Dispersed Fiber-Reinforced Constitutive Models	107
6.1.	Introduction	107
6.2.	Mathematical methods	110
6.3.	Results	112
6.4.	Discussion	116
A.	Appendix for Chapter 5	119
A.1.	Active Elasticity Tensors in Lagrangian and Eulerian Description	119
B.	Appendix for Chapter 6	121
B.1.	The Stress Equations as a Function of Applied Stretch λ_f or Applied Shear γ	121
B.2.	Convexity and Ellipticity of Distributed Functions	123
	References	127

1. INTRODUCTION AND MOTIVATION

1.1. Biomechanical Modeling

The world health organization (WHO) has stated that cardiovascular disease (CVD) is the leading cause of death in world. In Europe, for example, CVD comprises nearly half of all deaths (48 %) while in the United States nearly one of every third death (32.8 %) is attributed to CVD. Also in China, over one third of every death (35.8 %) is caused by some form of CVD [132, 134, 188]. The health care costs of CVD is estimated to be € 110 billion in the European Union alone, which is about 10 % of the total health care cost. Adding to that is another € 83 billion in indirect costs that includes production losses and informal care [132]. To put these staggering costs in perspective, NASA estimates that the cost to launch a space shuttle is about € 340 million (US\$ 450 million) [101]. Thus, the total costs for CVD in the European Union alone is equivalent to nearly 570 space shuttle launches per year. The need for improvements in identification, understanding and treatment of CVD's is, therefore, of utmost importance. To this goal, biological mechanisms that underly CVD needs to be studied, e.g., chemical, electrical and mechanical mechanisms. In this thesis, we have developed a framework that includes electrophysiology and that can easily be extended to incorporate ionic cellular models. The focus, however, lies on the mechanical mechanisms in biomaterials. It is known that the mechanics of biological systems has been studied since the antiquity with Aristotle's book 'On the Motion of Animals' approximately 350 B.C.E., but it is with Fung's early works in the 1960's and 70's that modern day biomechanical modeling and the phrase biomechanics is born [74]. Today, modeling in biomechanics plays an important role in simulating biological functions and has great potential to aid medical clinicians in determining the cause of a disease, the type of treatment or by aiding in the training of a surgical procedure. Furthermore, through mechanobiology we know that mechanical stimulus on cells and tissue may affect biological processes. Thus, by modeling the progression of biological and mechanical processes, biomaterials can be better understood and phenomenon such as growth and remodeling as well as the development of various diseased states may be studied.

The most widely used framework for modeling soft tissue biomechanics is continuum mechanics, in which the discrete particles of a biological material is considered to be a continuum and the material behavior of each particle is translated to the overall behavior of the continuum. Continuum mechanical models can be used on a range of spatial scales, from individual cells or entire organs. Therefore, Section 1.2 offers a brief overview of the necessary continuum mechanical framework that is used throughout this thesis. To model any type of biological tissue, it is also essential to understand the responses and underlying

structure of the material. The following two Sections 1.3 and 1.4, therefore, describe the constituents and material behavior of two fascinating materials that is studied in this thesis, namely cerebral aneurysms and ventricular myocardium. However, as the focus of this thesis is dedicated to myocardial mechanics, this will be mirrored in the introduction.

1.2. Continuum Mechanical Framework

The basic relations in kinematics, stress, constitutive equations, incompressibility, invariant formulations and strong and weak forms of a boundary-value problem, needed for the completeness of this thesis, are covered in this section. For a more complete background on nonlinear continuum mechanics see the book by Holzapfel [53] and references therein.

1.2.1. Kinematics

A continuum body $\mathcal{B} = \{P_k\}$, where the mass and volume of the body is at least piecewise continuous, consists of a set of discrete particles P_k . At a given time t , the body occupies a region $\Omega(t)$ set in a reference frame with origin O and orthonormal basis vectors \mathbf{e}_i , $i = \{1, 2, 3\}$, in a three-dimensional Euclidean space, as seen in Fig. 1.1. At some reference time t_0 , a particle P set in a reference region Ω_0 can be described by the position vector $\mathbf{X}(P, t_0)$. Here, $t_0 = 0$ is denoted as the initial time and the region $\Omega_0(t_0)$ as the initial (undeformed) configuration. At any time $t > t_0$ the body \mathcal{B} may have transformed to occupy the current (deformed) configuration $\Omega(t)$. The position of the particle P in the current configuration can be described by the position vector $\mathbf{x}(P, t) = \chi(\mathbf{X}, t)$, where χ is denoted as the motion of body \mathcal{B} . Thus, the deformation gradient

$$\mathbf{F}(\mathbf{X}, t) = \frac{\partial \chi(\mathbf{X}, t)}{\partial \mathbf{X}} \quad (1.1)$$

is used to describe the deformation of the body \mathcal{B} . Using infinitesimal volume elements dV and dv in the reference and current configurations, respectively, the volume change of a body may be described by $J = dv/dV$. The volume change can also be retrieved using the determinant of the deformation gradient, i.e. $J = \det \mathbf{F}(\mathbf{X}, t) > 0$, where J is known as the Jacobian determinant.

The deformation gradient is also used to transform a vector (e.g., a fiber) \mathbf{a}_0 with length $|\mathbf{a}_0| = 1$ in the reference configuration to its deformed counterpart \mathbf{a} in the current configuration by $\mathbf{a} = \mathbf{F}\mathbf{a}_0$. The length of the deformed fiber is now $|\mathbf{a}| = \lambda$ which is called the stretch ratio or just the stretch. Through the deformation, the deformation gradient has rotated and stretched the undeformed vector to its deformed counterpart which is the motivation behind the polar decomposition of \mathbf{F} into

$$\mathbf{F} = \mathbf{R}\mathbf{U} = \mathbf{v}\mathbf{R}, \quad (1.2)$$

where \mathbf{R} is a rotation tensor and \mathbf{U} and \mathbf{v} are the right and left stretch tensors, respectively. Thus, \mathbf{F} is decomposed into a pure stretch and a pure rotation in which a line element

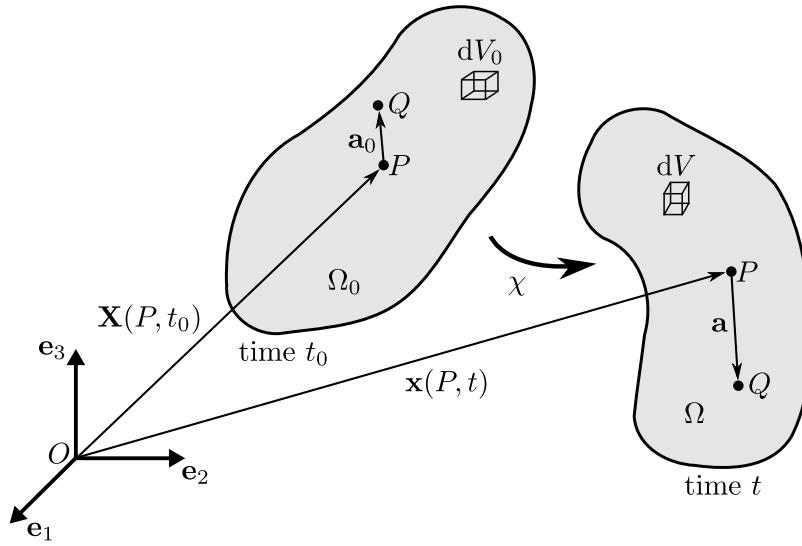


Figure 1.1.: Deformation of a continuum body \mathcal{B} from the reference configuration Ω_0 to the deformed configuration Ω .

at \mathbf{X} may first be stretched by \mathbf{U} and then rotated to \mathbf{x} by \mathbf{R} , or first rotated to \mathbf{x} by \mathbf{R} followed by the stretch \mathbf{v} . The unique and proper orthogonal \mathbf{R} has the properties $\mathbf{R}^T \mathbf{R} = \mathbf{I}$ and $\det \mathbf{R} = 1$, where \mathbf{I} is the second-order identity tensor. The unique and positive definite stretch tensors are symmetric, i.e. $\mathbf{U} = \mathbf{U}^T$ and $\mathbf{v} = \mathbf{v}^T$, and the square of these tensors are

$$\mathbf{C} = \mathbf{F}^T \mathbf{F} = \mathbf{U}^2 \quad \text{and} \quad \mathbf{b} = \mathbf{F} \mathbf{F}^T = \mathbf{v}^2, \quad (1.3)$$

which are called the right and left Cauchy-Green stretch tensors, respectively. Using these stretch tensors, the well known Green-Lagrange strain-tensor is now given by

$$\mathbf{E} = \frac{1}{2}(\mathbf{C} - \mathbf{I}), \quad (1.4)$$

which describes the strain in Ω_0 while the Euler-Almansi strain-tensor is given by

$$\mathbf{e} = \frac{1}{2}(\mathbf{I} - \mathbf{b}^{-1}), \quad (1.5)$$

which describes the strain in Ω . The push-forward and pull-back operations are defined, respectively, for covariant tensors as

$$\chi_*(\bullet)^b = \mathbf{F}^{-T}(\bullet)^b \mathbf{F}^{-1} \quad \text{and} \quad \chi_*^{-1}(\bullet)^b = \mathbf{F}^T(\bullet)^b \mathbf{F}, \quad (1.6)$$

and for contravariant tensors as

$$\chi_*(\bullet)^\sharp = \mathbf{F}(\bullet)^\sharp \mathbf{F}^T \quad \text{and} \quad \chi_*^{-1}(\bullet)^\sharp = \mathbf{F}^{-1}(\bullet)^\sharp \mathbf{F}^{-T}. \quad (1.7)$$

Examples of covariant tensors are \mathbf{E}^b , \mathbf{C}^b , \mathbf{e}^b and $(\mathbf{b}^{-1})^b$ while examples of contravariant tensors are $(\mathbf{C}^{-1})^\sharp$, \mathbf{b}^\sharp and many of the common stress tensors.

1.2.2. Stress measures

Considering an infinitesimal surface ds with a unit vector \mathbf{n} normal to the surface on a part of the deformed body Ω and an infinitesimal force $d\mathbf{f}$, the Cauchy traction vector \mathbf{t} is obtained through the relation $d\mathbf{f} = \mathbf{t}ds$. Cauchy's stress principle states further that

$$\mathbf{t} = \boldsymbol{\sigma}\mathbf{n}, \quad (1.8)$$

where $\boldsymbol{\sigma}$ is the second-order Cauchy stress tensor which is symmetric, i.e. $\boldsymbol{\sigma} = \boldsymbol{\sigma}^T$. That $\boldsymbol{\sigma}$ is symmetric will be shown in Section 1.2.3. The often used engineering (first Piola-Kirchhoff) stress tensor, \mathbf{P} , may be retrieved using the Nanson's formula

$$\mathbf{P} = J\boldsymbol{\sigma}\mathbf{F}^{-T} \quad (1.9)$$

and is, in general, not symmetric but instead fulfills the relation $\mathbf{P}\mathbf{F}^T = \mathbf{F}^T\mathbf{P}$. Other convenient stress measures that are often used are the symmetric Kirchhoff stress tensor

$$\boldsymbol{\tau} = J\boldsymbol{\sigma} \quad (1.10)$$

or the symmetric second Piola-Kirchhoff stress tensor obtained using the Piola transformation

$$\mathbf{S} = \mathbf{F}^{-1}\mathbf{P} = J\mathbf{F}^{-1}\boldsymbol{\sigma}\mathbf{F}^{-T}. \quad (1.11)$$

The stress tensors \mathbf{S} and $\boldsymbol{\tau}$ are both related using the pull-back and push-forward operators

$$\mathbf{S} = \chi_*^{-1}(\boldsymbol{\tau}^\sharp) = \mathbf{F}^{-1}\boldsymbol{\tau}\mathbf{F}^{-T} \quad \text{and} \quad \boldsymbol{\tau} = \chi_*(\mathbf{S}^\sharp) = \mathbf{F}\mathbf{S}\mathbf{F}^T, \quad (1.12)$$

respectively.

1.2.3. Balance laws

Based on experience, basic axioms are formulated called the balance laws. These laws relate the state variables of the continuum to influences of actions outside the continuum.

Reynolds' transport theorem. To formulate the balance laws, we first need to state the Reynolds' transport theorem. Let Ω be a closed spatial boundary region with a smooth boundary $\partial\Omega$. Also, assume we have a spatial scalar field $\phi = \phi(\mathbf{x}, t)$ that is continuously differentiable in both \mathbf{x} and t . Taking the time derivative of a volume integral of ϕ , i.e.

$$\frac{D}{Dt} \int_{\Omega} \phi(\mathbf{x}, t) dv, \quad (1.13)$$

where V is the volume of Ω , is not straightforward as the region Ω depends on time. The quantities are, therefore, transformed to the referential configuration Ω_0 with volume V_0 ,

which is time independent, i.e. $\mathbf{x} = \chi(\mathbf{X}, t)$ and $dv = J(\mathbf{X}, t) dV$. Now, using the chain-rule, (1.13) can be reformulated as

$$\begin{aligned}
\frac{D}{Dt} \int_{\Omega} \phi(\mathbf{x}, t) dv &= \frac{D}{Dt} \int_{\Omega_0} \phi(\chi(\mathbf{X}, t), t) J(\mathbf{X}, t) dV \\
&= \int_{\Omega_0} \left[\frac{\partial \phi(\chi(\mathbf{X}, t), t)}{\partial t} J(\mathbf{X}, t) + \phi(\chi(\mathbf{X}, t), t) \frac{\partial J(\mathbf{X}, t)}{\partial t} \right] dV \\
&= \int_{\Omega_0} [\dot{\phi}(\chi(\mathbf{X}, t), t) J(\mathbf{X}, t) + \phi(\chi(\mathbf{X}, t), t) J(\mathbf{X}, t) \operatorname{div} \mathbf{v}] dV \\
&= \int_{\Omega} [\dot{\phi}(\mathbf{x}, t) + \phi(\mathbf{x}, t) \operatorname{div} \mathbf{v}] dv, \tag{1.14}
\end{aligned}$$

where $\partial J / \partial t = J \operatorname{div} \mathbf{v}$ is used and $\mathbf{v}(\mathbf{x}, t)$ is a vector function in Ω . Equation (1.14) is called the Reynolds' transport theorem, which we here rewrite in another useful form. Utilizing that the material time derivative of $\phi(\mathbf{x}, t)$ is

$$\dot{\phi}(\mathbf{x}, t) = \frac{\partial \phi(\mathbf{x}, t)}{\partial t} + \operatorname{grad} \phi \cdot \mathbf{v}, \tag{1.15}$$

we can further reformulate (1.14)₄ as

$$\begin{aligned}
\frac{D}{Dt} \int_{\Omega} \phi(\mathbf{x}, t) dv &= \int_{\Omega} \left(\frac{\partial \phi(\mathbf{x}, t)}{\partial t} + \operatorname{grad} \phi \cdot \mathbf{v} + \phi(\mathbf{x}, t) \operatorname{div} \mathbf{v} \right) dv \\
&= \int_{\Omega} \left\{ \frac{\partial \phi(\mathbf{x}, t)}{\partial t} + \operatorname{div} [\phi(\mathbf{x}, t) \mathbf{v}] \right\} dv, \tag{1.16}
\end{aligned}$$

and using the divergence theorem on (1.16)₂, yields the well known Reynolds' transport theorem as

$$\frac{D}{Dt} \int_{\Omega} \phi(\mathbf{x}, t) dv = \int_{\Omega} \frac{\partial \phi(\mathbf{x}, t)}{\partial t} dv + \int_{\partial \Omega} \phi(\mathbf{x}, t) \mathbf{v} \cdot \mathbf{n} ds, \tag{1.17}$$

where the first term on the right hand side of (1.17) denotes the rate of change of $\phi(\mathbf{x}, t)$ within the region Ω , while the second term denotes the rate of the outward normal flux of $\phi(\mathbf{x}, t) \mathbf{v}$ out of Ω across the surface $\partial \Omega$ and ds is an infinitesimal surface.

Conservation of mass. The mass m in a closed system can neither be created nor destroyed and is thus an invariant during motion for all times. This may be shown as

$$\dot{m} = \frac{Dm}{Dt} = \frac{D}{Dt} \int_{\Omega} \rho_m(\mathbf{x}, t) dv = 0, \tag{1.18}$$

where $\rho_m(\mathbf{x}, t)$ is the spatial mass density. Using the Reynolds' transport theorem (1.14), \dot{m} can be rewritten as

$$\dot{m} = \int_{\Omega} [\dot{\rho}_m(\mathbf{x}, t) + \rho_m(\mathbf{x}, t) \operatorname{div} \mathbf{v}] \, dv, \quad (1.19)$$

and using the localization theorem it follows that

$$\dot{\rho}_m(\mathbf{x}, t) + \rho_m(\mathbf{x}, t) \operatorname{div} \mathbf{v} = 0 \quad \text{or} \quad \frac{\partial \rho_m(\mathbf{x}, t)}{\partial t} + \operatorname{div}[\rho_m(\mathbf{x}, t) \mathbf{v}]. \quad (1.20)$$

The continuity of mass equation relates the mass density $\rho_{m0}(\mathbf{X})$ in the reference configuration to the mass density $\rho_m(\mathbf{x}, t) = \rho_m(\chi(\mathbf{X}, t), t)$ in the current configuration as

$$\rho_{m0}(\mathbf{X}) = \rho_m(\chi(\mathbf{X}, t), t) J(\mathbf{X}, t). \quad (1.21)$$

Balance of linear and angular momentum. The balance of linear and angular momentum states that the change in linear momentum for a region Ω equals the external forces acting on that region and that the change in angular momentum equals the external moments acting on that region. In addition, the balance between external forces and moments and the rate of change in linear and angular momentums are valid for all parts of the continuum body. Let $\mathbf{b}_F = \mathbf{b}_F(\mathbf{x}, t)$ be body forces, $\mathbf{t} = \mathbf{t}(\mathbf{x}, t, \mathbf{n})$ be contact forces acting on a unit area with the surface normal \mathbf{n} and $\mathbf{v} = \mathbf{v}(\mathbf{x}, t)$ be a velocity field. In the following, the arguments of the tensors are dropped for notational simplicity. The balance of linear momentum takes the form

$$\frac{D}{Dt} \int_{\Omega} \rho_m \mathbf{v} \, dv = \int_{\Omega} \rho_m \mathbf{b}_F \, dv + \int_{\partial\Omega} \mathbf{t} \, ds, \quad (1.22)$$

and the balance of angular momentum takes the form

$$\frac{D}{Dt} \int_{\Omega} \mathbf{r} \times \mathbf{v} \, dv = \int_{\Omega} \mathbf{r} \times \rho_m \mathbf{b}_F \, dv + \int_{\partial\Omega} \mathbf{r} \times \mathbf{t} \, ds, \quad (1.23)$$

where \mathbf{r} is the position vector associated with the infinitesimal volume element. Through the relations (1.22) and (1.23), and in comparison with Eq. (1.17), it is seen that if $\mathbf{b}_F = \mathbf{0}$ in the region Ω and $\mathbf{t} = \mathbf{0}$ on the surface $\partial\Omega$, the linear and angular momentum are conservative quantities in Ω . If instead $\mathbf{v} = \mathbf{0}$, the sum of internal and external forces and moments vanish, which is the condition in the classical statics equilibrium equations.

Cauchy's equations of motion. By using Cauchy's stress principle $\mathbf{t} = \boldsymbol{\sigma} \mathbf{n}$, see Eq. (1.8), and the divergence theorem, it is straightforward to show for the second term on the right hand side of (1.22) that

$$\int_{\partial\Omega} \mathbf{t} \, ds = \int_{\partial\Omega} \boldsymbol{\sigma} \mathbf{n} \, ds = \int_{\Omega} \operatorname{div} \boldsymbol{\sigma} \, dv. \quad (1.24)$$

Substituting this into (1.22) and using the relation

$$\frac{D}{Dt} \int_{\Omega} \rho_m \mathbf{v} dv = \int_{\Omega} \rho_m \dot{\mathbf{v}} dv \quad (1.25)$$

yields Cauchy's first equation of motion as

$$\int_{\Omega} (\operatorname{div} \boldsymbol{\sigma} + \mathbf{b}_F - \rho_m \dot{\mathbf{v}}) dv = \mathbf{0}. \quad (1.26)$$

As (1.26) holds for any volume V , it may also be rewritten in its local form as

$$\operatorname{div} \boldsymbol{\sigma} + \mathbf{b}_F = \rho_m \dot{\mathbf{v}}. \quad (1.27)$$

If there is no acceleration of the body, i.e. $\dot{\mathbf{v}} = \mathbf{0}$, Eq. (1.27) becomes

$$\operatorname{div} \boldsymbol{\sigma} + \mathbf{b}_F = \mathbf{0}, \quad (1.28)$$

which is the classical Cauchy's equation of static equilibrium. Using the Cauchy stress principle on the second term on right hand side of Eq. (1.23) and using the divergence theorem yields

$$\int_{\partial\Omega} \mathbf{r} \times \mathbf{t} ds = \int_{\partial\Omega} \mathbf{r} \times \boldsymbol{\sigma} \mathbf{n} ds = \int_{\Omega} (\mathbf{r} \times \operatorname{div} \boldsymbol{\sigma} + \boldsymbol{\mathcal{E}} : \boldsymbol{\sigma}^T) dv, \quad (1.29)$$

where $\boldsymbol{\mathcal{E}}$ is the third order permutation tensor. Using (1.29) together with (1.25), the equation for angular momentum (1.23) can be rewritten as

$$\int_{\Omega} \mathbf{r} \times (\rho_m \dot{\mathbf{v}} - \operatorname{div} \boldsymbol{\sigma} - \mathbf{b}_F) dv = \int_{\Omega} \boldsymbol{\mathcal{E}} : \boldsymbol{\sigma}^T dv, \quad (1.30)$$

which using (1.27) and the fact that (1.30) holds for any volume V , becomes

$$\boldsymbol{\mathcal{E}} : \boldsymbol{\sigma}^T = \mathbf{0}. \quad (1.31)$$

Through Eq. (1.31) it is easy to show that the relations $\sigma_{12} - \sigma_{21} = 0$, $\sigma_{13} - \sigma_{31} = 0$ and $\sigma_{23} - \sigma_{32} = 0$ must hold, which is satisfied if and only if

$$\boldsymbol{\sigma} = \boldsymbol{\sigma}^T, \quad (1.32)$$

i.e. the Cauchy stress tensor is symmetric. The symmetry of the Cauchy stress tensor is thus retrieved using the angular momentum and is referred to as Cauchy's second equation of motion.

1.2.4. Constitutive equations

The relation between the deformation of a material, say represented by \mathbf{F} , and the stress in the material, say represented by $\boldsymbol{\sigma}$ or \mathbf{P} , is given by the constitutive relations. If we further consider hyperelastic materials, there must exist a Helmholtz free-energy (strain-energy) scalar-valued function $\Psi(\mathbf{F})$. A stress constitutive equation for a hyperelastic material can then be postulated as

$$\mathbf{P} = \frac{\partial \Psi(\mathbf{F})}{\partial \mathbf{F}}, \quad (1.33)$$

or

$$\boldsymbol{\sigma} = J^{-1} \frac{\partial \Psi(\mathbf{F})}{\partial \mathbf{F}} \mathbf{F}^T. \quad (1.34)$$

There are many restriction on the constitutive equations. For example, it must be invariant against rigid body motion (material objectivity), it must fulfill the balance laws (consistency) and it must be possible to write a function with a unique solution given initial values and boundary conditions (determinism). For a strain-energy function there is also the restriction that no energy is stored in the material if there is no deformation, i.e.

$$\Psi(\mathbf{F} = \mathbf{I}) = 0. \quad (1.35)$$

Also, the strain energy must be positive (or zero) for all deformations, i.e.

$$\Psi(\mathbf{F}) \geq 0. \quad (1.36)$$

In addition, the volume of a body can not be infinitely expanded or reduced to zero volume, i.e. the strain energy must go towards $+\infty$ according to

$$\Psi(\mathbf{F}) \rightarrow +\infty \quad \text{as} \quad \det \mathbf{F} \rightarrow +\infty, \quad (1.37)$$

$$\Psi(\mathbf{F}) \rightarrow +\infty \quad \text{as} \quad \det \mathbf{F} \rightarrow +0. \quad (1.38)$$

From the principle of frame indifference (material objectivity) it is also clear that the strain-energy function must follow the relation

$$\Psi(\mathbf{F}) = \Psi(\mathbf{U}) = \Psi(\mathbf{C}) = \Psi(\mathbf{E}), \quad (1.39)$$

where the symbol Ψ is used for all strain-energy functions for notational simplicity. The material stress constitutive relations may thus be written in terms of \mathbf{C} or \mathbf{E} as

$$\mathbf{P} = 2\mathbf{F} \frac{\partial \Psi(\mathbf{C})}{\partial \mathbf{C}} \quad \text{and} \quad \mathbf{P} = \mathbf{F} \frac{\partial \Psi(\mathbf{E})}{\partial \mathbf{E}}, \quad (1.40)$$

$$\mathbf{S} = 2 \frac{\partial \Psi(\mathbf{C})}{\partial \mathbf{C}} \quad \text{and} \quad \mathbf{S} = \frac{\partial \Psi(\mathbf{E})}{\partial \mathbf{E}}, \quad (1.41)$$

or

$$\boldsymbol{\sigma} = 2J^{-1} \mathbf{F} \frac{\partial \Psi(\mathbf{C})}{\partial \mathbf{C}} \mathbf{F}^T \quad \text{and} \quad \boldsymbol{\sigma} = J^{-1} \mathbf{F} \frac{\partial \Psi(\mathbf{E})}{\partial \mathbf{E}} \mathbf{F}^T. \quad (1.42)$$

1.2.5. Incompressibility and near incompressibility

Many soft biological tissues exhibit an incompressible, or nearly incompressible, behavior. The strain-energy function for an incompressible material may be obtained by introducing the hydrostatic pressure p_h as

$$\Psi = \Psi(\mathbf{F}) - p_h(J - 1), \quad (1.43)$$

where p_h is determined from the boundary conditions. The Cauchy stress and the second Piola-Kirchhoff stress tensors for an incompressible material are thus, e.g., using $\Psi(\mathbf{C})$,

$$\boldsymbol{\sigma} = 2J^{-1}\mathbf{F}\frac{\partial\Psi(\mathbf{C})}{\partial\mathbf{C}}\mathbf{F}^T - p_h\mathbf{I} \quad \text{and} \quad \mathbf{S} = 2\frac{\partial\Psi(\mathbf{C})}{\partial\mathbf{C}} - p_h\mathbf{C}^{-1}, \quad (1.44)$$

respectively. Although the formulations in (1.44) are convenient to use in an analytical setting, in a computational setting it is often more advantageous to use a compressible formulation, where the (near) incompressibility of biological tissues is achieved through a penalization of the volumetric terms. To separate the strain-energy function into a volumetric (volume changing) and an isochoric (volume preserving) term, a multiplicative decomposition of the deformation gradient is performed according to

$$\mathbf{F} = (J^{1/3}\mathbf{I})\bar{\mathbf{F}}, \quad (1.45)$$

where $J^{1/3}\mathbf{I}$ is associated with the volumetric deformation and $\bar{\mathbf{F}}$ is associated with the isochoric deformation. The isochoric right and left Cauchy-Green tensors may also be retrieved using $\bar{\mathbf{F}}$ by

$$\bar{\mathbf{C}} = \bar{\mathbf{F}}^T\bar{\mathbf{F}} = J^{-2/3}\mathbf{C} \quad \text{and} \quad \bar{\mathbf{b}} = \bar{\mathbf{F}}\bar{\mathbf{F}}^T = J^{-2/3}\mathbf{b}, \quad (1.46)$$

respectively. Thus the strain energy function may be decoupled, say into $\Psi(\mathbf{C}) = \Psi_{\text{vol}}(J) + \Psi_{\text{iso}}(\bar{\mathbf{C}})$, where the subscripts vol and iso stands for the volumetric and isochoric parts, respectively.

This enables an additive split of the second Piola-Kirchhoff stress tensor into a purely volumetric and a purely isochoric contribution according to

$$\mathbf{S} = \mathbf{S}_{\text{vol}} + \mathbf{S}_{\text{iso}}, \quad (1.47)$$

where

$$\mathbf{S}_{\text{vol}} = 2\frac{\partial\Psi_{\text{vol}}(J)}{\partial\mathbf{C}} = Jp_h\mathbf{C}^{-1} \quad \text{and} \quad \mathbf{S}_{\text{iso}} = 2\frac{\partial\Psi_{\text{iso}}(\bar{\mathbf{C}})}{\partial\mathbf{C}} = J^{-2/3}\text{Dev}\bar{\mathbf{S}}, \quad (1.48)$$

and where the hydrostatic pressure p_h and the fictitious second Piola-Kirchhoff stress tensor $\bar{\mathbf{S}}$ are defined by

$$p_h = \frac{d\Psi_{\text{vol}}(J)}{dJ} \quad \text{and} \quad \bar{\mathbf{S}} = 2\frac{\partial\Psi_{\text{iso}}(\bar{\mathbf{C}})}{\partial\bar{\mathbf{C}}}, \quad (1.49)$$

and where the Lagrangian deviatoric operator is defined by the relation $\text{Dev}(\bullet) = (\bullet) - (1/3)[(\bullet) : \mathbf{C}]\mathbf{C}^{-1}$ so that $\text{Dev}\bar{\mathbf{S}} : \mathbf{C} = 0$ is fulfilled, (the symbol $:$ denotes the double contraction operation).

In terms of the Cauchy stress tensor, the same procedure is only possible for isotropic materials, where the decoupled strain-energy function may be formulated as $\Psi(\mathbf{b}) = \Psi_{\text{vol}}(J) + \Psi_{\text{iso}}(\bar{\mathbf{b}})$ and where an additive split of the Cauchy stress tensor leads to $\boldsymbol{\sigma} = \boldsymbol{\sigma}_{\text{vol}} + \boldsymbol{\sigma}_{\text{iso}}$. However, since none of the materials covered in this theses are isotropic, those terms will not be explicitly given here.

The Cauchy stress tensor for an anisotropic nearly incompressible material is instead given by a push-forward transformation, using (1.7), of the second Piola-Kirchhoff stress tensor, $\mathbf{S} = \mathbf{S}_{\text{vol}} + \mathbf{S}_{\text{iso}}$, according to

$$\boldsymbol{\sigma} = J^{-1}\chi_*(\mathbf{S}^\sharp) = 2J^{-1}\mathbf{F} \left(\frac{\partial\Psi_{\text{vol}}(J)}{\partial\mathbf{C}} + \frac{\partial\Psi_{\text{iso}}(\bar{\mathbf{C}})}{\partial\mathbf{C}} \right) \mathbf{F}^T \quad (1.50)$$

which yields the components

$$\boldsymbol{\sigma}_{\text{vol}} = p\mathbf{I} \quad \text{and} \quad \boldsymbol{\sigma}_{\text{iso}} = J^{-1}\bar{\mathbf{F}}(\mathbb{P} : \bar{\mathbf{S}})\bar{\mathbf{F}}^T, \quad (1.51)$$

where the projection tensor $\mathbb{P} = \mathbb{I} - 1/3\mathbf{C}^{-1} \otimes \mathbf{C}$ is used and \mathbb{I} is the fourth-order identity tensor, (the symbol \otimes denotes the dyadic (tensor) product operation).

The elasticity tensor, needed in computational solutions of nonlinear boundary-value problems, is in terms of \mathbf{E} , \mathbf{C} or $\Psi(\mathbf{C})$ retrieved as

$$\mathbb{C} = \frac{\partial\mathbf{S}(\mathbf{E})}{\partial\mathbf{E}} = 2\frac{\partial\mathbf{S}(\mathbf{C})}{\partial\mathbf{C}} = 4\frac{\partial^2\Psi(\mathbf{C})}{\partial\mathbf{C}\partial\mathbf{C}}. \quad (1.52)$$

In a decoupled form, $\mathbb{C} = \mathbb{C}_{\text{vol}} + \mathbb{C}_{\text{iso}}$ may be obtained, e.g., using (1.52)₂, by

$$\mathbb{C}_{\text{vol}} = 2\frac{\partial\mathbf{S}_{\text{vol}}}{\partial\mathbf{C}} \quad \text{and} \quad \mathbb{C}_{\text{iso}} = 2\frac{\partial\mathbf{S}_{\text{iso}}}{\partial\mathbf{C}}. \quad (1.53)$$

The elasticity tensor in the deformed configuration, labeled \mathbb{c} , may be obtained using the Piola transformation of \mathbb{C} on each large index according to

$$\mathbb{c} = J^{-1}\chi_*(\mathbb{C}), \quad \text{or in index notation} \quad c_{abcd} = J^{-1}F_{aA}F_{bB}F_{cC}F_{dD}C_{ABCD}. \quad (1.54)$$

1.2.6. Invariant formulation

For an isotropic hyperelastic material the strain-energy function may be written in terms of the principal invariants as

$$\Psi(\mathbf{C}) = \Psi(I_1, I_2, I_3), \quad (1.55)$$

where these invariants are given by

$$I_1(\mathbf{C}) = \text{tr}\mathbf{C} = \lambda_1^2 + \lambda_2^2 + \lambda_3^2, \quad (1.56)$$

$$I_2(\mathbf{C}) = \frac{1}{2}[(\text{tr}\mathbf{C})^2 - \text{tr}\mathbf{C}^2] = \lambda_1^2\lambda_2^2 + \lambda_1^2\lambda_3^2 + \lambda_2^2\lambda_3^2, \quad (1.57)$$

$$I_3(\mathbf{C}) = \det\mathbf{C} = \lambda_1^2\lambda_2^2\lambda_3^2. \quad (1.58)$$

For an anisotropic material with a directionally dependent orientation, say in a fiber family direction \mathbf{a}_0 , a pseudo-invariant I_4 may be formulated as

$$I_4 = \mathbf{F}\mathbf{a}_0 \cdot \mathbf{F}\mathbf{a}_0 = \mathbf{a}_0 \cdot \mathbf{C}\mathbf{a}_0 = \mathbf{C} : \mathbf{A}_0 = \lambda_a^2, \quad (1.59)$$

where $\mathbf{A}_0 = \mathbf{a}_0 \otimes \mathbf{a}_0$ is a structure tensor and λ_a is the stretch in the fiber direction. The invariant I_4 is thus equal to the square of the stretch in the direction of the fiber family. An additional invariant for the fiber family \mathbf{a}_0 is given by

$$I_5 = \mathbf{a}_0 \cdot \mathbf{C}^2 \mathbf{a}_0 = \mathbf{C}^2 : \mathbf{A}_0, \quad (1.60)$$

although this invariant has no physical interpretation. If an additional fiber family is present, say in the direction \mathbf{g}_0 , the equivalent invariants to (1.59) and (1.60) are given by

$$I_6 = \mathbf{C} : \mathbf{G}_0 = \lambda_g^2 \quad \text{and} \quad I_7 = \mathbf{C}^2 : \mathbf{G}_0, \quad (1.61)$$

where λ_g is the stretch in the direction of the second fiber family and $\mathbf{G}_0 = \mathbf{g}_0 \otimes \mathbf{g}_0$. Further, a coupling invariant between these two fiber families may be defined as

$$I_8 = \mathbf{a}_0 \cdot \mathbf{C}\mathbf{g}_0. \quad (1.62)$$

A hyperelastic anisotropic material with two fiber families may thus be represented by the strain-energy function $\Psi = \Psi(\mathbf{C}, \mathbf{A}_0, \mathbf{G}_0) = \Psi(I_1, \dots, I_8)$ and the stress response may thus be retrieved as

$$\mathbf{S} = 2 \frac{\partial \Psi(I_1, \dots, I_8)}{\partial \mathbf{C}} = 2 \sum_{a=1}^8 \frac{\partial \Psi(I_1, \dots, I_8)}{\partial I_a} \frac{\partial I_a}{\partial \mathbf{C}}, \quad (1.63)$$

using the chain-rule. For some deformation modes, all eight invariants are not independent why the number of invariants used may be reduced. Also, through (1.46)₁, the isochoric counterpart of the invariants are simply retrieved as, e.g., $\bar{I}_4 = \bar{\mathbf{C}} : \mathbf{A}_0 = J^{-2/3} I_4$.

1.2.7. Strong and weak form of a boundary-value problem

In finite element simulations of biological tissues the weak formulation of the boundary-value problem needs to be formulated. This section, therefore, shows one example of how to form the strong and weak equations needed for solving a finite deformation elasticity equations in a left ventricular (LV) passive cardiac mechanical simulation. It is, however, equally valid for arterial mechanical simulations.

In LV mechanical problems, the following static mechanical equilibrium mixed boundary-value problem, in the material (reference) configuration, is often posed,

$$\text{Div}(\mathbf{FS}) = \mathbf{0} \quad \text{in} \quad \Omega_0 \quad (1.64a)$$

$$\mathbf{FSN} = -pJ(\mathbf{F}^{-1})^T \mathbf{N} \quad \text{on} \quad \partial\Omega_{0t1} \quad (1.64b)$$

$$\mathbf{FSN} = \mathbf{0} \quad \text{on} \quad \partial\Omega_{0t2} \quad (1.64c)$$

$$\mathbf{u}(\mathbf{X}) = \mathbf{0} \quad \text{on} \quad \partial\Omega_{0u1} \quad (1.64d)$$

where $\text{Div}(\bullet)$ denotes the divergence operator with respect to the reference configuration and \mathbf{N} is the surface normal of the body Ω_0 . Equation (1.64b) is the natural boundary condition where a pressure p is applied (the surface $\partial\Omega_{0t1}$ is usually defined as the endocardial surface of the LV). Equation (1.64c) is the natural boundary condition which is traction free (the surface $\partial\Omega_{0t2}$ is usually defined as the epicardial surface of the LV) and (1.64d) is the essential condition of a zero displacement surface (the surface $\partial\Omega_{0u1}$ is often defined as the basal plane of a truncated LV). Also other more complex boundary conditions may be used where, e.g., the entire surface $\partial\Omega_{0u1}$ is not displacement free or where displacements are prescribed in certain directions.

The pressure loading (1.64b) is a follower load, i.e. it is deformation dependent, and is, in general, not conservative and can not be derived from a potential [191]. The principal of virtual work is, therefore, not used as the basis for the finite element solution method. Instead, the weak formulation is derived directly from the strong formulation, i.e. the equations in (1.64), in the following manner; let $\boldsymbol{\phi} = \boldsymbol{\phi}(\mathbf{X})$ be a suitable vector-valued test function that is satisfying homogeneous prescribed displacement boundary conditions, i.e. $\boldsymbol{\phi} = \mathbf{0}$, on $\partial\Omega_{0u1}$. By forming the inner product of Eq. (1.64a) with $\boldsymbol{\phi}$ and integrating over the domain Ω_0 , the weak equilibrium equations are obtained. By using the identity

$$\boldsymbol{\phi} \cdot \text{Div}(\mathbf{FS}) = \text{Div} [(\mathbf{FS})^T \boldsymbol{\phi}] - \text{Tr} [(\mathbf{FS})^T \text{Grad} \boldsymbol{\phi}], \quad (1.65)$$

we get

$$\int_{\Omega_0} \text{Div}(\mathbf{FS}) \cdot \boldsymbol{\phi} \, dv = \int_{\Omega_0} \text{Div} [(\mathbf{FS})^T \boldsymbol{\phi}] \, dv - \int_{\Omega_0} \text{Tr} [(\mathbf{FS})^T \text{Grad} \boldsymbol{\phi}] \, dv = 0. \quad (1.66)$$

Further, by using Gauss' divergence theorem

$$\int_{\Omega_0} \text{Div} [(\mathbf{FS})^T \boldsymbol{\phi}] \, dv = \int_{\partial\Omega_0} [(\mathbf{FS})^T \boldsymbol{\phi}] \cdot \mathbf{N} \, dA, \quad (1.67)$$

we get

$$\int_{\Omega_0} \text{Tr}(\mathbf{SF}^T \text{Grad} \boldsymbol{\phi}) \, dv - \int_{\partial\Omega_0} \mathbf{FSN} \cdot \boldsymbol{\phi} \, dA = 0, \quad (1.68)$$

where the relations $\mathbf{S} = \mathbf{S}^T$ and $[(\mathbf{F}\mathbf{S})^T \boldsymbol{\phi}] \cdot \mathbf{N} = (\mathbf{F}\mathbf{S}\mathbf{N}) \cdot \boldsymbol{\phi}$ are used. Given the load p (and potential boundary displacements), as well as the necessary material data specifying the material function in, e.g., (1.47) and (1.48), we obtain the weak equilibrium formulation by finding the displacement \mathbf{u} such that

$$\int_{\Omega_0} \text{Tr} [\mathbf{S}(\mathbf{F}^T \text{Grad} \boldsymbol{\phi})^S] dv + \int_{\partial\Omega_{0t1}} pJ(\mathbf{F}^{-1})^T \mathbf{N} \cdot \boldsymbol{\phi} dA = 0 \quad \text{in } \Omega_0 \quad (1.69a)$$

$$\mathbf{u}(\mathbf{X}) = \mathbf{0} \quad \text{on } \partial\Omega_{0u1} \quad (1.69b)$$

is satisfied. Note that only the symmetric part, denoted $(\bullet)^S$, will remain of $\mathbf{F}^T \text{Grad} \boldsymbol{\phi}$ using a Cartesian decomposition. Furthermore, the discrete equations can instead be written in terms of the displacements as $\mathbf{F}(\mathbf{u}) = \mathbf{0}$, which is nonlinear in \mathbf{u} . By using an incremental iterative Newton-Raphson procedure, the solution \mathbf{u} , for a given p (and potential boundary displacements), is found. The equations in (1.69) may be used as a foundation for the finite element equations formed using, e.g., the multipurpose finite element software FEAP, but is often pushed forward to the spatial (deformed) configuration, see [164, 191] for more details.

Regardless of which material that is studied, or which numerical solution scheme that is used to model it, the constitutive models should try to capture the material behavior to ‘some’ desired accuracy, and thus it is essential to understand the underlying mechanics of the material that is studied. The following two sections, therefore, describe the constituents and material behavior of a cerebral aneurysm and of the myocardium.

1.3. Cerebral Aneurysms

A cerebral aneurysm is an unhealthy dilation of the arterial vessels in the brain. In contrast to abdominal aneurysm, which are fusiform in shape, cerebral aneurysms are often saccular, or berry shaped. They are present in 2–5 % of the general population and if ruptured have a high mortality and morbidity rate [173]. However, most often a cerebral aneurysm grows in a stable manner and only ruptures in 1.3 % cases per year [70]. Cerebral aneurysms are generally found at arterial bifurcations, with the majority at the anterior part of the Circle of Willis [6].

1.3.1. Arterial wall

The artery surrounding the aneurysm is often healthy and consists of three layers as seen in Fig. 1.2, the intima which is the innermost layer, the media which is the middle and thickest layer and the adventitia which is the outermost layer. In healthy or young arteries, the intimal layer is a very thin sheet consisting of endothelial cells laying on a basal membrane and is often considered not to bear any load. With age or disease, however, it becomes significantly thicker and the no-load bearing assumption is no longer valid [59]. The media is a relatively thicker layer and consists of smooth muscle cells, elastin and collagen fibrils.

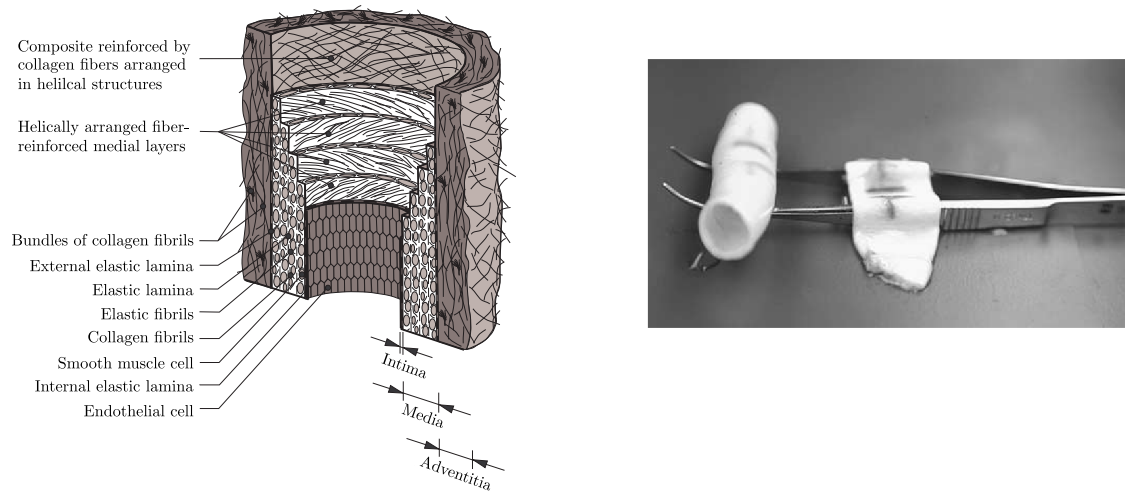


Figure 1.2.: Diagram showing the components of a healthy artery and the three layers intima, media and adventitia (left panel). Mechanically separated medial and adventitial layers (right panel) into a stiff medial tube, shown on the left side, and the limp adventitia, shown to the right, adapted from [54].

The smooth muscles can contract and thus alter the diameter and flow through the artery. The collagen fibrils are arranged in a helical pathway, but with a small pitch, making them nearly circumferential in orientation [54]. The media is fairly stiff even at a load-free configurations, as seen in Fig. 1.2. The adventitia is composed mainly of collagen which are arranged in a helical structure to reinforce the arterial wall. The adventitia is soft at low loads, or a load-free state, as seen in Fig. 1.2, but stiffens significantly at higher loads and is thus thought to protect the artery from rupture at instances of increased blood pressure [54].

In addition, the arterial wall is residually stressed. However, as shown by Holzapfel et al. [58], each layer of the artery is stressed in different directions. Thus, a single material parameter, such as the opening angle suggested by Liu and Fung [88], is not enough to characterize the three-dimensional residual stress state of arteries.

1.3.2. Evolving aneurysm

Structural changes in arterial walls and, more specifically, structural evolution of developing aneurysms have been addressed in several studies. Different approaches are used, but the continuous turnover of collagen fibers is widely accepted to be the driving mechanism in the development of aneurysms. Humphrey and Rajagopal [65] suggest a general theoretical framework for growth and remodeling of soft tissues, incorporating collagen turnover. This framework is utilized by Baek et al. [7], who model aneurysm growth and assume that the collagen production rate is governed by the current in-plane wall stress of the aneurysm. They also assume that the orientation of newly deposited collagen is governed by a specific criterion, based on the principal stresses or stretches in the aneurysm

wall, and the outcome for different criteria is evaluated. Driessen et al. [34] also model collagen remodeling in an artery wall. In that study, the collagen fibers are assumed to be aligned in a few fiber directions, and these alignments are assumed to evolve depending on the principal stretches in the material.

Watton et al. [178] model aneurysm growth by assuming that collagen fibers are continuously attached in a pre-stretched state and configured such that the strain in these fibers at systole is constant. Kroon and Holzapfel [82] presented a theoretical model for the growth of a saccular cerebral aneurysm. The growth model was assessed for an axisymmetric problem, where the aneurysm was described as a circular membrane hinged along the boundary and exposed to an inflation pressure. The aneurysm wall was assumed to consist of a number of distinct collagen fiber layers. The continuous turnover of collagen in the layers was responsible for the growth of the aneurysm, and the collagen production in the layers was driven by a deformation measure. A parameter study was performed to outline the general behavior of the model, and a stability analysis was provided. In Chapter 2, this model is used to investigate the influence of an anisotropic medial layer on an evolving cerebral aneurysm and the effects of axial in situ stretch.

1.4. Cardiac Mechanics

The heart is a complex organ which essentially acts as an electro-mechanical pump of blood. It is comprised of four chambers, the right and left atrium and the right and left ventricles. Oxygen poor blood enters the right atrium from the superior and inferior vena cava, as well as the coronary sinus. The right atrium pumps the blood through the tricuspid valve into the right ventricle which in turn pumps the blood through the pulmonary valve and pulmonary trunk into the pulmonary artery and lungs where the blood gets re-oxygenated. Oxygen rich blood enters the left atrium from the pulmonary veins and pumps it through the mitral valve to the left ventricle. Finally, the left ventricle pumps the blood through the aortic valve into the aorta where it continues throughout the body via the aortic tree. The heart itself is supplied by blood from the right coronary artery which is attached to the aortic branch.

The heart wall is comprised of three layers, the endocardium which is the innermost layer, the myocardium which is the middle layer and the epicardium which is the outermost layer. The heart is enclosed in a fluid which is contained in a doubled-walled sac (the pericardium), which keeps the motion of the heart frictionless against the surrounding tissue, where the innermost layer of the pericardium is connected to the epicardium which is a thin protective layer of connective tissue. Also the endocardium is a very thin layer but is comprised of cells similar to the endothelial cells of arteries. The myocardium, on the other hand, is by far the thickest of the three layers. It is comprised of striated muscle cells (myocytes), which work together to generate the contraction of the heart and is thus responsible for the large pumping force.

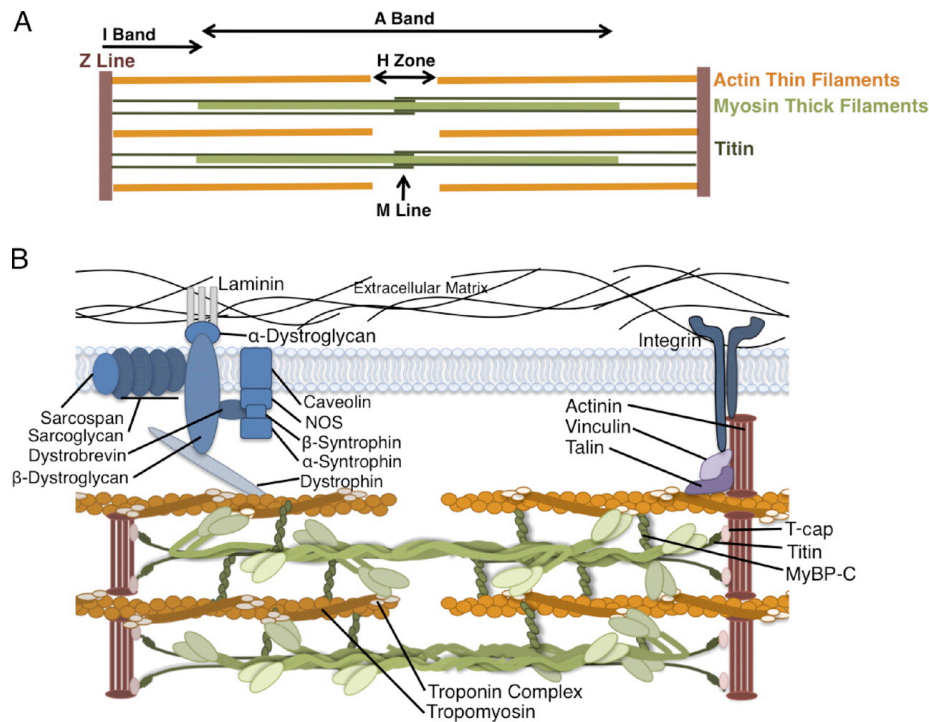


Figure 1.3.: Simplified model showing the basic organization of a sarcomere (top) and a representation of the major proteins of a sarcomere (bottom), adapted from [51].

1.4.1. Contractile unit

Each myocyte is built up of myofibrils which in turn contains several sarcomeres. The sarcomeres, shown in Fig. 1.3, are the basic building blocks of the cardiac muscle and are what causes the heart to contract by sliding actin and myosin filaments (thin and thick filaments, respectively) along each other. In order for sliding to be achieved, calcium ions have to bind to the tropomyosin (on troponin-C molecules) which covers the actin filaments, thus altering the tropomyosin and exposing binding sites where cross-bridges can be formed between myosin heads and the actin filament. The myosin heads are bound to an adenosine diphosphate (ADP) and a phosphate ion in the resting position (a resting position is when the myosin head is not attached to the actin filament, but where the myosin head is in a high-energy configuration). The exposure of the binding site on the actin filament causes the myosin head to connect, forming a cross-bridge, and release the attached phosphate. The remaining ADP is released causing the myosin head, still attached to the actin filament, to move in a power-stroke that also moves the actin filament. After the power-stroke, an adenosine triphosphate (ATP) molecule is attached to the myosin head, causing a release of the cross-bridge. The myosin head now hydrolyzes the ATP into ADP and a phosphate ion, causing a recovery stroke in which a release of energy moves the head back to its resting, but high-energy, configuration. This sequence of power-strokes and recovery strokes are

repeated until the calcium ions are removed and the binding sites on the actin filaments are again covered by the tropomyosin.

The increase in calcium in a myocyte, responsible for the contraction, is triggered by a phenomenon called calcium-induced calcium release. An action potential travels through gap junctions to the contractile unit where it travels through the T-tubules in the Z-band (seen in Fig. 1.3 top panel). There, the potential triggers a flux of calcium ions through L-type calcium channels into the cell. Inside the cell, the sarcoplasmic reticulum contains a large storage of calcium ions and it has the possibility to sense the flux increase of calcium ions to the cytosol. When the sarcoplasmic reticulum senses this increase, it triggers an additional release of its stored calcium ions which can then bind to the troponin-C molecules. During muscle relaxation, the calcium ions in the cytosol are again retained in the sarcoplasmic reticulum.

The action potential is generated by the pacemaker cells located at the sinoatrial node in the right atrium. The pacemaker cells are modified myocytes which do not contract, but instead spontaneously discharge. The action potential travels from the sinoatrial node to the myocytes via a fast conduction network called the Purkinje system (PS). The Purkinje fibers comprising this complex three-dimensional system are modified myocytes which end at Purkinje-ventricular junctions. These sites may be viewed as point sources of electrical wavefronts to the myocardium. The electrical wavefront in the myocardium travels at different speeds determined by the structure of the myocardium (as described in Section 1.4.2) and is fastest along the myocyte fiber direction and slowest in the sheet-normal direction.

1.4.2. Structural organization of the myocardium

In general, myocyte orientation in the LV follows a right-handed helical pathway from the endocardium towards the mid-wall, and a left-handed helical pathway from the mid-wall towards the epicardium [93, 135, 169], as shown in Fig. 1.4 (a). As described by, e.g., Hort [63], the myocytes are further bundled into layers that are four to six cells thick creating sheets as shown in Fig. 1.4 (b). The orientation of the sheets vary both transmurally and in the apico-basal direction [85, 135, 142, 190]. Labeling the local myocyte direction as the fiber direction, we may thus characterize the myocardium as an orthotropic material with a fiber, sheet and sheet-normal direction labeled f , s and n , respectively.

In addition, the fiber alignment in the helical pathway is quite strong in a healthy heart where the angular dispersion (AD) is only $\sim 12\text{-}15^\circ$. In a diseased heart, e.g., with hypertrophic cardiomyopathy (HCM), the AD may locally increase to $\sim 25^\circ$ [71, 72, 171]. An increased disarray in both collagen and muscle fiber orientation is also found in other diseases, such as myocardial infarction [157, 181, 192]. Experiments have further shown that in healthy hearts, the sheet direction is also locally dispersed [28, 62, 143] and although it

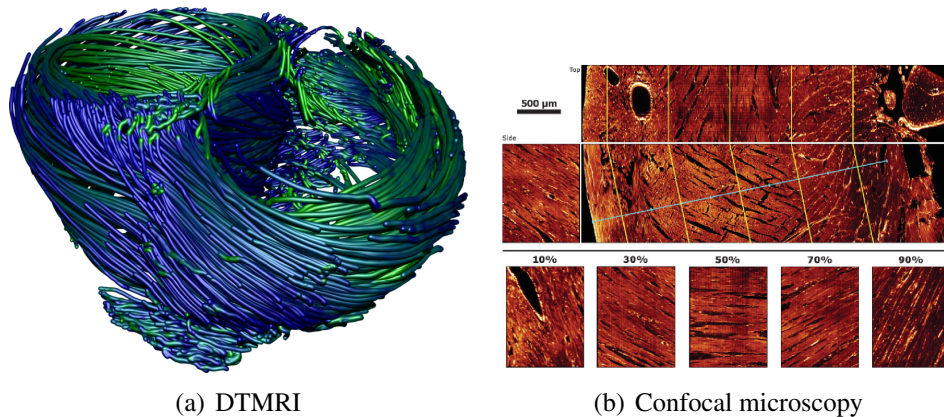


Figure 1.4.: Fiber and sheet orientation in the ventricular wall: (a) diffusion tensor magnetic resonance imaging (DTMRI) showing the helical structure of the myocyte orientation, adapted from [135]; (b) confocal microscopy showing the sheet structure (top) and the transmural change in the fiber structure (bottom), adapted from [142].

has not been studied in as great detail as that of the fiber direction, it may still play a significant role in the function of myocardium [21]. However, further experiments quantifying the sheet dispersion on diseased human hearts are needed as no data is available today.

1.4.3. Modeling cardiac mechanics

In its simplest form, the heart can be considered to act as a pump generating pressure and blood flow. This inspired early work to model the tension in the heart wall using the law of Laplace for thin walled spheres [186]. Although this method provides an easy way to calculate wall stresses based on pressure and dimension, it does not capture any mechanical properties of the myocardium. Linear strain theory was later used in an attempt to capture the distribution of stresses within the ventricular wall [185], but as the deformations in many biological tissues can exceed 50–100%, small strain theory has been shown to yield unrealistic stress values [96]. Nonlinear finite deformation theory has now become the standard tool, used together with the finite element method (FEM), to solve the complex boundary-value problem associated with the heart. It has enabled the incorporation of complex geometrical description, anisotropic fiber reinforcement and many different constitutive models.

Constitutive models for myocardium. For myocardium, constitutive models often assumed that the tissue is hyperelastic and thus can be characterized by a strain-energy function, as shown in Section 1.2.4. Models for myocardium that includes the muscle fiber response are either i) transversely isotropic models or ii) orthotropic models. As pointed out in an excellent review of cardiac models by Holzapfel and Ogden [56], the transversely isotropic models does not capture the orthotropic behavior of myocardium, but they may

nevertheless be useful as they often contain fewer material parameters which may be more easily determined in vivo [106]. Common transversely isotropic models are the exponential Fung-type models (based on [43]), e.g., the model developed by Omens et al. [113],

$$\Psi(\mathbf{E}) = \frac{1}{2}a[\exp(Q) - 1], \quad (1.70)$$

where

$$Q = b_1 E_{\text{ff}}^2 + b_2 (E_{\text{ss}}^2 + E_{\text{nn}}^2 + E_{\text{sn}}^2) + 2b_3 (E_{\text{fs}}^2 + E_{\text{fn}}^2), \quad (1.71)$$

or the model by Costa et al. [24] where Q changes to

$$Q = 2b_1 (E_{\text{ff}} + E_{\text{ss}} + E_{\text{nn}}) + b_2 E_{\text{ff}}^2 + b_3 (E_{\text{ss}}^2 + E_{\text{nn}}^2 + 2E_{\text{sn}}^2) + 2b_4 (E_{\text{fs}}^2 + E_{\text{fn}}^2), \quad (1.72)$$

and f, s and n pertain to the fiber, sheet and sheet-normal directions, respectively.

For models that can capture the orthotropic behavior of myocardium, a common exponential Fung-type models is, e.g., the model developed by Costa et al. [22], where $\Psi(\mathbf{E})$ is given by (1.70) and Q takes the form

$$Q = b_{\text{ff}} E_{\text{ff}}^2 + b_{\text{ss}} E_{\text{ss}}^2 + b_{\text{nn}} E_{\text{nn}}^2 + b_{\text{fs}} E_{\text{fs}}^2 + b_{\text{fn}} E_{\text{fn}}^2 + b_{\text{sn}} E_{\text{sn}}^2. \quad (1.73)$$

The advantage of this model is that it only has 7 material parameters, however, although interpretations for the material parameters were attempted by Costa et al. [22], those parameters are all coupled through a in (1.70), which means that their individual parameter interpretation is questionable. Other orthotropic models are motivated by equi-biaxial tension tests, e.g., the pole-zero model developed by Hunter et al. [68],

$$\begin{aligned} \Psi(\mathbf{E}) = & \frac{k_{\text{ff}} E_{\text{ff}}^2}{|a_{\text{ff}} - |E_{\text{ff}}||^{b_{\text{ff}}}} + \frac{k_{\text{fn}} E_{\text{fn}}^2}{|a_{\text{fn}} - |E_{\text{fn}}||^{b_{\text{fn}}}} + \frac{k_{\text{nn}} E_{\text{nn}}^2}{|a_{\text{nn}} - |E_{\text{nn}}||^{b_{\text{nn}}}} \\ & + \frac{k_{\text{fs}} E_{\text{fs}}^2}{|a_{\text{fs}} - |E_{\text{fs}}||^{b_{\text{fs}}}} + \frac{k_{\text{ss}} E_{\text{ss}}^2}{|a_{\text{ss}} - |E_{\text{ss}}||^{b_{\text{ss}}}} + \frac{k_{\text{ns}} E_{\text{ns}}^2}{|a_{\text{ns}} - |E_{\text{ns}}||^{b_{\text{ns}}}}. \end{aligned} \quad (1.74)$$

Here the material parameters are more easily related to the principal directions of the material, however, the obvious drawback is that the model needs 18 material parameters, see Schmid et al. [146, 147] for a discussion on the fit of these models to the experimental data of Dokos et al. [32].

Both the orthotropic ‘Costa’ model and the pole-zero model uses the material strain to define the strain-energy function, and through the relations $2E_{ii} = I_{4i}$, where $i \in \{f, s, n\}$ and $2E_{ij} = I_{8ij}$, where $i \neq j$, they may be seen as a special case of the model developed by Holzapfel and Ogden [56], which uses the strain (and pseudo) invariants according to

$$\begin{aligned} \Psi(I_1, I_{4f}, I_{4s}, I_{8fs}) = & \frac{a}{2b} \{\exp[b(I_1 - 3)] - 1\} + \sum_{i=f,s} \frac{a_i}{2b_i} \{\exp[b_i(I_{4i} - 1)^2] - 1\} \\ & + \frac{a_{\text{fs}}}{2b_{\text{fs}}} [\exp(b_{\text{fs}} I_{8\text{fs}}^2) - 1]. \end{aligned} \quad (1.75)$$

This model is micro-structurally based with only eight material parameters and each term in the strain-energy function has a clear physical interpretation, see [56] for details.

Myocardial stress. Constitutive models are used to determine the passive stress in the myocardium, i.e. the stress in the tissue due to the deformation. This deformation, in turn, originates from the contraction of the myocytes and is often modeled using either the active strain approach or the active stress approach, see [1, 137] for a review of these approaches. In the active strain approach, the deformation gradient \mathbf{F} is multiplicatively decomposed into an active part \mathbf{F}_a , described by a constitutive relations that does not store energy, and an elastic part \mathbf{F}_e , described by a passive constitutive model [100, 161]. In the active stress approach, the stress tensor $\boldsymbol{\sigma}$ (defined in Section 1.2.5) is additively decomposed into an active stress tensor $\boldsymbol{\sigma}_a$ and a passive stress tensor $\boldsymbol{\sigma}_p$ [119, 154]. The active stress can be modeled in several ways. A popular approach is to use a cellular tension model calculated either from the ionic concentrations [102, 107] or directly from the electrical potential [103]. It has also been proposed to additively separate the strain-energy function Ψ into an active part Ψ_a and a passive part Ψ_p [177]. However, as pointed out by Skallerud et al. [152], such a function Ψ_a is not a true strain-energy function but merely a term that generate the active stress tensor, see Trayanova and Rice [166] for an excellent review of active cardiac electro-mechanical models and coupling.

Cardiac electro-physiology. The myocardium is often approximated as a continuous media of electrical activation and repolarization. Two common models describing this behavior are the reaction-diffusion equations referred to as the bidomain or monodomain models [160]. Through a conductivity tensor present in these models, with the eigenaxes in the fiber, sheet and sheet-normal directions, the wavefront of electrical activation spreads with a ratio 3:2:1 along the three axis, respectively [10, 12, 144]. To generate the action potential, many generic models are based on the famous Hodgkin-Huxley model for currents in an axon [52], which was reduced to a two-variable model in the FitzHugh-Nagumo model [41]. Phenomenological models, such as the Fenton-Karma or the Mahajan models [39, 91], are also used because of the simplicity to fit these models directly to experimental data, see Clayton et al. [20] for a review of models for cardiac tissue electrophysiology.

Electro-mechanical coupling. To couple the multi-scale tissue models and the biophysical models a variety of techniques are available. Perhaps the simplest and most often used technique is the weakly coupled approach [77]. In this approach, it is assumed that the mechanics has a limited influence on the electrophysiology so the electrical quantities are first calculated separately and then relevant parameters are fed into a mechanical simulation of deformation and stress. The main advantages of the weakly coupled approach is its simplicity, stability and low computation time [128]. In the strongly coupled approach it is instead assumed that the mechanical quantities influence the electrophysiology. The mechanical quantities are, therefore, continuously passed back to the electrical simulation which enables the modeling of subtle effects such as myocardial mechano-electrical feedback [103, 117]. The strongly coupled approach is more complex than the weakly coupled approach and it is prone to numerical instabilities, although those issues are being

addressed [107, 120], see Nordsletten et al. [111] for a review on issues of coupling the multi-physics models to cardiac mechanics.

Pressure calculations. The pressure volume relation in cardiac ventricular simulations are often modeled to follow the classical pressure volume loops as defined by experiments, see, e.g., [140]. This entails that the follower type pressure load p is calculated in five consecutive steps. The first step is an initialization load, where the pressure is increased linearly to the end diastolic pressure. This represent the filling of blood into the ventricle, which at this point is in a relaxed state. The second step involves an isochoric (volume preserving) contraction as both the mitral and aortic valves are considered to be closed while the ventricle is contracting. The third load step is the ejection phase. This represent the release of blood from the ventricle as the aortic valve opens. The fourth load step is again an isochoric deformation, this time as the ventricle is relaxing, while the aortic valve is closed to hinder regurgitation (back-flow). In the fifth and final step, the pressure and volume is increasing again as the mitral valve opens and blood enters the ventricle. In simulations of several heart beats, the cycle then starts over from the second load step.

The first and fifth load steps are usually simulated using a linear increase of pressure. The two isochoric loads, steps 2 and 4, may be calculated iteratively for each time step to keep the volume V constant using $p_{n+1} = p_n + (V_{n+1} - V_n)/C_p$ as described in [168], where C_p is a penalty parameter. The value of C_p is then set to give a computationally efficient convergence for the isochoric solution.

The ejection phase, load step 3, is often calculated using the 2, 3 or 4-element Windkessel models. The two element Windkessel model [116], for example, is described as

$$C \frac{dp}{dt} + \frac{p}{R} = -\frac{dv}{dt}, \quad (1.76)$$

where C and R relate to arterial compliance and resistance, respectively. Most often C and R are considered constants, and do not account for the nonlinear behavior of arteries [130, 131]. Equation (1.76) may, e.g., be solved iteratively as described in Kerckhoffs et al. [76], or alternatively, to achieve both the isochoric deformation and the Windkessel deformations, the pressure and volume change can directly be prescribed in the finite deformation elasticity equations, i.e., make them part of Eq. (1.69).

1.5. Organization of the Thesis

The thesis is a compilation of five scientific papers, which focus on different computational aspects in biomechanics. The papers span from modeling the growth of a cerebral aneurysm to simulating the behavior of the left ventricle with an emphasis on the material behavior. The papers are presented in the following chapters:

2. *'Influence of Medial Collagen Organization and Axial In Situ Stretch on Saccular Cerebral Aneurysm Growth'*, T.S.E. Eriksson, M. Kroon and G.A. Holzapfel, ASME Journal of Biomechanical Engineering, 131:101010 (7 pages), 2009

The study focuses on the influence of an anisotropic medial layer on an evolving cerebral aneurysm. The middle cerebral artery is modelled as a two-layered cylinder, where the layers correspond to the media and the adventitia. Local and instant loss of media is considered responsible for the aneurysm growth. The adventitia is composed of several distinct layers with collagen fibers that are the only load bearing constituent in the aneurysm wall. Their production and degradation are depending on the stretch of the wall and are also responsible for the growth of the aneurysm. The anisotropy of the medial layer is modeled using a strain-energy function valid for an elastic material with two families of fibers. The results shows that including fiber reinforcement in the medial layer reduces the maximum principal stress, thickness increase and shear stress in the aneurysm wall. A variation of the initial fiber angles is shown to have little effect whereas the axial in situ stretch has a much larger effect in terms of shape and stresses in the aneurysm wall.

3. *'Tensors Needed for Finite Element Implementation of an Invariant Based Constitutive Model for Passive Myocardium'*, T.S.E. Eriksson, G. Plank and G.A. Holzapfel

The study focuses on the constituents needed for implementation of an invariant based orthotropic model for passive myocardium. The stress and elasticity tensors are shown together with a fit of the model to experimental data. A comparison is made between the proposed invariant based model and a commonly used Green-Lagrange strain based model and it is shown that using material parameters retrieved when both models are fitted against a simple shear mode experiment, the proposed model is better suited to predict the stress in the myocardium for other modes of deformation. In addition, the finite element implementation is used on a model of the left ventricle and it is shown that passively increasing the pressure on the endocardial wall results in steep stress gradients through the wall thickness. This suggests that residual stresses may need to be included in future models.

4. *'Influence of Spatial Heterogeneity in Tissue Orthotropy upon Mechanical Contraction in the Left Ventricle'*, T.S.E. Eriksson, A.J. Prassl, G. Plank and G.A. Holzapfel

The study focuses on spatial heterogeneity in myocardial tissue. A coupled model of the left ventricle was presented where pressure was calculated as a response to change in internal volume. The passive behavior was modeled as a hyperelastic material using an orthotropic strain-energy function and an evolution equation was used to generate the active stresses. The influence of myocardial fiber and sheet distributions was investigated by using two different fiber and sheet distribution setups, a generic setup and one based on experiments. It was found that spatial heterogeneity

may play a critical role in mechanical contraction of the LV and that geometrical descriptions of deformations are needed when evaluating the accuracy of a ventricular model.

5. '*Modeling the Disarray in Cardiac Fiber and Sheet Orientations*', T.S.E. Eriksson, A.J. Prassl, G. Plank and G.A. Holzapfel

The study focuses on a novel approach to model the disarray of both fiber and sheet orientations in cardiac tissue. A material structure parameter describing the relation between an isotropic invariant and a directionally dependent invariant was fitted to experimental data of angular dispersion in both the fiber and sheet direction. The parameter was used to model the dispersion in myocardial tissue by augmenting an invariant based orthotropic strain-energy function and in a structure tensor used to determine the direction of active stress. Simulations showed that dispersion has a great effect on myocardial stress and deformation development as well as on pressure volume loops of a left ventricle.

6. '*On Tension-Compression Switching in Dispersed Fiber-Reinforced Constitutive Models*', T.S.E. Eriksson, D.M. Pierce and G.A. Holzapfel

The study focuses on tension-compression switching of a dispersed fiber-reinforced constitutive model. Large-strain, fiber-reinforced constitutive models are commonly used for solving complex boundary-value problems in the context of the finite element method. Although the mathematical and physical motivation for including a tension-compression fiber 'switch' may be clear when using models which do not include fiber dispersion, neither the mathematical nor physical motivation for tension-compression fiber switching is so clear for cases where fiber-reinforced models are extended to include the effect of distributed fiber orientations. Here we explore methods to study such switching mechanisms by analyzing six potential switching cases, and draw some conclusions about the mathematical robustness and physical interpretation of the different possible approaches. We propose using two different permutations of the dispersed fiber-reinforced models, depending on whether one can assume that the fibers are (nearly) uncoupled or strongly coupled to the isotropic ground matrix.

The following conference proceedings and accepted (extended) abstracts were also part of the thesis:

- W. Rachowicz, A. Zdunek and T.S.E. Eriksson: Application of the adaptive FEM to computational biomechanics. 6th European Congress on Computational Methods in Applied Sciences and Engineering (ECCOMAS), Vienna, Austria, September 10–14, 2012.

- G.A. Holzapfel, T.S.E. Eriksson, A.J. Prassl and G. Plank: An electro-mechanically computational model for the myocardium including fiber and sheet disarray. 23rd International Congress of Theoretical and Applied Mechanics, Beijing (ICTAM), China, August 19–24, 2012.
- T.S.E. Eriksson, G. Plank and G.A. Holzapfel: A structurally motivated model for myocardial fiber and sheet disarray. 8th European Solid Mechanics Conference (ESMC), Graz, Austria, July 9–13, 2012.
- W. Rachowicz, A. Zdunek and T.S.E. Eriksson: Application of the adaptive FEM to computational biomechanics. 8th European Solid Mechanics Conference (ESMC), Graz, Austria, July 9–13, 2012.
- C. Augustin, E. Hoetzl, T.S.E. Eriksson, A.J. Prassl, G.A. Holzapfel, O. Steinbach and G. Plank: Application of advanced bidomain solver techniques to cardiac electromechanics. 8th European Solid Mechanics Conference (ESMC), Graz, Austria, July 9–13, 2012.
- G.A. Holzapfel, T.S.E. Eriksson and M. Unterberger: Structurally-based computation of the biomechanical response of cardiovascular tissues. 11th International Conference on Computational Plasticity. Fundamentals and Applications (COMPLAS XI), Barcelona, Spain, September 7–9, 2011.
- W. Rachowicz, A. Zdunek and T.S.E. Eriksson: Application of hp-adaptive FEM to medical diagnostics. Higher Order Finite Element and Isogeometric Methods (HOFEIM), Krakow, Poland, June 27-29, 2011.
- T.S.E. Eriksson, G. Plank and G.A. Holzapfel: A coupled model for the left ventricle including regional differences in structure and function, *Proceedings in Applied Mathematics and Mechanics (PAMM)*, 11:85–86, 2011.
- T.S.E. Eriksson, G. Plank and G.A. Holzapfel: A coupled model of the left ventricle including regional differences in structure and function. 82nd Annual Meeting of the International Association of Applied Mathematics and Mechanics (GAMM), Graz University of Technology, Austria, April 18-22, 2011.
- T.S.E. Eriksson, R. Höller, G. Plank and G.A. Holzapfel: New material model for the passive response of the myocardium: numerical realization and new experimental data. 6th World Congress on Biomechanics, Singapore, August 1-6, 2010.
- T.S.E. Eriksson, G. Plank and G.A. Holzapfel: A new invariant-based constitutive model for the passive response of the myocardium and constituents needed for FE implementation. 1st International Conference on Material Modelling (ICMM), Dortmund, Germany, September 15–17, 2009.

2. INFLUENCE OF MEDIAL COLLAGEN ORGANIZATION AND AXIAL IN SITU STRETCH ON SACULAR CEREBRAL ANEURYSM GROWTH

Abstract A model for saccular cerebral aneurysm growth, proposed by Kroon and Holzapfel (*J. Theor. Biol.*, 2007, 247:775–787; *J. Biomech. Eng.*, 2008, 130:051012), is further investigated. A human middle cerebral artery is modeled as a two-layer cylinder, where the layers correspond to the media and the adventitia. The immediate loss of media in the location of the aneurysm is taken to be responsible for the initiation of the aneurysm growth. The aneurysm is regarded as a development of the adventitia, which is composed of several distinct layers of collagen fibers perfectly aligned in specified directions. The collagen fibers are the only load bearing constituent in the aneurysm wall; their production and degradation depend on the stretch of the wall and are responsible for the aneurysm growth. The anisotropy of the surrounding media was modeled using the strain-energy function proposed by Holzapfel et al. (*J. Elasticity*, 2000, 61:1–48) valid for an elastic material with two families of fibers. It was shown that the inclusion of fibers in the media reduced the maximum principal Cauchy stress and the maximum shear stress in the aneurysm wall. The thickness increase of the aneurysm wall due to material growth was also decreased. Varying the fiber angle in the media from a circumferential direction to a deviation of 10° from the circumferential direction did, however, only show a little effect. Altering the axial in situ stretch of the artery had a much larger effect in terms of the steady-state shape of the aneurysm and the resulting stresses in the aneurysm wall. The peak values of the maximum principal stress and thickness increase, both became significantly higher for larger axial stretches.

2.1. Introduction

Saccular cerebral aneurysms are detected in less than 5% of the human population, and are usually diagnosed in elder people between the fifth and the seventh decade. High blood pressure, which is rather specific for man, appears to have some influence on the development of cerebral aneurysms [81]. A subarachnoid hemorrhage due to the rupture of an intracranial aneurysm is a devastating event associated with high rates of morbidity and mortality. Approximately 12% of patients die before receiving medical attention, 40% of hospitalized patients die within one month after the event, and more than one third of those who survive have major neurological deficits [145].

Cerebral aneurysms generally form and grow at arterial bifurcations in connection to the Circle of Willis, where the internal elastic membrane is partially destroyed, and where the media is diminished [6]. Approximately 80% of all these aneurysms occur at one of three main sites, i.e. the carotid/posterior communicating respectively anterior choroidal artery junction, the anterior communicating artery, and the middle cerebral artery main bifurcation [156].

Determination of the structure of the aneurysm wall is a necessary precursor to establish suitable constitutive relations for this type of tissue. For this purpose, experimental investigations of aneurysmal tissue, for example, in terms of tensile testing and histological examinations, are necessary, but theoretical modeling may also provide important insights. Structural changes of artery walls and, more specifically, structural evolution of developing aneurysms have been addressed in previous theoretical studies [7, 34, 65, 82, 83, 178]. Kroon and Holzapfel [82, 83] proposed a theoretical model for the growth of a saccular cerebral aneurysm. In this model, the aneurysm wall was assumed to consist of a number of distinct collagen fiber layers. The continuous turnover of collagen in the layers was responsible for the growth of the aneurysm, and the collagen production in the layers was governed by the embedded fibroblasts.

In the present paper, this aneurysm model is further developed. A realistic 3D setting is now employed in the form of a human middle cerebral artery. More specifically, the middle cerebral artery is modeled as a two-layer cylinder, where the layers correspond to the media and the adventitia. The constitutive behavior of the adventitia is governed by the aneurysm growth model, and the media is modeled as a neo-Hookean material reinforced by two families of collagen fibers [54]. The structural integrity of an artery or aneurysm is to a large extent determined by the organization of the collagen fabric. The collagen of the adventitia or an aneurysm wall is mainly Type I [6, 182], whereas the collagen of the media is mainly of Type III [14, 139]. In a previous study, the influence of the organization of the Type I collagen fabric of the adventitia was investigated [83]. Instead, the present study focuses on the influence of the orientation of the medial collagen on aneurysm growth. In addition, the consequences of different axial *in situ* stretches are studied. The influence is quantified in terms of stress distributions, wall thickness distributions and aneurysm shape at steady-state.

A short review of the aneurysm growth model is given in the next section. The current problem is then formulated, followed by a presentation of the numerical model and the numerical results. Finally, a discussion and some concluding remarks are provided.

2.2. Growth Model of a Saccular Cerebral Aneurysm

The saccular cerebral aneurysmal wall is considered to be the development of the adventitia of the originally healthy parent artery. The aneurysm wall is modeled as a hyperelastic material and is characterized by a strain-energy function Ψ . The only load-bearing constituent

is the collagen that is produced by fibroblasts, spread throughout the collagen network. The aneurysm wall is assumed to consist of n distinct and discrete layers of collagen fibers that can be considered as plies forming a laminate. The collagen fibers within layer i are perfectly aligned in direction ϕ_i , and as the fibroblasts are aligned in the same direction as the collagen fibers, newly produced collagen will be deposited at this angle as well during the growth process. The collagen mass production rate per unit reference volume, say \dot{m}_i , depends on both the stretching of individual fibroblasts and the proliferation of fibroblasts which are taken to be governed by the global stretching of the aneurysm wall. The mass production rate in layer i at time t is [82]

$$\dot{m}_i(t) = \beta_0 C_i^\alpha, \quad (2.1)$$

where β_0 is the normal mass production rate in a reference configuration of a healthy artery considered to be the density of fibroblasts multiplied by the collagen production rate per fibroblast [7]. In (2.1) C_i is a scalar defined as $C_i = \mathbf{C} : \mathbf{A}(\phi_i)$, where \mathbf{C} is the right Cauchy-Green tensor, $\mathbf{A}(\phi_i) = \mathbf{M} \otimes \mathbf{M}$ is a structure tensor and the unit vector \mathbf{M} has components $\cos \phi_i$ and $\sin \phi_i$, [54]. Thus, C_i is the projection of \mathbf{C} in the direction ϕ_i of the fibers, and the influence of C_i on the mass production rate $\dot{m}_i(t)$ is modulated by the exponent α .

Fiber deposition occurs at time t_{dp} and at any time between $-\infty$ and current time t . The related deformation gradient is then $\mathbf{F}(t_{dp}) = \mathbf{R}(t_{dp})\mathbf{U}(t_{dp})$, where $\mathbf{R}(t_{dp})$ is the rotation tensor, with $\det \mathbf{R}(t_{dp}) = 1$, and $\mathbf{U}(t_{dp})$ is the right stretch tensor at time t_{dp} , with $\mathbf{U} = \mathbf{U}^T$, [53]. Decomposing the current deformation gradient at t yields $\mathbf{F}(t) = \mathbf{R}'(t, t_{dp})\mathbf{U}_{loc}(t, t_{dp})\mathbf{U}(t_{dp})$, where $\mathbf{U}_{loc}(t, t_{dp})$ is the current local material stretch to which collagen, deposited at time t_{dp} , is exposed, and $\mathbf{R}'(t, t_{dp})$ is another rotation tensor. Thus, the local right Cauchy-Green tensor \mathbf{C}_{loc} is

$$\mathbf{C}_{loc}(t, t_{dp}) = \mathbf{U}_{loc}^2(t, t_{dp}) = \mathbf{U}^{-1}(t_{dp})\mathbf{C}(t)\mathbf{U}^{-1}(t_{dp}), \quad (2.2)$$

where $\mathbf{C}(t) = \mathbf{F}^T(t)\mathbf{F}(t) = \mathbf{U}(t)^2$.

Collagen fibers are deposited by the fibroblasts with a pre-stretch λ_{pre} . An expression of the resulting deformation of individual fibers is, therefore, made according to

$$C_{fib} = \lambda_{pre}^2 \mathbf{C}_{loc} : \mathbf{A}(\phi_i). \quad (2.3)$$

A simple polynomial characterizes the strain-energy function ψ_{fib} per unit mass stored in the collagen fibers, namely

$$\psi_{fib} = \mu_c (C_{fib} - 1)^3, \quad C_{fib} \geq 1, \quad (2.4)$$

where $\mu_c > 0$ is a positive material parameter that is governed by the stiffness of collagen fibers. The fibers are considered to have no stiffness in compression ($C_{fib} < 1$) so that ψ_{fib} is only active when the fibers are in tension.

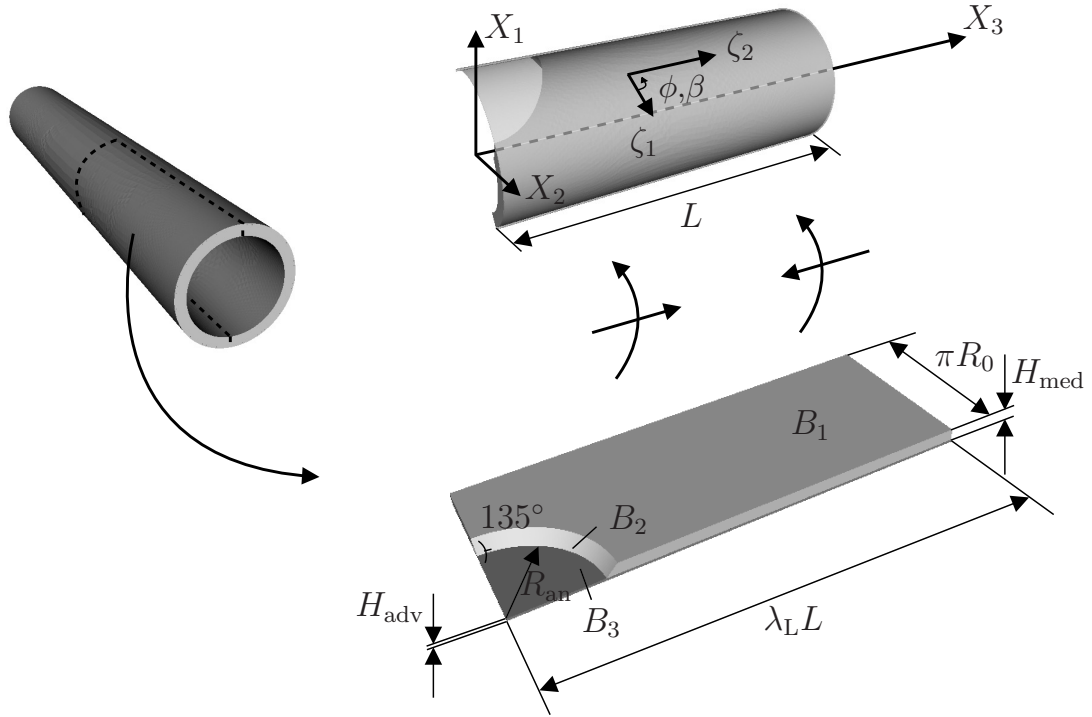


Figure 2.1.: Middle cerebral artery modeled as a two-layer cylinder (media and adventitia). The cylindrical structure (top right figure) constitutes the reference configuration of the posed problem.

The initial thickness of each collagen layer H_{adv}/n is assumed to be the same for all n layers, where H_{adv} is the total initial thickness of the adventitia. The total strain energy Ψ for all plies is integrated according to

$$\Psi(t) = \frac{1}{n} \sum_{i=1}^n \Psi_i(t) = \frac{1}{n} \sum_{i=1}^n \int_{-\infty}^t g(t, t_{\text{dp}}) \dot{m}_i(t_{\text{dp}}) \psi_{\text{fib}}(t, t_{\text{dp}}) dt_{\text{dp}}, \quad (2.5)$$

where the turnover of collagen is accounted for by the use of a pulse function $g(t, t_{\text{dp}})$, which is equal to 1 for $t_{\text{dp}} \in [t - t_{\text{lf}}, t]$ and 0 otherwise; t_{lf} is the life-time of the collagen fibers.

2.3. Problem Formulation

2.3.1. Model geometry, boundary and loading conditions

The intima is not considered to contribute significantly to the mechanics of the arterial wall. Hence, the artery is modeled as a two-layered cylinder, i.e. media and adventitia,

see Fig. 2.1. Due to symmetry only one quarter of a cylinder needs to be modeled. The model geometry is first defined as a plane sheet with a total thickness of $H_{\text{med}} + H_{\text{adv}}$ and side lengths πR_0 and $\lambda_L L$. The thicknesses of the media and the adventitia are denoted by H_{med} and H_{adv} , respectively. Aneurysm growth is initiated by the removal of the media in a circular region, characterized by the radius R_{an} , as shown in Fig. 2.1. The angle between the exposed adventitia in this circular region, plane B_3 , and the cut in the remaining media, plane B_2 , is 135° . This plane sheet is then mapped onto a cylindrical surface with outer radius R_0 . In that mapping, the geometry is also scaled in the X_3 -direction by a factor $1/\lambda_L$, giving the cylindrical structure the length L . Thus, the cylindrical structure, as shown at the top right in Fig. 2.1, constitutes the reference configuration of the posed problem.

The external loading imposed on the model aneurysm consists of an internal pressure p and an axial stretch λ_L . Boundary conditions in terms of tractions \mathbf{t} and prescribed displacements \mathbf{u} are thus imposed at time $t = 0^+$ according to (accounting for symmetry)

$$\begin{aligned} B_1, B_2, B_3 : t_n = -p, \quad X_1 = -R_0 : u_1 = 0, \quad X_2 = 0 : u_2 = 0, \\ X_3 = 0 : u_3 = 0, \quad X_3 = L : u_3 = (\lambda_L - 1)L, \end{aligned} \quad (2.6)$$

where B_1, B_2, B_3 are the surfaces defined in Fig. 2.1 on which the pressure acts and t_n is the normal component of the traction vector \mathbf{t} .

2.3.2. Stress response

Aneurysm growth is initiated by a local loss of media. This damage process occurs in a loaded state in which the artery is exposed to a blood pressure and an axial *in situ* stretch. Subsequently we model the following process: (i) a healthy (undamaged) artery is exposed to an (internal) pressure p and an axial stretch λ_L ; (ii) a local loss of media occurs in a region defined by the radius R_{an} ; (iii) growth of the aneurysm starts. In order to model this process, the reference geometry is initially defined as a plane sheet with length $\lambda_L L$ and with a circular damage zone; and this plane sheet is then scaled in the axial direction by the factor $1/\lambda_L$ (and mapped onto a cylindrical shape) to obtain the mentioned reference configuration.

The adventitia of a healthy artery (and the aneurysm wall) is not able to withstand any (or very little) bending, whereas the media of healthy arteries has a significant bending stiffness. Therefore, the adventitia is modeled as a membrane and the media as a three-dimensional continuum (tetrahedral solid elements). The adventitia is built up of n layers with distinct collagen fiber angle ϕ_i for each layer i , where $i = 1, \dots, n$. The fiber angles are defined by the 2D reference coordinate system ζ_1 - ζ_2 , as shown in Figs 2.1, 2.2, in which ζ_1 follows the circumferential direction of the artery and ζ_2 the axial direction; X_3 and ζ_1 - ζ_2 is a local coordinate system defined in every point on the artery surface. As shown in Fig. 2.2, the fiber distribution is uniform and the fiber direction ϕ_1 is taken to coincide with the ζ_1 -axis, see Fig. 2.1.

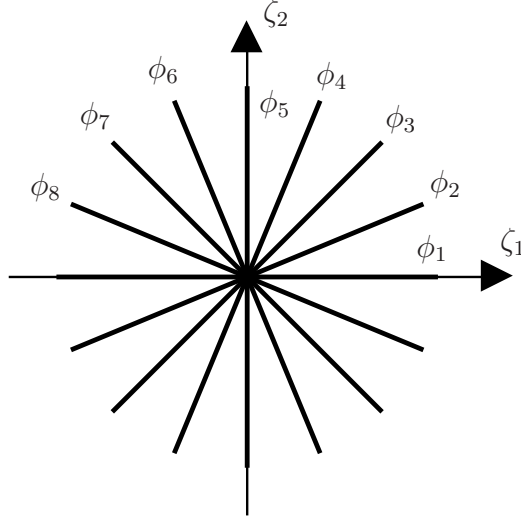


Figure 2.2.: Uniform fiber distribution in the aneurysm wall shown for eight layers; the coordinate system ζ_1 - ζ_2 corresponds to the tangential and axial directions, as shown in Fig. 2.1.

For the strain-energy function (2.5) that governs the constitutive response of the adventitia the in-plane second Piola-Kirchhoff stress components $S_{\alpha\beta}$ are given as

$$S_{\alpha\beta} = \frac{2}{n} \sum_{i=1}^n \frac{\partial \Psi_i}{\partial C_{\alpha\beta}} = \frac{2}{n} \sum_{i=1}^n \int_{-\infty}^t g(t, t_{dp}) \dot{m}_i(t_{dp}) \frac{\partial \psi_{fib}}{\partial C_{\alpha\beta}} dt_{dp}, \quad \alpha, \beta = 1, 2, \quad (2.7)$$

where $C_{\alpha\beta}$ are the components of the 2D right Cauchy-Green tensor, and indices α and β pertain to the local 2D in-plane reference coordinate system ζ_1 - ζ_2 in the plane of the adventitial membrane.

When modeling the media, the components are smooth muscle cells, elastin and collagen (Type III), [13, 27]. Elastin and smooth muscle cells are expected to have a fairly linear response. As both the smooth muscle cells and the collagen tend to be aligned approximately in the circumferential direction, the total response of the media is, in general, anisotropic, see [14, 40, 55, 59, 60]. In order to model the anisotropic mechanical behavior of the media, the strain-energy function as proposed by Holzapfel et al. [54] was adopted. Thus,

$$\Psi_{med} = \frac{\mu_M}{2} (I_1 - 3) + \frac{k_{1,med}}{2k_{2,med}} \sum_{i=4,6} \{ \exp[k_{2,med}(I_i - 1)^2] - 1 \}, \quad (2.8)$$

where the parameter μ_M denotes the shear modulus of the media describing the isotropic non-collagenous matrix material (mainly elastin and passive response of smooth muscle). The anisotropic part is related to the response of the collagen and described by $k_{1,med}$ and

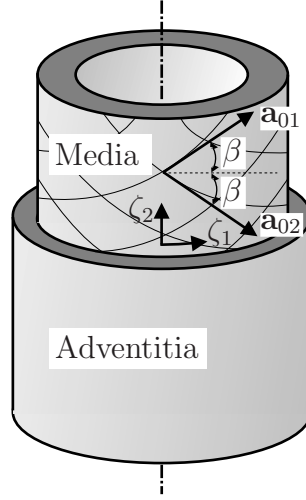


Figure 2.3.: Orientations \mathbf{a}_{01} and \mathbf{a}_{02} of two families of fibers in the media symmetrically disposed with respect to the cylinder axis. The parameter β is the angle between the collagen fiber and the circumferential direction ζ_1 .

$k_{2,\text{med}}$, where $k_{1,\text{med}} > 0$ is a stress-like parameter and $k_{2,\text{med}} > 0$ is dimensionless. They do not depend on the geometry or fiber angle; those effects are instead introduced through the invariants I_4 and I_6 , and are defined as

$$I_1 = \mathbf{C} : \mathbf{I}, \quad I_4 = \mathbf{C} : \mathbf{A}_1, \quad I_6 = \mathbf{C} : \mathbf{A}_2. \quad (2.9)$$

The structure tensors \mathbf{A}_1 and \mathbf{A}_2 are

$$\mathbf{A}_1 = \mathbf{a}_{01} \otimes \mathbf{a}_{01}, \quad \mathbf{A}_2 = \mathbf{a}_{02} \otimes \mathbf{a}_{02}, \quad (2.10)$$

where the column matrices $[\mathbf{a}_{01}] = [\cos \beta \ \sin \beta \ 0]^T$ and $[\mathbf{a}_{02}] = [\cos \beta \ -\sin \beta \ 0]^T$ collect the components of the unit vectors \mathbf{a}_{01} and \mathbf{a}_{02} , respectively, with 2β being the angle between the collagen fibers, as shown in Fig. 2.3. The principal values of the second Piola-Kirchhoff stress that corresponds to the media are calculated as [53],

$$S_a = \frac{1}{\lambda_a} \frac{\partial \Psi_{\text{med}}}{\partial \lambda_a}, \quad (2.11)$$

where the three principal directions are indexed $a = 1, 2, 3$.

A stress measure that is physically relevant for the aneurysm wall is the co-rotated Cauchy-like stress measure $\sigma_{\alpha\beta}^*$, [53]. The in-plane membrane stress is defined as

$$\sigma_{\alpha\beta}^* = \frac{1}{J^*} U_{\alpha\gamma}^* S_{\gamma\delta}^* U_{\delta\beta}^* = \frac{2}{\lambda_3 J^*} U_{\alpha\gamma}^* \frac{1}{n} \sum_{i=1}^n \frac{\partial \Psi_i}{\partial C_{\gamma\delta}^*} U_{\delta\beta}^*, \quad (2.12)$$

where α and β again pertain to the local 2D in-plane reference coordinate system. The deformation tensor \mathbf{C}^* with components $C_{\gamma\delta}^*$ are given as $\mathbf{C}^*(t) = \mathbf{C}_{\text{loc}}(t, t_{\text{dp}} = t - t_{\text{lf}})$, where $\mathbf{C}^*(t) = \mathbf{U}^{*2}(t)$ and $J^*(t) = \det \mathbf{U}^*(t)$. This is the deformation experienced by the ‘oldest’ and most stretched fibers in the aneurysm wall. The components $S_{\gamma\delta}^*$ are seen as modified second Piola-Kirchhoff stress components that result from a differentiation of the strain-energy function with respect to $C_{\gamma\delta}^*$. In addition, the thickness change of the membrane (due to material growth) is introduced as λ_3 , which is defined as the ratio between the current and initial aneurysm wall thickness. This ratio is estimated as

$$\lambda_3 = \frac{1}{n\lambda_1\lambda_2} \sum_{i=1}^n \frac{m_i}{m_0}, \quad (2.13)$$

where λ_1 and λ_2 are the total principal in-plane stretches of the membrane, and m_i and m_0 denote the current and reference collagen mass content, respectively. It is important to emphasize that it is the production of new tissue that is described by the entity λ_3 and *not* an actual stretching. Thus, material parameters that need to be supplied are: $\beta_0\mu_{ct_{\text{lf}}}$, α , λ_{pre} , n , ϕ_1, \dots, ϕ_n (adventitia); μ_{M} , $k_{1,\text{med}}$, $k_{2,\text{med}}$ (media).

In the half-closed interval $t \in (-\infty, 0]$, the modeled reference configuration is unloaded which for the adventitia corresponds to a uniform deformation $\mathbf{C} = \mathbf{I}$, where \mathbf{I} is the 2D identity tensor. A uniform deformation in turn corresponds to a constant collagen production rate $\dot{m}_i(t \leq 0) = \beta_0$, a constant fiber deformation of $C_{\text{fib}}(t \leq 0) = \lambda_{\text{pre}}^2$, and a constant strain energy per unit reference volume, i.e. $\Psi(t \leq 0) = \mu_c\beta_0(\lambda_{\text{pre}}^2 - 1)^3 t_{\text{lf}}$. At time $t = 0^+$, prescribed boundary conditions are imposed and the aneurysm starts to evolve.

2.3.3. Model specification, numerics

The considered model geometry is according to a healthy human middle cerebral artery [99, 153]: $R_0 = 1.2$ mm, $H_{\text{med}} = 0.25$ mm, $H_{\text{adv}} = 0.30$ μm . The size of the damage region, where the media is absent, is characterized by the radius R_{an} set to be $\pi R_0/2$. On the basis of investigations conducted by Monson et al. [99], material stiffness parameters are set to $\mu_{\text{M}} = 0.3$ MPa and $\beta_0\mu_{ct_{\text{lf}}} = 14$ MPa (in [99] there is a substantial variation in results and the parameters chosen are from test specimens with a relatively low stiffness). The parameters $k_{1,\text{med}}$ and $k_{2,\text{med}}$ are based on material parameters for a carotid artery from a rabbit [19], for which $k_{1,\text{med}}^{\text{r}} = 2.3632$ kPa, $k_{2,\text{med}}^{\text{r}} = 0.8393$, $\mu_{\text{M}}^{\text{r}} = 3.0$ kPa, where the superscript ‘r’ stands for ‘rabbit’. The non-dimensional parameter is taken to be the same for a human middle cerebral artery as for the rabbit ($k_{2,\text{med}} = k_{2,\text{med}}^{\text{r}}$), whereas $k_{1,\text{med}}$ for a human cerebral artery is estimated by assuming that the relation

$$\frac{k_{1,\text{med}}}{\mu_{\text{M}}} \approx \frac{k_{1,\text{med}}^{\text{r}}}{\mu_{\text{M}}^{\text{r}}} \quad (2.14)$$

holds, leading to the estimation $k_{1,\text{med}} = 0.24$ MPa. The length of the (quarter) model is $L = 8R_0$, which is considered to be sufficient in order for the ends of the artery not to have any influence on the stress distribution in the aneurysm wall.

The stability properties of the aneurysm model were investigated by Kroon and Holzapfel [82]. It was found that the stabilization of the evolving aneurysmal wall was drastically increased when the parameter α was in the range $1.5 < \alpha < 2$. Therefore, in the present study α is set to 1.7, as most aneurysms do grow in a stabilizing manner. It was also found that the pre-stretching of fibers in the aneurysm wall λ_{pre} should be set to a relatively low value when compared to the *in situ* stretch of arteries. Hence, the pre-stretch is, therefore, set to $\lambda_{\text{pre}} = 1.02$. The influence of the number of layers n in the media was also investigated by Kroon and Holzapfel [82, 83], and it was found that as long as $n \geq 4$, the number of layers does not influence the model behavior to a large degree. Hence, the number of layers n is, therefore, set to $n = 8$.

The internal pressure p is set to 7 kPa which is in accordance to the internal pressure for human carotid arteries [17]. The axial *in situ* stretch of human arteries depends on the location and is in the range 1.0-1.5 [149, 150]. An *in situ* mean stretch for cerebral arteries of 1.31 was found by Monson et al. [98]. Three axial stretches are investigated, namely $\lambda_L = 1.0$, $\lambda_L = 1.2$ and $\lambda_L = 1.4$.

The open source finite element analysis program FEAP [164] is used to analyze the problem, and the growth model of the aneurysm was implemented as a user membrane element. Three different finite element meshes are used in the study pertaining to the different axial stretches. The resulting mesh sizes are 13 492, 13 608, and 13 886 finite elements. Collapsed, 4-node, bi-linear, membrane elements are used to model the adventitia which includes the developing aneurysm wall, and 4-node, tri-linear, tetrahedral solid elements are used for the media. On the surfaces B_1, B_2, B_3 , surface pressure elements are used to impose the pressure p which acts on the deformed configuration. In the region of the aneurysmal expansion, the mesh is refined and the elements there have a characteristic size of $\pi R_0/80$ which is sufficient to obtain converging results. In the solution scheme, a time-independent procedure calculating the steady state solution directly, is used.

2.4. Numerical Results

In the present numerical study we investigate the influence of the medial collagen organization, i.e. the fiber angle β , and the axial *in situ* stretch λ_L of the artery on the growth of the saccular cerebral aneurysm.

2.4.1. Influence of medial collagen organization

In Fig. 2.4 the distributions of the maximum principal Cauchy stress σ_1^* are displayed. Solutions are shown for the cases with $\beta = 0^\circ, 5^\circ, 10^\circ$ (Figs 2.4(a)–(c)), and, as a reference, the solution with no medial collagen fibers is also included (Fig. 2.4(d)). The axial stretch is $\lambda_L = 1.2$. For all cases the stress distribution varies smoothly over the aneurysm surface with a peak value at the fundus. When fibers are included in the media, the peak value is lower when compared to a model without fibers. For an axial stretch of $\lambda_L = 1.2$ and $\beta = 0^\circ$, the maximum principal stress reaches a peak value of 0.622 MPa (Fig. 2.4 (a)).

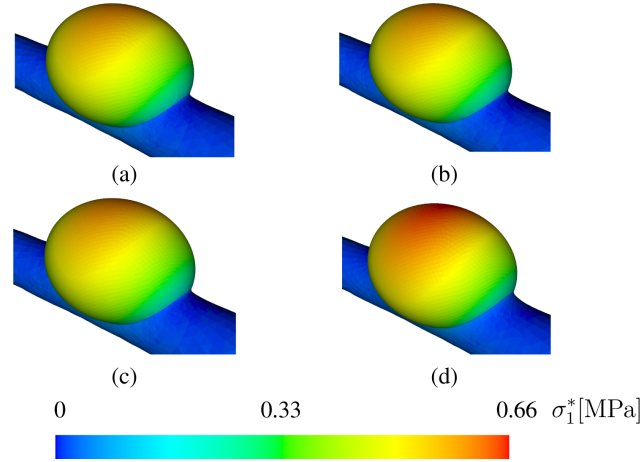


Figure 2.4.: Distributions of maximum principal Cauchy stress σ_1^* (axial *in situ* stretch $\lambda_L = 1.2$). The fiber angle of the medial collagen varies according to: (a) $\beta = 0^\circ$; (b) 5° ; (c) 10° ; in (d) no collagen fibers are included in the media, and the related aneurysm size is noticeably larger. Including collagen fibers in the media decreases the peak stress of 7.2%. The peak values are at the fundus.

When the fiber angle in the media is increased to 5° and 10° , the maximum principal stress becomes 0.624 MPa for both cases (Figs 2.4 (b),(c)). This is a very small change when compared to the model without medial fibers, where the maximum principal stress is 0.670 MPa (Fig. 2.4 (d)). Thus, including collagen fibers in the media decreases the peak stress of 7.2% compared to the solution without medial fibers. The size of the aneurysm does not differ much between the cases with fibers (Figs 2.4(a)–(c)), but the aneurysm without medial fibers is noticeably larger.

The corresponding distributions of the steady-state thickness change λ_3 , i.e. according to Eq. (2.13), are shown in Fig. 2.5. For the three cases $\beta = 0^\circ$; 5° ; 10° the largest thickness increase is 4.34 and occurs at the fundus (Figs 2.5 (a)–(c)). This value is lower when compared to the case with no fibers in the media (Fig. 2.5 (d)) which has a thickness increase of 4.56 at the fundus.

The maximum in-plane Cauchy shear stress τ for the four investigated cases is plotted in Fig. 2.6. The maximum values are 0.093 MPa, 0.094 MPa and 0.095 MPa for the cases with fibers in the media, as shown in Figs 2.6 (a)–(c), respectively. These values are all lower compared to the case with no fibers in the media, which experienced a maximum shear stress of 0.102 MPa (Fig. 2.6 (d)). The peak values do not appear at the fundus but are located close to the neck at the long side of the aneurysm, as can be seen in Fig. 2.6. The largest shear stress are about 15% of the largest maximum principal stresses. The minimum values are located between the fundus and the neck in the plane $X_2 = 0$. It may be noted that the maximum shear stress quantifies the difference between the two in-plane principal stresses. Thus, we may conclude that the maximum difference between the prin-

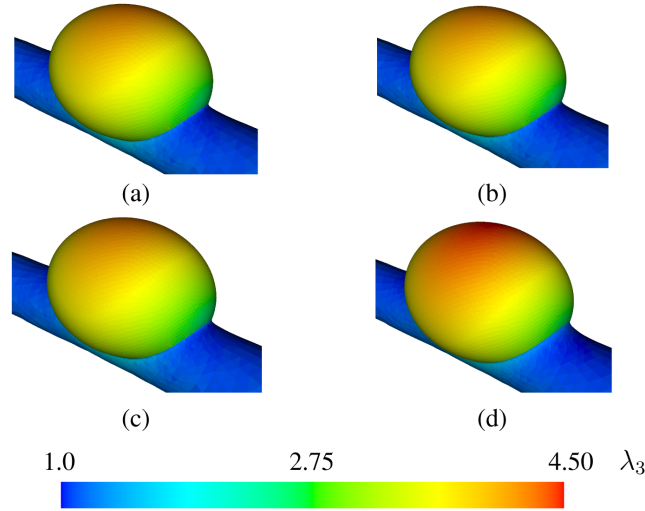


Figure 2.5.: Distributions of the thickness increase λ_3 (axial *in situ* stretch $\lambda_L = 1.2$), i.e. according to Eq. (2.13). The fiber angle varies: (a) $\beta = 0^\circ$; (b) 5° ; (c) 10° ; in (d) no fibers are included in the media. The largest thickness increases occur at the fundus; 4.34 for (a)–(c) and 4.56 for (d).

cipal stresses is about 0.2 MPa and occurs close to the neck of the aneurysm. We emphasize that the stress distributions in Fig. 2.6 are symmetric with respect to the X_1 - X_3 -plane, even though this is not obvious from Fig. 2.6.

2.4.2. Influence of axial in situ stretch

In this part of the study a constant fiber angle $\beta = 0^\circ$ is used, and solutions for three different axial stretches $\lambda_L = 1.0, 1.2$ and 1.4 are compared. For the different axial stretches, the maximum principal Cauchy stress σ_1^* (again occurring at the fundus) is found to be 0.580, 0.622, 0.626 MPa, as shown in the Figs 2.7 (a)–(c), respectively. The difference in the resulting steady-state geometry of these three cases are clearly shown in Fig. 2.7. No axial stretch ($\lambda_L = 1.0$) results in a more spherical shape (Fig. 2.7(a)), whereas an axial stretch of $\lambda_L = 1.4$ results in a more elliptic shape (Fig. 2.7(c)).

The thickness increases λ_3 for the cases with the three axial stretches reach values of 4.07, 4.34 and 4.55 at the fundus, see Figs 2.8 (a)–(c), respectively. However, the maximum thickness increase is not always at the fundus. For $\lambda_L = 1.4$, for example, the maximum value of λ_3 is not located in the aneurysm but rather in the intact artery close to the neck of the aneurysm. The value of the maximum thickness increase in that point is 5.64.

The resulting maximum in-plane Cauchy shear stress τ reaches the maximum values 0.115, 0.0933, 0.116 MPa, respectively (Figs 2.9 (a)–(c)). As can be seen, the maximum shear stress is lowest for $\lambda_L = 1.2$, whereas the peak values are almost identical for $\lambda_L = 1.0$ and $\lambda_L = 1.4$. The location of the maximum value also changes when altering the stretch. The

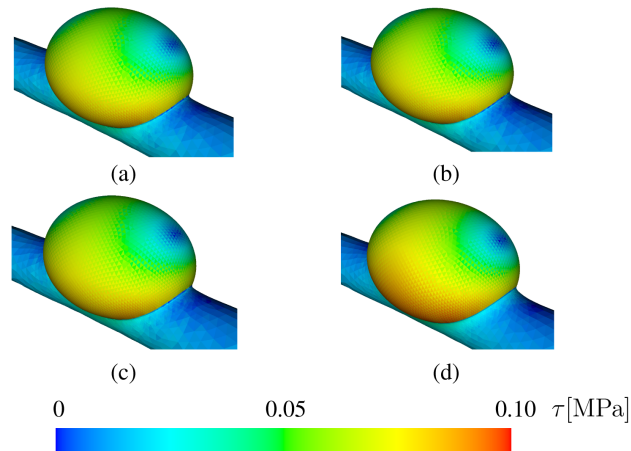


Figure 2.6.: Distributions of maximum in-plane Cauchy shear stress τ (axial *in situ* stretch $\lambda_L = 1.2$). The fiber angle varies: (a) $\beta = 0^\circ$; (b) 5° ; (c) 10° ; in (d) no fibers are included in the media. The peak values are located close to the neck at the long side of the aneurysm (0.093, 0.094, 0.095 MPa for (a)–(c) and 0.102 MPa for (d)). The minimum values are located between the fundus and the neck in the plane $X_2 = 0$.

location of the maximum values for $\lambda_L = 1.0$ and 1.2 is at the long side of the aneurysm, whereas it is on the short side for $\lambda_L = 1.4$, see Fig. 2.9.

2.5. Discussion

In the process of saccular cerebral aneurysm growth several stages can be identified. During the initial stage, wall shear stress, which are induced by the blood flow, act on the intima and may cause degradation of the media and the internal elastic lamina of the artery. As a result, an increased load has to be carried by the adventitia, which is triggered to dilate. If this process is continued, this dilatation may develop into a saccular aneurysm. In the present aneurysm model, processes that relate to fluid dynamics and mechanochemical processes leading to aneurysm growth initiation are not considered explicitly. Instead, an initial and instant loss of the media and the internal elastic lamina is assumed to occur initiating aneurysm growth. In previous works, the proposed aneurysm growth model has been assessed for axisymmetric growth [82] and also for a more realistic 3D setting in the form of a human middle cerebral artery [83]. In the present paper the saccular aneurysm growth model is extended to include collagen fibers in the media of the parent artery surrounding the aneurysm. A parameter study is performed to investigate the influence of collagen fiber organization in the media and axial *in situ* stretch of the artery on the aneurysm growth. The driving mechanism for the aneurysm growth is the continuous turnover of collagen fibers in the aneurysm wall. The model response is quantified in terms of the principal Cauchy stresses, the thickness increase of the aneurysm wall and the maximum in-plane

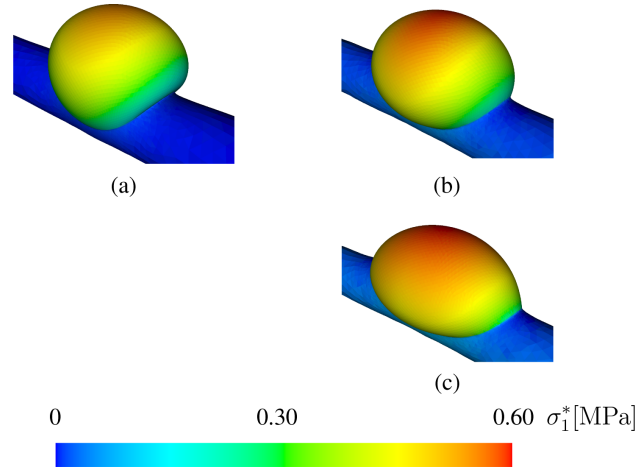


Figure 2.7.: Distributions of maximum principal Cauchy stress σ_1^* (fiber angle $\beta = 0^\circ$). The axial stretch varies: (a) $\lambda_L = 1.0$; (b) 1.2; (c) 1.4. The peak values are at the fundus. No axial stretch results in a more spherical shape, whereas an axial stretch of 1.4 results in a more elliptic shape.

Cauchy shear stresses. The model parameters are chosen on the basis of experiments and previous numerical results.

By introducing fibers in the media, the size of the developed aneurysm decreased noticeably. However, in terms of aneurysm size, there was no significant difference between the models with different medial fiber angles. It was also noted that the maximum stress, appearing at the fundus of the aneurysm, decreased by introducing fibers in the media. Fibers add stiffness to the vessel and, thereby, reduce the compliance at the boundary between the aneurysm and the artery. With a decreased boundary compliance, the resulting aneurysm size becomes smaller and the aneurysm wall stresses decrease. By increasing the fiber angle β the peak value of the maximum principal Cauchy stress σ_1^* increases somewhat. When β increases, the compliance in the circumferential direction of the artery increases, and this results in a slightly wider aneurysm neck. This may in turn explain why the aneurysm wall stress increases with increasing β .

The most drastic change in the aneurysm geometry is, however, seen by altering the axial stretch imposed on the model. The case with no axial stretch ($\lambda_L = 1.0$) produced a berry-shaped aneurysm with a very sharp neck. For the largest stretch investigated ($\lambda_L = 1.4$), the neck was much less pronounced, and the aneurysm clearly became less berry-shaped. Due to the loss of media in the aneurysm region, there is a localization in the remaining media below the aneurysm. The reference geometry and the modeling method correspond to an instant loss of media in a circular damage region. The size of this damage region is defined by the radius R_{an} which is independent of the axial stretch. However, it should be noted that the level of applied axial stretch will still affect how strong the localization becomes in the

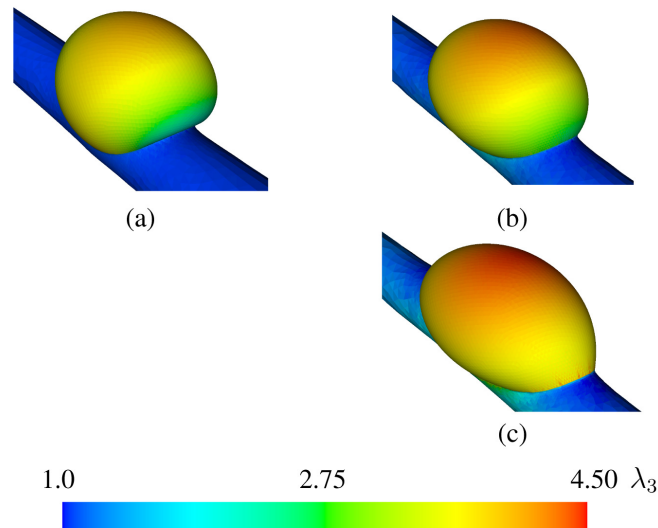


Figure 2.8.: Distributions of the thickness increase λ_3 (fiber angle $\beta = 0^\circ$). The axial stretch varies: (a) $\lambda_L = 1.0$; (b) 1.2; (c) 1.4. The increase in λ_3 is not always at the fundus. For $\lambda_L = 1.4$ the maximum value of λ_3 is located in the intact artery close to the neck of the aneurysm, with value 5.64.

remaining media below the aneurysm. The character of this localization will strongly affect the shape of the aneurysm, where a higher axial stretch tends to enhance the localization and make the aneurysm more ellipsoidal.

The axial *in situ* stretch of arteries is known to vary, and the values used here are in accordance with clinical observations [98]; $\lambda_L = 1.31$ has been observed for cerebral arteries. The axial *in situ* stretch had a stronger influence on the maximum principal stress in the aneurysm than the fiber angle; higher stretches resulted in higher stresses. The surface area of the aneurysm on which the internal pressure acts is larger for larger axial stretches, which explains the higher stresses. The stress, however, is also influenced by the thickness increase of the aneurysmal wall, which is larger for higher axial stretches and thereby reduces the stress to some extent. The strength of cerebral aneurysmal tissue has been experimentally estimated to 0.5-2.0 MPa [64, 90]. The peak stresses in our model for the various axial stretches and the medial collagen fiber angles are 0.58-0.63 MPa, and are of the same order.

Adding fibers in the media reduced the maximum thickness at the fundus from $137 \mu\text{m}$ ($\lambda_3 = 4.56$) to $130 \mu\text{m}$ ($\lambda_3 = 4.34$) for $\lambda_L = 1.2$. As the thickness increase is governed by the total stretch of the material (with respect to the reference configuration) and as the inclusion of medial fibers reduced the aneurysmal stretching by stiffening the borders between aneurysm and artery, this is an expected outcome. Changing the fiber angle in the media resulted in a minimal increase in stretch and, thereby, a minimal increase in thickness of the adventitia, whereas increasing the axial stretch of the artery resulted in

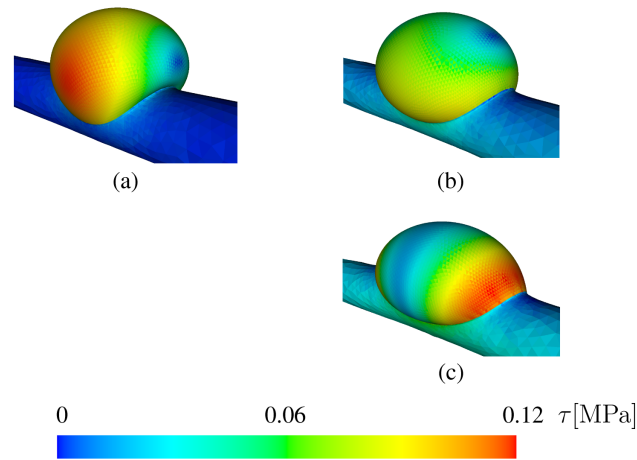


Figure 2.9.: Distributions of maximum in-plane Cauchy shear stress τ (fiber angle $\beta = 0^\circ$). The axial stretch varies: (a) $\lambda_L = 1.0$; (b) 1.2; (c) 1.4. The maximum value is lowest for $\lambda_L = 1.2$, whereas the peak values are almost identical for $\lambda_L = 1.0$ and 1.4. The location of the maximum values for $\lambda_L = 1.0$ and 1.2 is at the long side of the aneurysm and on the short side for 1.4.

relatively large stretches in the aneurysm, leading to increasing thickness. For the lowest axial stretch considered ($\lambda_L = 1.0$), the thickness was $122 \mu\text{m}$, and for the largest ($\lambda_L = 1.4$) $137 \mu\text{m}$. The thickness increases are in the range of experimentally determined values [90], where the thickness of larger cerebral aneurysms is between 116 and $212 \mu\text{m}$.

In summary, saccular cerebral aneurysm growth has been modeled. In particular, the influences of the medial collagen organization (fiber angles) and the axial *in situ* stretch on the aneurysm growth have been investigated. The previously proposed aneurysm model was extended to include fibers in the media of the parent artery surrounding the aneurysm, and a parameter study was performed by changing the collagen fiber angle in the media and the axial *in situ* stretch of the artery. When collagen fibers were included in the media, the peak stress in the aneurysm was reduced by 7.2% (compared to a case without fibers). Increasing axial stretch led to increasing steady-state aneurysm wall stresses. The numerical results predicted by the model are in good agreement with experimental data documented in the literature. The present study indicates that improved estimations of the mechanical properties of the medial collagen and, in particular, of the axial *in situ* stretches of arteries are necessary for a refined prediction of aneurysm growth.

Acknowledgement

Financial support for this research was partly provided by @neurIST, an Integrated EU Project (Call Identifier FP6-2004-IST-4). This support is gratefully acknowledged.

3. TENSORS NEEDED FOR FINITE ELEMENT IMPLEMENTATION OF AN INVARIANT BASED CONSTITUTIVE MODEL FOR PASSIVE MYOCARDIUM

Abstract In this paper constituents needed for implementation of a new structurally based constitutive law describing the behavior of passive myocardium is shown. The model captures the orthotropic behavior of passive myocardium with respect to its three orthogonal fiber, sheet and sheet-normal directions. Both the structure of the material model, in particular the separation of invariants into separate terms, and the coordinate frame independence caused by the invariants, leads to stress and elasticity tensors which may be implemented in a finite element software with relative ease when compared, for example, a material model based on Green-Lagrange strains. The analytical Cauchy and second Piola-Kirchhoff stress expressions of the model are also showed for uniaxial, biaxial and simple shear deformation modes. The model is fitted against experimental data of passive myocardium and a near perfect fit is shown. The sensitivity of the material parameters retrieved from the fit is examined where parameter b_s is found to be the most sensitive for the fit against a simple shear test. In addition, a comparison is made between the newly proposed invariant based model and a commonly used Green-Lagrange strain based model. Using material parameters retrieved when both models was fitted against a simple shear mode experiment, the newly proposed model was better suited to predict the stress in myocardium for a biaxial deformation when compared to experimental data. The finite element implementation was tested on a model with an ellipsoidal geometry which is a commonly used geometrical model to represent the left ventricle of the heart. In the geometrical model, the fiber, sheet and sheet-normal directions were included and for a simple case with internal pressure, a gradient of the fiber stress component is evident through the wall thickness which suggests that also residual stresses may need to be included in a future model describing the heart. It is also shown that the gradient is steeper if the fiber direction are all aligned in the circumferential direction of the ellipsoid which also results in a much larger deformation at the apex.

3.1. Introduction

Heart failure is the major cause of morbidity and mortality in the industrialized world. A large percentage of patients suffers from dilated cardiomyopathy and many of these individuals develop left ventricular dyssynchrony where the electrical activation sequence of the heart, which orchestrates mechanical contraction, is disturbed. This entails a less

synchronized and thus less efficient mechanical contraction of the ventricles which impairs the heart's ability to drive blood through the circulatory system.

Inquiries into these regulatory mechanisms by experimental means are hampered by the inability of currently available methodology to simultaneously record electrical and mechanical activity in 3D with sufficient spatio-temporal resolution. Further, the multi-scale nature of the phenomenon exacerbates the reintegration of disparate experimental data into comprehensive models of cardiac electromechanics. For instance, the regulation of active tension generation occurs at cellular and subcellular spatial scales, however, important regulatory input is provided via mechanical deformation of the myocardial walls, which is governed by spatial scales at the tissue and organ level.

Computational modeling almost naturally suggests itself as a complementary approach to tackle these multi-scale challenges by facilitating the explicit representation of interactions across multiple temporal and spatial scales within a single comprehensive computational model. Such biophysically detailed multiscale models of ventricular electromechanics may play a pivotal role in the quest of conceiving better therapeutical strategies by enabling basic research to fully elucidate underlying mechanisms with high spatio-temporal resolution. Although the cardiac modeling community was striving for developing such modeling tools since more than three decades [66], the methodological complexities involved and the lack of adequate computational resources prevented major progress for many years.

Over the past few years, multi-scale computational models of ventricular electrical activity have been routinely used in numerous studies [2, 31, 165] where models have been discretized at a paracellular resolution [11, 124] using highly detailed representations of cellular dynamics with integrated models of excitation-contraction coupling and mitochondrial energetics [125]. In comparison, a fairly small number of studies employed organ level models of ventricular cardiac mechanics, and, even less frequent, models of ventricular electromechanics. In most of the cardiac organ level mechanics studies researchers resorted to simplifications by using electrical-only models to predict effects on mechanical performance [136], by employing simplified models of cellular dynamics [104, 117] and active tension [79], by simplified representation of organ geometry [78, 104] and by neglecting orthotropic properties of tissue structure [104, 117] and, finally, by largely neglecting the impact of pathological alterations onto ventricular electromechanics, although exceptions do exist [170]. Evidence of the progress made in the field of computational modeling is the introduction of models into clinical application as an additional modality which supports clinical decisions in treating ischemic heart disease [172], the assessment of effects of heart surgery [29] and ventricular pacing [79, 108, 170]. Undoubtedly, despite the computational complexity of the current state of the art, current models are still in their infancy and, clearly, many of the physiological mechanisms which are aimed at to be modeled need to be further investigated. Nonetheless, these studies provide a first glimpse into future applications and nicely highlight the high potential and the predictive power of biophysically detailed multi-scale models of ventricular electromechanics.

From an organ level modeling point of view, the constitutive laws which describe the mechanical properties of the myocardial wall are of pivotal importance for quantitatively realistic predictions of deformation feedback which serves as input to cellular regulatory loops. In this context the fibrous and laminar arrangement of intracellular and extracellular matrices composing the myocardial wall is of particular importance. There is accumulating evidence that rotationally isotropic material descriptions overly simplify biophysical reality. This notion is strongly supported by the observation that such models fail to quantitatively reproduce myocardial wall thickening during systole [86]. Further, it is becoming increasingly more apparent that regional variations in material properties are an important factor in itself to understand the fundamental mechanisms underlying ventricular mechanics. For instance, a recent experimental study demonstrated that myocardial wall thickening is highly heterogeneous despite the absence of any heterogeneity in systolic fiber shortening [18]. These findings support the hypothesis put forward in earlier studies by numerous authors [26, 86, 155] that rearrangement of laminar sheets of fibers, and thus, the presence of tissue orthotropy, is a key contributor which amplifies systolic fiber shortening into adequate myocardial wall thickening. Finally, constitutive relations are not only spatially varying throughout the heart, they are also affected by pathologies such as myocardial infarction [187] or dilated cardiomyopathy [114] which clearly alter passive mechanical tissue properties significantly as a disease progresses.

It is expected that current advances made in computational modeling and the advent of the next generation petaflops supercomputers will help to leverage a new generation of electromechanically coupled multi-scale models of the ventricles which, eventually, enable novel investigations of cardiac function at an unprecedented level of physiological detail. At the very core of coupling organ level mechanics to cellular signaling is a mechanistically sound representation of the constitutive material parameters of the myocardium which allow accurate prediction of stresses throughout the myocardial wall. The present study describes a numerical realization of a recently published novel constitutive law for the myocardial wall which is a further important step towards predictive computational models of ventricular electromechanics.

Passive myocardium has been found to be a nearly incompressible, pseudo-elastic and anisotropic material [30], with a hyperelastic stress response often modeled by a strain-energy function [22]. The myocytes in the myocardium of the left ventricle of the heart is in general organized in a right-handed helical pathway from the endocardium towards the midwall, and a left-handed helical pathway from the midwall towards the epicardium, [93, 135, 169]. Furthermore, the myocytes are bundled and form layers with a direction that vary through the thickness of the ventricle wall, [85, 135, 142, 190]. This organization of the myocyte, in both a fiber and sheet direction, is responsible for the twisting motion of the heart during systole [162]. Orthotropic models are available that have shown a good fit against experimental data. However, as the material parameters are coupled in many of those models, for instance the model proposed by Costa et al. [22], it is often difficult to find a clear physical interpretation what those material parameters relate to. For models

with uncoupled material parameters, as for instance the Pole-Zero model proposed by Hunter et al. [67], the problem is the total number of parameters, in this case 18. Such a high number of material parameters may lead to non-uniqueness when fitting the model to experimental data.

For a recent review of both transversally isotropic and orthotropic constitutive models describing the passive behavior of myocardium, see Holzapfel and Ogden [56], where a structurally based constitutive model for myocardium was introduced that includes the orthotropic structure of the myocardium and for which the material parameters have a clear physical interpretation. In this paper the full expression of the constituents needed for implementation of this model in a finite element framework is shown. Also, analytical expressions needed for fitting the model to experimental data as well as the fit against two available experiments is shown. Further, the model is compared to the often used constitutive model showed by Costa et al. [22], and an example is made calculating the stress response when applying internal pressure on an ellipsoidal geometry which represents the left ventricle of the heart.

3.2. Material Model

As described earlier, myocardium, the material in the left ventricle midwall, may be characterized by a strain-energy function, Ψ , where the deformation has a hyperelastic stress response. In this section the volumetric and isochoric expressions of the newly proposed model for left ventricular myocardium [56] is shown together with the resulting stress and elasticity tensors in both the Lagrangian and Eulerian description.

3.2.1. Volume-preserving continuum mechanical framework

We introduce the deformation gradient \mathbf{F} and its multiplicative decomposition into a volume-changing part $J^{1/3}\mathbf{I}$ and a volume-preserving part $\bar{\mathbf{F}}$ so that $\mathbf{F} = J^{1/3}\bar{\mathbf{F}}$, where $J = \det \mathbf{F} > 0$ is the volume ratio, and \mathbf{I} is the second-order unit tensor (see, for example, [53]). The right and left Cauchy-Green tensors follow as $\mathbf{C} = J^{2/3}\bar{\mathbf{C}}$ and $\mathbf{b} = J^{2/3}\bar{\mathbf{b}}$, respectively, where $\bar{\mathbf{C}} = \bar{\mathbf{F}}^T\bar{\mathbf{F}}$ and $\bar{\mathbf{b}} = \bar{\mathbf{F}}\bar{\mathbf{F}}^T$ denote the modified tensor quantities. Additionally we are introducing three modified invariants as

$$\bar{I}_1 = \text{Tr}\bar{\mathbf{C}}, \quad \bar{I}_{4a} = \mathbf{a}_0 \cdot (\bar{\mathbf{C}}\mathbf{a}_0), \quad \bar{I}_{8ab} = \mathbf{a}_0 \cdot (\bar{\mathbf{C}}\mathbf{b}_0) = \mathbf{b}_0 \cdot (\bar{\mathbf{C}}\mathbf{a}_0), \quad (3.1)$$

where \mathbf{a}_0 and \mathbf{b}_0 are unit vectors along the undeformed directions. The related derivatives of \bar{I}_1 , \bar{I}_{4a} and \bar{I}_{8ab} with respect to $\bar{\mathbf{C}}$ are given by

$$\frac{\partial \bar{I}_1}{\partial \bar{\mathbf{C}}} = \mathbf{I}, \quad \frac{\partial \bar{I}_{4a}}{\partial \bar{\mathbf{C}}} = \mathbf{a}_0 \otimes \mathbf{a}_0, \quad \frac{\partial \bar{I}_{8ab}}{\partial \bar{\mathbf{C}}} = \frac{1}{2}(\mathbf{a}_0 \otimes \mathbf{b}_0 + \mathbf{b}_0 \otimes \mathbf{a}_0), \quad (3.2)$$

where the symbol \otimes denotes the tensor product. The three invariants I_1 , I_{4a} and I_{8ab} are defined in an analogous way to (3.1) and read $I_1 = \text{Tr}\mathbf{C}$, $I_{4a} = \mathbf{a}_0 \cdot (\mathbf{C}\mathbf{a}_0)$ and $I_{8ab} = \mathbf{a}_0 \cdot$

$(\mathbf{Cb}_0) = \mathbf{b}_0 \cdot (\mathbf{Ca}_0)$ so that the relations

$$\bar{I}_1 = J^{-2/3}I_1, \quad \bar{I}_{4a} = J^{-2/3}I_{4a}, \quad \bar{I}_{8ab} = J^{-2/3}I_{8ab} \quad (3.3)$$

hold.

3.2.2. Strain-energy function for the passive mechanical response of the myocardium

Myocardial tissue is an orthotropic material with fiber, sheet and sheet-normal directions denoted by the direction vectors \mathbf{f}_0 , \mathbf{s}_0 and \mathbf{n}_0 , respectively, as shown in Fig. 3.1.

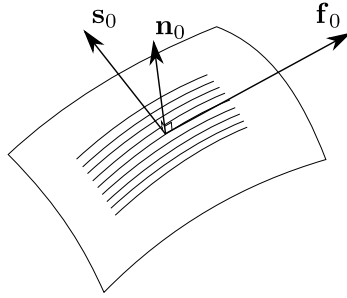


Figure 3.1.: Orthotropic myocardial tissue showing the vectors in the fiber, sheet and sheet-normal directions (\mathbf{f}_0 , \mathbf{s}_0 , \mathbf{n}_0).

We postulate here a unique *decoupled* representation of the strain-energy function Ψ (per unit reference volume). It is based on the kinematic assumption as introduced above, and is of the specific form

$$\Psi = \Psi_{\text{vol}}(J) + \Psi_{\text{iso}}(\bar{I}_1, \bar{I}_{4f}, \bar{I}_{4s}, \bar{I}_{8fs}), \quad (3.4)$$

where Ψ_{vol} and Ψ_{iso} are given scalar-valued functions of J and the modified invariants $\bar{I}_1, \bar{I}_{4f}, \bar{I}_{4s}, \bar{I}_{8fs}$, respectively. Note that these invariants are according to (3.1) where \mathbf{a}_0 and \mathbf{b}_0 are replaced by \mathbf{f}_0 and \mathbf{s}_0 , as shown in Fig. 3.1. The two scalar-valued functions then describe the volumetric and isochoric elastic responses of the material.

The function Ψ_{vol} is treated as a penalty function enforcing the incompressibility constraint $J = 1$. We use here

$$\Psi_{\text{vol}} = \frac{\mu_K}{2}(J - 1)^2, \quad (3.5)$$

where μ_K is the bulk modulus, which serves as a user-specified penalty parameter. With increasing μ_K the violation of the constraint is reduced. If the restriction on the value $\mu_K \rightarrow \infty$ is taken, the constraint condition is exactly enforced, and then (3.4) represents a functional for an incompressible material with $J = 1$. The specification of the strain-energy function Ψ_{iso} is based on the formulation of Holzapfel and Ogden [56], and has the form

$$\begin{aligned} \Psi_{\text{iso}} = & \frac{a}{2b} \{ \exp[b(\bar{I}_1 - 3)] - 1 \} \\ & + \sum_{i=f,s} \frac{a_i}{2b_i} \{ \exp[b_i(\bar{I}_{4i} - 1)^2] - 1 \} + \frac{a_{fs}}{2b_{fs}} [\exp(b_{fs}\bar{I}_{8fs}^2) - 1]. \end{aligned} \quad (3.6)$$

As discussed in [56], the eight material parameters a , b , a_f , b_f , a_s , b_s , a_{fs} and b_{fs} are all positive and the terms containing the directionally dependent invariants are included in Eq. (3.6) only if $\bar{I}_{4f} > 1$ and $\bar{I}_{4s} > 1$ is fulfilled.

3.2.3. Stress tensors

According to the form of the strain-energy function (3.4) the second Piola-Kirchhoff stress tensor $\mathbf{S} = 2\partial\Psi/\partial\mathbf{C}$ is also separated into a purely volumetric part (\mathbf{S}_{vol}) and a purely isochoric (\mathbf{S}_{iso}) part, i.e. $\mathbf{S} = \mathbf{S}_{\text{vol}} + \mathbf{S}_{\text{iso}}$. The volumetric part is

$$\mathbf{S}_{\text{vol}} = J p_h \mathbf{C}^{-1} \quad \text{where} \quad p_h = \frac{d\Psi_{\text{vol}}(J)}{dJ} = \mu_K(J-1) \quad (3.7)$$

is the hydrostatic pressure, and the function (3.5) has been introduced. From (3.6), by using the chain rule, the isochoric second Piola-Kirchhoff stress tensor takes on the form

$$\mathbf{S}_{\text{iso}} = 2 \frac{\partial\Psi_{\text{iso}}}{\partial\mathbf{C}} = 2 \left(\bar{\Psi}_1 \frac{\partial\bar{I}_1}{\partial\mathbf{C}} + \bar{\Psi}_{4f} \frac{\partial\bar{I}_{4f}}{\partial\mathbf{C}} + \bar{\Psi}_{4s} \frac{\partial\bar{I}_{4s}}{\partial\mathbf{C}} + \bar{\Psi}_{8fs} \frac{\partial\bar{I}_{8fs}}{\partial\mathbf{C}} \right), \quad (3.8)$$

where we have introduced the definitions

$$\bar{\Psi}_1 = \frac{\partial\Psi_{\text{iso}}}{\partial\bar{I}_1} = \frac{a}{2} \exp[b(\bar{I}_1 - 3)], \quad (3.9)$$

$$\bar{\Psi}_{4i} = \frac{\partial\Psi_{\text{iso}}}{\partial\bar{I}_{4i}} = a_i(\bar{I}_{4i} - 1) \exp[b_i(\bar{I}_{4i} - 1)^2], \quad i = f, s, \quad (3.10)$$

$$\bar{\Psi}_{8fs} = \frac{\partial\Psi_{\text{iso}}}{\partial\bar{I}_{8fs}} = a_{fs} \bar{I}_{8fs} \exp(b_{fs} \bar{I}_{8fs}^2), \quad (3.11)$$

which are the derivatives of (3.6) with respect to the four modified invariants \bar{I}_1 , \bar{I}_{4f} , \bar{I}_{4s} and \bar{I}_{8fs} . For (3.8) we have to specify the derivatives of the modified invariants with respect to \mathbf{C} . For the first modified invariant $\bar{I}_1 = J^{-2/3} \text{Tr}\mathbf{C}$ we may write by using the product rule

$$\frac{\partial\bar{I}_1}{\partial\mathbf{C}} = -\frac{1}{3} J^{-2/3} \mathbf{C}^{-1} \text{Tr}\mathbf{C} + J^{-2/3} \mathbf{I} = J^{-2/3} \left[\mathbf{I} - \frac{1}{3} (\text{Tr}\mathbf{C}) \mathbf{C}^{-1} \right] = J^{-2/3} \text{Dev}\mathbf{I}, \quad (3.12)$$

where $\text{Dev}(\bullet) = (\bullet) - (1/3)[(\bullet) : \mathbf{C}] \mathbf{C}^{-1}$ is the deviatoric operator in the Lagrangian description so that $\text{Dev}(\partial\Psi_{\text{iso}}/\partial\mathbf{C}) : \mathbf{C} = 0$. Next we need to specify the term $\partial\bar{I}_{4f}/\partial\mathbf{C}$. By using $\bar{I}_{4f} = J^{-2/3} I_{4f}$ and by taking into consideration that $\partial I_{4f}/\partial\mathbf{C} = \mathbf{f}_0 \otimes \mathbf{f}_0$ we get

$$\begin{aligned} \frac{\partial\bar{I}_{4f}}{\partial\mathbf{C}} &= J^{-2/3} \frac{\partial I_{4f}}{\partial\mathbf{C}} + I_{4f} \frac{\partial J^{-2/3}}{\partial\mathbf{C}} = J^{-2/3} \mathbf{f}_0 \otimes \mathbf{f}_0 + I_{4f} \left(-\frac{1}{3} J^{-2/3} \mathbf{C}^{-1} \right) \\ &= J^{-2/3} \left(\mathbf{f}_0 \otimes \mathbf{f}_0 - \frac{1}{3} I_{4f} \mathbf{C}^{-1} \right) = J^{-2/3} \left(\mathbf{f}_0 \otimes \mathbf{f}_0 - \frac{1}{3} \bar{I}_{4f} \bar{\mathbf{C}}^{-1} \right) \\ &= J^{-2/3} \text{Dev}(\mathbf{f}_0 \otimes \mathbf{f}_0). \end{aligned} \quad (3.13)$$

In an analogous manner we may write

$$\frac{\partial \bar{I}_{4s}}{\partial \mathbf{C}} = J^{-2/3} \text{Dev}(\mathbf{s}_0 \otimes \mathbf{s}_0), \quad \frac{\partial \bar{I}_{8fs}}{\partial \mathbf{C}} = \frac{1}{2} J^{-2/3} \text{Dev}(\mathbf{f}_0 \otimes \mathbf{s}_0 + \mathbf{s}_0 \otimes \mathbf{f}_0). \quad (3.14)$$

Hence, by substituting (3.12)–(3.14) into (3.8) and by adding (3.7)₁ we get the explicit expression for the second Piola-Kirchhoff stress tensor, i.e.

$$\begin{aligned} \mathbf{S} = & J p_h \mathbf{C}^{-1} + 2J^{-2/3} [\bar{\psi}_1 \text{Dev} \mathbf{I} + \bar{\psi}_{4f} \text{Dev}(\mathbf{f}_0 \otimes \mathbf{f}_0) + \bar{\psi}_{4s} \text{Dev}(\mathbf{s}_0 \otimes \mathbf{s}_0) \\ & + \frac{1}{2} \bar{\psi}_{8fs} \text{Dev}(\mathbf{f}_0 \otimes \mathbf{s}_0 + \mathbf{s}_0 \otimes \mathbf{f}_0)]. \end{aligned} \quad (3.15)$$

In order to get the spatial version of this expression, we need to perform a push-forward operation of the second Piola-Kirchhoff stress tensors to the current configuration which is $\boldsymbol{\sigma} = J^{-1} \mathbf{F}(\mathbf{S}_{\text{vol}} + \mathbf{S}_{\text{iso}}) \mathbf{F}^T$. By using (3.15) and $\mathbf{b} = J^{2/3} \bar{\mathbf{b}}$ it is straightforward to get the Cauchy stress tensor $\boldsymbol{\sigma}$ as

$$\begin{aligned} \boldsymbol{\sigma} = & p_h \mathbf{I} + 2J^{-1} [\bar{\psi}_1 \text{dev} \bar{\mathbf{b}} + \bar{\psi}_{4f} \text{dev}(\bar{\mathbf{f}} \otimes \bar{\mathbf{f}}) + \bar{\psi}_{4s} \text{dev}(\bar{\mathbf{s}} \otimes \bar{\mathbf{s}}) \\ & + \frac{1}{2} \bar{\psi}_{8fs} \text{dev}(\bar{\mathbf{f}} \otimes \bar{\mathbf{s}} + \bar{\mathbf{s}} \otimes \bar{\mathbf{f}})], \end{aligned} \quad (3.16)$$

where we have introduced the spatial vectors

$$\bar{\mathbf{f}} = \bar{\mathbf{F}} \mathbf{f}_0, \quad \bar{\mathbf{s}} = \bar{\mathbf{F}} \mathbf{s}_0, \quad (3.17)$$

and $\text{dev}(\bullet) = (\bullet) - (1/3)[(\bullet) : \mathbf{I}] \mathbf{I}$ is the deviatoric operator in the Eulerian description.

3.2.4. Elasticity tensor in the Lagrangian description

The elasticity tensor in the Lagrangian description is also separated into its volumetric and isochoric parts, i.e.

$$\mathbb{C} = 2 \frac{\partial \mathbf{S}}{\partial \mathbf{C}} = \mathbb{C}_{\text{vol}} + \mathbb{C}_{\text{iso}}, \quad (3.18)$$

where the volumetric part may be expressed as

$$\mathbb{C}_{\text{vol}} = 2 \frac{\partial (J p_h \mathbf{C}^{-1})}{\partial \mathbf{C}} = J \tilde{p}_h \mathbf{C}^{-1} \otimes \mathbf{C}^{-1} - 2J p_h \mathbf{C}^{-1} \odot \mathbf{C}^{-1}, \quad (3.19)$$

with $\tilde{p}_h = p_h + J d p_h / d J$ and $\mathbf{C}^{-1} \odot \mathbf{C}^{-1} = -\partial \mathbf{C}^{-1} / \partial \mathbf{C}$ (for details see [53]).

Due to the separation of the terms in (3.6), the isochoric part \mathbb{C}_{iso} of the elasticity tensor may further be separated as

$$\mathbb{C}_{\text{iso}} = 2 \frac{\partial \mathbf{S}_{\text{iso}}}{\partial \mathbf{C}} = \sum_{i=1,4f,4s,8fs} \mathbb{C}_{\text{iso}}^{\bar{I}_i}, \quad (3.20)$$

where the superscript refers to the invariant that is included in the tensor expression (3.15). Thus, by using the product rule we obtain the four expressions

$$\mathbb{C}_{\text{iso}}^{\bar{I}_i} = 4 \frac{\partial}{\partial \mathbf{C}} \left(\bar{\Psi}_i \frac{\partial \bar{I}_i}{\partial \mathbf{C}} \right) = 4 \bar{\Psi}_{ii} \frac{\partial \bar{I}_i}{\partial \mathbf{C}} \otimes \frac{\partial \bar{I}_i}{\partial \mathbf{C}} + 4 \bar{\Psi}_i \frac{\partial^2 \bar{I}_i}{\partial \mathbf{C} \partial \mathbf{C}}, \quad i = 1, 4f, 4s, 8fs, \quad (3.21)$$

where the four terms $\partial \bar{I}_i / \partial \mathbf{C}$ are provided in (3.12)–(3.14) and where the definition $\bar{\Psi}_{ii} = \partial^2 \Psi_{\text{iso}} / \partial \bar{I}_i \partial \bar{I}_i$ is introduced. With the strain-energy function (3.6) we get the specifications for $\bar{\Psi}_{ii}$, i.e.

$$\bar{\Psi}_{11} = \frac{\partial^2 \Psi_{\text{iso}}}{\partial \bar{I}_1 \partial \bar{I}_1} = \frac{ab}{2} \exp[b(\bar{I}_1 - 3)], \quad (3.22)$$

$$\bar{\Psi}_{4j4j} = \frac{\partial^2 \Psi_{\text{iso}}}{\partial \bar{I}_{4j} \partial \bar{I}_{4j}} = a_j [1 + 2b_j(\bar{I}_{4j} - 1)^2] \exp[b_j(\bar{I}_{4j} - 1)^2], \quad j = f, s, \quad (3.23)$$

$$\bar{\Psi}_{8fs8fs} = \frac{\partial^2 \Psi_{\text{iso}}}{\partial \bar{I}_{8fs} \partial \bar{I}_{8fs}} = a_{fs} (1 + 2b_{fs} \bar{I}_{8fs}^2) \exp(b_{fs} \bar{I}_{8fs}^2). \quad (3.24)$$

In addition, in (3.21)₂ we need to specify the second derivative of the modified invariants with respect to \mathbf{C} . For the modified invariant \bar{I}_1 we obtain with (3.12)₃ that

$$\begin{aligned} \frac{\partial^2 \bar{I}_1}{\partial \mathbf{C} \partial \mathbf{C}} &= \frac{\partial (J^{-2/3} \text{Dev} \mathbf{I})}{\partial \mathbf{C}} \\ &= -\frac{1}{3} J^{-2/3} \mathbf{C}^{-1} \otimes \text{Dev} \mathbf{I} - \frac{1}{3} J^{-2/3} \left(\mathbf{I} \otimes \mathbf{C}^{-1} + \text{Tr} \mathbf{C} \frac{\partial \mathbf{C}^{-1}}{\partial \mathbf{C}} \right) \\ &= -\frac{1}{3} J^{-2/3} (\mathbf{C}^{-1} \otimes \text{Dev} \mathbf{I} + \text{Dev} \mathbf{I} \otimes \mathbf{C}^{-1}) + \frac{1}{3} J^{-2/3} I_1 \tilde{\mathbb{P}}, \end{aligned} \quad (3.25)$$

where

$$\tilde{\mathbb{P}} = \mathbf{C}^{-1} \odot \mathbf{C}^{-1} - \frac{1}{3} \mathbf{C}^{-1} \otimes \mathbf{C}^{-1} \quad (3.26)$$

is the modified projection tensor of fourth-order [53]. In an analogous manner we may derive the second derivative of \bar{I}_{4f} with respect to \mathbf{C} , i.e.

$$\frac{\partial^2 \bar{I}_{4f}}{\partial \mathbf{C} \partial \mathbf{C}} = -\frac{1}{3} J^{-2/3} [\mathbf{C}^{-1} \otimes \text{Dev}(\mathbf{f}_0 \otimes \mathbf{f}_0) + \text{Dev}(\mathbf{f}_0 \otimes \mathbf{f}_0) \otimes \mathbf{C}^{-1}] + \frac{1}{3} J^{-2/3} I_{4f} \tilde{\mathbb{P}}, \quad (3.27)$$

and $\partial^2 \bar{I}_{4s} / \partial \mathbf{C} \partial \mathbf{C}$ we get by writing s instead of f in Eq.(3.27). Finally, we may derive (3.14)₂ with respect to \mathbf{C} in an analogous way, which leads to

$$\begin{aligned} \frac{\partial^2 \bar{I}_{8fs}}{\partial \mathbf{C} \partial \mathbf{C}} &= -\frac{1}{6} J^{-2/3} [\mathbf{C}^{-1} \otimes \text{Dev}(\mathbf{f}_0 \otimes \mathbf{s}_0 + \mathbf{s}_0 \otimes \mathbf{f}_0) \\ &\quad + \text{Dev}(\mathbf{f}_0 \otimes \mathbf{s}_0 + \mathbf{s}_0 \otimes \mathbf{f}_0) \otimes \mathbf{C}^{-1}] + \frac{1}{3} J^{-2/3} I_{8fs} \tilde{\mathbb{P}}. \end{aligned} \quad (3.28)$$

Hence, substituting (3.12)₃ and (3.25)₃ into (3.21)₂ we get the final expression for the isochoric elasticity tensor with respect to the isotropic invariant, i.e.

$$\mathbb{C}_{\text{iso}}^{\bar{I}_1} = 4J^{-4/3}\bar{\psi}_{11}\text{Dev}\mathbf{I} \otimes \text{Dev}\mathbf{I} - \frac{4}{3}J^{-2/3}\bar{\psi}_1(\mathbf{C}^{-1} \otimes \text{Dev}\mathbf{I} + \text{Dev}\mathbf{I} \otimes \mathbf{C}^{-1} - I_1\tilde{\mathbb{P}}). \quad (3.29)$$

Using (3.13)₅ and (3.27) in (3.21)₂ gives

$$\begin{aligned} \mathbb{C}_{\text{iso}}^{\bar{I}_{4f}} &= 4J^{-4/3}\bar{\psi}_{4f4f}\text{Dev}(\mathbf{f}_0 \otimes \mathbf{f}_0) \otimes \text{Dev}(\mathbf{f}_0 \otimes \mathbf{f}_0) \\ &\quad - \frac{4}{3}J^{-2/3}\bar{\psi}_{4f}[\mathbf{C}^{-1} \otimes \text{Dev}(\mathbf{f}_0 \otimes \mathbf{f}_0) + \text{Dev}(\mathbf{f}_0 \otimes \mathbf{f}_0) \otimes \mathbf{C}^{-1} - I_{4f}\tilde{\mathbb{P}}], \end{aligned} \quad (3.30)$$

while the isochoric elasticity tensor $\mathbb{C}_{\text{iso}}^{\bar{I}_{8fs}}$ follows from (3.21)₂ by means of (3.14)₂ and (3.28), i.e.

$$\begin{aligned} \mathbb{C}_{\text{iso}}^{\bar{I}_{8fs}} &= J^{-4/3}\bar{\psi}_{8fs8fs}\text{Dev}(\mathbf{f}_0 \otimes \mathbf{s}_0 + \mathbf{s}_0 \otimes \mathbf{f}_0) \otimes \text{Dev}(\mathbf{f}_0 \otimes \mathbf{s}_0 + \mathbf{s}_0 \otimes \mathbf{f}_0) \\ &\quad - \frac{2}{3}J^{-2/3}\bar{\psi}_{8fs}[\mathbf{C}^{-1} \otimes \text{Dev}(\mathbf{f}_0 \otimes \mathbf{s}_0 + \mathbf{s}_0 \otimes \mathbf{f}_0) \\ &\quad + \text{Dev}(\mathbf{f}_0 \otimes \mathbf{s}_0 + \mathbf{s}_0 \otimes \mathbf{f}_0) \otimes \mathbf{C}^{-1} - 2I_{8fs}\tilde{\mathbb{P}}]. \end{aligned} \quad (3.31)$$

Note that the elasticity tensor $\mathbb{C}_{\text{iso}}^{\bar{I}_{4s}}$ can simply be achieved by writing s instead of f in eq. (3.30). Hence, with the relations (3.29)–(3.31) we have now an explicit expression for the isochoric elasticity tensor (3.20)₂ expressed in terms of material quantities.

3.2.5. Elasticity tensors in the Eulerian description

The elasticity tensor \mathbb{c} in the Eulerian description may be calculated by using the push-forward operation of \mathbb{C} , i.e. $[\mathbb{c}]_{abcd} = F_{aA}F_{bB}F_{cC}F_{dD}[\mathbb{C}]_{ABCD}$, so that $\mathbb{c} = \mathbb{c}_{\text{vol}} + \mathbb{c}_{\text{iso}}$, which is the analogue of eq. (3.18)₂. In the following we show each term of the Eulerian elasticity tensor.

The volumetric elasticity tensor \mathbb{c}_{vol} in the Eulerian description may be written as the push-forward operation of (3.19)₂ which is

$$\mathbb{c}_{\text{vol}} = J(\tilde{p}_h\mathbf{I} \otimes \mathbf{I} - 2p_h\mathbb{I}), \quad (3.32)$$

where \mathbb{I} is the fourth-order unit tensor. It is also straightforward to provide the spatial version of (3.20)₂, i.e. the isochoric elasticity tensor

$$\mathbb{c}_{\text{iso}} = \sum_{i=1,4f,4s,8fs} \mathbb{C}_{\text{iso}}^{\bar{I}_i}, \quad (3.33)$$

with the four contributions which may be derived from (3.29)–(3.31). By using the modified left Cauchy-Green tensor $\bar{\mathbf{b}} = \overline{\mathbf{F}\mathbf{F}^T}$ and the definitions (3.3) and (3.17) we obtain the

isochoric elasticity tensors which are needed in (3.33), i.e.

$$\mathbf{c}_{\text{iso}}^{\bar{I}_1} = 4\bar{\psi}_{11}\text{dev}\bar{\mathbf{b}} \otimes \text{dev}\bar{\mathbf{b}} - \frac{4}{3}\bar{\psi}_1(\mathbf{I} \otimes \text{dev}\bar{\mathbf{b}} + \text{dev}\bar{\mathbf{b}} \otimes \mathbf{I} - \bar{I}_1\mathbb{P}), \quad \mathbb{P} = \mathbb{I} - \frac{1}{3}\mathbf{I} \otimes \mathbf{I}, \quad (3.34)$$

$$\begin{aligned} \mathbf{c}_{\text{iso}}^{\bar{I}_{4f}} &= 4\bar{\psi}_{4f4f}\text{dev}(\bar{\mathbf{f}} \otimes \bar{\mathbf{f}}) \otimes \text{dev}(\bar{\mathbf{f}} \otimes \bar{\mathbf{f}}) \\ &\quad - \frac{4}{3}\bar{\psi}_{4f}[\mathbf{I} \otimes \text{dev}(\bar{\mathbf{f}} \otimes \bar{\mathbf{f}}) + \text{dev}(\bar{\mathbf{f}} \otimes \bar{\mathbf{f}}) \otimes \mathbf{I} - \bar{I}_{4f}\mathbb{P}], \end{aligned} \quad (3.35)$$

$$\begin{aligned} \mathbf{c}_{\text{iso}}^{\bar{I}_{8fs}} &= \bar{\psi}_{8fs8fs}\text{dev}(\bar{\mathbf{f}} \otimes \bar{\mathbf{s}} + \bar{\mathbf{s}} \otimes \bar{\mathbf{f}}) \otimes \text{dev}(\bar{\mathbf{f}} \otimes \bar{\mathbf{s}} + \bar{\mathbf{s}} \otimes \bar{\mathbf{f}}) \\ &\quad - \frac{2}{3}\bar{\psi}_{8fs}[\mathbf{I} \otimes \text{dev}(\bar{\mathbf{f}} \otimes \bar{\mathbf{s}} + \bar{\mathbf{s}} \otimes \bar{\mathbf{f}}) + \text{dev}(\bar{\mathbf{f}} \otimes \bar{\mathbf{s}} + \bar{\mathbf{s}} \otimes \bar{\mathbf{f}}) \otimes \mathbf{I} - 2\bar{I}_{8fs}\mathbb{P}]. \end{aligned} \quad (3.36)$$

Note that in this form the volume ratio J does not appear explicitly.

3.3. Analytical Expression of the Stress Tensor

When implementing a new material model in a finite element framework, the implementation itself needs to be verified. For that reason, analytical expressions of the material model is presented in this section. Expressions are shown for uniaxial deformation, biaxial deformation and simple shear. The same analytical expressions may also be used for retrieving the material parameters of the model by fitting them to experimental data.

3.3.1. General analytical expression for incompressible material

For an incompressible material there is no change of volume which means the volume ratio $J = 1$ and there is no deviatoric part. The analytical expression of the Cauchy stress shown in (3.6) is thus

$$\boldsymbol{\sigma} = p_h\mathbf{I} + 2(\psi_1\mathbf{b} + \psi_{4f}\mathbf{f} \otimes \mathbf{f} + \psi_{4s}\mathbf{s} \otimes \mathbf{s}) + \psi_{8fs}(\mathbf{f} \otimes \mathbf{s} + \mathbf{s} \otimes \mathbf{f}). \quad (3.37)$$

Here, p_h is a penalty parameter enforcing incompressibility, determined by the boundary conditions, and may be seen as the hydrostatic pressure. Using

$$[\mathbf{b}] = \begin{bmatrix} b_{11} & b_{12} & b_{13} \\ b_{21} & b_{22} & b_{23} \\ b_{31} & b_{32} & b_{33} \end{bmatrix} \quad \text{and} \quad \begin{aligned} [\mathbf{f}] &= [f_1, f_2, f_3]^T \\ [\mathbf{s}] &= [s_1, s_2, s_3]^T \\ [\mathbf{n}] &= [n_1, n_2, n_3]^T \end{aligned} \quad (3.38)$$

the components of the symmetric Cauchy stress tensor (3.37) are

$$\sigma_{11} = p_h + 2(\psi_1 b_{11} + \psi_{4f}f_1^2 + \psi_{4s}s_1^2 + \psi_{8fs}f_1s_1), \quad (3.39)$$

$$\sigma_{22} = p_h + 2(\psi_1 b_{22} + \psi_{4f}f_2^2 + \psi_{4s}s_2^2 + \psi_{8fs}f_2s_2), \quad (3.40)$$

$$\sigma_{33} = p_h + 2(\psi_1 b_{33} + \psi_{4f}f_3^2 + \psi_{4s}s_3^2 + \psi_{8fs}f_3s_3), \quad (3.41)$$

$$\sigma_{12} = 2(\psi_1 b_{12} + \psi_{4f}f_1f_2 + \psi_{4s}s_1s_2) + \psi_{8fs}(f_1s_2 + f_2s_1), \quad (3.42)$$

$$\sigma_{13} = 2(\psi_1 b_{13} + \psi_{4f}f_1f_3 + \psi_{4s}s_1s_3) + \psi_{8fs}(f_1s_3 + f_3s_1), \quad (3.43)$$

$$\sigma_{23} = 2(\psi_1 b_{23} + \psi_{4f}f_2f_3 + \psi_{4s}s_2s_3) + \psi_{8fs}(f_2s_3 + f_3s_2). \quad (3.44)$$

If not stated otherwise in the following, the undeformed fiber, sheet and sheet-normal directions are assumed to coincide with the global cartesian axis, $[\mathbf{f}_0] = [1, 0, 0]^T$, $[\mathbf{s}_0] = [0, 1, 0]^T$ and $[\mathbf{n}_0] = [0, 0, 1]^T$. Further, we are assuming the material is incompressible and we are looking at a plain stress state.

3.3.2. Analytical uniaxial expression

For a uniaxial stretch, λ_{ff} in the \mathbf{f}_0 direction, the deformation gradient and left Cauchy Green tensor are

$$[\mathbf{F}] = \begin{bmatrix} \lambda_{ff} & 0 & 0 \\ 0 & 1/\sqrt{\lambda_{ff}} & 0 \\ 0 & 0 & 1/\sqrt{\lambda_{ff}} \end{bmatrix}, \quad [\mathbf{b}] = \begin{bmatrix} \lambda_{ff}^2 & 0 & 0 \\ 0 & 1/\lambda_{ff} & 0 \\ 0 & 0 & 1/\lambda_{ff} \end{bmatrix}, \quad (3.45)$$

Remembering that the terms correlating to the fiber and sheet direction in the strain energy function are only active if they are in tension, i.e., $\psi_{4s} = 0$, and the components of the Cauchy stress are

$$\sigma_{11} = 2\psi_1(\lambda_{ff}^2 - 1/\lambda_{ff}) + 2\psi_{4f}\lambda_{ff}^2, \quad (3.46)$$

$$\sigma_{22} = p_h + 2\psi_1(1/\lambda_{ff}) = 0, \quad (3.47)$$

$$\sigma_{33} = p_h + 2\psi_1(1/\lambda_{ff}) = 0, \quad (3.48)$$

$$\sigma_{12} = \sigma_{13} = \sigma_{23} = 0, \quad (3.49)$$

where p_h have been calculated from (3.47) or (3.48) and inserted in (3.46). The derivatives used in (3.46)–(3.48) are

$$\psi_1 = \frac{a}{2} \exp[b(\lambda_{ff}^2 + \frac{2}{\lambda_{ff}} - 3)] \quad \text{and} \quad \psi_{4f} = a_f(\lambda_{ff}^2 - 1) \exp[b_f(\lambda_{ff}^2 - 1)^2]. \quad (3.50)$$

3.3.3. Analytical biaxial expression

For an equibiaxial stretch, λ_{ff} and λ_{ss} in the \mathbf{f}_0 and \mathbf{s}_0 directions respectively, the deformation gradient and left Cauchy Green tensor are

$$[\mathbf{F}] = \begin{bmatrix} \lambda_{ff} & 0 & 0 \\ 0 & \lambda_{ss} & 0 \\ 0 & 0 & 1/(\lambda_{ff}\lambda_{ss}) \end{bmatrix} \quad \text{and} \quad [\mathbf{b}] = \begin{bmatrix} \lambda_{ff}^2 & 0 & 0 \\ 0 & \lambda_{ss}^2 & 0 \\ 0 & 0 & 1/(\lambda_{ff}\lambda_{ss})^2 \end{bmatrix}. \quad (3.51)$$

The components of the Cauchy stress tensor are

$$\sigma_{11} = 2\psi_1(\lambda_{ff}^2 - \frac{1}{\lambda_{ff}^2\lambda_{ss}^2}) + 2\psi_{4f}\lambda_{ff}^2, \quad (3.52)$$

$$\sigma_{22} = 2\psi_1(\lambda_{ss}^2 - \frac{1}{\lambda_{ff}^2\lambda_{ss}^2}) + 2\psi_{4s}\lambda_{ss}^2, \quad (3.53)$$

$$\sigma_{33} = p_h + 2\psi_1 \frac{1}{\lambda_{ff}^2\lambda_{ss}^2} = 0, \quad (3.54)$$

$$\sigma_{12} = \sigma_{13} = \sigma_{23} = 0, \quad (3.55)$$

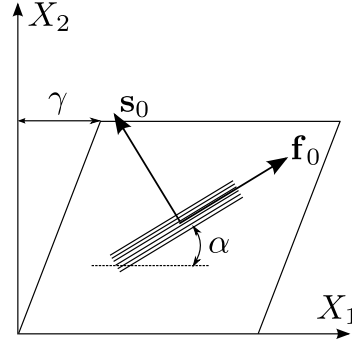


Figure 3.2.: Shear of a square block in the 21-plane with γ . The fiber direction is at angle α with respect to the global 1-axis, and the sheet axis is perpendicular to the fiber axis.

where p_h is calculated from (3.54) and inserted into (3.52) and (3.53). The derivatives used in (3.52)–(3.54) are

$$\psi_1 = \frac{a}{2} \exp\left[b\left(\lambda_{ff}^2 + \lambda_{ss}^2 + \frac{1}{\lambda_{ff}^2 \lambda_{ss}^2} - 3\right)\right], \quad (3.56)$$

$$\psi_{4f} = a_f(\lambda_{ff}^2 - 1) \exp[b_f(\lambda_{ff}^2 - 1)^2], \quad (3.57)$$

$$\psi_{4s} = a_s(\lambda_{ss}^2 - 1) \exp[b_s(\lambda_{ss}^2 - 1)^2]. \quad (3.58)$$

3.3.4. Analytical shear expression

For an analytical expression of simple shear, γ in the 21-plane, i.e. shearing the X_2 plane in the X_1 direction (see Fig. 3.2), the deformation gradient and corresponding left Cauchy Green tensor are

$$[\mathbf{F}] = \begin{bmatrix} 1 & \gamma & 0 \\ 0 & 1 & 0 \\ 0 & 0 & 1 \end{bmatrix}, \quad [\mathbf{b}] = \begin{bmatrix} 1 + \gamma^2 & \gamma & 0 \\ \gamma & 1 & 0 \\ 0 & 0 & 1 \end{bmatrix}. \quad (3.59)$$

This deformation gradient is valid for both *plain strain* and *plain stress*, as for an incompressible material the volume ratio $J = \det(\mathbf{F}) = 1$, always.

Adding some complexity to the analytical case, the undeformed fiber and sheet directions may vary with an angle α with respect to the global X_1 -axis, as shown in Fig. 3.2. The direction vectors for the fiber, sheet and sheet-normal axes are then

$$[\mathbf{f}_0] = \begin{bmatrix} \cos \alpha \\ \sin \alpha \\ 0 \end{bmatrix}, \quad [\mathbf{s}_0] = \begin{bmatrix} -\sin \alpha \\ \cos \alpha \\ 0 \end{bmatrix}, \quad [\mathbf{n}_0] = \begin{bmatrix} 0 \\ 0 \\ 1 \end{bmatrix}, \quad (3.60)$$

and the deformed direction vectors are

$$[\mathbf{f}] = \begin{bmatrix} \cos \alpha + \gamma \sin \alpha \\ \sin \alpha \\ 0 \end{bmatrix}, \quad [\mathbf{s}] = \begin{bmatrix} -\sin \alpha + \gamma \cos \alpha \\ \cos \alpha \\ 0 \end{bmatrix}, \quad [\mathbf{n}] = \begin{bmatrix} 0 \\ 0 \\ 1 \end{bmatrix}. \quad (3.61)$$

Using $s = \sin \alpha$, $c = \cos \alpha$ for a more simple notation, the Cauchy stress components, as shown in (3.39)–(3.44), are now

$$\sigma_{11} = 2[\psi_1 \gamma^2 + \psi_{4f}(c + \gamma s)^2 + \psi_{4s}(-s + \gamma c)^2 + \psi_{8fs}(c + \gamma s)(-s + \gamma c)], \quad (3.62)$$

$$\sigma_{22} = 2(\psi_{4f}s^2 + \psi_{4s}c^2 + \psi_{8fs}sc), \quad (3.63)$$

$$\sigma_{33} = p_h + 2\psi_1 = 0, \quad (3.64)$$

$$\sigma_{12} = 2[\psi_1 \gamma + 2\psi_{4f}s(c + \gamma s) + 2\psi_{4s}c(-s + \gamma c)] + \psi_{8fs}(2\gamma sc + 2c^2 - 1), \quad (3.65)$$

$$\sigma_{13} = \sigma_{23} = 0. \quad (3.66)$$

Again, p_h is calculated from (3.64) and is inserted in (3.62) and (3.63). For the special case where $\alpha = 0$ the stress components are

$$\sigma_{11} = 2(\psi_1 \gamma^2 + \psi_{4s} \gamma^2 + \psi_{8fs} \gamma), \quad (3.67)$$

$$\sigma_{22} = 2\psi_{4s}, \quad (3.68)$$

$$\sigma_{33} = 0, \quad (3.69)$$

$$\sigma_{12} = 2(\psi_1 + \psi_{4s})\gamma + \psi_{8fs}, \quad (3.70)$$

$$\sigma_{13} = \sigma_{23} = 0, \quad (3.71)$$

and for this case the derivatives used in (3.67), (3.68) and (3.70) are

$$\psi_1 = \frac{a}{2} \exp(b \gamma^2), \quad (3.72)$$

$$\psi_{4f} = 0, \quad (3.73)$$

$$\psi_{4s} = a_s \gamma^2 \exp(b_s \gamma^4), \quad (3.74)$$

$$\psi_{8fs} = a_{fs} \gamma \exp(b_{fs} \gamma^2). \quad (3.75)$$

These equations may be used for both validating an implementation of the proposed model in a finite element software as well as when fitting the model against experimental data to retrieve material parameters as shown in the next section.

3.4. Model Fit to Experimental Data

To verify that our model captures the behavior of myocardial tissue, it is fitted against experimental data using the MATLAB `lsqnonlin` function. Using the large-scale option in this function, it is possible to set lower boundaries on the fitting procedure which may be needed, as previously described in Section 3.2.2 and [56], to ensure that all material parameters are larger than zero.

3.4.1. Fit to a simple shear experiment

Plain stress, shear tests was performed by Dokos et al. [32], where cubic pieces was excised from porcine myocardium. In the experiments, the fiber, sheet and sheet-normal directions

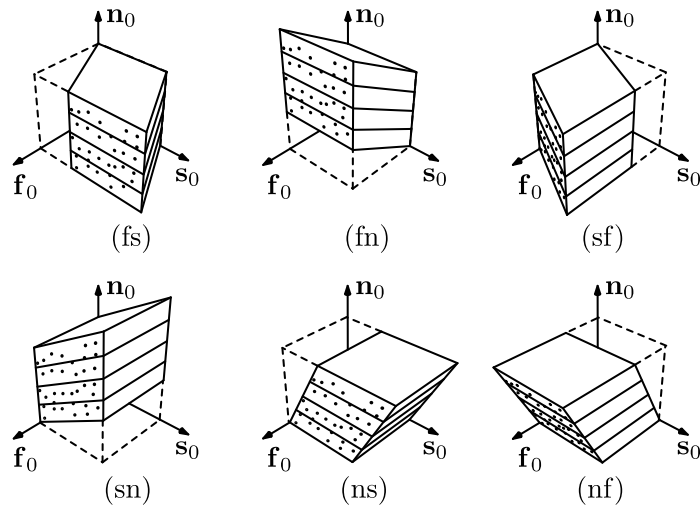


Figure 3.3.: Six possible shear directions of a cube with respect to fiber, sheet and sheet-normal directions \mathbf{f}_0 , \mathbf{s}_0 , \mathbf{n}_0 aligned in the global X_1 , X_2 , X_3 coordinate system.

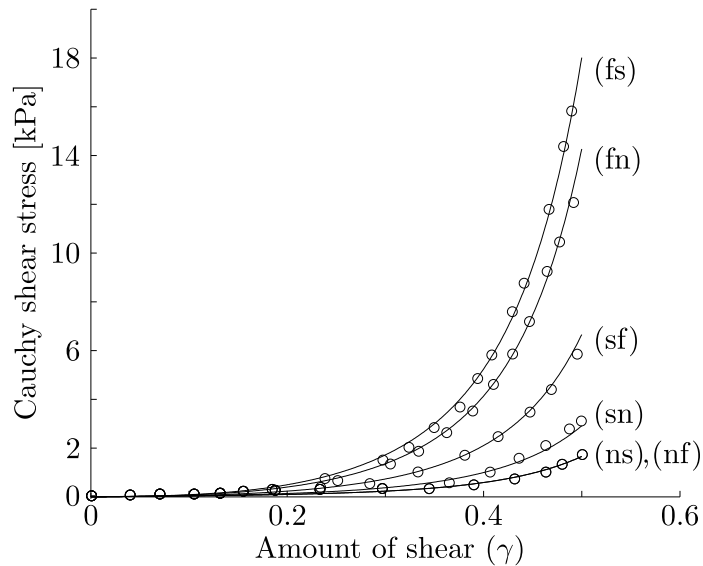


Figure 3.4.: Fit to data presented by Dokos et al. [32] where cubes of myocardial tissue was sheared in 6 different directions according to: fiber to sheet (fs); fiber to sheet-normal (fn); sheet to fiber (sf); sheet to sheet-normal (sn); sheet-normal to sheet (ns) and sheet-normal to fiber (nf).

of the myocardial cubes were identified and positioned in the global X_1 , X_2 and X_3 directions respectively. Thus, the undeformed direction vectors are $\mathbf{f}_0 = [1, 0, 0]^T$, $\mathbf{s}_0 = [0, 1, 0]^T$ and $\mathbf{n}_0 = [0, 0, 1]^T$. The cubes were then sheared in all six possible shearing directions as shown in Fig. 3.3. The shear stress corresponding to shear displacement were shown for each direction, see for instance Fig. 6 in [32]. Note however, that the ordering of the labels (fs) and (fn) in that figure is inconsistent with other figures in their paper. This is

experimental type	a (kPa)	b (-)	a_f (kPa)	b_f (-)	a_s (kPa)	b_s (-)	a_{fs} (kPa)	b_{fs} (-)
shear	0.330	9.242	18.535	15.972	2.564	10.446	0.417	11.602
biaxial	2.280	9.726	1.685	15.779	0.000	0.000	-	-

Table 3.1.: Material parameters retrieved when fitting the model against shear experimental data by Dokos et al. [32] shown in Fig. 3.4 and biaxial experimental data by Yin et al. [189] shown in Fig. 3.5.

corrected by switching the roles of these labels in the fitting procedure. We are assuming the deformation mode is simple shear, and thus the analytical equations for the shear stress are

$$\sigma_{12}^{(fs)} = 2(\psi_1 + \psi_{4f})\gamma + \psi_{8fs}, \quad (3.76)$$

$$\sigma_{13}^{(fn)} = 2(\psi_1 + \psi_{4f})\gamma, \quad (3.77)$$

$$\sigma_{21}^{(sf)} = 2(\psi_1 + \psi_{4s})\gamma + \psi_{8fs}, \quad (3.78)$$

$$\sigma_{23}^{(sn)} = 2(\psi_1 + \psi_{4s})\gamma, \quad (3.79)$$

$$\sigma_{32}^{(ns)} = 2\psi_1\gamma, \quad (3.80)$$

$$\sigma_{31}^{(nf)} = 2\psi_1\gamma. \quad (3.81)$$

It may be noted that the expressions (3.78) and (3.70) are the same as it is the same case. The fit of the stress Eqs. (3.76)-(3.81) is shown in Fig. 3.4 and as may be seen the procedure leads to a near perfect fit with the corresponding values in Table 3.1. Except for (3.80) and (3.81), the expressions for shear stress all look different and thus individual stresses may be calculated for all shear stresses. The small difference between the stresses of (3.80) and (3.81), as seen in the test performed by Dokos et al. [32], motivates that they have a similar expression. However, if a variation is needed, it could easily be achieved by adding the following additional term to (3.6),

$$\Psi_{8sn} = \frac{a_{sn}}{2b_{sn}} [\exp(b_{sn}\bar{I}_{8sn}^2) - 1]. \quad (3.82)$$

This term would lead to the addition $\bar{\psi}_{8sn}$, to equations (3.79) and (3.80) which result in a total separation of all values, see [56] for more details. The meaning of the indices for the invariant and material parameters in (3.82) are consistent with those previously shown.

3.4.2. Fit to a biaxial experiment

A biaxial test was made by Yin et al. [189], and the result is shown in Fig. 4 in that paper, where they expressed the the second Piola Kirchhoff stress tensor \mathbf{S} as a function of the Green-Lagrange strain $\mathbf{E} = (\mathbf{C} - \mathbf{I})/2$. Described briefly, they cut slices of myocardial

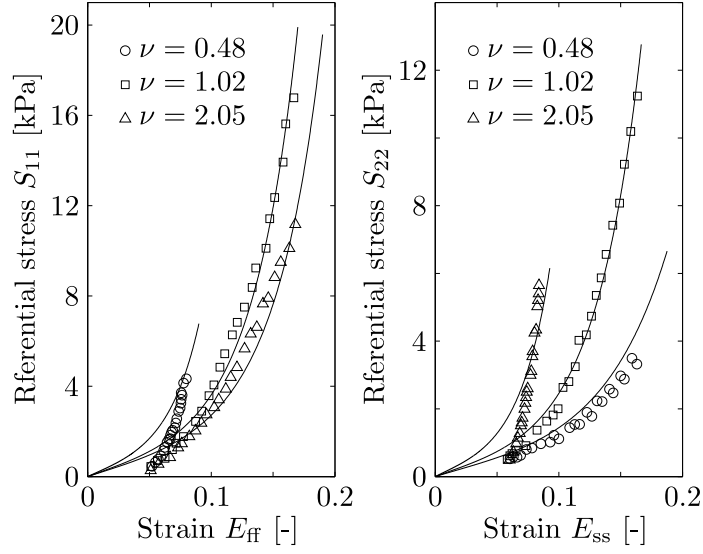


Figure 3.5.: Solid curves represent the fit to data presented by Yin et al. [189], where the circles, squares and triangles represent data points at varying ratios $\nu = E_{ff}/E_{ss}$.

tissue, identified the fiber direction, and stretched the slices in the fiber and cross-fiber direction. They also varied the stretch ratio between the two directions of stretch, here labeled $\nu = E_{ff}/E_{ss}$. Since $I_{8fs} = 0$, always in a biaxial test (when stretching in the fiber and sheet direction, with $[\mathbf{f}_0] = [1, 0, 0]$, $[\mathbf{s}_0] = [0, 1, 0]$), the ψ_{8fs} term may be excluded from the stress formulation, and using the pull-back operation $\mathbf{S} = \mathbf{J}\mathbf{F}^{-1}\boldsymbol{\sigma}\mathbf{F}^{-T}$ to retrieve the second Piola-Kirchhoff stress tensor from the Cauchy stress tensor (3.52) and (3.53), the following non-zero components are obtained

$$S_{11} = 2\psi_1\left(1 - \frac{\lambda_{nn}^2}{\lambda_{ff}^2}\right) + 2\psi_{4f} \quad \text{and} \quad S_{22} = 2\psi_1\left(1 - \frac{\lambda_{nn}^2}{\lambda_{ss}^2}\right) + 2\psi_{4s}, \quad (3.83)$$

where $\lambda_{nn} = (\lambda_{ff}\lambda_{ss})^{-1}$. Expressing the stretch λ_i , $i \in \{ff, ss, nn\}$, in the Green-Lagrange strain E_{ff} , results in

$$\lambda_{ff}^2 = 2E_{ff} + 1, \quad \lambda_{ss}^2 = 2E_{ff}/\nu + 1 \quad \text{and} \quad \lambda_{nn}^2 = \frac{1}{(2E_{ff} + 1)(2E_{ff}/\nu + 1)}. \quad (3.84)$$

The non-zero second Piola-Kirchhoff stress components, in terms of Green-Lagrange strains, are then

$$S_{11} = 2\psi_1 \left[1 - \frac{1}{(2E_{ff} + 1)^2(2E_{ff}/\nu + 1)} \right] + 2\psi_{4f}, \quad (3.85)$$

$$S_{22} = 2\psi_1 \left[1 - \frac{1}{(2E_{ff} + 1)(2E_{ff}/\nu + 1)^2} \right] + 2\psi_{4s}, \quad (3.86)$$

where the derivatives used in Eqs. (3.85) and (3.86) are

$$\psi_1 = \frac{a}{2} \exp \left\{ b \left[2(E_{\text{ff}} + E_{\text{ff}}/\nu) + \frac{2}{(2E_{\text{ff}} + 1)(2E_{\text{ff}}/\nu + 1)} - 1 \right] \right\}, \quad (3.87)$$

$$\psi_{4f} = 2a_f E_{\text{ff}} \exp(b_f 4E_{\text{ff}}^2), \quad (3.88)$$

$$\psi_{4s} = 2a_s \frac{E_{\text{ff}}}{\nu} \exp\left(b_s 4 \frac{E_{\text{ff}}^2}{\nu^2}\right). \quad (3.89)$$

These equations were fitted against the biaxial test by Yin et al. [189], and the fit is shown in Fig. 3.5. The corresponding values of the material parameters are shown in Table 3.1 and as seen, the value for $a_s = 0$, which implies that the material parameters are expressed for a transversally isotropic material. This shows that to retrieve accurate material parameters a biaxial fit alone may not be sufficient to describe the orthotropic behavior which we know is evident in myocardium. Furthermore, due to the size of the specimen in a biaxial fit it is, to the authors knowledge, not possible to extract a test specimen that is aligned in both the fiber and sheet direction. Therefore, without knowing the underlying variation of the sheet structure in the specimen tested, it is not really possible to fit a model that has a specified sheet direction incorporated.

3.4.3. Comparison to available model

A commonly used orthotropic model for the passive behavior of myocardial tissue that has been shown to give a good fit against experimental data, [146–148], is a Fung-type model based on Green-Lagrange strains, shown by Costa et al. [22],

$$\Psi(\mathbf{E}) = \frac{C}{2} [\exp(Q) - 1], \quad (3.90)$$

$$Q = c_1 E_{\text{ff}}^2 + c_2 E_{\text{ss}}^2 + c_3 E_{\text{nn}}^2 + 2c_4 E_{\text{fs}} E_{\text{sf}} + 2c_5 E_{\text{sn}} E_{\text{ns}} + 2c_6 E_{\text{fn}} E_{\text{nf}}. \quad (3.91)$$

To compare this Costa-model with our new model, we use the same fitting procedure against the experimental data presented by Dokos et al. [32] as was shown previously in Section 3.4.1. The Cauchy stress is calculated (for $J = 1$) by

$$\boldsymbol{\sigma} = \mathbf{F} \frac{\partial \Psi(\mathbf{E})}{\partial \mathbf{E}} \mathbf{F}^T, \quad (3.92)$$

and the fit of this equation on all experimentally retrieved shear stresses is shown in Fig. 3.6 with the corresponding material parameters shown in Table 3.2. We omit here to write the full expression of the equations used for the fit. As seen in Fig. 3.6 the Costa model is also capable of capturing a near perfect fit against these experimental data. A very simple measure of the goodness of fit is the R^2 value, which is calculated as $R^2 = 1.0 - SS_{\text{reg}}/SS_{\text{tot}}$, where SS_{reg} is the sum of squares of the distances of the data points to the best fitted curve and SS_{tot} is the sum of squares of the distances from the data points to a horizontal line through the mean of all data points. An R^2 value of 1 means a perfect fit, and an R^2 value of 0 means that the curve have no fit at all.

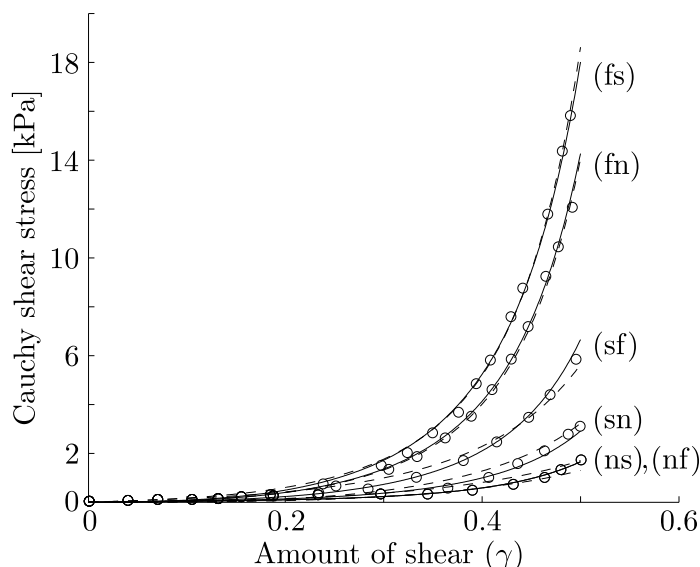


Figure 3.6.: Fit to data presented by Dokos et al. [32]. The fit of the Costa model is shown with dashed curves, and the fit of our new proposed model is shown with solid curves.

The overall fit of our model using this measure gives $R^2 = 0.981344$ and for the Costa model $R^2 = 0.955929$. Our model shows a slightly higher R^2 value than the Costa model, but both models are well within the expected error in measurements of the experiment and thus it is not possible to say which model fits the material behavior best with this measure.

C (kPa)	c_1 (-)	c_2 (-)	c_3 (-)	c_4 (-)	c_5 (-)	c_6 (-)
1.193	62.354	27.947	14.021	2.236	0.000	0.698

Table 3.2.: Material parameters retrieved when fitting the Costa model shown in [22], to the data by Dokos et al. [32].

Ultimately, the perfect set of material parameters for a constitutive material model is able to predict, for example, the stress in another state of deformation than in the experiment from which the material parameters were retrieved. We therefore use the material parameters, retrieved from the shear experiment and shown in Table 3.1 and 3.2, for our model and the Costa model, and calculate the analytical stress for a biaxial deformation where a unit cube is stretched equally in the fiber and sheet direction and is free to deform in the sheet-normal direction.

The analytical stress for both models is shown in Fig. 3.7 and there is a clear difference in the predicted stress response for the two models. To the authors knowledge, there have been no experiments made quantifying the biaxial stress-strain relationship for porcine myocardium in the fiber and cross-fiber direction. Instead in Fig. 3.7 the experimental

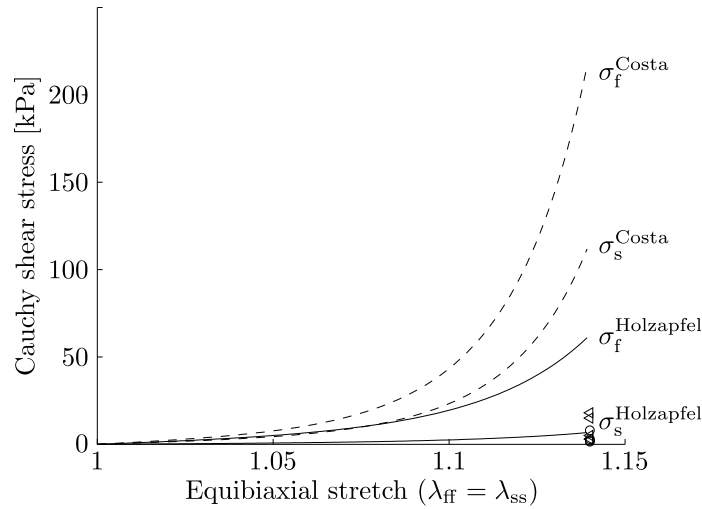


Figure 3.7.: Analytical stress for a biaxial deformation using our model (solid curves) and the Costa model (dashed curves). Various experimental values from biaxial tests [48, 87, 113, 174] are plotted where triangles represent stresses in the fiber direction and circles represent stresses in the sheet direction.

values of the stresses in the fiber and cross-fiber direction for different materials are plotted as triangles and circles respectively. The materials tested and shown here are bovine, rabbit, rat and canine [48, 87, 113, 174]. Our model predicts much more conservatively the stresses in the fiber and sheet direction and when compared to the data from Yin et al. [189], the stress in the fiber direction is about three times that what Yin reported, $\sigma_f \sim 3 \sigma_f^{Yin}$, and in the sheet direction it is almost exactly the same as their reported values for the cross-fiber direction, $\sigma_s \sim \sigma_s^{Yin}$. Whereas for the Costa model, the predicted fiber stress is about twelve times that of the reported values, $\sigma_f^{Costa} \sim 12 \sigma_f^{Yin}$, and for the sheet direction about fourteen times those reported, $\sigma_s^{Costa} \sim 14 \sigma_s^{Yin}$. One needs to remember that the material parameters were retrieved from shear tests on porcine myocardium [32] and the comparison is again canine myocardium [189] which are two different materials. However, for all experiments found in the literature our model is more accurate than the Costa model by an order of magnitude, as shown in Fig. 3.7.

3.5. Model Sensitivity

In this section a brief investigation into how sensitive the model response is to individual changes of the material parameters is presented as well as the sensitivity of the fit. As a measure of the sensitivity when fitting the material parameters, the stress datapoints used as input parameters for the fit of the model are changed randomly with $\pm 0-2\%$ of its original value, and the model is fitted again. This may also be considered as the sensitivity to a poorly performed experiment. A plot of the material parameters from one hundred such fits are shown in Fig. 3.8(a), where the fit against the data by Dokos et al. [32] show

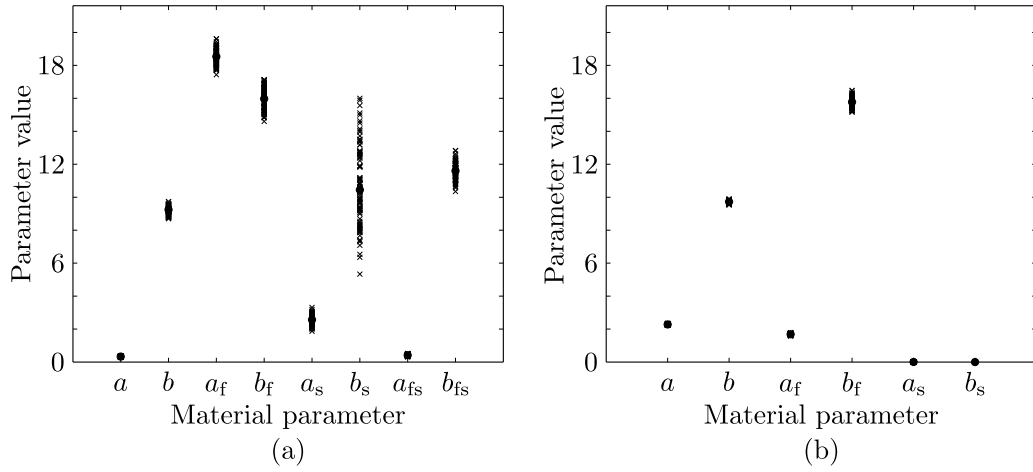


Figure 3.8.: Dispersion of one hundred best fitted material parameters when individually varying the experimental data points arbitrary by $\pm 0-2\%$ in: (a) simple shear experiment by Dokos et al. [32]; (b) biaxial experiment by Yin et al. [189].

that the material parameter b_s is the most sensitive. For the fit against the data by Yin et al. [189], shown in Fig. 3.8(b), the material parameter b_f shows the highest sensitivity.

Another example showing the model sensitivity is made by changing the material parameters retrieved from the fit against both experiments individually by $\pm 10\%$ of their original value, and look at the respective response in the change in peak stress. As seen in Table 3.3, the peak stress for σ_{ns} and σ_{nf} have the largest change for the shear experiment, about 25%, when changing the material parameter b . For the biaxial experiment, the largest change in stress is in the σ_{11} direction, by about 36%, when changing the material parameter b_f .

3.6. Ellipsoidal Model

Any implementation of a constitutive model into a finite element software also needs to be tested on a larger scale, meaning a more complex geometry with many nodes and elements, to ensure its stability. A geometrical model that is often used in computational modelling of the left ventricle is an ellipsoid truncated at the base [23, 110, 162, 169]. Here we use such a model to test the implementation of the passive material model (3.6).

The ellipsoid is characterized by its major and minor radii, $a_{i,o}$ and $b_{i,o}$ respectively, where the indexes ‘i,o’ stands for inner or outer surface of the ellipsoid. The geometry of the ellipsoid is described using prolate spheroidal coordinates ξ_1 , ξ_2 and ξ_3 , see Fig. 3.9. Those may be expressed in a cartesian coordinate system by

$$x_1 = d \cosh \xi_1 \cos \xi_2, \quad (3.93)$$

$$x_2 = d \sinh \xi_1 \sin \xi_2 \cos \xi_3, \quad (3.94)$$

$$x_3 = d \sinh \xi_1 \sin \xi_2 \sin \xi_3, \quad (3.95)$$

Material parameter	Peak stress change in % for a 10% change in the material parameter						Biaxial stress	
	σ_{fs}	σ_{fn}	Shear stress		σ_{ns}	σ_{nf}	σ_{11}	σ_{22}
a	± 0.9	± 1.2	± 2.5	± 5.7	± 10.0	± 10.0	± 0.2	± 2.2
b	+2.3	+3.0	+6.3	+14.5	+25.5	+25.5	+0.6	+8.5
	-1.9	-2.4	-5.0	-11.5	-20.3	-20.3	-0.5	-6.1
a_f	± 7.0	± 8.8	-	-	-	-	± 9.8	-
b_f	+7.5	+9.4	-	-	-	-	+36.3	-
	-6.8	-8.5	-	-	-	-	-26.5	-
a_s	-	-	± 1.9	± 4.3	-	-	-	± 7.8
b_s	-	-	+1.5	+3.4	-	-	-	+20.8
	-	-	-1.4	-3.2	-	-	-	-16.4
a_{fs}	± 2.1	-	± 5.6	-	-	-	-	-
b_{fs}	+2.0	-	+5.5	-	-	-	-	-
	-1.8	-	-5.0	-	-	-	-	-

Table 3.3.: Material parameters retrieved from the fit to the shear data from Dokos et al. [32] and biaxial data from Yin et al. [189] are changed individually by $\pm 10\%$ and the corresponding change in the peak stress values are shown.

where d is the focal length, defined as $d_{i,o}^2 = a_{i,o}^2 - b_{i,o}^2$. The inner radii chosen are $a_i = 42$ mm and $b_i = 19$ mm, and the outer radii are $a_o = 47$ mm and $b_o = 28$ mm, consistent with the data for a canine heart shown in [94] and references therein. The longitudinal coordinate ξ_2 varies from 2° to 120° in 15 steps and the circumferential coordinate ξ_3 varies from 0° to 180° , also in 15 steps. Using (3.95), ξ_1 is simply calculated with the relation $a = d \cosh \xi_1$ or $b = d \sinh \xi_1$ and is determined in 4 steps between the inner and outer values, ξ_{1i} and ξ_{1o} . This leads to an ellipsoidal model with 14 elements in the longitudinal direction, 15 elements in the circumferential direction and 5 elements through the thickness in the radial direction. The geometrical model consists of 1350 nodes and 1050 hexahedral elements.

To have an easily interpretable geometrical model, the fiber and sheet directions are set to vary linearly throughout the material. The fiber direction varies between $+60^\circ$ and -60° in the ξ_2 - ξ_3 plane and the sheet direction vary between $+85^\circ$ and -85° in the ξ_1 - ξ_2 plane, both going from the subepicardial side towards the subendocardial side. The fiber directions are shown in red in Fig. 3.9, and the sheet directions are projected on the cut surface and shown in blue in the same figure. Bear in mind that the sheet direction is in fact orthogonal to the fiber direction. Internal pressure is applied as a follower load on 210 pressure elements located on the inner surfaces of the subepicardial elements. All nodes located

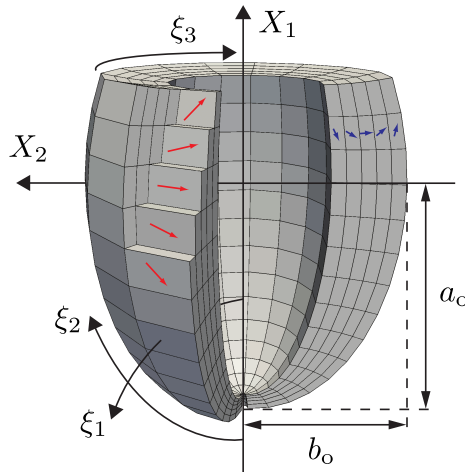


Figure 3.9.: Ellipsoidal geometrical model representing the left ventricle of the heart. A section is removed in the figure as well as selected elements, enabling visualization of sheet and fiber directions. The orientation of the fiber directions are shown in red, projected at the surface of five elements with a norm in the ξ_1 -direction. The sheet directions are shown in blue projected on the surface of five elements with a norm in the ξ_3 -direction.

at the base of the ellipsoid is fixed against translation in all directions. Three pressure levels are shown which are in accordance with the physiological pressure levels for the canine left ventricle, [4, 45, 176, 183]. The pressure levels are 7 mmHg which was reported for end diastole, 116 mmHg as reported for end systole and an intermediate pressure of 70 mmHg.

The result of the simulation is shown in Fig. 3.10, where contour plots of the stress component in the fiber direction is shown, and in Fig. 3.11, where the shear stress component between the fiber and sheet direction is shown as contour plots. Contour plots for the stress in the sheet direction is omitted as they show zero values for all pressure levels. For (d) in Figs. 3.10 and 3.11 the initial geometry is changed with respect to the fiber direction. Instead of a varying fiber angle from the epicardium to the endocardium as described earlier, we now set the fiber angle to zero degrees, i.e. the fibers are in the circumferential direction for all elements, and a pressure of 116 mmHg is applied. Notable first of all, in Fig. 3.10 is the much higher displacement at the apex when comparing (d) with (c). Also the stress gradient for (d) is much steeper than for (c). Evident in Fig. 3.11(a)–(c) is a difference of positive and negative values of the shear stress. The difference is on either side of the midwall element where the fiber angle is in the circumferential direction and where the shear stress component is zero. This is also seen in Fig. 3.11(d) where the fiber direction is circumferential for all element and thus the shear stress component is zero throughout the geometry.

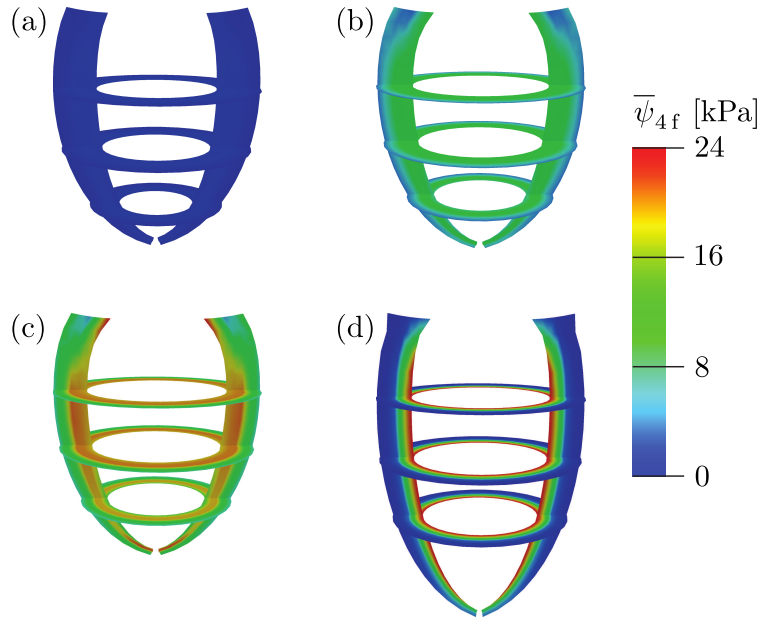


Figure 3.10.: Contour plots of the fiber stress component $\bar{\psi}_{4f}$ for different levels of internal pressure. The pressure levels for (a) to (c) are 7, 70 and 116 mmHg, respectively. In (d) the fiber angle with respect to the circumferential direction is set to zero throughout the thickness of the ellipsoidal and the pressure level is 116 mmHg.

3.7. Concluding Remarks

In this paper we have shown the full expressions of the stress and elasticity tensors needed for implementing the recently proposed constitutive model for passive myocardium. We have shown that relatively simple expression of the stress and elasticity tensor may be derived as the invariants in the strain energy function comprising the material model are all separated in different terms. Those simple expression makes it easy to implement in any finite element software. Basing the model on invariants, not only contributes to the simple implementation, but also ensures coordinate frame independence and thus only locally preferred directions of the material is needed when calculating the stress and elasticity tensor.

Analytical expressions for three modes of deformation was presented which may be used, not only to verify the implementation of the model, but also when fitting the model to experimental data which was shown for a simple shear and a biaxial experiment. The model has a near perfect fit against the shear experiments and a reasonable fit against the biaxial experiment. As already discussed by Holzapfel and Ogden [56], the quality of the biaxial experiment is limited and there is a need for more complete experimental data. The sensitivity of the material parameters of the constitutive model was investigated and the parameters in the exponents were the most sensitive. For the simple shear deformation

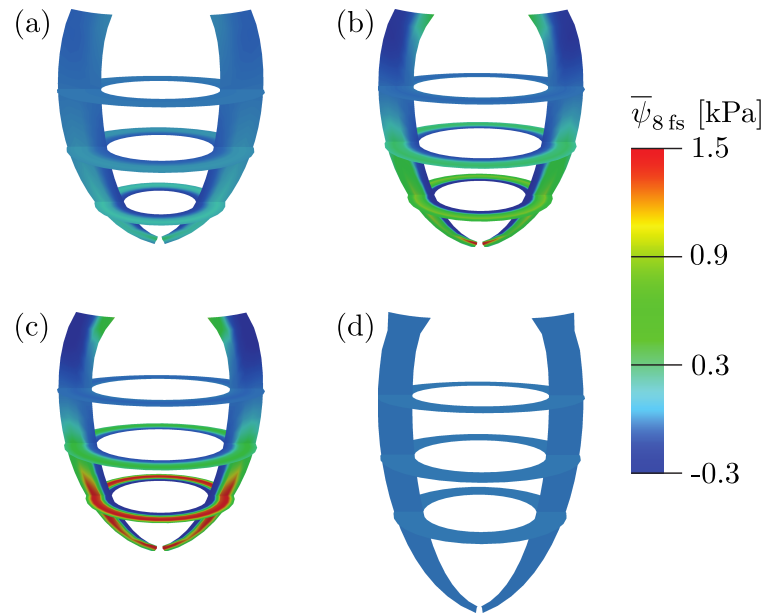


Figure 3.11.: Contour plots of the shear stress component $\bar{\psi}_{8 fs}$ for different levels of internal pressure. The pressure levels for (a) to (c) are 7, 70 and 116 mmHg, respectively. In (d) the fiber angle with respect to the circumferential direction is set to zero throughout the thickness of the ellipsoidal and the pressure level is 116 mmHg.

the model was most sensitive in the sheet-normal to sheet and sheet-normal to fiber direction, which is reasonable as those directions of shear have the lowest stress and are only governed by the isotropic part of the strain-energy function and thus only by two material parameters. In the comparison made between our newly proposed model and that of Costa et al. [22], both models displays a near perfect fit against experimental shear data of porcine myocardium. But, when using the material parameters retrieved from that fit, our model seems to be better at predicting the stress for a biaxial mode of deformation. This is a statement made with caution as the species, and thus the materials, are not the same in the comparison. The reason for this is that, to the authors knowledge, there exists no biaxial experiments of porcine myocardium in the literature today. However, looking at the range of stress values retrieved from biaxial experiments found in the literature for different species, our model is closer on all by an order of magnitude than that of the model by Costa et al. [25] and it is unlikely that stress values from a biaxial experiment on porcine myocardium will be that much higher.

In a numerical example the results of internal pressure on an ellipsoidal geometry was investigated. A stress gradient through the thickness of the ellipsoid was found which is natural when applying internal pressure. It may be noted, however, that in vivo the situation is different as it is not pressurized from within and extended outwards, but rather it is the active compression of the wall that leads to an increase in pressure on the endocar-

dial surface. Furthermore, a strong stress gradient in a living tissue might be physically unrealistic and would be compensated by the residual stresses that are evident in the ventricular wall [25]. Interestingly, the stress gradient is less steep when the fiber direction in the wall varies through the thickness as is seen when comparing (c) and (d) in Fig. 3.10. An explanation for this may be that the fiber angles generate a twisting motion in different direction at the subepicardial and subendocardial site and therefore the shear stress evident in Fig. 3.11(c) as opposed to (d), leads to the reduction of the stress gradient through the thickness. The large difference in the displacement at the apex may be explained by the lack of a fiber component in the longitudinal direction anywhere in the geometry for (d), together with the much lower stiffness in the sheet direction than the fiber direction due to a lower value of the material parameter a_s compared to a_f . The kink seen at the base of the ellipsoid in Figs. 3.10(d) and 3.11(d) arises from the boundary condition on the nodes at the base. This is not evident in Figs. 3.10(c) and 3.11(c) as the displacements are not as large due to the fiber orientation, as discussed earlier.

With internal pressure on the ellipsoid and a sheet angle that varies through the thickness, the sheet component of stress was found to be near zero. This is not surprising when only applying internal pressure, since the wall thickness will decrease with an increasing pressure. This results in a compression in the sheet direction and thus the sheet component of the stress is set to zero in accordance to the requirement for material stability previously explained in Section 3.2.2.

Acknowledgements

This project is in part supported by the SFB Research Center ‘Mathematical Optimization and Applications in Biomedical Sciences’, project F3210-N18 granted by the Austrian Science Fund. This support is gratefully acknowledged.

4. INFLUENCE OF SPATIAL HETEROGENEITY IN TISSUE ORTHOTROPY UPON MECHANICAL CONTRACTION IN THE LEFT VENTRICLE

Abstract Modeling cardiac function is an important tool to increase the understanding of the physiological responses of the heart and to determine how complex structural components of the heart influence its behavior. Organization of cardiomyocytes in sheets with a preferred fiber direction enables to model the myocardium as an orthotropic material characterized by a strain-energy function. Thus, a coupled model for myocardium is presented where an orthotropic strain-energy function based on an invariant formulation is used for the passive stress formulation together with an evolution equation responsible for generating the active stress. A model of the left ventricle is presented where pressure is calculated as a response to change in internal volume in order to ensure physiologically realistic pressure-volume loops and the influence of myocardial fiber and sheet distribution is investigated by using two different setups, a generic setup and one based on experiments. The resulting deformation differs significantly between the two model setups and especially in torsion where using a fiber-sheet setup based on experiments yield a more realistic ventricular response. Classical measures like PV-loops, cardiac output and ejection fraction match experimental data very well for both models and thus they did not capture the significant differences in deformation that was found. This implies spacial heterogeneity may play a critical role in mechanical contraction of the LV and that geometrical descriptions of deformation are needed when evaluating the accuracy of a ventricular model.

4.1. Introduction

Under healthy conditions the heart pumps blood around the circulatory system with a remarkable efficiency. The underlying electro-mechanical function is governed by an ordered cascade of events which interact across a broad range of spatial and temporal scales in a complex fashion. A heartbeat is initiated with an electrical activation that triggers the release of Ca^{2+} from intracellular stores, which, in turn, activates sarcomeres and generates the active stresses which make the heart contract. The regulation of these processes depends crucially on both the active and passive electrical and mechanical material properties of the myocardial muscle.

The structural organization of the left ventricle (LV), i.e. the main pumping chamber of the heart, is a key factor in this process. In general, myocyte orientation in the LV follows

a right-handed helical pathway from the endocardium towards the mid-wall, and a left-handed helical pathway from the mid-wall towards the epicardium [93, 135, 169]. This transmural change in prevailing myocyte orientation is usually referred to as ‘fiber rotation’ where ‘fiber’ refers to the dominating orientation averaged over an ensemble of cells. In addition, myocytes are bundled and form layers of a width of four to six cells, referred to as laminae or sheets. The orientation of these sheets also varies, not only transmurally, but also in the apico-basal direction [85, 135, 142, 190]. Therefore, at any point in space, the myocardium may be viewed as an orthotropic material with three preferred mutually orthogonal directions, namely along fibers, transverse to the fibers, but within a sheet, and perpendicular to the sheets.

These orthotropic material properties of the LV influence both the spread of electrical activation and repolarization as well as the mechanical response to pressure loads and active myocyte contraction and relaxation. Electrical activation of the LV under healthy conditions is mediated by the Purkinje system (PS), a topologically complex and dense network which distributes the electrical impulse quickly over the endocardium. Purkinje-ventricular junctions (PVJs) couple the virtually one-dimensional endings of the PS to the three-dimensional mass of the LV. Sites, at which PVJs successfully transmitted the electrical impulse to the LV, can be seen as electrical point sources which emanate wavefronts in the LV where the conduction velocity is a function of direction. Wavefronts travel fastest along the fibers and slowest in the sheet normal direction, with velocity ratios of roughly 3:2:1 along the three axes [10, 12, 144]. Owing to the numerous PVJs along the LV endocardium, individual wavefronts merge quickly in the subendocardium and travel then preferentially in a transmural direction.

The spatio-temporal pattern of electrical activation is translated into active stress transients via mechanisms referred to as electro-mechanical coupling [9, 80]. The onset of these transients, which are often modeled as stresses acting in the fiber direction in an Eulerian description [102, 107], follows the instant of activation with a certain electro-mechanical delay, which is not constant throughout the LV due to the pre-stretching of late activated regions [50]. The mechanical response, that is, the spatio-temporal pattern of deformations such as contraction and torsion, is then largely determined by both the passive hyperelastic orthotropic properties of the tissue and the generated active stresses [162].

Based on experimental data in a recent report [135] this study focuses on investigating the impact of spatial heterogeneity in orthotropic material properties upon the electrical and mechanical response of the LV. For this sake, a weakly coupled electro-mechanical model of a rabbit LV is employed where the LV anatomy is approximated as a truncated ellipsoid [24, 77, 104]. The model is equipped with two sets of fiber and sheet arrangement, a generic rule-based dataset with constant sheet angles as used in previous studies [49, 69, 104, 115], and an experimentally measured dataset where both fiber orientation and sheet angle are spatially varying throughout the LV. Simulation results reveal that the generic homogeneous fiber-sheet setup yields a torsion that is five times larger than what

is observed in experiments using MRI tagging [16, 112, 163], as opposed to the spatially varying orthotropic setup where torsion was found to be in the expected range.

4.2. Modeling Framework

4.2.1. Electrophysiological modeling

The spread of electrical activation and repolarization is described by a reaction-diffusion equation referred to as the monodomain equation, given by

$$\beta C_m \frac{\partial V_m}{\partial t} + \beta I_{\text{ion}}(V_m, \boldsymbol{\eta}) = \nabla \cdot (\boldsymbol{\sigma}_m \nabla V_m) + I_{\text{tr}}, \quad (4.1)$$

where β is the ratio between surface and volume of the membrane, C_m is the capacitance of the membrane, V_m is the transmembrane voltage, I_{ion} , which is the density of the total ionic current, is a function of the state variables $\boldsymbol{\eta}$ and V_m , I_{tr} is a transmembrane stimulus current, and $\boldsymbol{\sigma}_m$ is the monodomain conductivity tensor with the eigenaxes $\zeta = f$ along the fibers, $\zeta = s$ perpendicular to the fibers, but within a laminar sheet, and $\zeta = n$ perpendicular to the sheets. The eigenvalues of $\boldsymbol{\sigma}_m$, are chosen as the harmonic mean of intracellular conductivity, $\sigma_{i\zeta}$, and interstitial conductivity, $\sigma_{e\zeta}$, which renders the monodomain equations axially equivalent to the more general bidomain equations [92, 109].

Numerical solution. The reaction and diffusion part of the monodomain equations were split [129] which leads to a time stepping scheme given by

$$V_m^{k*} = V_m^k + \frac{\Delta t}{\beta C_m} \left[\theta \nabla \cdot (\boldsymbol{\sigma}_m \nabla V_m^{k*}) + (1 - \theta) \nabla \cdot (\boldsymbol{\sigma}_m \nabla V_m^k) \right], \quad (4.2)$$

$$\boldsymbol{\eta}_f^{k+1} = \boldsymbol{\eta}_f^k e^{-\frac{\Delta t}{\tau}} + \boldsymbol{\eta}_\infty \left(1 - e^{-\frac{\Delta t}{\tau}} \right), \quad (4.3)$$

$$\boldsymbol{\eta}_s^{k+1} = \boldsymbol{\eta}_s^k + \boldsymbol{g}(V_m^{k*}, \boldsymbol{\eta}_s^k) \Delta t, \quad (4.4)$$

$$V_m^{k+1} = V_m^{k*} - \frac{\Delta t}{C_m} I_{\text{ion}}(V_m^{k*}, \boldsymbol{\eta}^{k+1}). \quad (4.5)$$

The parabolic portion (4.2) is solved by choosing $\theta = 0.5$, which results in a Crank-Nicholson scheme. The overall system is then solved with an implicit-explicit (IMEX) scheme where the diffusion term is treated implicitly and the reaction term explicitly, using a time step dt of $20 \mu\text{s}$. Hybrid finite element meshes consisting of tetrahedra, hexahedra, pyramids and prisms were used for spatial discretization at an average spatial resolution of $198 \mu\text{m}$ using linear weighting functions [133].

The linear system was solved in parallel by employing a block Jacobi preconditioner with an iterative Conjugate Gradient (CG) solver, using an Incomplete Cholesky (ICC(0)) factorization as a subblock preconditioner [8]. The Rush-Larsen method [141] was used to solve the Mahajan-Shiferaw model where an analytical solution was used to update the

fast gating variables, $\boldsymbol{\eta}_f$, where the time constant τ and the steady-state $\boldsymbol{\eta}_\infty$ are functions of the rate coefficients which govern channel gating, and an explicit Euler step to update all other slower state variables, $\boldsymbol{\eta}_s$ [89, 125]. The Cardiac Arrhythmia Research Package (CARP) [175], which is built on top of the MPI-based library PETSc [8], was employed to solve Eqs. (4.2)–(4.5).

4.2.2. Active and passive mechanical modeling

The Cauchy stress tensor is separated into a passive and an active stress component. In the Eulerian description, this yields

$$\boldsymbol{\sigma} = \boldsymbol{\sigma}_p + \boldsymbol{\sigma}_a, \quad (4.6)$$

where $\boldsymbol{\sigma}_p$ is the passive stress component, describing the deformation of the myocardium when subjected to applied forces or stresses. $\boldsymbol{\sigma}_a$ is the active stress component, which is generated by the electrical activation of myocardial tissue.

Passive stress component. As described in the electrical setup, the myocardium is described by three orthogonal direction vectors \mathbf{f}_0 , \mathbf{s}_0 and \mathbf{n}_0 , which correspond to the fiber direction, sheet direction and sheet-normal direction, respectively, in the Lagrangian description. Using the multiplicative decomposition of the deformation gradient, \mathbf{F} , into a volumetric, $J^{1/3}\mathbf{I}$, and an isochoric, $\bar{\mathbf{F}}$, part, so that $\mathbf{F} = (J^{1/3}\mathbf{I})\bar{\mathbf{F}}$, where $J = \det\mathbf{F} > 0$ is the Jacobian given by the determinant of \mathbf{F} , the Lagrangian direction vectors are transformed into their isochoric Eulerian counterparts by

$$\bar{\mathbf{f}} = \bar{\mathbf{F}}\mathbf{f}_0, \quad \bar{\mathbf{s}} = \bar{\mathbf{F}}\mathbf{s}_0, \quad \bar{\mathbf{n}} = \bar{\mathbf{F}}\mathbf{n}_0. \quad (4.7)$$

A strain-energy function is used, suitable for describing the orthotropic nonlinear passive behavior of myocardium [35, 56] which is based on invariants which result in a coordinate frame independent stress tensor. The strain-energy function is separated into one volumetric and two volume preserving functions according to

$$\Psi = U(J) + \bar{\Psi}_{\text{iso}}(\bar{I}_1) + \bar{\Psi}_{\text{aniso}}(\bar{I}_{4f}, \bar{I}_{4s}, \bar{I}_{8fs}), \quad (4.8)$$

where $U(J)$ is the volumetric function and the volume preserving functions are $\bar{\Psi}_i$, $i \in \{\text{iso}, \text{aniso}\}$, which relate to the isotropic and anisotropic behavior respectively. For the volumetric function

$$U(J) = \frac{\mu_K}{2} \ln(J)^2, \quad (4.9)$$

is used, where μ_K is the bulk modulus which serves as a user specified penalty parameter enforcing incompressibility. The volume preserving isotropic and anisotropic functions are described by

$$\bar{\Psi}_{\text{iso}} = \frac{a}{2b} \{\exp[b(\bar{I}_1 - 3)] - 1\}, \quad (4.10)$$

and

$$\bar{\Psi}_{\text{aniso}} = \sum_{i=f,s} \frac{a_i}{2b_i} \{\exp[b_i(\bar{I}_{4i} - 1)^2] - 1\} + \frac{a_{fs}}{2b_{fs}} [\exp(b_{fs}\bar{I}_{8fs}^2) - 1], \quad (4.11)$$

respectively, where in total eight material parameters, $a_{(\cdot, f, s, fs)}$ and $b_{(\cdot, f, s, fs)}$, are needed to fully describe the isochoric orthotropic material behavior. The isochoric invariants in (4.10) and (4.11) are defined, using the modified volume-preserving right Cauchy-Green tensor, $\bar{\mathbf{C}} = \bar{\mathbf{F}}^T \bar{\mathbf{F}}$, as

$$\bar{I}_1 = \text{tr}(\bar{\mathbf{C}}), \quad \bar{I}_{4f} = \mathbf{f}_0 \cdot (\bar{\mathbf{C}}\mathbf{f}_0), \quad \bar{I}_{4s} = \mathbf{s}_0 \cdot (\bar{\mathbf{C}}\mathbf{s}_0), \quad \bar{I}_{8fs} = \mathbf{f}_0 \cdot (\bar{\mathbf{C}}\mathbf{s}_0). \quad (4.12)$$

As shown in [56], the necessary conditions on (4.11) for material stability are as follows; all material parameters must be larger than (or equal to) zero and the invariants \bar{I}_{4f} and \bar{I}_{4s} must be larger than one. If any of those invariants is less than one, the function containing it is dropped from the anisotropic strain-energy function, $\bar{\Psi}_{\text{aniso}}$, shown in (4.11). The Cauchy stress tensor for the passive part is given by

$$\boldsymbol{\sigma}_p = J^{-1/3} \bar{\mathbf{F}} \left(2 \frac{\partial \bar{\Psi}}{\partial \bar{\mathbf{C}}} \right) \bar{\mathbf{F}}^T, \quad (4.13)$$

which, using (4.8), result in

$$\begin{aligned} \boldsymbol{\sigma}_p = & p_h \mathbf{I} + 2J^{-1} [\bar{\psi}_1 \text{dev}(\bar{\mathbf{b}}) + \bar{\psi}_{4f} \text{dev}(\bar{\mathbf{f}} \otimes \bar{\mathbf{f}}) + \bar{\psi}_{4s} \text{dev}(\bar{\mathbf{s}} \otimes \bar{\mathbf{s}}) \\ & + \frac{1}{2} \bar{\psi}_{8fs} \text{dev}(\bar{\mathbf{f}} \otimes \bar{\mathbf{s}} + \bar{\mathbf{s}} \otimes \bar{\mathbf{f}})], \end{aligned} \quad (4.14)$$

where $p_h = \frac{dU(J)}{dJ}$ is a Lagrange multiplier, sometimes seen as the hydrostatic pressure enforcing incompressibility, $\bar{\mathbf{b}} = \bar{\mathbf{F}}\bar{\mathbf{F}}^T$ is the isochoric modified left Cauchy-Green tensor and $\text{dev}(\bullet) = (\bullet) - (1/3)[(\bullet) : \mathbf{I}]\mathbf{I}$ is the deviatoric operator in the Eulerian description [53]. Also in (4.14), the following definitions are used

$$\bar{\psi}_i = \frac{\partial \bar{\Psi}}{\partial \bar{I}_i}, \quad i = 1, 4f, 4s, 8fs. \quad (4.15)$$

Active stress component. The active stress tensor, $\boldsymbol{\sigma}_a$, is defined as

$$\boldsymbol{\sigma}_a = \sigma_a (\bar{\mathbf{f}} \otimes \bar{\mathbf{f}}), \quad (4.16)$$

where σ_a is a scalar value of the active stress and $\bar{\mathbf{f}}$ is the deformed isochoric fiber direction vector, given by (4.7). In this paper we choose to calculate σ_a using a single ODE which originates from [103], where the active stress value develops according to

$$\dot{\sigma}_a = \varepsilon(V_m)(k_\sigma \Delta V_m - \sigma_a), \quad (4.17)$$

where $\varepsilon(V_m)$ is a delay function controlling the rate of activation and relaxation of σ_a . k_σ regulates the amplitude of σ_a given the difference in transmembrane potential $\Delta V_m = V_m - V_r$, where V_m is the current action potential and V_r is the myocyte resting potential.

Instead of the Heaviside function proposed in [103], we use the smoother delay function, $\varepsilon = \varepsilon(V_m)$ as proposed in [49], which is given by

$$\varepsilon(V_m) = \varepsilon_0 + (\varepsilon_\infty - \varepsilon_0) \exp\{-\exp[-\xi(V_m - V_s)]\}, \quad (4.18)$$

where ε_0 and ε_∞ are the limiting values of the delay function when the action potential, V_m , is respectively larger or lower than a given phase shift V_s . Further, the transition rate of the delay function is controlled by the parameter ξ .

Note, however, that there is an erratum in the delay function shown in Eq. (23) in [103], namely that the limiting value $\varepsilon_\infty = 10\varepsilon_0$. With this condition, a delay of the peak active stress with respect to the peak action potential, as shown in Fig. 2 in [103], is unobtainable. In order to reproduce this time course the material parameters for the delay function must follow $\varepsilon_\infty < \varepsilon_0$. Also in [49] the wrong parameter relation was used, leading to a delay function that goes from lower to higher values, as shown in Fig. 3 in [49]. The differences in active stress behavior as well as in shape of the delay function is illustrated in Fig. 4.1(a)-(b).

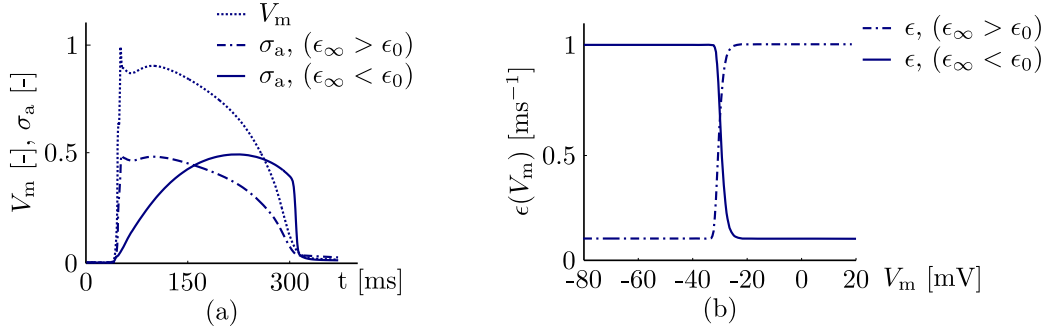


Figure 4.1.: (a) Potential V_m , dotted line, and corresponding delay in active stress values using $\varepsilon_\infty > \varepsilon_0$, dash-dotted line, and $\varepsilon_\infty < \varepsilon_0$, solid line, the values are scaled in the image for clarity; (b) shape of the delay function using $\varepsilon_\infty > \varepsilon_0$, dash-dotted line, and $\varepsilon_\infty < \varepsilon_0$, solid line, when shifted around $V_s = -30$ mV.

Using a backward Euler scheme to compute the current value of σ_a for a time step $\Delta t = t^n - t^{n-1}$, we obtain

$$\sigma_a^n = \sigma_a^{n-1} + \Delta t \varepsilon(k_\sigma \Delta V_m - \sigma_a^n), \quad (4.19)$$

which results in the closed-form expression of the current value of the active stress component

$$\sigma_a^n = \frac{1}{1 + \Delta t \varepsilon} (\sigma_a^{n-1} + \Delta t \varepsilon k_\sigma \Delta V_m). \quad (4.20)$$

Equation (4.6) together with (4.14), (4.16) and (4.20) are implemented in the finite element software FEAP [164], where σ_a is calculated at each gauss point.

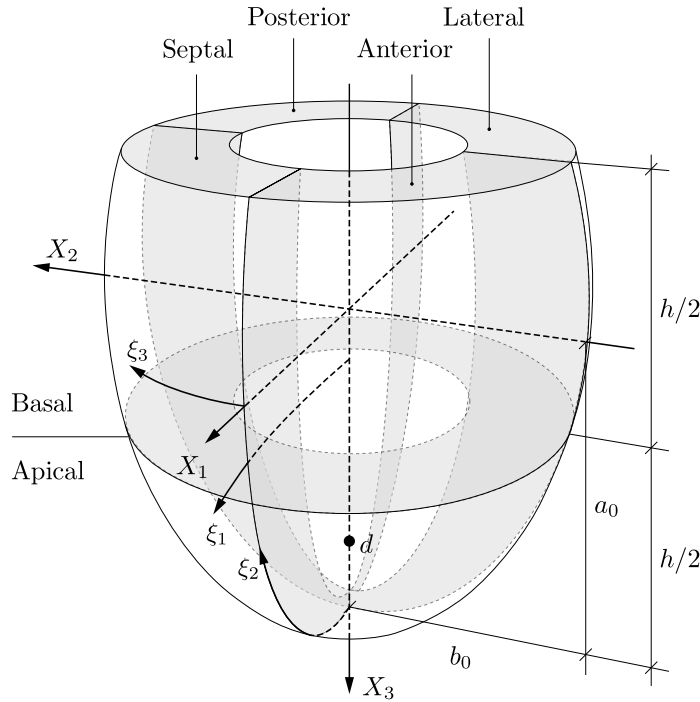


Figure 4.2.: Ellipsoidal model representing a rabbit LV with both the global X_1 , X_2 and X_3 coordinates and prolate spheroidal coordinates ξ_1 , ξ_2 and ξ_3 . The plane separating the basal and apical regions is at half of the LV height h . The septal region lies in the X_1, X_2 quadrant, the anterior region lies in the $X_1, -X_2$ quadrant, the lateral region lies in the $-X_1, -X_2$ quadrant and the posterior region lies in the $-X_1, X_2$ quadrant.

4.3. Electro-mechanically Coupled Model of a Rabbit Left Ventricle

4.3.1. Definition of geometry

The geometry of a rabbit LV is modeled as an ellipsoid truncated at the base using prolate spheroidal coordinates ξ_1 , ξ_2 and ξ_3 , see Fig. 4.2. Using the focal length $d = \sqrt{a_0^2 - b_0^2}$, where a_0 and b_0 are the polar and equatorial axis respectively, the prolate spheroidal coordinates may be expressed in a Cartesian coordinate system by

$$x_1 = d \sinh \xi_1 \sin \xi_2 \cos \xi_3, \quad x_2 = d \sinh \xi_1 \sin \xi_2 \sin \xi_3, \quad x_3 = d \cosh \xi_1 \cos \xi_2. \quad (4.21)$$

This geometry correlates to a rabbit LV [174] where the dimensions of the epicardium are $a_{\text{epi}} = 19.3$ mm, $b_{\text{epi}} = 12.7$ mm and the dimensions of the endocardium are $a_{\text{endo}} = 18.0$ mm, $b_{\text{endo}} = 6.9$ mm. The ξ_2 -angle has a maximum value of 120° at the endocardial surface. When going in the ξ_1 -direction towards the epicardial surface the maximum ξ_2 -angle is decreased so that the basal surface remains flat in the global X_3 -direction. Two

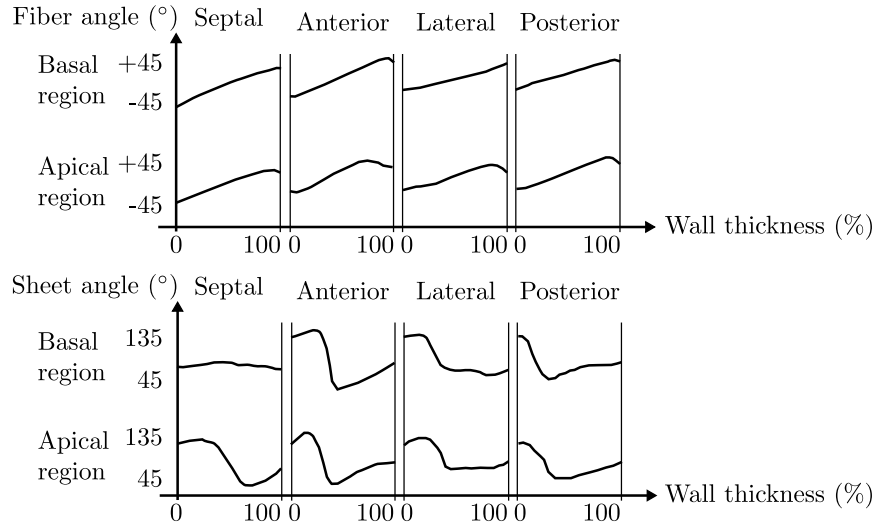


Figure 4.3.: Fiber and sheet angles through the wall thickness of the LV starting from the epicardium, adapted from [135].

overlapping finite element meshes of the same ellipsoidal domain were generated, a fully structured hexahedral mesh using MATLAB for solving mechanics, and, a fully unstructured hybrid mesh of an average resolution of $\sim 200 \mu m$ using an image-based mesh generation technique [127] implemented in the commercial mesh generator Tarantula (CAE Software Solution, Eggenberg, Austria) for solving electrics. The mechanical mesh consisted of 5406 nodes, comprising 5310 hexahedral mixed $Q1/P0$ finite elements, whereas the electrical mesh consisted of 1054146 nodes, comprising 1201507 linear hybrid finite elements [133]. Both grids were partitioned for parallel execution using parMETIS [73].

Model I - Generic fiber-sheet setup. For a generic fiber-sheet setup, the fiber direction in the wall of the myocardium varies linearly, from -60° at the epicardium to $+60^\circ$ at the endocardium, when looking in the $(-\xi_3), \xi_2$ direction seen in Fig. 4.2. The sheet orientation is also introduced with a linear distribution through the thickness of the myocardium and varies from $+85^\circ$ at the epicardium to -85° at the endocardium, looking in the ξ_1, ξ_2 direction. There is no difference in the fiber or sheet orientations between the different regions of the LV, i.e. anterior, posterior, lateral or septal regions, or between apical or basal regions. Thus, since both the fiber and sheet orientations are rule-based and vary in the transmural direction only, this setup is spatially homogeneous.

Model II - Experimentally based LV fiber-sheet setup. As an alternative to the generic setup, a fiber-sheet setup based on experiments may be constructed. Here, the fiber and sheet directions are modified to fit the measured data by Rohmer et al. [135] shown in Fig. 4.3. Using diffusion tensor MRI, they reported fiber and sheet angles for eight different regions, Ω_i , of the LV, where $i \in \{1 - 8\}$ corresponds to *septal*, *anterior*, *lateral* and *posterior* sides for both the *basal* and *apical* regions respectively. In our model, a linear

weighting function is used in-between these regions to ensure a smooth transition of the angles. The fiber and sheet angles for each region Ω_i in Fig. 4.3 are interpolated as a function of the transmural location, ξ_1 , thus giving the values $\alpha^{\Omega_i}(\xi_1)$ and $\beta^{\Omega_i}(\xi_1)$ for fiber and sheet angle, respectively. In Fig. 4.4, a conceptual representation of four adjacent re-

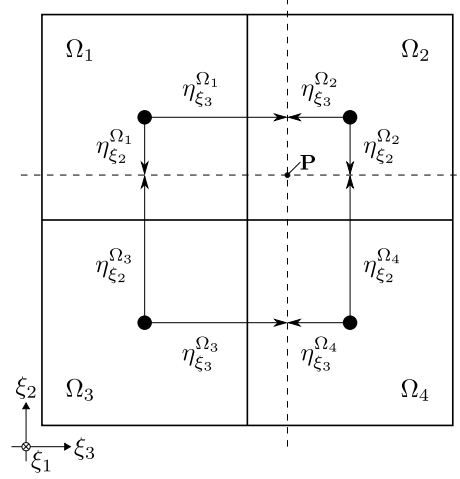


Figure 4.4.: Conceptual image of four adjacent regions Ω_i , $i \in \{1, 2, 3, 4\}$. Two weights, η , for each region are calculated based on the distance to a point, \mathbf{P} , in the ξ_2 and ξ_3 directions.

gions is shown with the weighting functions to a point $\mathbf{P} = [P_{\xi_1}, P_{\xi_2}, P_{\xi_3}]^T$. The values of the weighting functions, $\eta_{\xi_2}^{\Omega_i}$ and $\eta_{\xi_3}^{\Omega_i}$, goes from $1 \rightarrow 0$ when $\eta_{\xi_2}^{\Omega_i}$ and $\eta_{\xi_3}^{\Omega_i}$ goes from the center of its own region towards the center of a neighboring region in the ξ_2 and ξ_3 directions, respectively. Thus, the weighting functions for a region Ω_i to a point \mathbf{P} , are given by $\eta_{\xi_2}^{\Omega_i}(P_{\xi_2})$ and $\eta_{\xi_3}^{\Omega_i}(P_{\xi_3})$, while the values for the fiber and sheet angles for each region are $\alpha^{\Omega_i}(P_{\xi_1})$ and $\beta^{\Omega_i}(P_{\xi_1})$. The calculated values for the fiber and sheet angles at point \mathbf{P} , are thus

$$\alpha(\mathbf{P}) = \sum_{i=1}^8 \eta_{\xi_2}^{\Omega_i}(P_{\xi_2}) \eta_{\xi_3}^{\Omega_i}(P_{\xi_3}) \alpha^{\Omega_i}(P_{\xi_1}), \quad \beta(\mathbf{P}) = \sum_{i=1}^8 \eta_{\xi_2}^{\Omega_i}(P_{\xi_2}) \eta_{\xi_3}^{\Omega_i}(P_{\xi_3}) \beta^{\Omega_i}(P_{\xi_1}). \quad (4.22)$$

Using this setup for both fiber and sheet orientation, we have a transmurally varying spatially heterogeneous model.

4.3.2. Material parameters

For solving the monodomain equations, conductivities were chosen as $\sigma_{i\xi} = 0.302$ S/m, 0.1796 S/m, 0.0443 S/m in the intracellular domain, and as $\sigma_{e\xi} = 0.625$ S/m, 0.236 S/m, 0.236 S/m in the extracellular domain, with ξ being the principal tensor axes f , s and n , respectively. These choices correspond to monodomain bulk conductivities of $\sigma_{m,f} = 0.204$ S/m, $\sigma_{m,s} = 0.102$ S/m and $\sigma_{m,n} = 0.037$ S/m which led to conduction velocities of

0.6 m/s, 0.4 m/s and 0.2 m/s along the principal tensor axes f , s and n . Standard values of $C_m = 1 \mu F/cm^2$ and $\beta = 1400 \text{ cm}^{-1}$ were chosen for the membrane capacitance and surface-to-volume ratio.

Mechanical material parameters are summarized in Table 4.1. The passive material parameters are adapted from [35] where the model was fitted against experimental data reported by Dokos et al. [32]. The active material parameters are in part adapted from [103], and in part adapted to give an electro-mechanical delay of 110 ms between peak action potential and peak active stress as shown in [97]. The pressure parameters are adapted to keep pressure calculations numerically stable and to obtain realistic pressure-volume loops.

<i>Passive stress</i>	<i>Active stress</i>	<i>Pressure terms</i>
$\mu_K = 3333 \text{ kPa}$	$k_\sigma = 0.50 \text{ kPa mV}^{-1}$	$C = 0.2 \text{ ml mmHg}^{-1}$
$a = 0.333 \text{ kPa}$	$V_r = -86.796 \text{ mV}$	$R = 750 \text{ mmHg ms ml}^{-1}$
$b = 9.242 \text{ (-)}$	$V_s = -80.0 \text{ mV}$	$C_p = -900 \text{ mmHg ml}^{-1}$
$a_f = 18.535 \text{ kPa}$	$\epsilon_0 = 1.0 \text{ ms}^{-1}$	
$b_f = 15.972 \text{ (-)}$	$\epsilon_\infty = 0.1 \text{ ms}^{-1}$	
$a_s = 2.564 \text{ kPa}$	$\xi = 0.1 \text{ mV}^{-1}$	
$b_s = 10.446 \text{ (-)}$		
$a_{fs} = 0.417 \text{ kPa}$		
$b_{fs} = 11.602 \text{ (-)}$		

Table 4.1.: Material parameters used in both analytical and numerical calculations. The passive stress material parameters are adapted from [35], and the active stress material parameters are adapted from [49].

4.3.3. Initial values and boundary conditions

Electrics. The Mahajan model [91] is employed to describe cellular dynamics. The model was initialized by pacing a single cell at a pacing cycle length of 350 ms until a stable limit cycle was observed. The state vector $\boldsymbol{\eta}$ at the end of this pre-pacing procedure was used to populate the LV model with an initial state vector, $\boldsymbol{\eta}_0$. Transmembrane current injection applied to the endocardial surface at $t = 0$ ms initiated the propagation of the action potentials at the endocardium to approximate a predominantly transmural activation sequence, as induced by activation via the Purkinje system. In this approximation the whole endocardium was activated synchronously, electrical activation delays within the endocardium remained unaccounted for. 350 ms of activity were simulated to cover one full depolarization and repolarization cycle over the entire LV.

Mechanics, circulatory components and pressure-volume loops. All elements on the endocardial surface of the LV are subjected to a follower pressure load p . On the base of the LV, where $\xi_2 = \xi_{2\max}$ for all ξ_3 and ξ_1 , all nodes have displacement boundaries restricting movement in the ξ_2 -direction. Nodes on the basal plane at the epicardium, located where

BC	Coordinates	Description
$t_n = -p$	$\xi_1 = \xi_{1 \min}$	for all ξ_3, ξ_2 Endocardial surface
$u_{\xi_2} = 0$	$\xi_2 = \xi_{2 \max}$	for all ξ_3, ξ_1 Basal surface
$u_{\xi_3} = 0$	$\xi_2 = \xi_{2 \max}$ $\xi_1 = \xi_{1 \max}$	for all ξ_3 Outer ring at base

Table 4.2.: Mechanical boundary conditions in terms of prescribed tractions \mathbf{t} and displacements \mathbf{u} for the mechanical mesh. t_n is the normal component of the traction vector to the endocardial surface on which p acts.

$\xi_1 = \xi_{1 \max}$, $\xi_2 = \xi_{2 \max}$ and for all ξ_3 , have additional displacement boundaries restricting movement in the ξ_3 -direction. The boundary conditions are summarized in Table 4.2. The follower type pressure load p is calculated in five consecutive steps, (i)–(v). The first step, (i), is a non-physiological initialization load and is used before electrical activation has started, i.e. when time $t \leq 0$. The pressure is increased linearly from 0 to 20 mmHg, which is considered the end diastolic pressure, EDP, [140]. When the pressure reaches EDP, electrical activation starts and thus an isochoric contraction ensues since both the mitral and aortic valves are considered to be closed. The pressure in this load step, (ii), is increased iteratively for each time step to keep the volume V constant using

$$p_{n+1} = p_n + (V_{n+1} - V_n)/C_p, \quad (4.23)$$

as described in [168], where C_p is a penalty parameter. The value of C_p is set to give a computationally efficient convergence for the isochoric solution. When p reaches 95 mmHg [140], the ejection phase starts simulating the opening of the aortic valve. In this step, (iii), the pressure is modeled using the two element Windkessel model [116] described as

$$C \frac{dp}{dt} + \frac{p}{R} = -\frac{dV}{dt}, \quad (4.24)$$

where C and R relate to arterial compliance and resistance, respectively. Since C and R are considered constants, they do not account for the nonlinear behavior of arteries [130, 131]. Their values are chosen to generate realistic pressure-volume (PV) loops. When dV/dt becomes positive (reversed blood flow), the aortic valve closes. The current pressure is considered to be the end systolic pressure and isochoric relaxation of the LV starts, load step (iv), again modeled using the pressure iteration shown in (4.23). Finally, when p reaches 12.5 mmHg [140], passive filling is assumed to start as the mitral valve opens. This final pressure load, called load step (v), is modeled using a linear increase in pressure until EDP is reached, after which the pressure loop starts over at load step (ii). The load steps are summarized as

- (i) Non-physiological initial phase with linear pressure increase to EDP
- (ii) Isochoric LV compression phase using (4.23)

- (iii) Ejection phase using (4.24)
- (iv) Isochoric LV relaxation phase using (4.23)
- (v) Filling phase with linear pressure increase to EDP

To calculate volume and area of the LV cavities, the quadrilateral faces of the hexahedral elements along endocardial and epicardial surfaces are triangulated. Using the Gauss divergence theorem

$$\iiint_V (\nabla \cdot \mathbf{R}) dV = \oiint_S \mathbf{R} \cdot \mathbf{n} ds, \quad (4.25)$$

the volume V is calculated using $\nabla \cdot \mathbf{R} = 1$ with, for example, the vector field $[\mathbf{R}] = [x, 0, 0]^T$. The volume enclosed by the triangulated surface elements is thus calculated by summing up the signed surfaces as follows; the coordinates of the nodal points, $\mathbf{u}, \mathbf{v}, \mathbf{w}$, of each triangular face i are $[\mathbf{u}]_i = [u_x, u_y, u_z]^T$, $[\mathbf{v}]_i = [v_x, v_y, v_z]^T$ and $[\mathbf{w}]_i = [w_x, w_y, w_z]^T$. The edges $\mathbf{a}_i = \mathbf{v}_i - \mathbf{u}_i$ and $\mathbf{b}_i = \mathbf{w}_i - \mathbf{u}_i$ span the triangle i , and the cross product, $\mathbf{c}_i = \mathbf{a}_i \times \mathbf{b}_i$, is perpendicular to the surface, with the magnitude of its length being twice the element area. Thus, the area of the triangle i is $A_i = \|\mathbf{c}_i\|/2$, and the normal vector is $\mathbf{n}_i = \mathbf{c}_i/\|\mathbf{c}_i\|$. The center of a triangle i is found as $\mathbf{p}_i = (\mathbf{u}_i + \mathbf{v}_i + \mathbf{w}_i)/3$. Since the vector field $[\mathbf{R}] = [x, 0, 0]^T$ is used, only the x -components, $p_i^{(x)}$ of \mathbf{p}_i and $n_i^{(x)}$ of \mathbf{n}_i , are required to evaluate the surface integral in Eq. (4.25). Thus the enclosed volume and its surface are computed by summing over the surface triangles n_{el}

$$V = \sum_{i=1}^{n_{el}} p_i^{(x)} n_i^{(x)} A_i \quad \text{and} \quad A = \sum_{i=1}^{n_{el}} A_i. \quad (4.26)$$

Note that this formulation requires, in general, that the surface is closed and that all surface normals are pointing outwards. However, for this specific LV geometry and BC defined here, however, this is not required since the vector field $[\mathbf{R}] = [x, 0, 0]^T$ is co-planar with the LV opening at the base. Surface normals were enforced to point outwards by computing $\langle \mathbf{o}_i, \mathbf{n}_i \rangle$ where $\mathbf{o}_i = \mathbf{h}_i - \mathbf{a}_i$ with \mathbf{h}_i being the center of the hexahedron to which the triangle is attached. In the case of a negative dot product two nodes spanning the triangle are swapped.

By using this strategy on both the epicardial and endocardial surfaces, an average thickness, h , of the LV wall is calculated, in accordance with [33], as $h = 2V_{\text{wall}}/(A_{\text{endo}} + A_{\text{epi}})$, where A_{endo} and A_{epi} are the endocardial and epicardial areas, respectively, and V_{wall} is the volume of the myocardial wall, defined as the difference between the volumes enclosed by the endocardial and epicardial surfaces. Defining h_{ed} and h_{es} as the thickness corresponding to the end diastolic volume, EDV, and end systolic volume, ESV, respectively, fractional thickening, h_f , is calculated as

$$h_f = \frac{h_{\text{es}} - h_{\text{ed}}}{h_{\text{ed}}} 100. \quad (4.27)$$

As a metric for examining incompressibility the fractional change in myocardial volume is calculated as

$$V_f(t) = \frac{V_{\text{wall}}(t) - V_{\text{wall}}^0}{V_{\text{wall}}^0} 100, \quad (4.28)$$

where $V_{\text{wall}}(t)$ and V_{wall}^0 are the volume of the myocardium as a function of time and in the initial unloaded configuration, respectively. The largest, positive or negative, change in volume fraction $V_f(t)$ is labeled V_f^{max} , which may be used to gauge how well the incompressibility constraints were enforced in the simulation. Furthermore, stroke volume is defined as $SV = EDV - ESV$, cardiac output is defined as $CO = SV \cdot HR$, where HR is the heart rate and ejection fraction is defined as $EF = (SV/EDV) 100$.

4.3.4. Transferring data between electrical and mechanical grid

Solving the electrical and mechanical problem poses different constraints on the choice of spatio-temporal resolution in the respective discretization schemes. The fastest electrical processes are governed by time constants in the μs range and the spatial extent of a propagating depolarization wavefront is in the sub-millimeter-meter range. On the other hand, mechanical processes tend to occur at slower space and time scales. Consequently, these differences in spatio-temporal characteristics suggest the use of different spatio-temporal discretization, which necessitates the transfer of data between electrical and mechanical grid. In this study where a weak coupling scenario was considered, only one scalar quantity, the transmembrane voltage V_m , had to be transferred uni-directionally, i.e. from the electrical grid to the mechanical grid. This procedure was implemented by using the nodal values of V_m on the electrical grid, and interpolating these values onto the Gauss points of the $Q1/P0$ elements of which the mechanical grid is comprised. To facilitate an efficient search for finite elements in the electrical grid which enclose corresponding Gauss points of the mechanical grid, an Octree data structure was employed [127].

4.3.5. Validation of implementation and passive mechanical properties of LV model

Both the numerical implementation as well as the model of the rabbit LV were subjected to a set of tests to ensure the soundness of the framework as well as good agreement with experimental observations. To test the numerical framework, an analytical test case was designed. A unit cube, free to deform, with the fiber, sheet and sheet-normal directions organized in the global X , Y and Z directions, respectively, as shown in Fig. 4.5(b), i.e.

$$[\mathbf{f}_0] = [1, 0, 0]^T, \quad [\mathbf{s}_0] = [0, 1, 0]^T, \quad [\mathbf{n}_0] = [0, 0, 1]^T, \quad (4.29)$$

is subjected to a scalar value of active stress, resulting in a contraction in the global X direction. The material is assumed to be incompressible and therefore the cube must expand

in the global directions Y and Z . Thus, the corresponding deformation gradient is

$$[\mathbf{F}] = \begin{bmatrix} \lambda_f & 0 & 0 \\ 0 & \lambda_s & 0 \\ 0 & 0 & \lambda_n \end{bmatrix}, \quad (4.30)$$

where the stretch in the fiber direction, $\lambda_f < 1$, and the stretch in the sheet and sheet-normal directions, $\lambda_s > 1$ and $\lambda_n > 1$, with a smaller deformation in the s -direction than in the n -direction due to the orthotropic material properties. Incompressibility in an analytical case enforces $J = 1$, leading to the simplified Cauchy stress tensor

$$\boldsymbol{\sigma} = p_h \mathbf{I} + 2(\psi_1 \mathbf{b} + \psi_{4f} \mathbf{f} \otimes \mathbf{f} + \psi_{4s} \mathbf{s} \otimes \mathbf{s}) + \psi_{8fs} (\mathbf{f} \otimes \mathbf{s} + \mathbf{s} \otimes \mathbf{f}) + \sigma_a \mathbf{f} \otimes \mathbf{f}, \quad (4.31)$$

where $\mathbf{f} = \mathbf{F}\mathbf{f}_0$ and $\mathbf{s} = \mathbf{F}\mathbf{s}_0$ are the deformed direction vectors, $\mathbf{b} = \mathbf{F}\mathbf{F}^T$ is the left Cauchy-Green tensor and

$$\psi_i = \frac{\partial \Psi}{\partial I_i}, \quad i = 1, 4f, 4s, 8fs. \quad (4.32)$$

With the deformation gradient (4.30) the components of (4.31) are

$$\sigma_{11} = p_h + 2\psi_1 \lambda_f^2 + 2\psi_{4f} \lambda_f^2 + \sigma_a \lambda_f^2, \quad (4.33)$$

$$\sigma_{22} = p_h + 2\psi_1 \lambda_s^2 + 2\psi_{4s} \lambda_s^2, \quad (4.34)$$

$$\sigma_{33} = p_h + 2\psi_1 \lambda_n^2, \quad (4.35)$$

$$\sigma_{12} = \sigma_{13} = \sigma_{23} = 0. \quad (4.36)$$

As the unit cube is free to deform, the stress at equilibrium is zero for all components of $\boldsymbol{\sigma}$ and p_h is readily determined from σ_{33} . Using (4.33) and (4.34) together with the condition of a volume preserving incompressible material, i.e. $\det \mathbf{F} = 1$, the following nonlinear systems of equations may be deduced,

$$\sigma_{11} = 2\psi_1 (\lambda_f^2 - \lambda_n^2) + (2\psi_{4f} + \sigma_a) \lambda_f^2 = 0, \quad (4.37)$$

$$\sigma_{22} = 2\psi_1 (\lambda_s^2 - \lambda_n^2) + 2\psi_{4s} \lambda_s^2 = 0, \quad (4.38)$$

$$\lambda_f \lambda_s \lambda_n = 1. \quad (4.39)$$

Keeping in mind that ψ_{4f} vanishes if $\lambda_f^2 < 1$ [56], which is always the case in this particular example, the system of Eqs. (4.37)–(4.39) can be solved for λ_f , λ_s and λ_n and a given value of σ_a (calculated using equation (4.20)). This system was solved using the MATLAB function *fsolve()*. The material parameters used is shown in Table 4.1. The same problem is solved in FEAP and the resulting stretches are compared to the analytical solution for several values of the action potential V_m .

To our knowledge, there are no data available in the literature which would specifically characterize the passive mechanical material parameters of the rabbit myocardium. Instead,

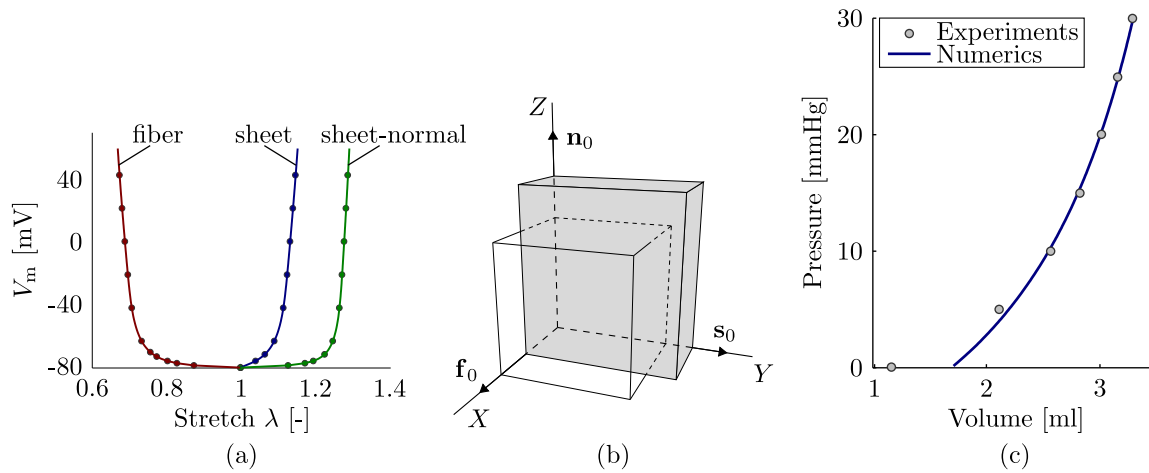


Figure 4.5.: (a) Potential-stretch curves for the analytical solution (solid lines, sub-index A) and the FEAP solution (circles, sub-index F) in the fiber f , sheet s , and sheet-normal n , directions; (b) unit cube before deformation (outlined) and after deformation (solid); (c) overlay of FEM calculation of passive inflation on experimental data from passive inflation of a rabbit LV. The experimental data points are adapted from Fig. 4 in [46], and the FEM calculation is shifted to the left to account for the difference in initial volumes between model and experiment.

the passive material parameters used and shown in Table 4.1, were fitted against porcine myocardium [35]. To verify that they are also reasonably valid for a rabbit LV, Model I is passively inflated to 30 mmHg and compared to experimental data of passive inflation [46].

4.4. Results

4.4.1. Model validation

Validation results of the numerical implementation are shown in Fig. 4.5(a). The perfect match between analytical and numerical solution suggests that the implementation of the model can be considered to be correct. Results of the passive inflation experiments are shown in Fig. 4.5(c). The FEM solution agrees very well with the experimental data beyond 5 mmHg, indicating that the material parameters retrieved from porcine experiments are also well suited for models of a rabbit LV.

4.4.2. Effect of heterogeneity in orthotropy upon mechanical contraction

To study the impact of spatial heterogeneities in the arrangement of fibers and laminae pressure-volume loops were computed for a full cardiac cycle using model I and II . In both cases the LV is modeled as an electrically and mechanically orthotropic material. Both models were subjected to the exact same stimulation protocol and the same boundary

conditions, with the only difference being that the material structure is described using a spatially heterogeneous orthotropic tensor in model *II* based on experimental measurements, as opposed to a rule based spatially homogeneous orthotropic tensor in model *I*. Overall, the mechanical behavior observed is fairly similar between the two models, however, in some aspects striking differences were observed. Both Models *I* and *II* are in good agreement with experimentally observed PV loops [140]. In Fig. 4.6(a), Model *II* is shown together with experimental values, both using a normalized volume to account for the difference in initial LV volumes. Fig. 4.6(b) shows the PV loops for both Models *I* and *II*. The relative comparison reveals that Model *II* predicts a larger EDV, whereas the ESV's are fairly similar between the models. No major differences were observed in any

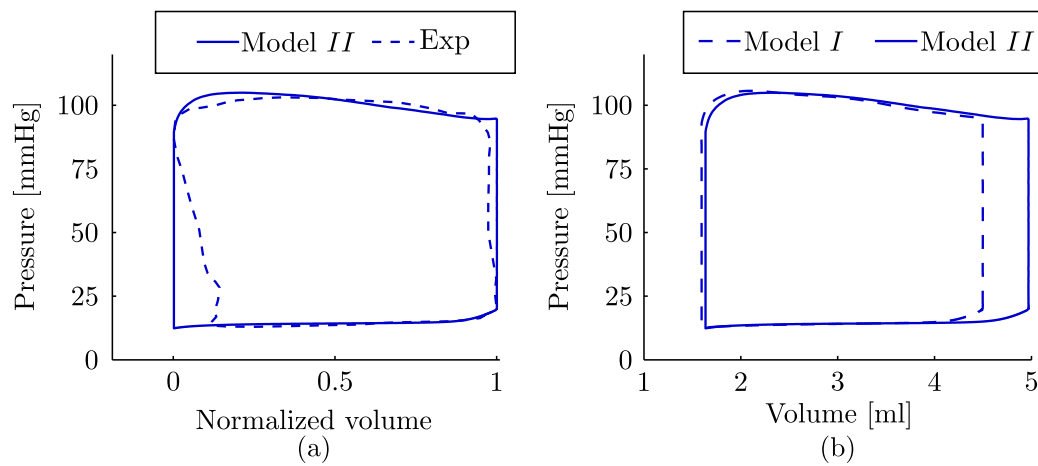


Figure 4.6.: (a) Comparison of PV-loops between data-based model and experimental results adapted from [140]. The volume is normalized between EDV and ESV for both model and experiment to account for the difference in initial volume; (b) comparison of PV-loops between Models *I* and *II*.

parameters which characterize mechanical performance globally, such as wall thickening, maximum change in myocardial wall volume, stroke volume, ejection fraction and cardiac output. A comparison of these parameters is summarized in Table 4.3. SV is slightly lower with Model *I*, and thus, since HR was the same, CO was lower too.

Despite these similarities, with regard to torsion the difference in predictions was strikingly different. The average torsion in the short axis plane with Model *II* was 4.5° (Fig. 4.7(c)), whereas the spatially homogeneous fiber and sheet setup in Model *I* resulted in equal torsion in all short axis cross sections of 53.5° (Fig. 4.7(d)). A further noticeable difference arose with regard to the movement of the apex. In Model *I* the apex moved only along the apico-basal direction, aligned with the global X_3 -direction in our setup, whereas in Model *II* a significant movement of the apex towards the septal wall was observed (Fig. 4.7(b)). Therefore, to analyze the torsion of the LV in model *II*, the long and short axis orientation required adjustments with Model *II*, since the long axis is assumed to be aligned with the main direction of the septal wall. The short axis is perpendicular to the long axis and is

Results	Model <i>I</i>	Model <i>II</i>	Experiment
h_f (%)	33	29	35.2 [151]
V_f^{\max} (%)	-0.42	-0.51	-7.2 [3] [†]
HR (bpm)	171	171	198 [158]
SV (ml)	2.7	3.1	1.8 [158]
EF (%)	61	63	53 [158]
CO (l/min)	0.46	0.53	0.421 [158]

Table 4.3.: Comparison of results between Models *I*, *II* and experiment. h_f =fractional thickening, V_f^{\max} =volume fraction of the wall (maximum change in wall volume), SV = stroke volume, EF =ejection fraction, CO =cardiac output. [†]Average value of through-thickness volume change.

chosen to be close to the endocardial apex, as shown in Fig. 4.7(a). Aligning the centroid of the cavity in short axis images, taken from EDV and ESV, the torsion may be calculated by tracking the movement of the mesh.

The radial contraction from EDV to ESV of the endocardium and the epicardium may be viewed in the septal-lateral and posterior-anterior directions. In both Models *I* and *II*, this contraction is quite similar except for the septal-lateral direction at the epicardial border. This contraction is visible in Fig. 4.7 as the difference between the dashed lines (EDV) and solid lines (ESV). Both models also match experimental data quite well [118], except for the epicardial contraction in the septal-lateral direction where Model *II* is significantly closer to experimental values than Model *I*. A further fundamental difference was observed with regard to fiber and sheet stresses. This is illustrated in Fig. 4.8 which visualizes fiber and sheet stresses in a cross section through the septal and lateral wall. As shown, Model *I* predicts much higher stress gradients than Model *II* at the basal epicardial border.

4.5. Discussion

A computational model of the rabbit LV was used to investigate the impact of spatial heterogeneity in structural orthotropy upon mechanical contraction. While numerous simplifying assumption were made in constructing this model with regard to ventricular geometry, mechanical boundary conditions, electro-mechanical coupling and the generation of active stresses which all clearly may influence simulation results, relative comparisons are possible, allowing to dissect the effects of the one model parameter under study, i.e. spatial variations in orthotropy. Simulation results suggest that spatial heterogeneity in structural orthotropy may play a critically important role in mechanical contraction of the LV. While the predictions of both models, i.e. with and without spatial heterogeneity in orthotropy, were very similar and matched fairly well with experimental data in terms of most lumped system parameters such as pressure-volume loops, in some aspects striking differences were observed. Most notably, this was the case with torsion which turned out

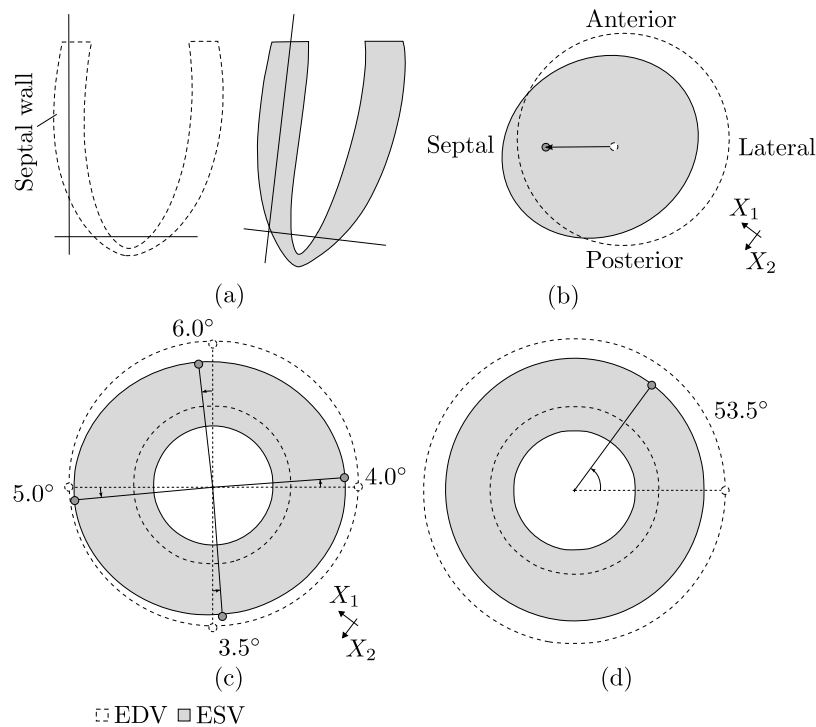


Figure 4.7.: Geometry at EDV shown with empty regions and dashed lines, and ESV shown with filled regions and solid lines: (a) the short-axis plane is perpendicular to the long-axis plane which is always aligned with the main direction of the septal wall; (b) the outlined epicardial surface viewed from the apex towards the base of the LV. The apex in both EDV and ESV are marked with a circle and show the movement of the apex towards the septal region; (c) torsion at the short-axis plane for Model II. The average torsion is 4.5° ; (d) torsion at the short-axis plane for Model I. The torsion is the same for all regions and is 53.5° .

to be significantly larger in the presence of orthotropic heterogeneity.

Effects of heterogeneity in orthotropy. While the influence of heterogeneity in structural orthotropy turned out to be very minor with respect to lumped parameters such as PV loops which characterize ventricular mechanical performance at a global scale, deformation was quite sensitive, with torsion being strikingly different between the models.

On the other hand, despite the better match achieved with experimental data in several regards, the use of experimental data on orthotropy led to unphysiological predictions which were not present in the simpler model. In particular, using model II predicted a longitudinal elongation of the LV which is in contradiction to the longitudinal shortening, as it is seen in experiments [159].

Potential reasons are: i) the maximum active stress generated, regulated by the parameter

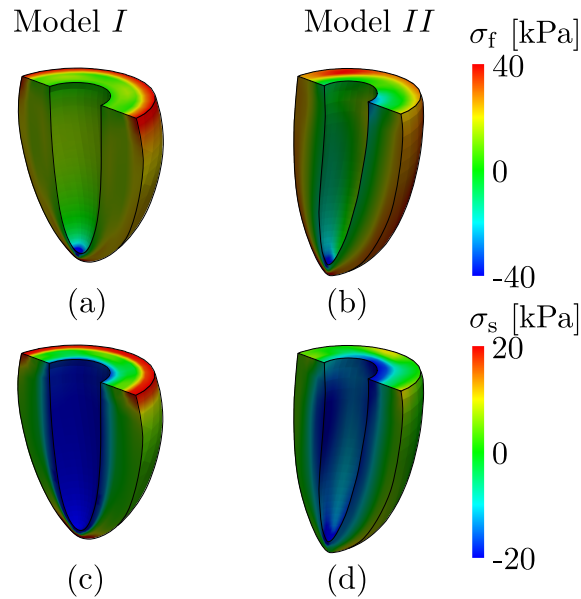


Figure 4.8.: Fiber and sheet stress in Models *I* and *II*: (a) fiber stress in Model *I*; (b) fiber stress in Model *II*; (c) sheet stress in Model *I*; (d) sheet stress in Model *II*.

k_σ , was not large enough, and therefore, with a smaller fiber component in the longitudinal direction relative to Model *II*, the internal pressure of the LV dominated. This highlights the difficulty of obtaining accurate material properties also for the active material model. It is unclear whether this would also occur in the presence of a RV. ii) the mapping of orthotropic data from an anatomically realistic model onto a simplified ellipsoidal model may have led to distortions, considering that the geometric differences between the ellipsoidal model and the real geometry in which the measurements of the structure tensors were performed, were significant. This potential problem could be circumvented by using datasets which provide both anatomical information via high resolution MRI, and structural information, acquired by Diffusion-tensor MRI. A further potential discrepancy stems from the fact that the complex trabeculation of the endocardium remains unaccounted for in our model, a limitation that is shared with all other modeling studies on ventricular mechanics. iii) the mean values as presented by Rohmer were taken and linearly interpolated, however, the noise and variance in these data is significant. The data were averaged over large sectors of the ventricles, more detailed data on a per voxel base were not available. iv) fiber angles in the Rohmer data tended to be smaller than those observed in detailed histological studies [93, 126] upon which most rule-based approaches are built upon.

Validation. Even though material parameters for the passive behavior of the LV are inherently difficult to obtain, the excellent agreement between experimental data and the LV model for passive inflation, shown in Fig. 4.5, can be considered as an indication of accuracy and a justification of using the given passive material parameters in this study. The

behavior of the passive model differs from experimental observations only for very low pressures, < 5 mmHg, where the model behaves stiffer. A potential cause underlying this discrepancy is the folding of the LV wall under these very low cavitory pressures. Upon inflation, as the pressure increases and the folds unravel, the cavitory volume may increase without generating any relevant stresses in the LV walls. This behavior, however, would not be evident in-vivo since low pressures of < 5 mmHg are clearly below the physiological range in a rabbit LV [140].

Despite obvious differences in deformation between the models, the predicted PV loops were quite similar (see Fig. 4.6 (b), suggesting that PV loops alone are an insufficient criterion for assessing accuracy and adequacy of a model. Therefore additional quantities were computed such as myocardial torsion, the thickening of the myocardial wall, radial contraction, stresses and global LV functions such as stroke volume, ejection fraction and cardiac output. Ideally, experimentally recorded displacement fields along with strain measurements and detailed transmural electrical mapping data should be used to better gauge the model performance, however, such data are not readily available at a sufficiently high spatio-temporal resolution in 3D.

For Models *I* and *II*, the torsion of the myocardium at ESV is shown in Fig. 4.7(c) and (d). For Model *I*, the torsion was 53.5° which is much higher than the average torsion in Model *II* which was only 4.5° . Physiologically measured values found in the literature are in the range of ~ 8 - 12° [16, 112, 163], which means Model *I* predicts torsions which are far too large. Possible reasons for the pronounced torsion in Model *I* are the simplified representation of LV geometry and the absence of the RV which would likely reduce torsional significantly in the LV myocardial wall, particularly in the septal region. The difference in the fiber and sheet stresses between Models *I* and *II*, seen in Fig. 4.8, is probably caused by the reduced torsion in Model *II*. This means that Model *II* is not as influenced from the applied BC as Model *I*, which implies that Model *II* is preferable from a computational point of view. The averaged thickening, h_f , of the ventricular wall for both Models *I* and *II* are close to experimentally observed values for rabbits, as shown in Table 4.3. Using an averaged value does not capture regional differences in thickening [18, 159], but with the simplified geometrical model used here, it may provide a more useful comparison as the thickening alters significantly in the longitudinal direction.

Stroke volume, ejection fraction and cardiac output are all close to experimentally obtained values, as seen in Table 4.3, for a rabbit LV. Also the heart rate, 171 bpm, is within the reported values in the literature corresponding to a conscious rabbit. Thus, similar to the argument concerning the PV-loops, with these values it is only possible to partially differentiate between, or determine the accuracy of, the models. The discrepancy between experimentally observed and simulated values for the compressibility of wall volume, V_f^{\max} shown in Table 4.3, is not surprising as the setup of the model assumes near incompressibility, while experimental observations show that there is some compression of the wall volume due to, for example, blood leaving the coronary arteries during systole [3]. Thus,

as near incompressibility was intended to be modeled, the low values of V_f^{\max} shown for both models indicate that a large enough value of the bulk modulus was chosen.

The asymmetric contraction pattern in Model *II* gives a slightly more realistic value of radial contraction in the septal-lateral direction at the epicardial border when compared to experimental values [118]. Both Models *I* and *II* show realistic values in all other directions of radial contraction when compared to the same experiments, indicating that radial contraction is not heavily affected by torsion which is much larger in Model *I*.

Limitations of the study. An important limitation is the use of a stylized geometry where the real geometry of a LV is approximated by an ellipsoid. Further, the presence of the RV influences the mechanical action of the LV, but these effects were neglected in this study. Apart from the macro-anatomical differences between a real bi-ventricular geometry and an ellipsoid, as in any other modeling study on cardiac mechanics, the complex trabeculation of the endocardium remain unaccounted for. A simplified phenomenological model of electro-mechanical coupling was used where the generated active stresses depend only on the transmembrane potential, ignoring all major physiological factors implicated in the process of active stress generation such as calcium transients, the interactions of calcium with myofilaments and metabolic aspects. The absence of a filament model also prevents modeling of a transverse component of the active stress tensor, as postulated in [128].

Further, as in most previous studies [77, 106, 168], electrical and mechanical model were weakly coupled. That is, the solution of the electrical quantities is calculated on a static mesh first, and relevant parameters are then fed into a separate subsequent simulation of deformation and stress analysis. The main advantage of a weakly coupled approach is lower complexity and compute time [128], however, in contrast to strong coupling approaches [104, 108] the modeling of phenomena where mechanical stresses influence upon the electrophysiological properties that govern cellular dynamics, is not possible. That is, effects of mechano-electric feedback are fully ignored [75]. While strongly coupled approaches are likely to be key when subtle electro-mechanical effects are to be captured, most modeling studies refrained from taking a strong coupling approach, mainly due to the increased complexity of computation schemes and potential problems with numerical instabilities, although those issues are being addressed [107, 120]. The striking effect of experiment based fiber and sheet orientations demonstrated in the simulation in this study clearly indicate the need for realistic geometrical modeling. However, with anatomically highly realistic models, as they are now state of the art in modeling cardiac electrophysiology [11, 124], the mesh density increases significantly to resolve finer anatomical details, which, in turn, entails a substantial increase in computational costs [105]. Using such high-resolution meshes for simulating deformation in cardiac mechanics require the consequent use of advanced numerical methods and parallelization techniques, to enable strongly scalable simulation on large scale high performance computing facilities which is key to keep such high-resolution simulations of cardiac electromechanics tractable.

Despite these many limitations which are shared by most contemporary modeling studies on cardiac electro-mechanics, the relative differences observed between Model *I* and Model *II* provides evidence on the non-negligible role of spatial heterogeneity in structural orthotropy. Particularly the significant influence upon torsion, which characterizes a striking difference, is a fairly robust feature which is almost certain to be seen in more advanced models where some of the above listed limitations are lifted.

Acknowledgement

This project is in part supported by the SFB Research Center ‘Mathematical Optimization and Applications in Biomedical Sciences’, project F3210-N18 granted by the Austrian Science Fund. This support is gratefully acknowledged.

5. MODELING THE DISARRAY IN CARDIAC FIBER AND SHEET ORIENTATIONS

Abstract We present a novel approach to model the disarray of both the fiber and sheet orientations evident in, especially diseased, myocardium. By utilizing a structure parameter, which determines the level between isotropy and transverse isotropy related to a preferred material direction, an existing orthotropic constitutive model developed for myocardium is augmented. The structure parameter can be fitted to experimentally observed angular dispersion data. It is used both for the passive behavior of the myocardium, and in the determination of the direction of applied active stress. Analytical and numerical simulations on a simple cube and passive inflation of a section of an LV show that the dispersion parameter has great effect on myocardial deformation and stress development. On a simulation of the entire left ventricle, represented by a truncated ellipsoidal finite-element model incorporating active stress, the dispersion parameter is included and fitted to both healthy and diseased myocardium. The results show that the dispersion parameter have a significant impact on pressure-volume loops, and in future simulations the presented dispersion model for myocardium may advantageously be used together with models of, e.g., growth and remodeling of various cardiac diseases.

5.1. Introduction

The left ventricle (LV) is the main pumping chamber of the heart which supplies blood through the circulatory system to the entire body. The LV builds up the necessary pressure by active contraction where the electrical activation of the heart triggers a cascade of events, referred to as electro-mechanical coupling, which leads to a shortening of the cardiac myocytes which make up the myocardial wall. Myocytes are arranged in a highly organized fashion, following a right-handed helical pathway from the endocardium towards the mid-wall, and a left-handed helical pathway from the mid-wall towards the epicardium [93, 135, 169]. This prevailing myocyte orientation is usually referred to as ‘fiber orientation’. In addition, fiber bundles are arranged into laminar sheets of four to six cell layers, where the prevailing sheet orientation also varies in both the transmural as well as the apico-basal direction [85, 135, 142, 190]. At any point in the LV, the structural arrangement of myocytes is reflected in three orthogonal directions along which both electrical as well as mechanical material parameters are different, thus necessitating to model electrical and mechanical response of the myocardium as an orthotropic material. These preferred directions are along the fibers, transverse to the fibers but within a laminar sheet, and per-

pendicular to the sheets; these directions are thus called the fiber, sheet and sheet-normal directions, respectively.

In the healthy heart, the fiber alignment follows very closely these helical pathways with only small angular dispersion (AD) in the range of $\sim 12\text{-}15^\circ$, whereas in diseases such as hypertrophic cardiomyopathy (HCM) or myocardial infarction (MI) the AD may locally increase with $\sim 65\%$ (at foci points within the septal wall) [71, 72, 171] or $\sim 50\%$ (at the site of infarction) [157, 181, 192] respectively. Less is known about the structural arrangement of laminae. Due to the importance of sheet orientation in myocardial wall thickening it has been speculated that dispersion of sheet orientations may play a significant physiological role [21]. There are experimental reports supporting the notion that there is quite a large dispersion of the sheet structure, even in healthy hearts [28, 62, 143]. Although to our knowledge there are no experimental reports which would quantify sheet dispersion in diseased hearts, it is likely that dispersion is elevated as well compared to healthy conditions. To the authors knowledge, there are no recently published biomechanical cardiac models with dispersion, the latest existing models being [169, 171], and there is none that include sheet dispersion which is why this study focuses on developing a novel approach for modeling fiber and sheet disarray using an invariant based framework. A previously published orthotropic and invariant based model which characterizes the nonlinear passive behavior of myocardium [56] is augmented with a structure parameter which allows to quantify the degree of dispersion based on experimental measurements of fiber and sheet angle data. This structure parameter is based on a distribution function developed for the collagen structure in arteries [47] by incorporating a dispersion parameter which reduces the directional dependence in the myocardium and may thus be used both for the fiber and sheet dispersion, something which, to the authors knowledge, has not been modeled before.

Simulation results indicate that the dispersion has a relevant impact on the myocardium both during passive deformation and active contraction by reducing the stress response and changing the deformation pattern. When including the dispersion parameter in a ventricular simulation incorporating electrical activation the pressure volume loop is considerably altered by reducing the stroke volume. Since the degree of dispersion is significantly elevated under various cardiac pathologies, dispersion should be taken into account when modeling myocardial tissue in diseased states.

5.2. Modeling Framework

5.2.1. Kinematics

The myocardium may be described by three orthogonal direction vectors \mathbf{f}_0 , \mathbf{s}_0 and \mathbf{n}_0 corresponding to the mean fiber, sheet and sheet-normal directions, respectively, in the Lagrangian description. The isochoric Eulerian counterpart of these direction vectors are retrieved through the relations $\bar{\mathbf{f}} = J^{-1/3}\mathbf{F}\mathbf{f}_0$, $\bar{\mathbf{s}} = J^{-1/3}\mathbf{F}\mathbf{s}_0$ and $\bar{\mathbf{n}} = J^{-1/3}\mathbf{F}\mathbf{n}_0$, where \mathbf{F}

is the deformation gradient and $J = \det \mathbf{F}$ is the Jacobian. The circular dispersion of the fiber and sheet direction vectors around their mean orientations may be modeled using the structure tensors

$$\mathbf{H}_f = \kappa_f \mathbf{I} + (1 - 3\kappa_f)(\mathbf{f}_0 \otimes \mathbf{f}_0), \quad \mathbf{H}_s = \kappa_s \mathbf{I} + (1 - 3\kappa_s)(\mathbf{s}_0 \otimes \mathbf{s}_0), \quad (5.1)$$

$$\bar{\mathbf{h}}_f = \kappa_f \bar{\mathbf{b}} + (1 - 3\kappa_f)(\bar{\mathbf{f}} \otimes \bar{\mathbf{f}}), \quad \bar{\mathbf{h}}_s = \kappa_s \bar{\mathbf{b}} + (1 - 3\kappa_s)(\bar{\mathbf{s}} \otimes \bar{\mathbf{s}}), \quad (5.2)$$

as described in [47], where \mathbf{H}_i is a Lagrangian structure tensor and $\bar{\mathbf{h}}_i = J^{-2/3} \mathbf{F} \mathbf{H}_i \mathbf{F}^T$ is an isochoric Eulerian structure tensor where $i \in \{f, s\}$ correlates to the fiber and sheet directions respectively. \mathbf{I} is the second order identity tensor and $\bar{\mathbf{b}} = J^{-2/3} \mathbf{F} \mathbf{F}^T$ is the modified isochoric left Cauchy Green tensor.

The formulation of the dispersion parameter κ_i is described in detail in [47]. Briefly, the range of valid values for κ_i are $\in [0, 1/3]$, where $\kappa_i = 0$ means perfect alignment and $\kappa_i = 1/3$ means complete dispersion. A formulation of κ_i may be derived through the probability density function (PDF), $\rho_i(\Theta)$, using the relation

$$\kappa_i = \frac{1}{4} \int_0^\pi \rho_i(\Theta) \sin^3 \Theta d\Theta, \quad (5.3)$$

where Θ are the distribution angles centered around $\Theta = 0$. The PDF used is given by

$$\rho(\Theta) = 4 \sqrt{\frac{b}{2\pi}} \frac{\exp\{b[\cos(2\Theta) + 1]\}}{\operatorname{erfi}(\sqrt{2b})}, \quad (5.4)$$

where b is a concentration parameter and $\operatorname{erfi}(x) = -i \operatorname{erf}(ix)$ denotes an imaginary error function. $\rho(\Theta)$ is the standard π -periodic von Mises PDF, normalized by

$$\frac{1}{4\pi} \int_{\omega} \rho(\Theta) d\omega = 1, \quad (5.5)$$

where ω is the unit sphere.

The values for κ_i may thus be fitted against histograms of the dispersion of fiber and sheet angles for myocardial tissue. To fit the PDF (5.4) to histogram data, the fiber angles Θ in the data are shifted to $\bar{\Theta}$ by centering around $\Theta = 0^\circ$ and the maximum likelihood estimates function in Matlab, *mle()*, is used together with a custom function describing Eq. (5.4). The parameter b is thus retrieved with a 95 % confidence interval and using (5.3), κ_i is obtained.

The fit of the PDF to fiber dispersion is shown both against healthy myocardial tissue, Fig. 5.1(a), and against tissue diseased by HCM, Fig. 5.1(b), where the dispersion data is adapted from [71]. The fit of the PDF to sheet dispersion, however, is only shown against

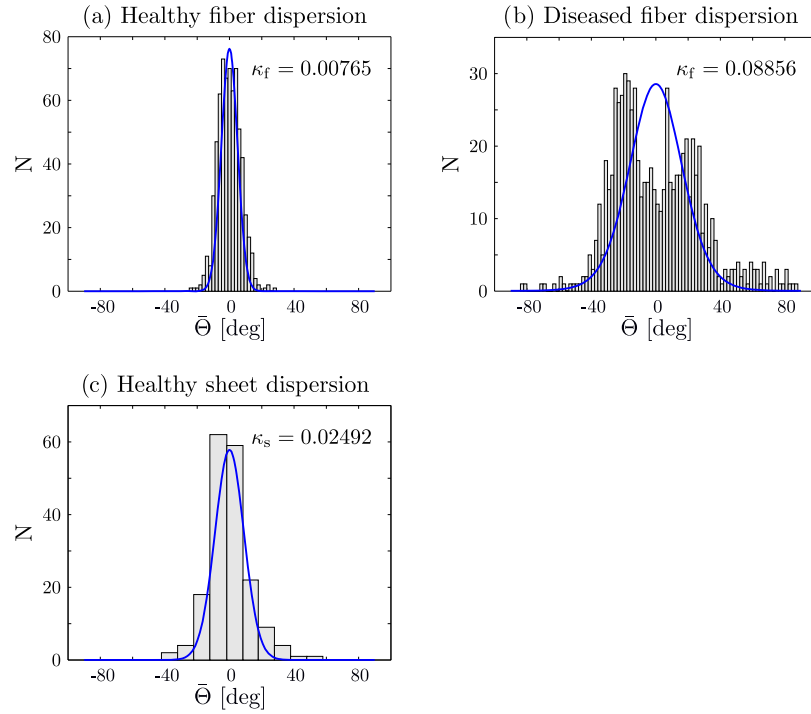


Figure 5.1.: Fit of histogram data for fiber and sheet arrays, adapted from [28, 71]: (a) healthy fiber dispersion with $\kappa_f = 0.00765$; (b) diseased fiber dispersion with $\kappa_f = 0.08856$; (c) healthy sheet dispersion with $\kappa_s = 0.02492$.

healthy subepicardium, Fig. 5.1(c), where the dispersion data is adapted from [28]. As, to the authors knowledge, the structure of sheet orientations in a diseased state has never been investigated, only healthy sheet disarray may be considered at the moment. As seen in Fig. 5.1, this procedure yields $\kappa_f = 0.00765$ and $\kappa_s = 0.02492$ for healthy myocardial tissue and $\kappa_f = 0.08856$ for diseased tissue.

5.2.2. Constitutive relations

The form of the strain-energy function used to model the myocardium is given by

$$\Psi = U(J) + \bar{\Psi}_p(\bar{I}_1, \bar{I}_{4f}, \bar{I}_{4s}, \bar{I}_{8fs}), \quad (5.6)$$

where U is a volumetric function and $\bar{\Psi}_p$ is an isochoric strain-energy function describing the passive behavior using the four modified isochoric invariants defined as $\bar{I}_1 = \text{tr}\bar{\mathbf{C}}$, $\bar{I}_{4f} = \mathbf{f}_0 \cdot \bar{\mathbf{C}}\mathbf{f}_0$, $\bar{I}_{4s} = \mathbf{s}_0 \cdot \bar{\mathbf{C}}\mathbf{s}_0$ and $\bar{I}_{8fs} = \mathbf{f}_0 \cdot \bar{\mathbf{C}}\mathbf{s}_0$, where $\bar{\mathbf{C}} = J^{-2/3}\mathbf{C}$ is the modified isochoric right Cauchy Green tensor. For the volumetric function

$$U(J) = \frac{\mu_K}{2}(\ln J)^2 \quad (5.7)$$

is used, where μ_K is the bulk modulus which servers as a user specified penalty parameter enforcing incompressibility. The volume preserving passive strain-energy function is

described by

$$\begin{aligned} \bar{\Psi}_p = & \frac{a}{2b} \{\exp[b(\bar{I}_1 - 3)] - 1\} + \sum_{i=f,s} \frac{a_i}{2b_i} \{\exp[b_i(\bar{I}_{4i}^* - 1)^2] - 1\} \\ & + \frac{a_{fs}}{2b_{fs}} [\exp(b_{fs}\bar{I}_{8fs}^2) - 1], \end{aligned} \quad (5.8)$$

where $\bar{I}_{4i}^* = \kappa_i \bar{I}_1 + (1 - 3\kappa_i)\bar{I}_{4i}$, $i \in \{f, s\}$ is a modified invariant, as formulated in [47, 122]. This formulation basically uses κ_i to describe the blending of the isotropic invariant I_1 and the directionally dependent invariant I_{4i} . It may be noted that in a limiting case, where $\kappa_i = 0$, the original model, as described in [56] and [36], is retrieved. The material parameters needed in (5.7) and (5.8) are μ_K , $a_{(\cdot, f, s, fs)}$ and $b_{(\cdot, f, s, fs)}$ plus the dispersion parameter κ_i . The passive Cauchy stress tensor is given by $\boldsymbol{\sigma}_p = 2J^{-1}\mathbf{F}(\partial\Psi/\partial\mathbf{C})\mathbf{F}^T$ and using the notations

$$\bar{\psi}_j = \frac{\partial\bar{\Psi}_p}{\partial\bar{I}_j}, \quad j = 1, 8fs, \quad \bar{\psi}_{4i}^* = \frac{\partial\bar{\Psi}_p}{\partial\bar{I}_{4i}^*}, \quad i = f, s, \quad (5.9)$$

this results in

$$\boldsymbol{\sigma}_p = p_h \mathbf{I} + 2J^{-1} [\bar{\psi}_1 \text{dev}(\bar{\mathbf{b}}) + \sum_{i=f,s} \bar{\psi}_{4i}^* \text{dev}(\bar{\mathbf{h}}_i) + \frac{1}{2} \bar{\psi}_{8fs} \text{dev}(\bar{\mathbf{f}} \otimes \bar{\mathbf{s}} + \bar{\mathbf{s}} \otimes \bar{\mathbf{f}})], \quad (5.10)$$

where $p_h = dU(J)/dJ$ is used to enforce the near incompressibility and $\text{dev}(\bullet) = (\bullet) - (1/3)[(\bullet) : \mathbf{I}]\mathbf{I}$ is the deviatoric operator in the Eulerian description [53]. A scalar valued active second Piola-Kirchhoff stress term S_a which originates from [103] is calculated in the Lagrangian description by

$$\frac{\partial S_a}{\partial t} = \varepsilon(V_m)(k_{S_a} \Delta V_m - S_a), \quad (5.11)$$

where $\varepsilon(V_m)$ is a delay function controlling the rate of activation and relaxation of S_a . The parameter k_{S_a} regulates the amplitude of S_a given the difference in the transmembrane potential $\Delta V_m = V_m - V_r$, where V_m is the current action potential and V_r is the myocyte resting potential. A smooth delay function $\varepsilon = \varepsilon(V_m)$, as proposed in [49], is used which is given by

$$\varepsilon(V_m) = \varepsilon_0 + (\varepsilon_\infty - \varepsilon_0) \exp[-\exp(-\zeta_r(V_m - V_s))], \quad (5.12)$$

where ε_0 and ε_∞ are the limiting values of the delay function when the action potential V_m is larger or lower than a given phase shift V_s . Further, the transition rate of the delay function is controlled by the parameter ζ_r . However, in contradiction to what is written in [49], the relation between the limiting values must follow $\varepsilon_0 > \varepsilon_\infty$ as discussed in [36] in order to achieve the delay of peak active stress with respect to the upstroke of the action potential. An active second Piola-Kirchhoff stress tensor \mathbf{S}_a is retrieved by introducing a dispersed structure tensor $\hat{\mathbf{H}}_a$ according to

$$\mathbf{S}_a = S_a \hat{\mathbf{H}}_a, \quad (5.13)$$

where

$$\hat{\mathbf{H}}_a = \frac{\kappa_f}{1 - 2\kappa_f} \mathbf{C}^{-1} + \frac{1 - 3\kappa_f}{1 - 2\kappa_f} I_{4f}^{-1} \mathbf{f}_0 \otimes \mathbf{f}_0. \quad (5.14)$$

The active Cauchy stress is now retrieved by the push-forward operation according to $\boldsymbol{\sigma}_a = J^{-1} \mathbf{F} \mathbf{S}_a \mathbf{F}^T$ which yields

$$\boldsymbol{\sigma}_a = J^{-1} S_a \hat{\mathbf{h}}_a, \quad (5.15)$$

where

$$\hat{\mathbf{h}}_a = \frac{\kappa_f}{1 - 2\kappa_f} \mathbf{I} + \frac{1 - 3\kappa_f}{1 - 2\kappa_f} \hat{\mathbf{f}} \otimes \hat{\mathbf{f}}, \quad (5.16)$$

and $\hat{\mathbf{f}} = \mathbf{f}/|\mathbf{f}|$ is the normalized fiber direction vector. The structure tensor (5.14) is formulated so that (5.16) may be seen as a normalization of (5.2)₁ where the length change of the mean fiber orientation does not affect the magnitude of the applied stress as well so that the condition $\hat{\mathbf{f}} \cdot \hat{\mathbf{h}}_a \hat{\mathbf{f}} = 1$ is fulfilled which together ensures that (5.15) is a true Cauchy stress tensor. The total stress tensor is now simply retrieved from the additive decomposition

$$\boldsymbol{\sigma} = \boldsymbol{\sigma}_p + \boldsymbol{\sigma}_a. \quad (5.17)$$

The elasticity tensors needed for implementing the passive stress $\boldsymbol{\sigma}_p$ in the finite element package FEAP [164] have been shown previously in [35, 47] and for the active stress $\boldsymbol{\sigma}_a$ the elasticity tensor both in Lagrangian and Eulerian description is shown in Appendix A.1.

5.2.3. Modeling electro-mechanically coupled myocardial tissue

The computation of electrical activation and repolarization and its coupling to passive and active tissue mechanics have been described previously in detail [36]. Briefly, the spread of electrical activation and repolarization is described by a reaction-diffusion equation referred to as the monodomain equation, given by

$$\beta C_m \frac{\partial V_m}{\partial t} + \beta I_{\text{ion}}(V_m, \boldsymbol{\eta}) = \nabla \cdot (\boldsymbol{\sigma}_m \nabla V_m) + I_{\text{tr}}, \quad (5.18)$$

where β is the membrane surface to volume ratio, C_m is the membrane capacitance, V_m is the transmembrane voltage, I_{ion} is the density of the total ionic current which is a function of V_m and a set of state variables $\boldsymbol{\eta}$, I_{tr} is a transmembrane stimulus current, and $\boldsymbol{\sigma}_m$ is the monodomain conductivity tensor with the eigenaxes $\zeta = f$ along the fibers, $\zeta = s$ perpendicular to the fibers, but within a laminar sheet, and $\zeta = n$ perpendicular to the sheets. No dispersion parameters are included in the formulation of the electrical activation. The eigenvalues of $\boldsymbol{\sigma}_m$ are chosen as the harmonic mean of intracellular conductivity, $\sigma_{i\zeta}$, and interstitial conductivity, $\sigma_{e\zeta}$, which renders the monodomain equations axially equivalent to the more general bidomain equations [92, 109].

The electrical and mechanical models are weakly coupled. That is, the solution of the electrical quantities is calculated on a static mesh first, using The Cardiac Arrhythmia Research Package (CARP) [175], which is built on top of the MPI-based library PETSc [8].

Relevant parameters are then fed into a separate subsequent simulation of deformation and stress analysis using FEAP [164]. In this study, electrical quantities are either calculated according to (5.18), as it is the case in the model of a left ventricle, Section 5.3.5, or the transmembrane potential V_m is prescribed directly as an input to the mechanical deformation analysis.

5.3. Representative Examples and Results

To illustrate the effect of the dispersed myocardial model five representative examples are studied. i) In Section 5.3.1 an analytical example of a small cube of myocardial tissue is constructed which is electrically activated to generate active tension. The impact of dispersion upon mechanical deformation is studied in this model when using the limit values of the dispersion parameters κ_f and κ_s ; ii) A second analytical example in Section 5.3.2 aims at showing the influence of dispersion under simple shear; iii) A FE model of a larger cube of myocardial tissue is used in Section 5.3.3 to investigate the relative influence of electrically generated active stress in the presence of dispersion of the fiber orientation. iv) A passive inflation experiment is performed using an LV slice model in Section 5.3.4 to study the transmural change in stress as a function of altered dispersion parameters both in the fiber and sheet directions; v) A fullblown electro-mechanically coupled LV model is used in Section 5.3.5 to study the influence of dispersion on pressure-volume loops over a cardiac cycle where dispersion parameters are chosen to account for both healthy and pathological conditions.

5.3.1. Cube with dispersion subjected to active stress

An analytical example may be constructed of a unit cube with mean material directions oriented according to $[\mathbf{f}_0] = [1, 0, 0]^T$, $[\mathbf{s}_0] = [0, 1, 0]^T$ and $[\mathbf{n}_0] = [0, 0, 1]^T$ in the global X_1 , X_2 and X_3 coordinate system as shown in Fig. 5.2(a). The cube is fixed against rigid body movement but otherwise free to deform. The cube is activated by increasing the transmembrane potential which generates contraction in the fiber direction. The corresponding deformation gradient is given as

$$[\mathbf{F}] = \begin{bmatrix} \lambda_f & 0 & 0 \\ 0 & \lambda_s & 0 \\ 0 & 0 & \lambda_n \end{bmatrix}, \quad (5.19)$$

where λ_f , λ_s and λ_n are the stretches in the fiber, sheet and sheet-normal directions, respectively. Since the activation in the fiber directions leads to a contraction of the fiber, the stretches follow the relation $\lambda_f < 1$, $\lambda_s > 1$ and $\lambda_n > 1$. The fulfillment of incompressibility in the analytical case, i.e. $J = 1$, leads to the following components of the Cauchy stress

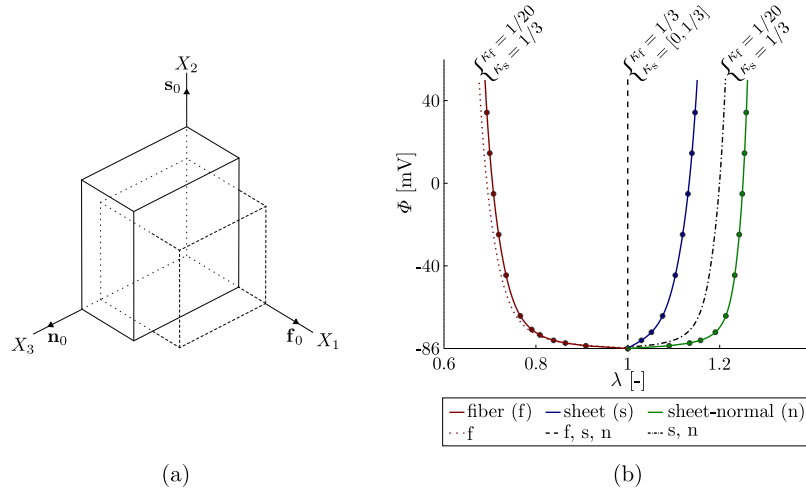


Figure 5.2.: (a) Deformation of a unit cube when activated in the fiber direction; (b) analytical result in the fiber, sheet and sheet-normal directions using the distribution parameters κ_f and κ_s . The solid lines represent the analytical solution with $\kappa_f = \kappa_s = 1/20$ (the filled circles show the FE-solution for comparison using the same parameters). Using $\kappa_f = 1/3$, the dashed line shows the stretch response for all three f, s and n-directions, regardless of κ_s -value. Using $\kappa_f = 1/20$ and $\kappa_s = 1/3$, the dotted line shows the stretch response in the f-direction and the dash-dotted line in the s and n-directions.

tensor

$$\sigma_{11} = p_h + 2[\psi_1 + \psi_{4f}^*(1 - 2\kappa_f) + \psi_{4s}^*\kappa_s]\lambda_f^2 + S_a, \quad (5.20)$$

$$\sigma_{22} = p_h + 2[\psi_1 + \psi_{4f}^*\kappa_f + \psi_{4s}^*(1 - 2\kappa_s)]\lambda_s^2 + S_a \frac{\kappa_f}{1 - 2\kappa_f}, \quad (5.21)$$

$$\sigma_{33} = p_h + 2(\psi_1 + \psi_{4f}^*\kappa_f + \psi_{4s}^*\kappa_s)\lambda_n^2 + S_a \frac{\kappa_f}{1 - 2\kappa_f}, \quad (5.22)$$

$$\sigma_{12} = \sigma_{13} = \sigma_{23} = 0. \quad (5.23)$$

Since the cube is free to deform, all total stress components in Eq. (5.20)–(5.22) are zero, i.e. $\boldsymbol{\sigma} = \boldsymbol{\sigma}_p + \boldsymbol{\sigma}_a = \mathbf{0}$, and p_h may be determined by, e.g., $\sigma_{33} = 0$. The unknowns are the stretches λ_f , λ_s and λ_n and using the incompressibility condition, $\lambda_f\lambda_s\lambda_n = 1$, the nonlinear systems of Eqs. in (5.20)–(5.22) is solved using the function *fsolve()* in MATLAB, with respect to λ_f , λ_s and λ_n using given values of S_a , κ_f and κ_s . With the material parameters shown in Table 5.1, and increasing the potential linearly from $V_m = V_r$ to $V_m = +50$ mV, the resulting deformation as a function of activation is shown in Fig. 5.2(b). Also, a comparison is made between the analytical and FE-values obtained for the same model setup using one set of dispersion parameters. For the limiting case where $\kappa_f = 1/3$ the active stress acts in all direction and due to the incompressibility the cube cannot deform, resulting in a straight line at $\lambda = 1$ for all directions shown as a dashed line in Fig. 5.2(b). For the limiting case

Used for	Parameter		
<i>Passive stress</i>	$\mu_K = 3333 \text{ kPa}$	$a = 0.333 \text{ kPa}$	$b = 9.242 \text{ (-)}$
	$a_f = 18.535 \text{ kPa}$	$b_f = 15.972 \text{ (-)}$	$a_s = 2.564 \text{ kPa}$
	$b_s = 10.446 \text{ (-)}$	$a_{fs} = 0.417 \text{ kPa}$	$b_{fs} = 11.602 \text{ (-)}$
<i>Active stress</i>	$k_{S_a} = 0.50 \text{ kPa mV}^{-1}$	$V_r = -86.796 \text{ mV}$	$V_s = -80.0 \text{ mV}$
	$\epsilon_0 = 1.0 \text{ ms}^{-1}$	$\epsilon_\infty = 0.1 \text{ ms}^{-1}$	$\zeta_r = 0.1 \text{ mV}^{-1}$

Table 5.1.: Material parameters used in both analytical and numerical calculations, except for the values for κ_f and κ_s which are shown in respective section. The passive stress material parameters are adapted from [35], and the active stress material parameters are adapted from [36, 49, 103].

where $\kappa_s = 1/3$ the sheet direction is isotropic and the sheet and sheet-normal responses are thus indistinguishable, shown as a dash-dotted line in Fig. 5.2(b). In effect, when $\kappa_s = 1/3$ the material model may be viewed as transversely isotropic.

5.3.2. Influence of dispersion on simple shear

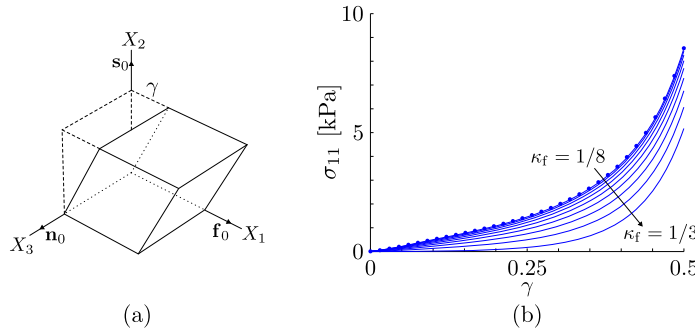


Figure 5.3.: (a) Deformation of a unit cube when sheared a distance γ in the 21-plane; (b) the σ_{11} stress response to simple shear of a cube when changing the dispersion in the fiber direction.

An analytical formulation of simple shear may be derived by assuming plane stress which leads to the determination of the hydrostatic pressure q . However, since the volume is constant in simple shear of an incompressible material, i.e. $\det \mathbf{F} = 1$, the deformation gradient of plane strain may also be used. Thus, with simple shear in, e.g., the 21-direction as seen in Fig. 5.3(a), the corresponding deformation gradient has the components

$$[\mathbf{F}] = \begin{bmatrix} 1 & \gamma & 0 \\ 0 & 1 & 0 \\ 0 & 0 & 1 \end{bmatrix}, \quad (5.24)$$

leading to the following (non-zero) components of the Cauchy stress tensor

$$\sigma_{11} = 2\{\psi_1 \gamma^2 + \psi_{4f}^*[1 + (\gamma^2 - 1)\kappa_f] + \psi_{4s}^*(1 - 2\kappa_s)\gamma^2\} + \psi_{8fs}\gamma + S_a \frac{1 - 3\kappa_f}{1 - 2\kappa_f}, \quad (5.25)$$

$$\sigma_{22} = 2\psi_{4s}^*(1 - 3\kappa_s), \quad (5.26)$$

$$\sigma_{12} = \sigma_{21} = 2[\psi_1 + \psi_{4f}^*\kappa_f + \psi_{4s}^*(1 - 2\kappa_s)]\gamma + \frac{1}{2}\psi_{8fs}, \quad (5.27)$$

where the incompressibility condition is retrieved through the plain stress relation $\sigma_{33} = 0$. Interesting to note is that although the direction of applied active stress is dispersed, there are no components of the active stress in the 22 or 33-direction due to the incompressibility assumption. The stress response in the X_1 -direction for different κ_f -values is shown in Fig. 5.3(b) where it is clearly seen that an increased fiber dispersion decreases the stress in the X_1 -direction. In this example, the active stress is zero in the reference configuration, and increases together with the increase of shear. In a FE-analysis of the same problem, using one set of distribution parameters, matching values are found which is shown as filled circles in Fig. 5.3(b).

5.3.3. Influence of increased myocyte dispersion

The influence of the level of myocyte dispersion may also be shown using a similar cube, but now discretized into $10 \times 10 \times 10$ mm mixed $Q1/P0$ finite elements with fixed displacement boundary conditions in all degrees of freedom on the faces of the cube where $X_2 = 0$ and $X_2 = 10$ mm.

Different values for κ_f are used whilst keeping $\kappa_s = 0$ constant. The cube is activated to a potential of $V_m = +30$ mV and the corresponding first principal stress σ_1 is shown in Fig. 5.4 for various values of κ_f . As seen in Fig. 5.4, increasing the isotropy in the myocardial tissue lowers the values of σ_1 , and also decreases the contraction in the X_1 direction. This is, on one hand, due to the increased dispersion of the fiber direction which leads to an increase in active stress components along the X_2 and X_3 -directions, and, on the other hand, again due to the incompressibility of the material which reduces the influence of the active stress in the fiber direction.

5.3.4. Passive inflation of ventricular section

A thin left ventricular slice model is constructed by approximating the cross section of the LV by a cylinder, as illustrated in Fig. 5.5a. Two models, *A* and *B*, of the same geometry, but with different fiber and sheet arrangements are constructed. In model *A*, the average fiber angle α varies from $+60^\circ$ to -60° and the average sheet angle β varies from $+85^\circ$ to -85° transmurally from the epicardium to the endocardium, where the fiber and sheet angles α and β are defined in Fig. 5.5(b). In Model *B*, the fiber and sheet angles are both $\alpha = \beta = 0$ and in Fig. 5.5(c) fiber directions are shown for both models for visual clarity. The slice geometry is meshed with 400 hexahedral mixed $Q1/P0$ elements which are fixed against translation in the ξ_2 -direction at the cut surfaces, and in the ξ_3 -direction at the

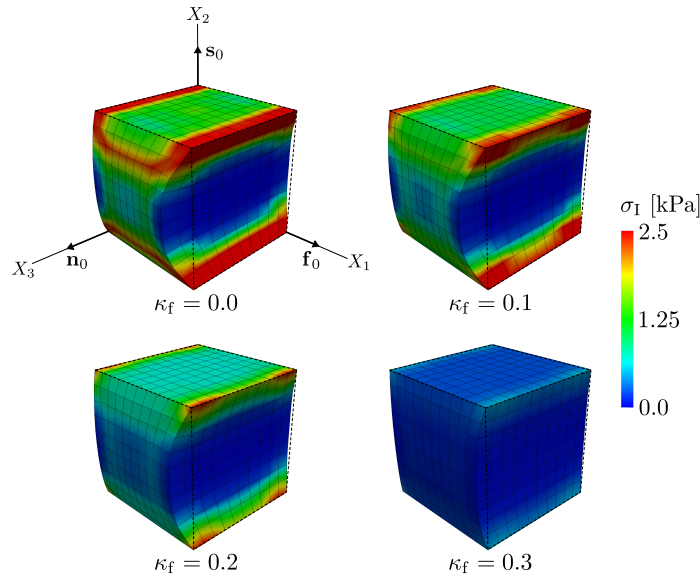


Figure 5.4.: Cube of myocardial tissue subjected to an active stress corresponding to +30 mV with $\kappa_f = \{0, 0.1, 0.2, 0.3\}$ and $\kappa_s = 0$.

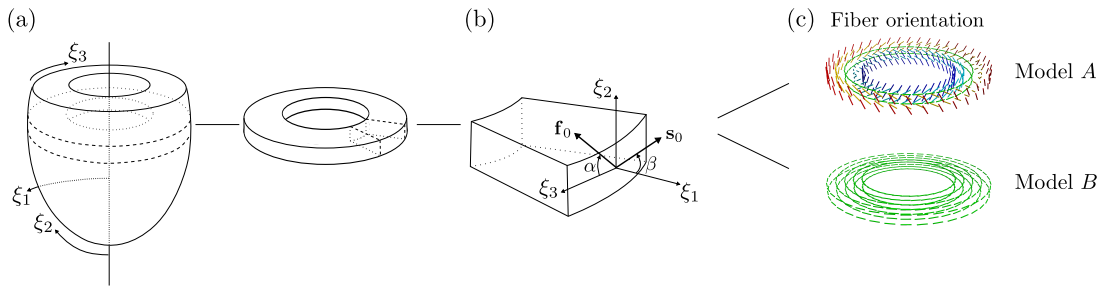


Figure 5.5.: (a) Coordinate system of an LV model and a section of the LV; (b) average fiber orientation defined by the angle α in the (ξ_2, ξ_3) -plane and average sheet orientation defined by the angle β in the (ξ_1, ξ_2) -plane. The arrows point in the positive directions for the angles; (c) average fiber orientation for Models A and B.

epicardial border to hinder rigid body movement. No electrical stimulus was applied, that is, the tissue remained electrically quiescent and thus no active stresses were generated. Instead, the slice is passively inflated by applying a pressure load of $p = 100$ mmHg to the endocardial surface in 200 incremental load steps of equal size. The influence of the κ_i parameters is investigated either by using a combination of the healthy and diseased dispersion parameters shown in Fig. 5.1, or by using a combination of perfectly aligned ($\kappa_i = 0.0$) and very dispersed ($\kappa_i = 0.2$) parameters. The resulting first principal Cauchy stress σ_I at $p = 100$ mmHg is shown for different dispersion parameters. In Fig. 5.6(a) the healthy dispersion parameters result in a band of higher stresses in the mid-myocardium. This band of higher stresses is noticeably reduced when using the diseased dispersion

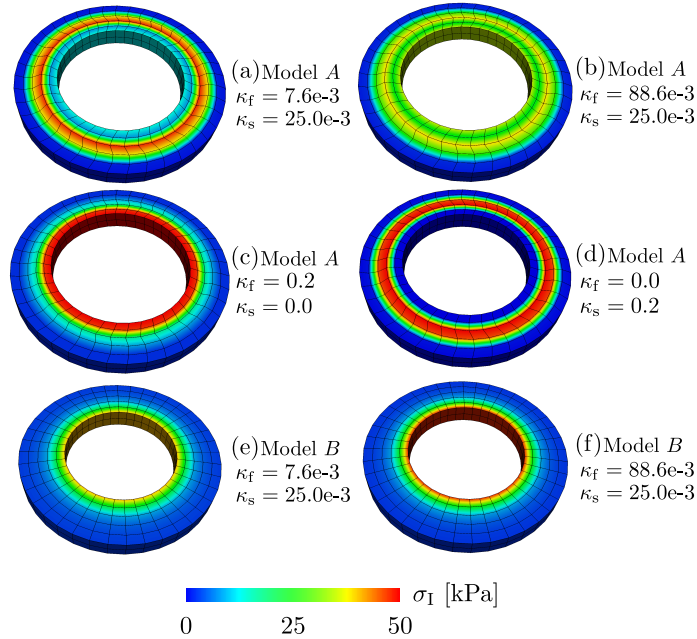


Figure 5.6.: First principal stress σ_I at $p = 100$ mmHg in a section of a ventricular model. Models *A* and *B* pertain to the different fiber and sheet-orientations shown in Fig. 5.5(b).

parameters, as shown in Fig. 5.6(b). Instead, stresses are more spread out radially and at the endocardial border stresses are higher relative to the setup (a) where healthy dispersion parameters were used. This suggests that fiber dispersion alone induces a radial stress gradient where the highest stresses arise at the inner wall, as commonly seen, for instance, in pressurized thick-walled isotropic tubes. This is exactly the case when using aligned sheets and a pronounced fiber dispersion, as can be seen in Fig. 5.6(c). In the opposite case, i.e. strong fiber alignment and pronounced sheet dispersion, the mid-myocardial band of increased stress gradients is more pronounced, as shown in Fig. 5.6d. Using both $\kappa_i = 0.0$ (not shown here) in model *A* leads to results which are virtually identical to Fig. 5.6(a). For the sake of comparing, in model *B* the first principal Cauchy stress are also shown for healthy and diseased dispersion parameters in Figs. 5.6(e) and (f), respectively. In this case the diseased tissue results in slightly higher stresses at the endocardial border when compared to the healthy tissue. This is probably due to the increase in dispersion in the diseased tissue which entails an increase in radial expansion, however, this effect is not nearly as pronounced as when comparing Figs. 5.6(a) and (b).

5.3.5. Simulation of an LV with healthy and diseased dispersion parameters

To study the influence of fiber and sheet dispersion upon contraction over a full cardiac cycle an ellipsoidal model of a LV was constructed where the dimensions correlate with a rabbit LV [174]. Details on model construction have been described elsewhere [36]. The coordinates of the LV are described in prolate spheroidal coordinates with the axes ξ_1 ,

ξ_3 and ξ_2 , pointing in the radial, circumferential and longitudinal direction, respectively. The coordinate system is illustrated in Fig. 5.5(a). The arrangement of fibers and sheets corresponds to model A in section 5.3.4. Pressure boundary conditions as imposed by the ventricular deformation and the response of the vascular system are applied on the endocardial surface. The pressure p in the cavity is governed by the following rules:

- (i) Non-physiological initial phase with linear pressure increase to the end diastolic pressure (EDP) ($p = 20$ mmHg).
- (ii) Isochoric LV compression phase, p increases from EDP up to 95 mmHg.
- (iii) Ejection phase where pressure-volume relationship is governed by a Windkessel model, i.e. $C \frac{dp}{dt} + \frac{p}{R} = -\frac{dV}{dt}$ until reversed blood flow.
- (iv) Isochoric LV relaxation phase, p drops down to 12.5 mmHg.
- (v) Filling phase with linear pressure increase to EDP.

In steps (ii) and (iv), the pressure p is computed using the iterative relation $p_{n+1} = p_n + (V_{n+1} - V_n)/C_p$ to keep the cavity volume, V , of the LV constant where C_p serves as a penalty parameter [168]. In step (iii), where a two-element Windkessel model is used, the parameters C and R relate to arterial compliance and resistance, respectively. Values for C and R are chosen to generate pressure-volume (PV) loops which match up with experimental recordings in rabbits [140]. Material parameters required for calculating the pressure are $C = 0.2$ ml mmHg⁻¹, $R = 700$ mmHg ms ml⁻¹ and $C_p = -900$ mmHg ml⁻¹. The material parameters used to describe both active and passive mechanical behavior of the model are summarized in Table 5.1, except for κ_f and κ_s which correspond to the healthy and diseased dispersion parameters given in Fig. 5.1 and the mechanical boundary conditions for the LV which are described in Table 5.2. The mesh consists of 5310 hexahe-

BC	Coordinates	Description
$t_n = -p$	$\xi_1 = \xi_{1\min}$	for all ξ_2, ξ_3 Endocardial surface
$u_{\xi_2} = 0$	$\xi_2 = \xi_{2\max}$	for all ξ_1, ξ_3 Basal surface
$u_{\xi_3} = 0$	$\xi_1 = \xi_{1\max}$ $\xi_2 = \xi_{2\max}$	for all ξ_3 Outer ring at base

Table 5.2.: Mechanical boundary conditions in terms of prescribed tractions \mathbf{t} where t_n is the normal component of the traction vector to the endocardial surface on which p acts, and displacements $[\mathbf{u}] = [u_{\xi_1}, u_{\xi_2}, u_{\xi_3}]$ in the direction of the coordinates given in Fig. 5.5(a).

dral mixed $Q1/P0$ finite elements used to solve the mechanics and 1 201 507 linear hybrid finite elements for solving the electrics [133]. The Mahajan model [91] is employed to describe cellular dynamics. The model was initialized by pacing a single cell at a pacing cycle length of 350 ms until a stable limit cycle was observed. The state vector $\boldsymbol{\eta}$ at the

end of this pre-pacing procedure was used to populate the LV model with an initial state vector, $\boldsymbol{\eta}_0$. Transmembrane current injection applied to the endocardial surface at $t = 0$ ms initiated the propagation of the action potentials at the endocardium to approximate a predominantly transmural activation sequence, as induced by activation via the Purkinje system. In this approximation the whole endocardium was activated synchronously, electrical activation delays within the endocardium remained unaccounted for. 350 ms of activity were simulated to cover one full depolarization and repolarization cycle over the entire LV. The resulting pressure-volume (PV) loops obtained from the simulation are shown in

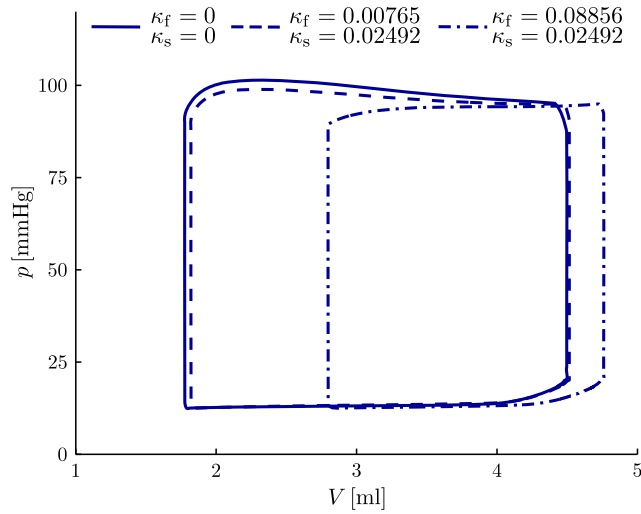


Figure 5.7.: PV-loops with different values for κ_f and κ_s .

Fig. 5.7, when using healthy and diseased values for the dispersion parameters, as well as a case with no dispersion, i.e. $\kappa_i = 0.0$. While only a minor shift in the PV loops between the cases no dispersion and healthy dispersion was observed, a strikingly different behavior manifested with the diseased dispersion parameters where end diastolic and systolic volumes was much larger.

5.4. Discussion

There are numerous reports in the literature which provide evidence for the presence of dispersion in fiber and sheet orientation in myocardial tissue. Under healthy conditions dispersion is rather mild, but under certain pathologies such as HCM [15, 33, 167] dispersion can be quite pronounced. In the vast majority of modeling studies, however, dispersion and its impact upon the mechanical response of the myocardium has been largely ignored. In this study, a novel mechanical model of myocardial tissue has been proposed which explicitly accounts for the dispersion in fiber and sheet arrangement. By changing two scalar parameters, κ_f and κ_s , dispersion of the model along fiber and sheet direction can be steered independently, thus allowing detailed mechanistic investigations of pathological changes upon the mechanical response. The dispersion parameters determine the

blend between the isotropic invariant I_1 and the directionally dependent invariant I_{4i} , thus together they give a dispersed orthotropic structure response where an increased dispersion leads to an increasingly more isotropic active and passive mechanical response.

Both the analytical and numerical examples investigated in this study suggest that dispersion may be a major factor in cardiac electro-mechanics. The increase in dispersion along the fiber direction showed the most striking effect. This is illustrated, for instance, in Fig. 5.4 where the increase in dispersion reduces contraction and first principal stresses. The enforced incompressibility condition is responsible for this reduced contraction, as seen in the analytical expressions (5.20)–(5.22) and (5.25)–(5.27). From a physiological point of view, there is a clear interpretation as well. As the dispersion increases, the orientation of myocytes which are responsible for active contraction, is more and more evenly distributed. When dispersion is large enough, there is no preferred myocyte orientation any more. This would entail a fully isotropic mechanical contraction which is, however, impossible without altering the volume. Moreover, besides distributing the direction of active contraction, fiber dispersion also has a major impact on the passive myocardial response. This is illustrated in Fig. 5.6(a) through (c) where the fiber dispersion is increased in a ventricular slice model. During passive inflation of the slice the first principal stresses change from being elevated in a mid-myocardial band for low fiber dispersion to being elevated at the endocardial border for high fiber dispersion. This shift in the location of principal stresses is similar to what is commonly seen when inflating a thick-walled tube.

Although the effects of dispersion in the fiber direction are clearly more striking, simulation results indicate that increases in sheet dispersion lead to significant alterations in model behavior as well. The overall material response changes gradually from orthotropic towards transversely isotropic where the sheet response becomes indistinguishable from the sheet-normal response. This can be seen either in the analytical example (5.21) and (5.22) where $\kappa_s = 1/3$ gives identical expressions for σ_{22} and σ_{33} , or, alternatively in Fig. 5.2(b) where the behavior is identical along sheet and sheet-normal directions. The difference in passive stress response between a (nearly) transversely isotropic and an orthotropic material can be appreciated by comparing Fig. 5.6(d) to Fig. 5.6(a) where the mid-myocardial stresses are even more elevated for the (nearly) transversely isotropic material. This large difference in stress response also highlights the importance of orthotropy as a factor which has to be taken into account when simulating ventricular electro-mechanics.

In Section 5.3.5 results are shown for an electro-mechanically coupled model of the LV for both healthy and pathological dispersion parameters. While the effects of using healthy fiber and sheet dispersion parameters were fairly minor, using pathological dispersion parameters had a major impact. As can be seen by comparing the PV loop traces in Fig. 5.7, a significant shift of the entire PV loop towards larger end diastolic and end systolic LV cavity volumes occurred.

In summary, our modeling result identified fiber and sheet dispersion as important determinants of electro-mechanical response of cardiac tissue which may need to be considered when matching model predictions on stress, volume change and deformation pattern with experimental observations under conditions of pathologically pronounced fiber and sheet dispersion.

Limitations of the study. The fit of the histogram data to the PDF assumes a bell-shaped data distribution. This may not be correct in pathological cases with increased fiber dispersion. As shown in Fig. 5.1(b), in this dataset of HCM-diseased tissue there appears to exist two predominant myocyte orientations in the region of interest. It is certainly possible to retrieve individual dispersion parameters for both predominant orientations, however, this increased dispersion in HCM was only found within small focal islands throughout the myocardial wall [71, 72] where both orientations were found within each individual island. Therefore, to appropriately account for the bimodal distribution of orientations, a significantly higher spatial resolutions would be required than those commonly used within concurrent FE modeling studies, including this study. Since the spatial extent of a single finite element in the models used exceeds the size of a focal island in which increased dispersion can be found, we opted for using only one average direction which corresponds to a fit of the bell-shaped function over both predominant orientations.

In the LV-model shown in Section 5.3.5, dispersion parameters corresponding to tissue diseased by HCM were used throughout the entire LV wall. This is not a realistic assumption as the dispersion in the small focal islands seems only to amount to approximately 25 % of the overall volume of the LV [71, 72]. Available data show sheet and fiber dispersion averaged over all the islands found in a given ventricle, but no data on spatial distribution and morphology of such islands are available. Therefore, simulation results show an overly diseased case which can be considered as a limiting case for dispersion effects. However, the focus of this study is mainly on presenting the modeling procedure and the potential effects of fiber dispersion, and not so much on developing a model that strives for a perfect patho-physiological match for a HCM-diseased LV. In future higher resolution FE-modeling studies, dispersion parameters may easily be set to vary in each finite element, however, considering the paucity of available data on spatial variation in dispersion such a detailed investigation would appear to be premature. Experimental studies which characterize spatial and morphological aspects of dispersion over the entire myocardium in health and disease are therefore of utmost importance to provide a more solid basis for detailed modeling studies which aim at making more specific predictions.

Further, in the LV-model the κ_i parameters affected only the mechanical response of the LV, but not the electrical activation sequence since dispersion remained unaccounted for in the monodomain equations. That is, the orthotropy in the propagation of the action potential in the LV model was governed by the mean orientation of fibers and sheets. Accounting for dispersion in the electrical model would reduce orthotropy as well, however,

the chosen activation sequence, which approximates a normal beat where the entire endocardium is activated almost simultaneously, leads to a strongly transmural activation where effects of electrical orthotropy are strongly attenuated. Under such conditions the electrical consequence of dispersion are very minor and can be neglected, particularly when considering the large uncertainty in experimental reports on conductivity values which vary up to 300% [138].

Acknowledgement

This project is in part supported by the SFB Research Center ‘Mathematical Optimization and Applications in Biomedical Sciences’, project F3210-N18 granted by the Austrian Science Fund. This support is gratefully acknowledged.

6. ON TENSION-COMPRESSION SWITCHING IN DISPERSED FIBER-REINFORCED CONSTITUTIVE MODELS

Abstract Large-strain, fiber-reinforced constitutive models are commonly used for solving complex boundary value problems in the context of the finite element method. In such models which do not include fiber dispersion, the mathematical and physical motivation for including a tension-compression fiber ‘switch’ (e.g., in which some portion of the model is not used if the fibers are in compression) is clear. In cases where fiber-reinforced models are extended to include the effect of distributed fiber orientations (i.e. models which include a parameter intended to capture fiber dispersion about a principal fiber direction, e.g., Gasser, Ogden and Holzapfel, *Journal of the Royal Society Interface*, 3:15-35, 2006) neither the mathematical nor physical motivation for tension-compression fiber switching is so clear, and in fact several choices exist for the material modeler. Here we explore methods to study such switching mechanisms by analyzing six potential switching cases, and draw some conclusions about the mathematical robustness and physical interpretation of the different possible approaches. We propose using two different permeations of the dispersed fiber-reinforced models, depending on whether one can assume that the fibers are (nearly) uncoupled or strongly coupled to the isotropic ground matrix.

6.1. Introduction

Large-strain, fiber-reinforced constitutive models are commonly used for solving complex boundary value problems in the context of the finite element method. Such materials are often considered to be hyperelastic and are modeled using a strain-energy function in the framework of continuum mechanics. Because soft biological tissues are commonly reinforced with collagen fibers, fiber-reinforced constitutive models play a crucial role in, e.g., determining the mechanical state of biological tissues.

The directions of collagen fiber-reinforcement in soft biological materials generally vary inhomogeneously within the tissues, and fibers are often bundled together to create fiber-families, in which the fibers are (to some degree) dispersed around a mean, or principal, fiber direction. Several models for fiber-reinforced materials are presented in the mechanics literature that incorporate a principal fiber direction, e.g., [84, 180], and many models have been presented for specific biological tissues, e.g., arteries [44, 54, 193], myocardium [22, 56, 67], and cartilage [123, 184]. Some of these models have been extended to further incorporate a measure of dispersion in the fibers orientations (i.e. they capture the distribution of the fiber orientations about a principal direction of reinforcement) [5, 37, 42, 47, 61, 121, 122, 171].

Although it is fairly straightforward to model fiber behavior under tension, it is not so clear what to do once the fibers go into compression. While a fiber, say a collagen fiber found in arterial tissue, bears load while in tension, it may buckle under compression and would thus not bear any compressive load alone. A common approach is to view the fiber as a tension-only quantity and superimpose this behavior with an isotropic matrix material which may handle compressive loads.

This approach is used in, e.g., the strain-energy function developed by Holzapfel, Gasser and Ogden [54], which is separated into two terms related to matrix and fiber behaviors of arterial tissue, i.e. $\Psi = \Psi_m + \Psi_f$, respectively. Here, the matrix material is considered to be isotropic and incompressible and can be modeled as a neo-Hookean material $\Psi_m = \mu(I_1 - 3)/2$, where μ is the shear modulus in the reference configuration and $I_1 = \text{tr}\mathbf{C}$ is an isotropic invariant of the right Cauchy-Green tensor $\mathbf{C} = \mathbf{F}^T\mathbf{F}$. The behavior of arterial tissue related to the collagen fiber structure is modeled using a directionally dependent pseudo-invariant $I_4 = \mathbf{C} : \mathbf{A}_0 = \lambda_f^2$ (the square of the stretch in the fiber direction), where $\mathbf{A}_0 = \mathbf{a}_0 \otimes \mathbf{a}_0$ is a material structure tensor for the fiber reinforcement with direction \mathbf{a}_0 in the reference configuration.

Assuming that the embedded collagen fibers are not highly-constrained in the matrix material, these fibers buckle under compression and thus the overall material response in compression is isotropic and captured by Ψ_m alone. Simplifying the strain-energy function for the fibers given in [54] to account for only one fiber family, Ψ_f may be written as

$$\Psi_f = \begin{cases} \Psi_f^t = \frac{k_1}{2k_2} \{ \exp [k_2(I_4 - 1)^2] - 1 \} & \text{if } I_4 > 1, \\ \Psi_f^c = 0 & \text{if } I_4 \leq 1, \end{cases} \quad (6.1)$$

where the superscript t and c stand for tension and compression respectively, $k_1 > 0$ is a stress-like material parameter and $k_2 > 0$ is a dimensionless parameter, both which control the nonlinear, equilibrium fiber fabric response. As discussed, e.g., in [54, 56], for both convexity and strong ellipticity to be fulfilled in tension, the material parameters in Ψ_f must fulfill the relations $k_1 > 0$ and $k_2 > 0$. Beyond the physical motivation for the compression ‘switch’ (the fibers buckle), there is also a mathematical reason for switching to $\Psi_f^c = 0$ in compression. Strong ellipticity can not be guaranteed without this switch, which may have a negative impact on numerical stability of the corresponding finite element implementations of the constitutive equations.

As the strain-energy function Ψ is separated into two terms, the Cauchy stress tensor

$$\boldsymbol{\sigma} = 2\mathbf{F} \frac{\partial \Psi}{\partial \mathbf{C}} \mathbf{F}^T - p_h \mathbf{I}, \quad (6.2)$$

can similarly be separated into $\boldsymbol{\sigma} = \boldsymbol{\sigma}_m + \boldsymbol{\sigma}_f - p_h \mathbf{I}$, where $\boldsymbol{\sigma}_m$ is the matrix contribution, $\boldsymbol{\sigma}_f$ is the fiber contribution and $p_h \mathbf{I}$ is a term used to enforce incompressibility via a Lagrange

multiplier p_h (a non-physical penalty parameter) and the second order identity tensor \mathbf{I} . The stress tensors $\boldsymbol{\sigma}_m$ and $\boldsymbol{\sigma}_f$ can be written as

$$\boldsymbol{\sigma}_m = 2\mathbf{F} \frac{\partial \Psi_m}{\partial \mathbf{C}} \mathbf{F}^T = \mu \mathbf{b}, \quad (6.3)$$

and

$$\boldsymbol{\sigma}_f = 2\mathbf{F} \frac{\partial \Psi_f}{\partial \mathbf{C}} \mathbf{F}^T = \begin{cases} \boldsymbol{\sigma}_f^t = 2k_1(I_4 - 1) \exp[k_2(I_4 - 1)^2] \mathbf{A} & \text{if } I_4 > 1, \\ \boldsymbol{\sigma}_f^c = 0 & \text{if } I_4 \leq 1, \end{cases} \quad (6.4)$$

where $\mathbf{b} = \mathbf{F}\mathbf{F}^T$ is the left Cauchy-Green tensor and $\mathbf{A} = \mathbf{F}\mathbf{a}_0\mathbf{F}^T = \mathbf{F}\mathbf{a}_0 \otimes \mathbf{F}\mathbf{a}_0 = \mathbf{a} \otimes \mathbf{a}$ is an Eulerian structure tensor associated with the fibers (characterized by the reference direction vector \mathbf{a}_0 , $|\mathbf{a}_0| = 1$) with direction \mathbf{a} in the Eulerian configuration.

In order to visualize the effects of fiber-term switching from tension to compression, we compare the Cauchy stresses $\boldsymbol{\sigma} = \boldsymbol{\sigma}_m + \boldsymbol{\sigma}_f - p_h \mathbf{I}$ and $\tilde{\boldsymbol{\sigma}}_f = \boldsymbol{\sigma}_f - p_h \mathbf{I}$ under uniaxial deformation of an incompressible material with the fiber orientation \mathbf{a}_0 in the global 11–direction. The material is stretched/compressed by λ_f in the global 11–direction and is free to deform (i.e. traction free) in the 22 and 33–directions. Thus the deformation gradient is $\mathbf{F} = \text{diag}(\lambda_f, \lambda_f^{-1/2}, \lambda_f^{-1/2})$ which assumes both transverse (in-plane) isotropy and material incompressibility, i.e. $\det \mathbf{F} = 1$. The Lagrange multiplier p is determined from the 33–component of the stress tensor.

Without loss of generality, the material parameters are chosen for a representative case as $\mu = 5 \text{ kPa}$, $k_1 = 10 \text{ kPa}$ and $k_2 = 15 [-]$, and are not matched to any experimental material data. In Fig. 6.1(a) we compare the 11–components of the stresses (coincident with the fiber direction by design); the fiber stress $\tilde{\boldsymbol{\sigma}}_f$ does not contribute to the total stress while the fibers are in compression, i.e. at $\lambda_f < 1$. In compression the total stress tensor $\boldsymbol{\sigma}$ is instead completely governed by the matrix contribution which yields the appropriate negative stresses. In Fig. 6.1(b) we show the invariants I_1 and I_4 during tension-compression

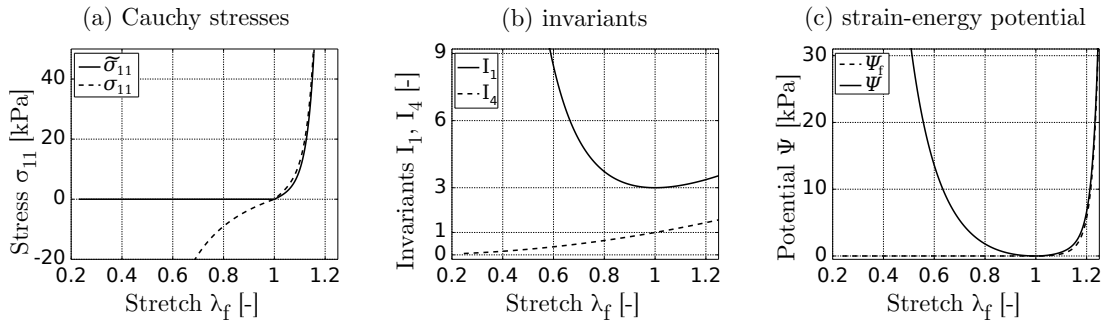


Figure 6.1.: Uniaxial tension-compression results for the fiber-reinforced model presented in [54]: (a) Cauchy stresses in the fiber direction for $\boldsymbol{\sigma}$ and $\tilde{\boldsymbol{\sigma}}_f$; (b) invariants relating to isotropy, I_1 , and fiber-reinforcement, I_4 ; (c) strain-energy potentials, both the total Ψ and the fiber contribution Ψ_f .

loading in the fiber direction. It is apparent that $I_4 \leq 1$ at $\lambda_f \leq 1$, while $I_1 = 3$ at $\lambda_f = 1$, and $I_1 > 3$ otherwise. In Fig. 6.1(c) we show the corresponding strain-energy response. Thus, setting the fiber-component of the strain-energy function to zero during compression, i.e. $\Psi_f^c = 0$ when $I_4 \leq 1$, is motivated in part from physical considerations and in part from numerical considerations.

For constitutive models with distributed fiber orientations, cf. [5, 37, 42, 47, 61, 171], stability of the fiber-terms in compression is still problematic, but a physical motivation to switch off fiber terms is now less clear. With fibers dispersed from the principal direction, single fibers oriented far from this principal direction may be in tension while the principal fiber direction is in compression (see, e.g., [57] for a related discussion on a dispersed model in tension). It must be noted though that such an assumption requires a very large dispersion or a very large compressions, both which are often outside the physiological range.

Nevertheless, a non-trivial choice must be made on how to handle compression in models with distributed fiber orientations. Here we analyze such a model, which includes a mixture of isotropic and transversely isotropic terms, for six different tension-compression switching assumptions. In Section 6.2 we outline our mathematical methods, in Section 6.3 we show results, and in Section 6.4 we provide a discussion and conclusion.

6.2. Mathematical methods

We examine the popular fiber dispersion model developed by Gasser, Holzapfel and Ogden [47]. It includes a dispersion parameter κ , based on the circular von Mises probability density function, which admits a physical interpretation. This dispersion parameter κ lives in the range $\kappa \in [0, 1/3]$ and is used in the combined pseudo-invariant

$$I_4^* = \kappa I_1 + (1 - 3\kappa)I_4, \quad (6.5)$$

which is a mixture of the isotropic invariant I_1 and the directionally dependent pseudo-invariant I_4 .

We generalize the presentation of the constitutive model from [47] to include six switching cases, which encompass different possible pseudo-invariants to trigger the tension-compression changes (Table 6.1, column 2; subsequently labeled as Table 6.1₂) and different possible strain-energy formulations for use in generalized compression Ψ_f^{ci*} , where the superscript i denotes the Case number, i.e. $i \in \{0, \dots, 6\}$ (Table 6.1₄). Note that each Case thus represent a different material model. The combined invariant I_4^* replaces I_4 in (6.1) according to

$$\Psi_f^* = \begin{cases} \Psi_f^{t*} = \frac{k_1}{2k_2} (\exp [k_2(I_4^* - 1)^2] - 1) & \text{if (Table 6.1}_2) > 1, \\ \Psi_f^{ci*} = (\text{Table 6.1}_4) & \text{if (Table 6.1}_2) \leq 1, \end{cases} \quad (6.6)$$

where again, for simplicity, we consider only one fiber direction. Note that when $\kappa = 0$ the fibers are perfectly aligned and $\Psi_f^{t*} = \Psi_f^t(I_4)$, but when $\kappa = 1/3$ the distribution is isotropic and $\Psi_f^{t*} = \Psi_f^t(I_1)$. As discussed in [47], for numerical stability (6.6) in tension needs to be modified for use in compression. Therefore, we investigate six possible switching cases shown in Table 6.1, where cases 1, 2 and 3 use as a ‘switch’ $I_4 \leq 1$, and cases 4, 5 and 6 use the combined invariant $I_4^* \leq 1$ as a ‘switch’. A zeroth case, where $\Psi_f^* = \Psi_f^{t*}$ for both tension and compression, i.e. no switch in compression, is also shown for illustrative purposes.

Case i	Switch	I_{ci}	Ψ_f^{ci*}	σ_f^{ci*}
0	-	I_4^*	$\frac{k_1}{2k_2} \left\{ \exp \left[k_2 (I_4^* - 1)^2 \right] - 1 \right\}$	$2k_1 (I_4^* - 1) \exp \left[k_2 (I_4^* - 1)^2 \right] \mathbf{h}$
1	$I_4 \leq 1$	κI_1	$\frac{k_1}{2k_2} \left\{ \exp \left[k_2 (\kappa I_1 - 1)^2 \right] - 1 \right\}$	$2k_1 (\kappa I_1 - 1) \exp \left[k_2 (\kappa I_1 - 1)^2 \right] \kappa \mathbf{b}$
2	$I_4 \leq 1$	-	0	0
3	$I_4 \leq 1$	$\frac{1}{3} I_1$	$\frac{k_1}{2k_2} \left\{ \exp \left[k_2 \left(\frac{1}{3} I_1 - 1 \right)^2 \right] - 1 \right\}$	$2k_1 \left(\frac{1}{3} I_1 - 1 \right) \exp \left[k_2 \left(\frac{1}{3} I_1 - 1 \right)^2 \right] \frac{1}{3} \mathbf{b}$
4	$I_4^* \leq 1$	κI_1	$\frac{k_1}{2k_2} \left\{ \exp \left[k_2 (\kappa I_1 - 1)^2 \right] - 1 \right\}$	$2k_1 (\kappa I_1 - 1) \exp \left[k_2 (\kappa I_1 - 1)^2 \right] \kappa \mathbf{b}$
5	$I_4^* \leq 1$	-	0	0
6	$I_4^* \leq 1$	$\frac{1}{3} I_1$	$\frac{k_1}{2k_2} \left\{ \exp \left[k_2 \left(\frac{1}{3} I_1 - 1 \right)^2 \right] - 1 \right\}$	$2k_1 \left(\frac{1}{3} I_1 - 1 \right) \exp \left[k_2 \left(\frac{1}{3} I_1 - 1 \right)^2 \right] \frac{1}{3} \mathbf{b}$

Table 6.1.: Six possible choices for tension-compression switching of the dispersed fiber-reinforced constitutive model presented in [47]. The columns represent: the Case number, the criteria for tension-compression switching, the invariant term used in compression, the corresponding strain-energy function for compression and the corresponding Cauchy stress for compression, N.B., all Cases use the same combined invariant, strain-energy and corresponding Cauchy stress in tension. Case zero, shown for comparative purposes, does not switch from tension to compression.

As seen in Table 6.1, exclusion of directional (i.e. fiber orientation) dependence for the strain-energy function in compression may be achieved by simply removing I_4 from the equation, as shown in Cases 1 and 4, or by assigning $\kappa = 1/3$ for the dispersion parameter, as shown in Cases 3 and 6, or alternatively, and in accordance with (6.1), the entire strain-energy function associated with the fibers may be removed (i.e. $\Psi_f^{ci*} = 0$), as shown in Cases 2 and 5. Note that all Cases use the same combined invariant, strain-energy and corresponding Cauchy stress in tension.

It is now straightforward to write the Cauchy stress for the fiber contribution as

$$\boldsymbol{\sigma}_f^* = 2\mathbf{F} \frac{\partial \Psi_f^*}{\partial \mathbf{C}} \mathbf{F}^T = \begin{cases} \boldsymbol{\sigma}_f^{t*} = 2k_1(I_4^* - 1) \exp[k_2(I_4^* - 1)^2] \mathbf{h} & \text{if (Table 6.1}_2) > 1, \\ \boldsymbol{\sigma}_f^{ci*} = (\text{Table 6.1}_5) & \text{if (Table 6.1}_2) \leq 1, \end{cases} \quad (6.7)$$

where $\mathbf{h} = \kappa \mathbf{b} + (1 - 3\kappa) \mathbf{a} \otimes \mathbf{a}$ is an Eulerian structure tensor incorporating the dispersed fiber structure.

We examine two loading conditions: uniaxial tension-compression in the principal fiber direction and simple shear (with a range of principal fiber directions). We use the material parameters from Section 6.1 (i.e., $k_1 = 10$ kPa and $k_2 = 15$ [-]), with the additional dispersion parameter κ [-] that is allowed to vary in the uniaxial tension-compression deformation state, and is set arbitrary to 0.15 in the shear deformation state. Given (6.7), we can determine the Cauchy stress analytically in terms of the applied deformations, i.e. the applied stretch λ_f or the shear γ . Full expressions for these stresses are given in Appendix B.1. For the uniaxial tension-compression loading state, we investigate the six switching cases in terms of (i) Cauchy stresses and (ii) the combined tension-compression invariant. For the simple shear loading state the switching cases are investigated in terms of (iii) the Cauchy stresses only.

6.3. Results

(i) The Cauchy stress – uniaxial tension-compression. Fig. 6.2 compares the fiber component of the Cauchy stress $\tilde{\boldsymbol{\sigma}}_f^* = \boldsymbol{\sigma}_f^* - p_h \mathbf{I}$ which aligns with the 11–direction by design, i.e. $\tilde{\sigma}_{ff}^* = [\tilde{\boldsymbol{\sigma}}_f^*]_{11}$, for Cases 0–6. The solid black line in Fig. 6.2(a)–(f) highlight the stress behavior at $\kappa = 0.15$ for illustrative purposes. The effect of dispersion in tension is shown in all cases (the behavior in tension is always the same) where increasing values of κ decreases the tensile stress response (although it is always positive for $\lambda_f > 1$). Case 0, as seen in Fig. 6.2(a), is used as a reference to show the effect of not changing the strain-energy function used in compression from that used in tension. For low κ -values and increased compressive stretches (λ_f increasingly < 1) the stress response will first turn strongly negative followed by a large positive stress. For very large values of κ the stress response will only be negative. Fig. 6.2(b) illustrates both cases 1 and 4 as they give a nearly identical stress response. Following the black line in compression, Cases 1 and 4 show a large positive stress in compression until $\lambda_f \sim 0.3$ where it becomes negative. For Case 2, Fig. 6.2(c), the stress in compression is always zero. For Case 3, Fig. 6.2 d), the compressive stress is always negative and independent of the κ -value, and increased compression leads to increasingly negative stresses. In Fig. 6.2(e), Case 5, we see the effects of using $I_4^* \leq 1$ as a switch. The stress in compression for Case 5 is zero until $\lambda_f \sim 0.3$ where it turns negative, and note that increasing κ shifts the point where Case 5 yields negative stresses towards lower levels of compression. Lastly, following the black line for

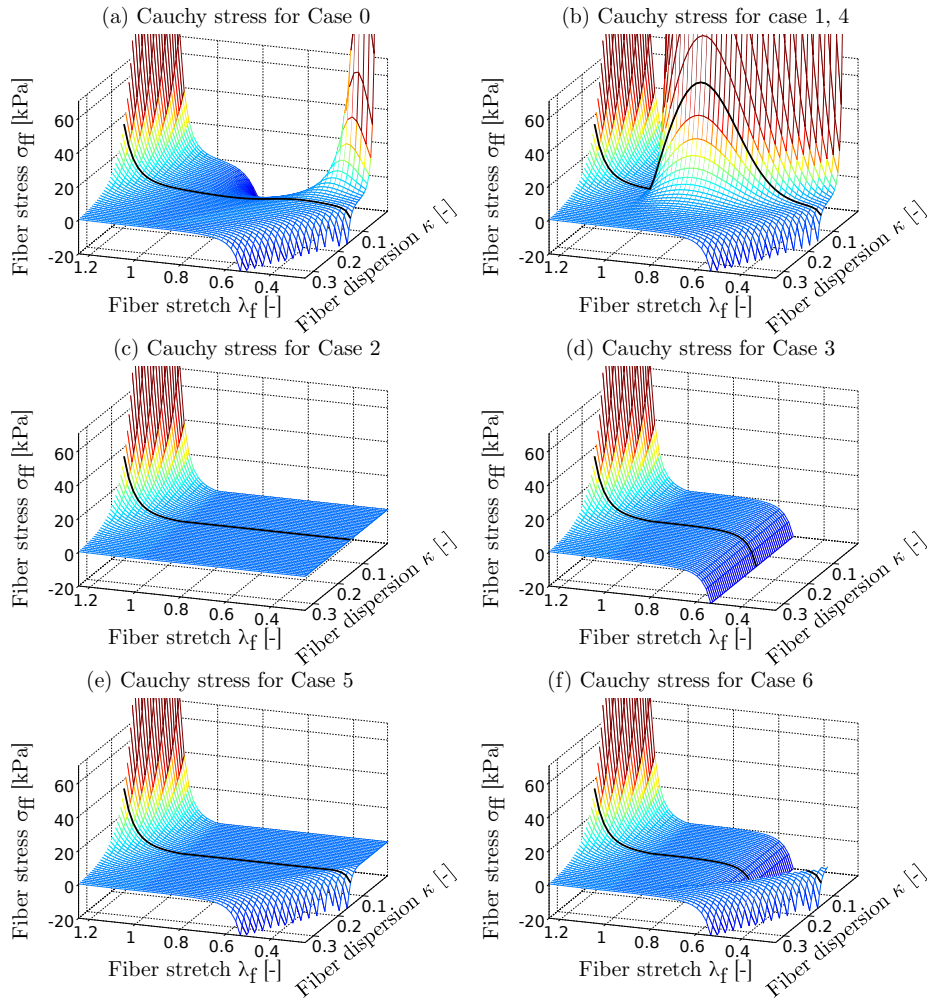


Figure 6.2.: Cauchy stress results in the fiber direction under uniaxial tension-compression for six possible choices of tension-compression switching for the dispersed fiber-reinforced constitutive model presented in [47]. Cases 0–6 shown in (a)–(f), respectively, cf. Table 6.1₅. A solid black line follows the stress results at $\kappa = 0.15$.

Case 6 in Fig. 6.2(f) shows that the fiber stress will drop to large negative values when initially compressed, but that further increasing compression will cause the stress to increase again.

(ii) The combined invariant – uniaxial tension-compression. Fig. 6.3(a)–(d) compares the combined invariant I_4^* for cases 0, 1, 3 and 4, respectively. A black line is again used to highlight the behavior when $\kappa = 0.15$. Two transparent planes are used as reference planes. The horizontal plane indicates $I_4^* = 1$ and the vertical plane indicates $\lambda_f = 1$. Case 0, seen in Fig. 6.3(a), shows the behavior of the combined invariant when going from tension to

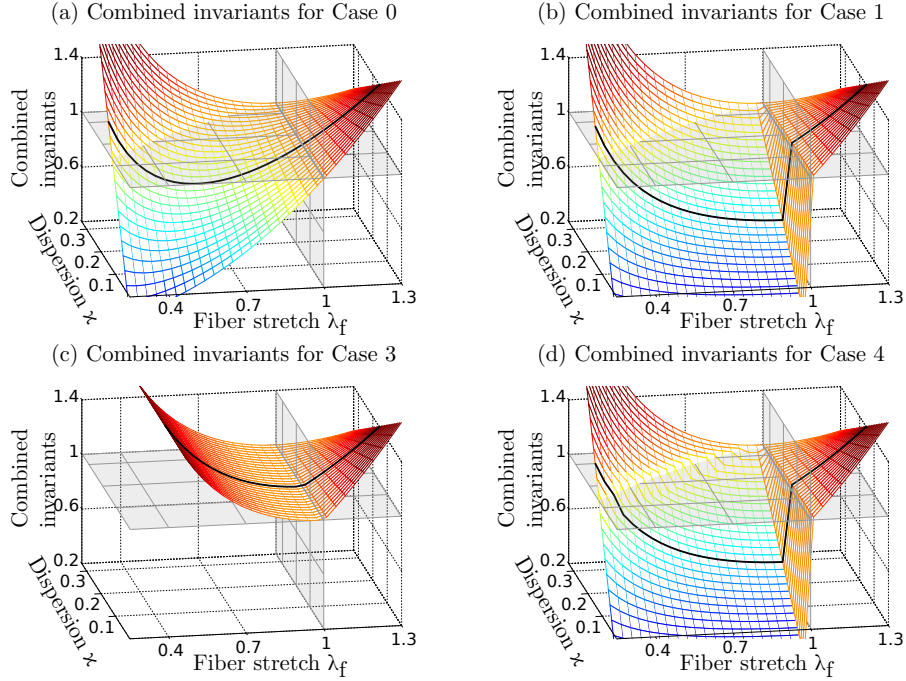


Figure 6.3.: Combined invariant results for 4 possible choices of a combined tension-compression invariant undergoing uniaxial tension-compression for Cases 0, 1, 3 and 4, cf. Table 6.1₃: (a) behavior of the combined invariant without using any switch, i.e. $I_{c0} = I_4^*$; (b) combined invariant $I_{c1} = \kappa I_1$ for Case 1; (c) combined invariant $I_{c3} = 1/3 I_1$ for Case 3; d) combined invariant $I_{c4} = \kappa I_1$ for Case 4, with switching determined by $I_4^* \leq 1$; N.B., all Cases use I_4^* for the combined invariant in tension. A solid black line follows the combined invariant results at $\kappa = 0.15$.

compression. Clearly, $I_4^* > 1$ may occur even at a large compression depending on the value of κ . Following the black line, as a representative case, $I_4^* > 1$ occurs at $\lambda_f \sim 0.3$, which corresponds to the compression level when Cases 0, 1, 4 and 5 show negative stresses along the same line (cf. Fig. 6.2(a), (b) and (e)). Following the black line in Fig. 6.3(b) further shows that I_4^* makes a sharp decrease for Case 1 at $\lambda_f = 1$ to $I_4^* \sim 0.45$. Increasing the level of compression yields larger values of I_4^* and again at $\lambda_f \sim 0.3$, $I_4^* > 1$, similar to Case 0. The behavior seen in Fig. 6.3 d) for Case 4, is nearly identical to Case 1, except for a jump in the values of I_4^* around $\lambda_f \sim 0.3$ that is seen when following the black line. For Case 3, however, I_4^* is always ≥ 1 , in both tension and compression as seen in Fig. 6.3(c).

(iii) The Cauchy stress – simple shear. As Cases 0, 1, 4 and 6 clearly demonstrate non-physical stress responses in uniaxial compression (cf. Fig. 6.2 (a), (b) and (f)), only Cases 2, 3 and 5 are investigated further in simple shear. Depending on the initial orientation of the fiber direction, simple shear (with applied displacement γ) may result in tension or compression of the Eulerian fiber direction. The stretch is shown in Fig. 6.4(a) as a

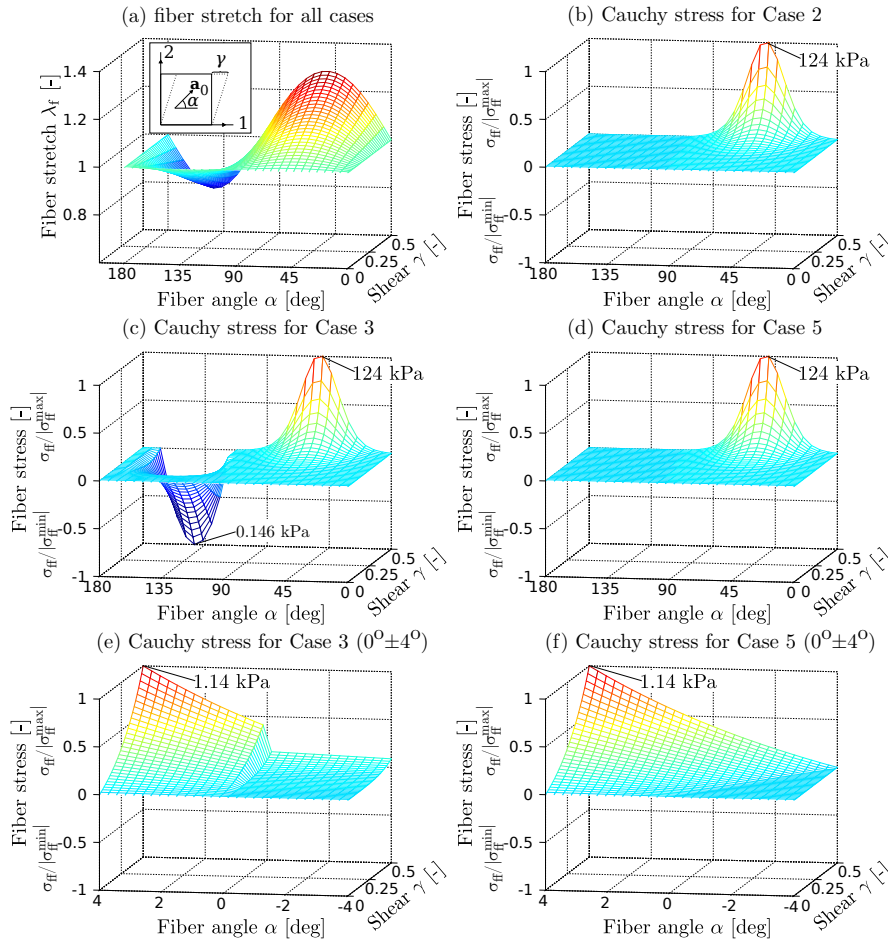


Figure 6.4.: Stretch and Cauchy stress results in the fiber direction with varying Lagrangian fiber angle α and shear γ under simple shear deformation in the 1–2 plane for Cases 2, 3 and 5, cf. Table 6.15: (a) stretch in the fiber direction for all cases (inset defines simple shear γ on a unit cube and fiber angle α); Cauchy stress in the deformed fiber direction σ_{ff} for: (b) Case 2; (c) Case 3; (d) Case 5; Closeup of Cauchy stress in the deformed fiber direction σ_{ff} when $\alpha = 0^\circ \pm 4^\circ$ for: (e) Case 3; (f) Case 5. N.B., positive stresses are normalized by the modulus of the maximum fiber stress $|\sigma_{ff}^{\max}|$ while negative stresses are normalized by the modulus of the minimum fiber stress $|\sigma_{ff}^{\min}|$ for visual clarity.

function of shear γ and the angle α between the fiber and the 11–direction (cf. inset in Fig. 6.4(a)). When the angle is zero, i.e. fibers are aligned in the shear direction, there is no stretch in the fiber direction regardless of the amount of shear. As the angle increases from zero, however, the stretch also increases with shear until $\alpha \sim 52^\circ$, where $\lambda_f \sim 1.28$, after which it decreases again. At $\alpha > 90^\circ$, low values of γ may yield $\lambda_f < 1$ whereas large values of γ yields $\lambda_f > 1$. For $\alpha \sim 142^\circ$ the largest compressive stretch, $\lambda_f \sim 0.78$, is found at $\gamma = 0.5$ and for $142^\circ < \alpha < 180^\circ$ only compressive stretches are seen (while

$\gamma \leq 0.5$). In Fig. 6.4(b), (c) and d), the Cauchy stress in the Eulerian fiber direction is shown for Cases 2, 3 and 5, respectively. In Fig. 4, positive stresses are normalized by the modulus of the maximum fiber stress $|\sigma_{ff}^{\max}|$ while negative stresses are normalized by the modulus of the minimum fiber stress $|\sigma_{ff}^{\min}|$ for visual clarity (as the difference in magnitude between positive and negative stress values is very large). As the Cauchy stress is zero in compression by design for Case 2, only one peak is seen in Fig. 6.4(b). Here the maximum value of the Cauchy stress in tension is 124 kPa and is centered around $\alpha \sim 52^\circ$. Because all cases have the same behavior in tension, the maximum tensile stress for all cases is identical. Case 3 has a minimum compressive stress of -0.146 kPa at $\alpha \sim 142^\circ$ as seen in Fig. 6.4(c). In Case 5, shown in Fig. 6.4 d), the stress is mostly zero in compression. At closer inspection, however, for very large initial fiber angles, i.e. where $180^\circ > \alpha > 175^\circ$, a small positive stress peak is seen (0.450 kPa) even as the principal fiber direction is in compression. This is illustrated in the closeup of the fiber stress at $\alpha = 0^\circ \pm 4^\circ$ for Case 5 seen in Fig. 6.4(f). However, looking at a similar closeup of the fiber stress for Case 3 in Fig. 6.4(e), we also see small positive stresses.

6.4. Discussion

Large-strain models for dispersed fiber-reinforced materials in, e.g., soft tissue biomechanics, need to solve the problem of switching the form of the fiber potential used in compression from that used in tension, to provide a consistent physical interpretation and to ensure both numerical stability and robustness. Cases 1 and 2, and models with similarities to Case 3, are often used approaches to deal with fiber compression, cf. [5, 38, 47]. In the dispersion models investigated here, Cases 3, 4 and 6 have, to the authors' knowledge, not previously been used or investigated in the mechanics literature (a model similar to Case 5 is employed in [179]).

The 'switch' used in Cases 4, 5 and 6, $I_4^* \leq 1$, correctly switches when $\lambda_f = 1$ for a uniaxial deformation, and is motivated by the comparison of (6.1) and (6.6). However, in contrast to the relation $I_4 < 1$ which is always true in fiber compression, the relation $I_4^* \not\leq 1$ for large fiber compressions, as seen in Fig. 6.3(a). The combined invariant I_4^* may become positive in compression because under increasingly large compression (λ_f increasingly < 1), I_1 becomes $\gg 3$ while I_4 is only < 1 , as seen in Fig. 6.1(b). At which compression point the combined invariant will shift from negative to positive depends on the value of the dispersion parameter κ . With progressively larger values of κ , i.e. larger dispersion, $I_4^* > 1$ will occur at progressively lower levels of compression in the fibers. Hence, with this switching approach the dispersion parameter κ has a non-physical and ambiguous meaning (cf. Cases 4–6), as it reflects both the fiber dispersion and some arbitrary switch whereby, e.g., negative/positive fiber stresses may occur in compression. For this reason, we believe that the switch parameter $I_4^* \leq 1$ should only be used under loading conditions which do not trigger $I_4^* > 1$ while $\lambda_f < 1$.

Perhaps the most startling results in this study are the positive stresses generated in compression for Cases 1 and 4 in uniaxial tension-compression and for Case 5 in simple shear (while the principal fiber direction is in compression). Clearly in the uniaxial case, when compressing a fiber reinforced material in the principal fiber direction, a positive stress in the direction of compression is not physiologically relevant, but it is seen nonetheless in Fig. 6.2(b) for Cases 1 and 4. The reason for the positive stress in these two cases is clear when looking at the combined invariants $I_{c1} = I_{c4} = \kappa I_1$, in compression. For any value of $\kappa \neq 1/3$, Fig. 6.3(b) and d) show that $I_4^* < 1$ at $\lambda_f = 1$, which leads to $\tilde{\sigma}_f^{c1*} > 1$ and $\tilde{\sigma}_f^{c4*} > 1$ according to (6.7). This occurrence violates a fundamental requirement that the reference configuration should be stress-free, i.e. here we see that $\Psi_f^*(\mathbf{F} = \mathbf{I}) \neq 0$ and thus $\tilde{\sigma}_f^*(\mathbf{F} = \mathbf{I}) \neq \mathbf{0}$, which should not be, cf. [53]. The condition requiring a stress-free reference state is naturally fulfilled for Cases 2 and 5, where $\Psi_f^{c2*} = \Psi_f^{c5*} = 0$ gives $\tilde{\sigma}_f^{c2*} = \tilde{\sigma}_f^{c5*} = \mathbf{0}$, cf. Fig. 6.2(c), (e) and 6.4(a), (c). Similarly, this condition is fulfilled for Case 3, whereby in compression the dispersion parameter is set to $\kappa = 1/3$, and thus $\Psi_f^*(\mathbf{F} = \mathbf{I}) = 0$ as $I_{c3}(\mathbf{F} = \mathbf{I}) = 1$.

The reason for positive stresses for Case 5 in simple shear (while the principal fiber direction is in compression) is perhaps not clear. For α close to (but less than) 180° , the isotropic response projected in the fiber direction is actually positive as seen, e.g., in Case 3 Fig. 6.4(e), or when using a neo-Hookean strain-energy function for this deformation (not shown here). The positive stress in Case 5 may be physiological as it incorporates a positive stress response for small perturbations of the principal fiber angle around 0 (equivalently 180°), given some level of dispersion. However, κ still has a dual meaning, the same as was seen for Case 5 in uniaxial tension-compression. Thus, in Case 5, κ determines both the degree of dispersion and the amount of shear required to generate positive stresses while the principal fiber direction is in compression. Therefore, it is less clear what the parameter κ represents for Case 5.

Although not shown here, using different material parameters in (6.6), within the required range ($k_1 > 0$ and $k_2 > 0$), only changes the magnitude of the stress response or the compression point where, e.g., $I_4^* > 1$ may occur. It does not alter the trends shown or the conclusions drawn from this analysis. We have shown that Cases 2 and 3 generate the most desirable results, both in terms of a physically consistent morphological interpretation, robustness and also consistency in the interpretation of the structural parameter κ . We implemented both of these models in the finite element analysis software FEAP [164], and verified that they yield numerically stable results identical to those shown in Fig. 6.2(c), (d) and 6.4(a), (b). Case 2, in the physical interpretation, corresponds to the situation wherein the fibers buckle under compression and are essentially uncoupled to the ground matrix (and furthermore, are not cross-linked). Thus, when the principal direction of fiber reinforcement is in compression the dispersed fibers have no stiffness and do not store strain-energy. Case 3, conversely, corresponds to another situation, wherein a matrix-fiber bonding does exist, and which results in an isotropic positive fiber potential (the dispersed fibers

store strain-energy) even in compression.

We have further shown that Case 5 may be used with caution. Although it may yield negative stresses in uniaxial deformation at some arbitrary (but high) level of compression, such levels are rarely reached in the physiological applications where the model is most often used. In effect, Case 5 will thus render an equal stress response as Case 2. However, as seen in Fig. 6.4(f), Case 5 may advantageously be used to capture positive stress responses for small perturbations of the principal fiber direction around some critical angle where the principal fiber direction switches between tension and compression and where, e.g., Case 2 would instantly set the stress values to zero. Case 5, using $I_4^* \leq 1$ as the switch, may thus be advantageous for numerical convergence in, e.g., a FE simulation, but as we have shown that this effect is regulated by the dispersion parameter κ , it is unclear how (or if) this phenomenon has a physical interpretation.

As a final note on numerical stability, we investigated the convexity and ellipticity of the strain-energy functions show here in Appendix B.2. Therein we show that the strain-energy function, proposed by Gasser, Holzapfel and Ogden [47], and also used here, is locally convex in \mathbf{C} for both tension and compression. However, from two simple examples we also show that ellipticity can not be guaranteed in general for incompressible models that couple the invariants I_1 and I_4 . Nevertheless, the strain-energy function (6.6) has been implemented in the FE framework FEAP [164], and for all types of deformations tested it has remained stable. Future investigations are needed to determine the conditions under which ellipticity is lost.

Acknowledgements

This project is supported in part by the SFB Research Center ‘Mathematical Optimization and Applications in Biomedical Sciences’, project F3210-N18 granted by the Austrian Science Fund. This support is gratefully acknowledged.

A. APPENDIX FOR CHAPTER 5

A.1. Active Elasticity Tensors in Lagrangian and Eulerian Description

Using the definition $\mathbf{M}_0 := \mathbf{f}_0 \otimes \mathbf{f}_0$ for shorter notation, (5.13) may be written as

$$\mathbf{S}_a = S_a \left(\frac{\kappa_f}{1 - 2\kappa_f} \mathbf{C}^{-1} + \frac{1 - 3\kappa_f}{1 - 2\kappa_f} I_{4f}^{-1} \mathbf{M}_0 \right). \quad (\text{A.1})$$

The Lagrangian elasticity tensor is given by $\mathbb{C}_a = 2\partial\mathbf{S}_a/\partial\mathbf{C}$ which leads to

$$\mathbb{C}_a = 2 \frac{S_a}{1 - 2\kappa_f} \left[\kappa_f \frac{\partial \mathbf{C}^{-1}}{\partial \mathbf{C}} + (1 - 3\kappa_f) \frac{\partial I_{4f}^{-1} \mathbf{M}_0}{\partial \mathbf{C}} \right]. \quad (\text{A.2})$$

Expanding the the derivative $\partial(I_{4f}^{-1} \mathbf{M}_0)/\partial \mathbf{C} = I_{4f}^{-2} \mathbf{M}_0 \otimes \mathbf{M}_0$, (A.2) is formulated as

$$\mathbb{C}_a = 2 \frac{S_a}{1 - 2\kappa_f} \left[\kappa_f \frac{\partial \mathbf{C}^{-1}}{\partial \mathbf{C}} + (1 - 3\kappa_f) I_{4f}^{-2} \mathbf{M}_0 \otimes \mathbf{M}_0 \right], \quad (\text{A.3})$$

and using the push-forward operation on \mathbb{C}_a by $[\mathbb{c}_a]_{abcd} = J^{-1} F_{aA} F_{bB} F_{cC} F_{dD} [\mathbb{C}_a]_{ABCD}$ leads to

$$\mathbb{c}_a = -2 \frac{S_a}{J(1 - 2\kappa_f)} \left[\kappa_f \mathbb{I} + (1 - 3\kappa_f) \hat{\mathbf{M}} \otimes \hat{\mathbf{M}} \right], \quad (\text{A.4})$$

where the fourth order identity tensor defined in index notation as $[\mathbb{I}]_{abcd} = (\delta_{ac}\delta_{bd} + \delta_{ad}\delta_{bc})/2$ is introduced from the push-forward relation $F_{aA} F_{bB} F_{cC} F_{dD} [\partial(\mathbf{C}^{-1})/\partial \mathbf{C}]_{ABCD} = -[\mathbb{I}]_{abcd}$ and the definition $\hat{\mathbf{M}} := \mathbf{F} I_{4f}^{-1} \mathbf{M}_0 \mathbf{F}^T = \hat{\mathbf{f}} \otimes \hat{\mathbf{f}}$ is used.

B. APPENDIX FOR CHAPTER 6

B.1. The Stress Equations as a Function of Applied Stretch λ_f or Applied Shear γ

As all stress components shown in the following are related to the fiber part of the stress, i.e. $\tilde{\boldsymbol{\sigma}}_f$ or $\tilde{\boldsymbol{\sigma}}_f^*$, the subindex f is not shown on a component level to simplify notation. The subindex ff, however, is used and denotes the component of the stress tensor aligned in the deformed fiber direction.

In uniaxial tension in the 11–direction, the corresponding deformation gradient is $\mathbf{F} = \text{diag}(\lambda_f, \lambda_f^{-1/2}, \lambda_f^{-1/2})$ when the fiber $[\mathbf{a}_0] = [1, 0, 0]^T$ aligned in the 11-direction (meaning that $\tilde{\boldsymbol{\sigma}}_{ff} = \tilde{\boldsymbol{\sigma}}_{11}$). Using (6.4), the only non-zero component of $\tilde{\boldsymbol{\sigma}}_f = \boldsymbol{\sigma}_f - p_h \mathbf{I}$ in tension is

$$\tilde{\sigma}_{11}^t = 2k_1 (\lambda_f^2 - 1) \exp[k_2 (\lambda_f^2 - 1)^2] \lambda_f^2, \quad (\text{B.1})$$

where p is determined from $\tilde{\sigma}_{33} = 0$, and in compression $\tilde{\sigma}_{11}^c = 0$. Using (6.7), the only non-zero component of $\tilde{\boldsymbol{\sigma}}_f^* = \boldsymbol{\sigma}_f^* - p_h \mathbf{I}$ in tension is

$$\begin{aligned} \tilde{\sigma}_{11}^{t*} = & 2k_1 [(1 - 2\kappa)\lambda_f^2 + 2\kappa\lambda_f^{-1} - 1] \exp\{k_2 [(1 - 2\kappa)\lambda_f^2 \\ & + 2\kappa\lambda_f^{-1} - 1]^2\} [(1 - 2\kappa)\lambda_f^2 - \kappa\lambda_f^{-1}], \end{aligned} \quad (\text{B.2})$$

where p is determined from $\tilde{\sigma}_{33}^* = 0$. In compression the Cauchy stresses in the 11-direction are instead

$$\tilde{\sigma}_{11}^{c1*} = 2k_1 [\kappa (\lambda_f^2 + 2\lambda_f^{-1}) - 1] \exp\{k_2 [\kappa (\lambda_f^2 + 2\lambda_f^{-1}) - 1]^2\} \kappa (\lambda_f^2 - \lambda_f^{-1}), \quad (\text{B.3})$$

$$\tilde{\sigma}_{11}^{c2*} = \tilde{\sigma}_{11}^{c5*} = 0, \quad (\text{B.4})$$

$$\tilde{\sigma}_{11}^{c3*} = 2k_1 [1/3(\lambda_f^2 + 2\lambda_f^{-1}) - 1] \exp\{k_2 [1/3(\lambda_f^2 + 2\lambda_f^{-1}) - 1]^2\} 1/3(\lambda_f^2 - \lambda_f^{-1}), \quad (\text{B.5})$$

$$\tilde{\sigma}_{11}^{c4*} = \tilde{\sigma}_{11}^{c1*}, \quad (\text{B.6})$$

$$\tilde{\sigma}_{11}^{c6*} = \tilde{\sigma}_{11}^{c3*}, \quad (\text{B.7})$$

where the superscript ci , $i \in \{1, \dots, 6\}$ represent the six cases shown in Table 6.1. Case 0 in compression equals the formulation in tension shown in (B.2), i.e. $\tilde{\sigma}_{11}^{c0*} = \tilde{\sigma}_{11}^{t*}$.

Similarly, during simple shear the deformation gradient is

$$[\mathbf{F}] = \begin{bmatrix} 1 & \gamma & 0 \\ 0 & 1 & 0 \\ 0 & 0 & 1 \end{bmatrix},$$

and with the fiber direction $[\mathbf{a}_0] = [\cos(\alpha), \sin(\alpha), 0]^T$ in the Lagrangian description, the 33-direction is stress free and is used to determine p . The non-zero components of $\tilde{\boldsymbol{\sigma}}_f^*$ in tension are

$$\tilde{\sigma}_{11}^{t*} = 2\psi_4^{t*} [\kappa\gamma^2 + (1 - 3\kappa)A_1^2], \quad (\text{B.8})$$

$$\tilde{\sigma}_{12}^{t*} = \tilde{\sigma}_{21}^{t*} = 2\psi_4^{t*} [\kappa\gamma + (1 - 3\kappa)A_1 \sin(\alpha)], \quad (\text{B.9})$$

$$\tilde{\sigma}_{22}^{t*} = 2\psi_4^{t*} (1 - 3\kappa) \sin^2(\alpha), \quad (\text{B.10})$$

where $A_1(\gamma, \alpha) := \gamma \sin(\alpha) + \cos(\alpha)$ is used to shorten notation, and $\psi_4^{t*} = \partial\Psi^{t*}/\partial I_4^*$ is given by

$$\psi_4^{t*} = k_1 [\kappa(\gamma^2 + 3) + (1 - 3\kappa)A_2 - 1] \exp\left\{k_2 [\kappa(\gamma^2 + 3) + (1 - 3\kappa)A_2 - 1]^2\right\}, \quad (\text{B.11})$$

where $A_2(\gamma, \alpha) := (\gamma \sin(\alpha) + \cos(\alpha))^2 + \sin^2(\alpha)$ is used to shorten notation, N.B., $A_2 = I_4$ for this deformation. Depending on Table 6.12, the value used to determine if the fiber direction is in compression is thus either $A_2 \leq 1$ or $I_4^* = \kappa(\gamma^2 + 3) + (1 - 3\kappa)A_2 \leq 1$. To determine the Cauchy stresses in compression, it is necessary to derive the derivatives of the strain-energy functions with respect to the combined invariants for Cases 1–6 in compression, i.e. $\psi_{ci}^{ci*} = \partial\Psi^{ci*}/\partial I_{ci}$, for $i = 1, 2, \dots, 6$:

$$\psi_{c1}^{c1*} = \psi_{c4}^{c4*} = k_1 [\kappa(\gamma^2 + 3) - 1] \exp\{k_2 [\kappa(\gamma^2 + 3) - 1]^2\}, \quad (\text{B.12})$$

$$\psi_{c2}^{c2*} = \psi_{c5}^{c5*} = 0, \quad (\text{B.13})$$

$$\psi_{c3}^{c3*} = \psi_{c6}^{c6*} = k_1 [1/3(\gamma^2 + 3) - 1] \exp\{k_2 [1/3(\gamma^2 + 3) - 1]^2\}. \quad (\text{B.14})$$

Now, for Cases 1–6, the 11-component of the Cauchy stresses in compression are

$$\tilde{\sigma}_{11}^{c1*} = \tilde{\sigma}_{11}^{c4*} = 2\psi_{c1}^{c1*} \kappa\gamma^2, \quad (\text{B.15})$$

$$\tilde{\sigma}_{11}^{c2*} = \tilde{\sigma}_{11}^{c5*} = 0, \quad (\text{B.16})$$

$$\tilde{\sigma}_{11}^{c3*} = \tilde{\sigma}_{11}^{c6*} = 2\psi_{c3}^{c3*} 1/3\gamma^2, \quad (\text{B.17})$$

and the 12-components (equally the 21-components) are

$$\tilde{\sigma}_{12}^{c1*} = \tilde{\sigma}_{12}^{c4*} = 2\psi_{c1}^{c1*} \kappa\gamma, \quad (\text{B.18})$$

$$\tilde{\sigma}_{12}^{c2*} = \tilde{\sigma}_{12}^{c5*} = 0, \quad (\text{B.19})$$

$$\tilde{\sigma}_{12}^{c3*} = \tilde{\sigma}_{12}^{c6*} = 2\psi_{c3}^{c3*} 1/3\gamma, \quad (\text{B.20})$$

and finally, the 22-direction components of the Cauchy stresses are all zero for all cases in compression, i.e. $\tilde{\sigma}_{22}^{ci*} = 0$. The projection of the stress tensor in the fiber direction, i.e. $\tilde{\boldsymbol{\sigma}}_f^* : \mathbf{a} \otimes \mathbf{a}$, yields the following fiber component of the stress in tension

$$\begin{aligned} \sigma_{ff}^{t*} &= 2\psi_4^{t*} \{A_1^2[\gamma^2 \kappa + (1 - 3\kappa)A_1^2] \\ &\quad + 2\sin(\alpha)A_1[(1 - 3\kappa)\sin(\alpha)A_1 + \gamma\kappa] + (1 - 3\kappa)\sin^4(\alpha)\}, \end{aligned} \quad (\text{B.21})$$

and in compression

$$\sigma_{\text{ff}}^{\text{c}1*} = \sigma_{\text{ff}}^{\text{c}4*} = 2\psi_4^{\text{c}1*} \kappa \gamma [\gamma A_1^2 + 2A_1 \sin(\alpha)], \quad (\text{B.22})$$

$$\sigma_{\text{ff}}^{\text{c}2*} = \sigma_{\text{ff}}^{\text{c}5*} = 0, \quad (\text{B.23})$$

$$\sigma_{\text{ff}}^{\text{c}3*} = \sigma_{\text{ff}}^{\text{c}6*} = 2\psi_4^{\text{c}1*} 1/3\gamma [\gamma A_1^2 + 2A_1 \sin(\alpha)]. \quad (\text{B.24})$$

To summarize, (B.1) and $\tilde{\sigma}_{11}^c = 0$ are used to generate Fig. 6.1, (B.2) and (B.3)–(B.7) are used to generate Fig. 6.2, while (B.11) and (B.12)–(B.14) together with (B.21) and (B.22)–(B.24) are used to generate Fig. 6.4.

B.2. Convexity and Ellipticity of Distributed Functions

In this section, convexity of Eq. (6.6) and ellipticity of models that include a coupling between invariants I_1 and I_4 are investigated. First considering tension only, the function $\mathcal{T}(I_4^*) := k_1/(2k_2) (\exp[k_2(I_4^* - 1)^2] - 1)$ is defined, which has the relations

$$\frac{\partial \mathcal{T}(I_4^*)}{\partial \mathbf{C}} = \mathcal{T}'(I_4^*) \mathbf{H} \quad \text{and} \quad \frac{\partial^2 \mathcal{T}(I_4^*)}{\partial \mathbf{C} \partial \mathbf{C}} = \mathcal{T}''(I_4^*) \mathbf{H} \otimes \mathbf{H}, \quad (\text{B.25})$$

where the primes denotes the differentiation of $\mathcal{T}(I_4^*)$ with respect to I_4^* and \mathbf{H} is the Lagrangian distributed structure tensor given by

$$\mathbf{H} = \frac{\partial I_4^*}{\partial \mathbf{C}} = \kappa \mathbf{I} + (1 - 3\kappa) \mathbf{A}_0, \quad (\text{B.26})$$

where \mathbf{I} is the second order identity tensor. Local convexity requires that

$$\mathbf{M} : \frac{\partial^2 \mathcal{T}(I_4^*)}{\partial \mathbf{C} \partial \mathbf{C}} : \mathbf{M} \equiv \mathcal{T}''(I_4^*) [\mathbf{H} : \mathbf{M}]^2 \geq 0 \quad (\text{B.27})$$

for all second order tensors \mathbf{M} (cf. Holzapfel and Ogden [56]). Thus, $\mathcal{T}(I_4^*)$ is convex in \mathbf{C} provided that $\mathcal{T}''(I_4^*) \geq 0$. The second derivative of $\mathcal{T}(I_4^*)$ with respect to I_4^* is

$$\mathcal{T}''(I_4^*) = k_1 \exp[k_2(I_4^* - 1)^2] [1 + 2k_2(I_4^* - 1)^2], \quad (\text{B.28})$$

and for $k_1 > 0$ and $k_2 > 0$, the inequality $\mathcal{T}''(I_4^*) \geq 0$ is fulfilled showing that $\mathcal{T}(I_4^*)$ is a convex function. In fact, $\mathcal{T}(I_4^*)$ is convex both in tension and in compression. However, given that tension-compression switching is necessary to obtain physically reasonable stresses (cf. Fig. 6.2 (a)), it remains to investigate convexity in compression for Case 3, (as all other cases are either zero or do not generate reasonable stresses in compression). We define a function $\mathcal{S}(I_1) := k_1/(2k_2) (\exp[k_2(1/3I_1 - 1)^2])$, which has the relations

$$\frac{\partial \mathcal{S}(I_1)}{\partial \mathbf{C}} = \mathcal{S}'(I_1) \mathbf{I} \quad \text{and} \quad \frac{\partial^2 \mathcal{S}(I_1)}{\partial \mathbf{C} \partial \mathbf{C}} = \mathcal{S}''(I_1) \mathbf{I} \otimes \mathbf{I}, \quad (\text{B.29})$$

where the primes denote differentiation of $\mathcal{S}(I_1)$ with respect to I_1 . Again, local convexity requires that

$$\mathbf{M} : \frac{\partial^2 \mathcal{S}(I_1)}{\partial \mathbf{C} \partial \mathbf{C}} : \mathbf{M} \equiv \mathcal{S}''(I_1) (\text{tr } \mathbf{M})^2 \geq 0, \quad (\text{B.30})$$

for all second order tensors \mathbf{M} , which is fulfilled when $\mathcal{S}''(I_1) \geq 0$. The second derivative of $\mathcal{S}(I_1)$ is

$$\mathcal{S}''(I_1) = k_1 \exp[k_2(1/3I_1 - 1)^2] [1 + 2k_2(1/3I_1 - 1)^2], \quad (\text{B.31})$$

and for $k_1 > 0$ and $k_2 > 0$, the inequality $\mathcal{S}''(I_1) \geq 0$ is fulfilled showing that $\mathcal{S}(I_1)$ is locally convex.

To demonstrate ellipticity in a 3-D general setting is very challenging. Given an incompressible strain-energy function $\hat{\Psi}(I_1, I_4)$, it was shown by Merodio and Ogden [95] (cf. Eq. 2.50 therein), that for 2-D plain strain, ellipticity is fulfilled in terms of the principal stretches λ_1 and λ_2 if

$$\begin{aligned} & 2\hat{\psi}_{11}(\lambda_1^2 - \lambda_2^2)^2 n_1^2 n_2^2 + \hat{\psi}_1(\lambda_1^2 n_1^2 + \lambda_2^2 n_2^2) \\ & + 4\hat{\psi}_{14}(\lambda_1^2 - \lambda_2^2) n_1 n_2 (n_1 a_1 + n_2 a_2)(n_2 a_1 - n_1 a_2) \\ & + 2\hat{\psi}_{44}(n_1 a_1 + n_2 a_2)^2 (n_2 a_1 - n_1 a_2)^2 + \hat{\psi}_4 (n_1 a_1 + n_2 a_2)^2 > 0, \end{aligned} \quad (\text{B.32})$$

where $\hat{\psi}_{ij}$, $i, j \in \{1, 4\}$ are the differentiation of $\hat{\Psi}$ with respect to the invariants I_1 and I_4 , respectively, n_1 and n_2 are the components of a unit vector \mathbf{n} , and a_1 and a_2 are the components of an Eulerian fiber direction vector $\mathbf{a} = \mathbf{F}\mathbf{A}_0$ (see [95] for details). The relation in (B.32) is here separated into three functions that correlate to the differentiation of $\hat{\Psi}$, namely $\mathcal{F}(\hat{\psi}_1, \hat{\psi}_{11}) + \mathcal{G}(\hat{\psi}_{14}) + \mathcal{H}(\hat{\psi}_4, \hat{\psi}_{44}) > 0$.

For an isotropic material, only $\mathcal{F}(\hat{\psi}_1, \hat{\psi}_{11})$ is non-zero and through manipulation of this function, Merodio and Ogden [95] showed that the relations

$$\hat{\psi}_1 > 0, \quad \text{and} \quad 2(I_1 - 3)\hat{\psi}_{11} + \hat{\psi}_1 > 0 \quad (\text{B.33})$$

can be used to show that ellipticity holds for 2-D plain strain. Given that ellipticity holds for isotropy, i.e. $\mathcal{F}(\hat{\psi}_1, \hat{\psi}_{11}) > 0$, and by assuming that I_1 and I_4 are *uncoupled*, they further showed that the fiber reinforcement is elliptic if $\mathcal{H}(\hat{\psi}_4, \hat{\psi}_{44}) > 0$. Again, through manipulation of \mathcal{H} , it became evident that the relations

$$\hat{\psi}_4 \geq 0, \quad \text{and} \quad \hat{\psi}_4 + 2I_4 \hat{\psi}_{44} \geq 0 \quad (\text{B.34})$$

are sufficient conditions to show ellipticity of the fiber reinforcement. It remains to investigate if a similar relation can be found when $\hat{\psi}_{14} \neq 0$, i.e. a *coupled* function (in terms of I_1 and I_4) is used. The relation

$$\mathcal{G}(\hat{\psi}_{14}) = 4\hat{\psi}_{14}(\lambda_1^2 - \lambda_2^2) n_1 n_2 (n_1 a_1 + n_2 a_2)(n_2 a_1 - n_1 a_2) \geq 0 \quad (\text{B.35})$$

must then be fulfilled for all allowable combinations of \mathbf{n} and \mathbf{a} , where the components of \mathbf{n} must obey $n_1^2 + n_2^2 = 1$ (\mathbf{n} is a unit vector). We can relate the deformed fiber direction vector \mathbf{a} to an angle α by $a_1 = \lambda_1 \cos \alpha$ and $a_2 = \lambda_2 \sin \alpha$ and I_4 may now be written as $I_4 = a_1^2 + a_2^2$. Similarly, the components of the surface vector \mathbf{n} are related to an angle β (representing the 2D direction) through components $n_1 = \cos \beta$ and $n_2 = \sin \beta$. From the incompressibility condition, $\lambda_1 \lambda_2 = 1$, the deformations are related by λ if $\lambda_1 = \lambda$ and $\lambda_2 = 1/\lambda$. Simple calculations using two sets of values for α , β and λ show that (B.35) is not easily fulfilled. For example, defining $\bar{\mathcal{G}} := \mathcal{G}(\hat{\psi}_{14})/\hat{\psi}_{14}$ for a shorter notation, with $\alpha = 45^\circ$ and $\beta = 40^\circ$ we have

$$\bar{\mathcal{G}} < 0 \quad \text{if} \quad \lambda = 1.09 \quad (I_4 > 1), \quad (\text{B.36})$$

$$\bar{\mathcal{G}} > 0 \quad \text{if} \quad \lambda = 1.10 \quad (I_4 > 1), \quad (\text{B.37})$$

while for $\alpha = 125^\circ$ and $\beta = 130^\circ$ we have

$$\bar{\mathcal{G}} < 0 \quad \text{if} \quad \lambda = 1.09 \quad (I_4 < 1), \quad (\text{B.38})$$

$$\bar{\mathcal{G}} > 0 \quad \text{if} \quad \lambda = 1.10 \quad (I_4 < 1). \quad (\text{B.39})$$

A coupled strain-energy function has to meet the requirement that $\mathcal{G}(\hat{\psi}_{14}) \geq 0$ for all deformation modes while the sign of $\bar{\mathcal{G}}$ varies, independent of whether $I_4 > 1$ or $I_4 < 1$, i.e. $\hat{\psi}_{14}$ has to change sign (seemingly) arbitrarily, and independent of the stretch in the fiber direction. Considering the difficulty in constructing such a strain-energy function, it is likely impossible in most (if not all) *coupled* models to guarantee ellipticity either for tension or compression in 2-D plain strain. For example, defining $\hat{\Psi}(I_1, I_4) := (6.6)_1$, the combined second derivative is

$$\hat{\psi}_{14} = k_1 \kappa (1 - 3\kappa) \exp[k_2(I_4^* - 1)^2][1 + 2k_2(I_4^* - 1)^2], \quad (\text{B.40})$$

which is ≥ 0 for all deformation modes, thus showing that (B.35) can not be fulfilled.

REFERENCES

- [1] D. Ambrosi and S. Pezzuto. Active stress vs. active strain in mechanobiology: Constitutive issues. *J. Elast.*, 107:199–212, 2012.
- [2] T. Ashihara, J. Constantino, and N. A. Trayanova. Tunnel propagation of postshock activations as a hypothesis for fibrillation induction and isoelectric window. *Circ. Res.*, 102:737–745, 2008.
- [3] H. Ashikaga, B. A. Coppola, K. G. Yamazaki, F. J. Villarreal, J. H. Omens, and J. W. Covell. Changes in regional myocardial volume during the cardiac cycle: implications for transmural blood flow and cardiac structure. *Am. J. Physiol. Heart Circ. Physiol.*, 295:H610–H618, 2008.
- [4] H. Ashikaga, J. H. Omens, N. B. Ingels, and J. W. Covell. Transmural mechanics at left ventricular epicardial pacing site. *Am. J. Physiol. Heart Circ. Physiol.*, 286:H2401–H2407, 2004.
- [5] G. A. Ateshian, V. Rajan, N. O. Chahine, C. E. Canal, and C. T. Hung. Modeling the matrix of articular cartilage using a continuous fiber angular distribution predicts many observed phenomena. *J. Biomech. Eng.*, 131:61003, 2009.
- [6] G. Austin, S. Fisher, D. Dickson, D. Anderson, and S. Richardson. The significance of the extracellular matrix in intracranial aneurysms. *Ann. Clin. Lab. Sci.*, 23:97–105, 1993.
- [7] S. Baek, K. R. Rajagopal, and J. D. Humphrey. A theoretical model of enlarging intracranial fusiform aneurysms. *J. Biomech. Eng.*, 128:142–149, 2006.
- [8] S. Balay, J. Brown, K. Buschelman, V. Eijkhout, W. D. Gropp, D. Kaushik, M. G. Knepley, L. Curfman McInnes, B. F. Smith, and H. Zhang. PETSc users manual. Technical report, Argonne National Laboratory, 2010.
- [9] D. M. Bers. Cardiac excitation-contraction coupling. *Nature*, 415:198–205, 2002.
- [10] M. J. Bishop and G. Plank. Representing cardiac bidomain bath-loading effects by an augmented monodomain approach: application to complex ventricular models. *IEEE T. Biomed. Eng.*, 58:1066–1075, 2011.

- [11] M. J. Bishop, G. Plank, R. A. Burton, J. E. Schneider, D. J. Gavaghan, V. Grau, and P. Kohl. Development of an anatomically detailed MRI-derived rabbit ventricular model and assessment of its impact on simulations of electrophysiological function. *Am. J. Physiol. Heart Circ. Physiol.*, 298:H699–H718, 2010.
- [12] B. J. Caldwell, M. L. Trew, G. B. Sands, D. A. Hooks, I. J. LeGrice, and B. H. Smaill. Three distinct directions of intramural activation reveal nonuniform side-to-side electrical coupling of ventricular myocytes. *Circ. Arrhythm. Electrophysiol.*, 2:433–440, 2009.
- [13] P. B. Canham, R. M. Korol, H. M. Finlay, R. R. Hammond, D. W. Holdsworth, G. G. Ferguson, and A. R. Lucas. Collagen organization and biomechanics of the arteries and aneurysms of the human brain. In G. A. Holzapfel and R. W. Ogden, editors, *Mechanics of Biological Tissue*, pages 307–322, Heidelberg, 2006. Springer-Verlag.
- [14] P. B. Canham, E. A. Talman, H. M. Finlay, and J. G. Dixon. Medial collagen organization in human arteries of the heart and brain by polarized light microscopy. *Connect. Tissue Res.*, 26:121–134, 1991.
- [15] S. Carasso, H. Yang, A. Woo, M. A. Vannan, M. Jamorski, E. D. Wigle, and H. Rakowski. Systolic myocardial mechanics in hypertrophic cardiomyopathy: novel concepts and implications for clinical status. *J. Am. Soc. Echocardiogr.*, 21:675–683, 2008.
- [16] F. Carreras, J. Garcia-Barnes, D. Gil, S. Pujadas, C. H. Li, R. Suarez-Arias, R. Leta, X. Alomar, M. Ballester, and G. Pons-Llado. Left ventricular torsion and longitudinal shortening: two fundamental components of myocardial mechanics assessed by tagged cine-MRI in normal subjects. *Int. J. Cardiovasc. Imaging*, 16:1–12, 2011.
- [17] I. Chatziprodromou, A. Tricoli, D. Poulidakos, and Y. Ventikos. Haemodynamics and wall remodelling of a growing cerebral aneurysm: a computational model. *J. Biomech.*, 40:412–426, 2007.
- [18] A. Cheng, T. C. Nguyen, M. Malinowski, G. T. Daughters, D. C. Miller, and N. B. Ingels Jr. Heterogeneity of left ventricular wall thickening mechanisms. *Circulation*, 118:713–721, 2008.
- [19] C. J. Chuong and Y. C. Fung. Three-dimensional stress distribution in arteries. *J. Biomech. Eng.*, 105:268–274, 1983.
- [20] R. H. Clayton, O. Bernus, E. M. Cherry, H. Dierckx, F. H. Fenton, L. Mirabella, A. V. Panfilov, F. B. Sachse, G. Seemann, and H. Zhang. Models of cardiac tissue electrophysiology: progress, challenges and open questions. *Prog. Biophys. Mol. Biol.*, 104:22–48, 2011.
- [21] B. A. Coppola and J. H. Omens. Role of tissue structure on ventricular wall mechanics. *Mech. Chem. Biosyst.*, 5:183–196, 2008.

- [22] K. D. Costa, J. W. Holmes, and A. D. McCulloch. Modeling cardiac mechanical properties in three dimensions. *Philos. T. Roy. Soc. A*, 359:1233–1250, 2001.
- [23] K. D. Costa, P. J. Hunter, J. M. Rogers, J. M. Guccione, L. K. Waldman, and A. D. McCulloch. A three-dimensional finite element method for large elastic deformations of ventricular myocardium: I–Cylindrical and spherical polar coordinates. *J. Biomech. Eng.*, 118:542–463, 1996.
- [24] K. D. Costa, P. J. Hunter, J. S. Wayne, L. K. Waldman, J. M. Guccione, and A. D. McCulloch. A three-dimensional finite element method for large elastic deformations of ventricular myocardium: II–Prolate spheroidal coordinates. *J. Biomech. Eng.*, 118:464–472, 1996.
- [25] K. D. Costa, K. May-Newman, D. Farr, W. G. O’Dell, A. D. McCulloch, and J. H. Omens. Three-dimensional residual strain in midanterior canine left ventricle. *Am. J. Physiol.*, 273:H1968–H1976, 1997.
- [26] K. D. Costa, Y. Takayama, A. D. McCulloch, and J. W. Covell. Laminar fiber architecture and three-dimensional systolic mechanics in canine ventricular myocardium. *Am. J. Physiol.*, 276:H595–H607, 1999.
- [27] R. J. Coulson, M. J. Cipolla, L. Vitullo, and N. C. Chesler. Mechanical properties of rat middle cerebral arteries with and without myogenic tone. *J. Biomech. Eng.*, 126:76–81, 2004.
- [28] J. W. Covell. Tissue structure and ventricular wall mechanics. *Circulation*, 118:699–701, 2008.
- [29] A. B. C. Dang, J. M. Guccione, P. Zhang, A. W. Wallace, R. C. Gorman, J. H. Gorman, 3rd, and M. B. Ratcliffe. Effect of ventricular size and patch stiffness in surgical anterior ventricular restoration: a finite element model study. *Ann. Thorac. Surg.*, 79:185–193, 2005.
- [30] L. L. Demer and F. C. P. Yin. Passive biaxial mechanical properties of isolated canine myocardium. *J. Physiol. London*, 339:615–630, 1983.
- [31] M. Deo, P. Boyle, G. Plank, and E. Vigmond. Arrhythmogenic mechanisms of the purkinje system during electric shocks: a modeling study. *Heart. Rhythm.*, 6:1782–1789, 2009.
- [32] S. Dokos, B. H. Smaill, A. A. Young, and I. J. LeGrice. Shear properties of passive ventricular myocardium. *Am. J. Physiol.*, 283:H2650–H2659, 2002.
- [33] S. J. Dong, J. H. MacGregor, A. P. Crawley, E. McVeigh, I. Belenkie, E. R. Smith, J. V. Tyberg, and R. Beyar. Left ventricular wall thickness and regional systolic function in patients with hypertrophic cardiomyopathy. A three-dimensional tagged magnetic resonance imaging study. *Circulation*, 90:1200–1209, 1994.

-
- [34] N. J. B. Driessen, W. Wilson, C. V. C. Bouten, and F. P. T. Baaijens. A computational model for collagen fibre remodelling in the arterial wall. *J. Theor. Biol.*, 226:53–64, 2004.
- [35] T. S. E. Eriksson, G. Plank, and G. A. Holzapfel. Tensors needed for finite element implementation of an invariant based constitutive model for passive myocardium, submitted.
- [36] T.S.E. Eriksson, A. J. Prassl, G. Plank, and G.A. Holzapfel. Influence of spatial heterogeneity in tissue orthotropy upon mechanical contraction in the left ventricle, submitted.
- [37] T.S.E. Eriksson, A.J. Prassl, G. Plank, and G.A. Holzapfel. Modeling the disarray in cardiac fiber and sheet orientations, submitted.
- [38] S. Federico and T. C. Gasser. Nonlinear elasticity of biological tissues with statistical fibre orientation. *J. R. Soc. Interface*, 7:955–966, 2010.
- [39] F. Fenton and A. Karma. Vortex dynamics in three-dimensional continuous myocardium with fiber rotation: Filament instability and fibrillation. *Chaos*, 8:20–47, 1998.
- [40] H. M. Finlay, L. McCullough, and P. B. Canham. Three-dimensional collagen organization of human brain arteries at different transmural pressures. *J. Vasc. Res.*, 32:301–312, 1995.
- [41] R. Fitzhugh. Impulses and physiological states in theoretical models of nerve membrane. *Biophys. J.*, 1:445–466, 1961.
- [42] A. D. Freed, D. R. Einstein, and I. Vesely. Invariant formulation for dispersed transverse isotropy in aortic heart valves: An efficient means for modeling fiber splay. *Biomech. Model. Mechanobiol.*, 4:100–117, 2005.
- [43] Y. C. Fung. Mathematical representation of the mechanical properties of the heart muscle. *J. Biomech.*, 269:441–515, 1970.
- [44] Y. C. Fung, K. Fronek, and P. Patitucci. Pseudoelasticity of arteries and the choice of its mathematical expression. *Am. J. Physiol.*, 237:H620–H631, 1979.
- [45] W. H. Gaasch, M. R. Zile, P. K. Hoshino, C. S. Apstein, and A. S. Blaustein. Stress–shortening relations and myocardial blood flow in compensated and failing canine hearts with pressure–overload hypertrophy. *Circulation*, 79:872–883, 1989.
- [46] A. M. Gallagher, J. H. Omens, L. L. Chu, and J. W. Covell. Alterations in collagen fibrillar structure and mechanical properties of the healing scar following myocardial infarction. *Cardiovasc. Pathol.*, 2:25–36, 1997.

-
- [47] T. C. Gasser, R. W. Ogden, and G. A. Holzapfel. Hyperelastic modelling of arterial layers with distributed collagen fibre orientations. *J. R. Soc. Interface*, 3:15–35, 2006.
- [48] H. Ghaemi, K. Behdinan, and A. D. Spence. In vitro technique in estimation of passive mechanical properties of bovine heart part I. Experimental techniques and data. *Med. Eng. Phys.*, 31:76–82, 2009.
- [49] S. Göktepe and E. Kuhl. Electromechanics of the heart: a unified approach to the strongly coupled excitation-contraction problem. *Comput. Mech.*, 45:227–243, 2010.
- [50] V. Gurev, J. Constantino, J. J. Rice, and N. A. Trayanova. Distribution of electromechanical delay in the heart: insights from a three-dimensional electromechanical model. *Biophys. J.*, 99:745–754, 2010.
- [51] P. A. Harvey and L. A. Leinwand. The cell biology of disease: cellular mechanisms of cardiomyopathy. *J. Cell. Biol.*, 194:355–365, 2011.
- [52] A. L. Hodgkin and A. F. Huxley. A quantitative description of membrane current and its application to conduction and excitation in nerve. *J. Physiol.*, 117:500–544, 1952.
- [53] G. A. Holzapfel. *Nonlinear Solid Mechanics. A Continuum Approach for Engineering*. John Wiley & Sons, Chichester, 2000.
- [54] G. A. Holzapfel, T. C. Gasser, and R. W. Ogden. A new constitutive framework for arterial wall mechanics and a comparative study of material models. *J. Elasticity*, 61:1–48, 2000.
- [55] G. A. Holzapfel, T. C. Gasser, and M. Stadler. A structural model for the viscoelastic behavior of arterial walls: Continuum formulation and finite element analysis. *Eur. J. Mech. A/Solids*, 21:441–463, 2002.
- [56] G. A. Holzapfel and R. W. Ogden. Constitutive modelling of passive myocardium: a structurally based framework for material characterization. *Philos. T. Roy. Soc. A*, 367:3445–3475, 2009.
- [57] G. A. Holzapfel and R. W. Ogden. Constitutive modelling of arteries. *Proc. R. Soc. Lond. A*, 466:1551–1597, 2010.
- [58] G. A. Holzapfel, G. Sommer, M. Auer, P. Regitnig, and R. W. Ogden. Layer-specific 3D residual deformations of human aortas with non-atherosclerotic intimal thickening. *Ann. Biomed. Eng.*, 35:530–545, 2007.

- [59] G. A. Holzapfel, G. Sommer, C. T. Gasser, and P. Regitnig. Determination of the layer-specific mechanical properties of human coronary arteries with non-atherosclerotic intimal thickening, and related constitutive modelling. *Am. J. Physiol. Heart Circ. Physiol.*, 289:H2048–2058, 2005.
- [60] G. A. Holzapfel, G. Sommer, and P. Regitnig. Anisotropic mechanical properties of tissue components in human atherosclerotic plaques. *J. Biomech. Eng.*, 126:657–665, 2004.
- [61] G. A. Holzapfel, M. Stadler, and T. C. Gasser. Changes in the mechanical environment of stenotic arteries during interaction with stents: Computational assessment of parametric stent design. *J. Biomech. Eng.*, 127:166–180, 2005.
- [62] D. A. Hooks, M. L. Trew, B. J. Caldwell, G. B. Sands, I. J. LeGrice, and B. H. Smaill. Laminar arrangement of ventricular myocytes influences electrical behavior of the heart. *Circ. Res.*, 101:e103–e112, 2007.
- [63] W. Hort. Untersuchungen über die Muskelfaserdehnung und das Gefüge des Myokards in der rechten Herzkammerwand des Meerschweinchens. *Virchows Arch*, 329:694–731, 1957.
- [64] J. D. Humphrey. *Cardiovascular Solid Mechanics. Cells, Tissues, and Organs*. Springer-Verlag, New York, 2002.
- [65] J. D. Humphrey and K. R. Rajagopal. A constrained mixture model for growth and remodeling of soft tissues. *Math. Model. Meth. Appl. Sci.*, 12:407–430, 2002.
- [66] P. J. Hunter. Proceedings: Development of a mathematical model of the left ventricle. *J. Physiol.*, 241:87P–88P, 1974.
- [67] P. J. Hunter, M. P. Nash, and G. B. Sands. Computational electromechanics of the heart. In A. V. Panfilov and A. V. Holden, editors, *Computational Biology of the Heart*, pages 345–407, Chichester, 1997. John Wiley & Sons.
- [68] P. J. Hunter, B. H. Smaill, P. M. F. Nielsen, and I. J. LeGrice. A mathematical model of cardiac anatomy. In A. V. Panfilov and A. V. Holden, editors, *Computational Biology of the Heart*, pages 171–215, Chichester, 1997. John Wiley & Sons.
- [69] C. S. Jhun, J. F. Wenk, Z. Zhang, S. T. Wall, K. Sun, H. N. Sabbah, M. B. Ratcliffe, and J. M. Guccione. Effect of adjustable passive constraint on the failing left ventricle: A finite element model study. *Ann. Thorac Surg.*, 89:132–137, 2010.
- [70] S. Juvela, M. Porras, and K. Poussa. Natural history of unruptured intracranial aneurysms: probability and risk factors for aneurysm rupture. *J. Neurosurg.*, 93:379–387, 2000.

- [71] W. J. Karlon, J. W. Covell, A. D. McCulloch, J. J. Hunter, and J. H. Omens. Automated measurement of myofiber disarray in transgenic mice with ventricular expression of ras. *Anat. Rec.*, 252:612–625, 1998.
- [72] W. J. Karlon, A. D. McCulloch, J. W. Covell, J. J. Hunter, and J. H. Omens. Regional dysfunction correlates with myofiber disarray in transgenic mice with ventricular expression of ras. *Am. J. Physiol. Heart Circ. Physiol.*, 278:H898–906, 2000.
- [73] G. Karypis, K. Schloegel, and V. Kumar. *ParMETIS: Parallel Graph Partitioning and Sparse Matrix Ordering Library*. University of Minnesota, Minneapolis, MN, Version 3.1, 2003. URL <http://glaros.dtc.umn.edu/gkhome/metis/parmetis/overview>.
- [74] G. S. Kassab. Y.C. "Bert" Fung: the father of modern biomechanics. *Mech. Chem. Biosyst.*, 1:5–22, 2004.
- [75] R. H. Keldermann, M. P. Nash, and A. V. Panfilov. Modeling cardiac mechano-electrical feedback using reaction-diffusion-mechanics systems. *Physica D: Non-linear Phenomena*, 238:1000–1007, 2009.
- [76] R. Kerckhoffs, M. Neal, Q. Gu, J. Bassingthwaighte, J. Omens, and A. McCulloch. Coupling of a 3d finite element model of cardiac ventricular mechanics to lumped systems models of the systemic and pulmonic circulation. *Ann. Biomed. Eng.*, 35:1–18, 2007.
- [77] R. C. P. Kerckhoffs, P. H. M. Bovendeerd, J. C. S. Kotte, F. W. Prinzen, K. Smits, and T. Arts. Homogeneity of cardiac contraction despite physiological asynchrony of depolarization: A model study. *Ann. Biomed. Eng.*, 31:536–547, 2003.
- [78] R. C. P. Kerckhoffs, O. P. Faris, P. H. M. Bovendeerd, F. W. Prinzen, K. Smits, E. R. McVeigh, and T. Arts. Timing of depolarization and contraction in the paced canine left ventricle: model and experiment. *J. Cardiovasc. Electrophysiol.*, 14:S188–S195, 2003.
- [79] R. C. P. Kerckhoffs, O. P. Faris, P. H. M. Bovendeerd, F. W. Prinzen, K. Smits, E. R. McVeigh, and T. Arts. Electromechanics of paced left ventricle simulated by straightforward mathematical model: comparison with experiments. *Am. J. Physiol. Heart. Circ. Physiol.*, 289:H1889–H1897, 2005.
- [80] R. C. P. Kerckhoffs, S. N. Healy, T. P. Usyk, and A. D. McCulloch. Computation methods for cardiac electromechanics. *Proc. IEEE*, 94:769–783, 2006.
- [81] C. Kim and J. Cervos-Navarro. Spontaneous saccular cerebral aneurysm in a rat. *Acta Neurochir.*, 109:63–65, 1991.
- [82] M. Kroon and G. A. Holzapfel. A model for saccular cerebral aneurysm growth by collagen fibre remodelling. *J. Theor. Biol.*, 247:775–787, 2007.

- [83] M. Kroon and G. A. Holzapfel. Modeling of saccular aneurysm growth in a human middle cerebral artery. *J. Biomech. Eng.*, 130:051012, 2008.
- [84] Y. Lanir. Constitutive equations for fibrous connective tissues. *J. Biomech.*, 16:1–12, 1983.
- [85] I. J. LeGrice, B. H. Smaill, L. Z. Chai, S. G. Edgar, J. B. Gavin, and P. J. Hunter. Laminar structure of the heart: Ventricular myocyte arrangement and connective tissue architecture in the dog. *Am. J. Physiol. Heart Circ. Physiol.*, 269:H571–H582, 1995.
- [86] I. J. LeGrice, Y. Takayama, and J. W. Covell. Transverse shear along myocardial cleavage planes provides a mechanism for normal systolic wall thickening. *Circ. Res.*, 77:182–193, 1995.
- [87] D. H. Lin and F. C. Yin. A multiaxial constitutive law for mammalian left ventricular myocardium in steady-state barium contracture or tetanus. *J. Biomech. Eng.*, 120:504–517, 1998.
- [88] S. Q. Liu and Y. C. Fung. Change of residual strains in arteries due to hypertrophy caused by aortic constriction. *Circ. Res.*, 65:1340–1349, 1989.
- [89] M. C. Maclachlan, J. Sundnes, and R. J. Spiteri. A comparison of non-standard solvers for ODEs describing cellular reactions in the heart. *Comput. Methods Biomech. Biomed. Engin.*, 10:317–326, 2007.
- [90] D. J. MacDonald, H. M. Finlay, and P. B. Canham. Directional wall strength in saccular brain aneurysms from polarized light microscopy. *Ann. Biomed. Eng.*, 28:533–542, 2000.
- [91] A. Mahajan, Y. Shiferaw, D. Sato, A. Baher, R. Olcese, L. H. Xie, M. J. Yang, P. S. Chen, J. G. Restrepo, A. Karma, A. Garfinkel, Z. Qu, and J. N. Weiss. A rabbit ventricular action potential model replicating cardiac dynamics at rapid heart rates. *Biophys. J.*, 94:392–410, 2008.
- [92] P. Colli Franzone, L. F. Pavarino, and B. Taccardi. Simulating patterns of excitation, repolarization and action potential duration with cardiac bidomain and monodomain models. *Math. Biosci.*, 197:35–66, 2005.
- [93] D. D. Streeter, Jr., H. M. Spotnitz, D. P. Patel, J. Ross, Jr., and E. H. Sonnenblick. Fibre orientation in the canine left ventricle during diastole and systole. *Circ. Res.*, 24:339–347, 1969.
- [94] A. D. McCulloch. Cardiac biomechanics. In D. R. Peterson and J. D. Bronzino, editors, *Biomechanics: Principles and Applications*, pages 1–20. CRC Press, Boca Raton, Florida, 2nd edition, 2007. Chapter 8.

- [95] J. Merodio and R. W. Ogden. Material instabilities in fiber-reinforced nonlinearly elastic solids under plane deformation. *Arch. Mech.*, 54:525–552, 2002.
- [96] I. Mirsky. Ventricular and arterial wall stresses based on large deformation analyses. *Biophys. J.*, 13:1141–1159, 1973.
- [97] M. M. Monasky, K. D. Varian, J. P. Davis, and P. M. Janssen. Dissociation of force decline from calcium decline by preload in isolated rabbit myocardium. *Pflügers Arch. – Eur. J. Physiol.*, 456:267–276, 2008.
- [98] K. L. Monson, W. Goldsmith, N. M. Barbaro, and G. T. Manley. Axial mechanical properties of fresh human cerebral blood vessels. *J. Biomech. Eng.*, 125:288–294, 2003.
- [99] K. L. Monson, W. Goldsmith, N. M. Barbaro, and G. T. Manley. Significance of source and size in the mechanical response of human cerebral blood vessels. *J. Biomech.*, 38:737–744, 2005.
- [100] P. Nardinocchi and L. Teresi. On the active response of soft living tissues. *J. Elasticity.*, 88:27–39, 2007.
- [101] NASA. "How much does it cost to launch a space shuttle?". http://www.nasa.gov/centers/kennedy/about/information/shuttle_faq.html\#10, April 2012.
- [102] M. P. Nash and P. J. Hunter. Computational mechanics of the heart. *J. Elasticity*, 61:113–141, 2000.
- [103] M. P. Nash and A. V. Panfilov. Electromechanical model of excitable tissue to study reentrant cardiac arrhythmias. *Prog. Biophys. Mol. Biol.*, 85:501–522, 2004.
- [104] D. Nickerson, N. Smith, and P. Hunter. New development in a strongly coupled cardiac electromechanical model. *Eurospace*, 7:S118–S127, 2005.
- [105] S. Niederer, L. Mitchell, N. Smith, and G. Plank. Simulating a human heart beat with near-real time performance. *Front. Physio.*, 2:1–7, 2011.
- [106] S. A. Niederer, G. Plank, P. Chinchapatnam, M. Ginks, P. Lamata, K. S. Rhode, C. A. Rinaldi, R. Razavi, and N. P. Smith. Length-dependent tension in the failing heart and the efficacy of cardiac resynchronization therapy. *Cardiovasc. Res.*, 89:336–343, 2011.
- [107] S. A. Niederer and N. P. Smith. An improved numerical method for strong coupling of excitation and contraction models in the heart. *Prog. Biophys. Mol. Biol.*, 96:90–111, 2008.

- [108] S. A. Niederer and N. P. Smith. The role of the Frank-Starling law in the transduction of cellular work to whole organ pump function: a computational modeling analysis. *PLoS Comput. Biol.*, 5:e1000371, 2009.
- [109] B. F. Nielsen, T. S. Ruud, G. T. Lines, and A. Tveito. Optimal monodomain approximations of the bidomain equations. *Appl. Math. Comput.*, 184:276–290, 2007.
- [110] P. M. F. Nielsen, I. J. LeGrice, B. H. Smaill, and P. J. Hunter. Mathematical model of geometry and fibrous structure of the heart. *Am. J. Physiol. Cell Physiol.*, 260:H1365–H1378, 1991.
- [111] D. A. Nordsletten, S. A. Niederer, M. P. Nash, P. J. Hunter, and N. P. Smith. Coupling multi-physics models to cardiac mechanics. *Prog. Biophys. Mol. Biol.*, 104:77–88, 2011.
- [112] Y. Notomi, P. Lysyansky, R. M. Setser, T. Shiota, Z. B. Popović, M. G. Martin-Miklovic, J. A. Weaver, S. J. Oryszak, N. L. Greenberg, R. D. White, and J. D. Thomas. Measurement of ventricular torsion by two-dimensional ultrasound speckle tracking imaging. *J. Am. Coll. Cardiol.*, 45:2034–2041, 2005.
- [113] J. H. Omens, D. A. MacKenna, and A. D. McCulloch. Measurement of strain and analysis of stress in resting rat left ventricular myocardium. *J. Biomech.*, 26:665–676, 1993.
- [114] J. H. Omens, T. P. Usyk, Z. Li, and A. D. McCulloch. Muscle LIM protein deficiency leads to alterations in passive ventricular mechanics. *Am. J. Physiol. Heart. Circ. Physiol.*, 282:H680–H687, 2002.
- [115] A. Opdahl, T. Helle-Valle, E. W. Remme, T. Vartdal, E. Pettersen, K. Lunde, T. Edvardsen, and O. A. Smiseth. Apical rotation by speckle tracking echocardiography: a simplified bedside index of left ventricular twist. *J. Am. Soc. Echocardiogr.*, 21:1121–1128, 2008.
- [116] F. Otto. Die Grundform des arteriellen Pulses. *Z. Bio.*, 37:483–586, 1899.
- [117] A. V. Panfilov, R. H. Keldermann, and M. P. Nash. Drift and breakup of spiral waves in reaction-diffusion-mechanics systems. *Proc. Natl. Acad. Sci. U. S. A.*, 104:7922–7926, 2007.
- [118] J. Parkinson, A. Brass, G. Canova, and Y. Brechet. The mechanical properties of simulated collagen fibrils. *J. Biomech.*, 30:549–554, 1997.
- [119] P. Pathmanathan, S. J. Chapman, D. J. Gavaghan, and J. P. Whiteley. Cardiac electromechanics: The effect of contraction model on the mathematical problem and accuracy of the numerical scheme. *Quart. J. Mech. Appl. Math.*, 63:375–399, 2010.
- [120] P. Pathmanathan and J. P. Whiteley. A numerical method for cardiac mechanoelectric simulations. *Ann. Biomed. Eng.*, 437:860–876, 2009.

- [121] D. M. Pierce, T. Ricken, and G. A. Holzapfel. A hyperelastic biphasic fiber-reinforced model of articular cartilage considering distributed collagen fiber orientations: continuum basis, computational aspects and applications. *Comput. Methods Biomech. Biomed. Engin.*, in press.
- [122] D. M. Pierce, W. Trobin, J. G. Raya, S. Trattnig, H. Bischof, Ch. Glaser, and G. A. Holzapfel. DT-MRI based computation of collagen fiber deformation in human articular cartilage: a feasibility study. *Ann. Biomed. Eng.*, 38:2447–2463, 2010.
- [123] D. M. Pierce, W. Trobin, S. Trattnig, H. Bischof, and G. A. Holzapfel. A phenomenological approach toward patient-specific computational modeling of articular cartilage including collagen fiber tracking. *J. Biomech. Eng.*, 131:091006, 2009.
- [124] G. Plank, R. A. Burton, P. Hales, M. Bishop, T. Mansoori, M. O. Bernabeu, A. Garny, A. J. Prassl, C. Bollensdorff, F. Mason, F. Mahmood, B. Rodriguez, V. Grau, J. E. Schneider, D. Gavaghan, and P. Kohl. Generation of histologically representative models of the individual heart: tools and application. *Philos. Transact. A Math. Phys. Eng. Sci.*, 367:2257–2292, 2009.
- [125] G. Plank, L. Zhou, J. L. Greenstein, S. Cortassa, R. L. Winslow, B. O’Rourke, and N. A. Trayanova. From mitochondrial ion channels to arrhythmias in the heart: computational techniques to bridge the spatio-temporal scales. *Philos. Transact. A Math. Phys. Eng. Sci.*, 366:3381–3409, 2008.
- [126] A. J. Pope, G. B. Sands, B. H. Smaill, and I. J. LeGrice. Three-dimensional transmural organization of perimysial collagen in the heart. *Am. J. Physiol. Heart Circ. Physiol.*, 295:H1243–H1252, 2008.
- [127] A. J. Prassl, F. Kicking, H. Ahammer, V. Grau, J. E. Schneider, E. Hofer, E. J. Vigmond, N. A. Trayanova, and G. Plank. Automatically generated, anatomically accurate meshes for cardiac electrophysiology problems. *IEEE T. Biomed. Eng.*, 56:1318–1330, 2009.
- [128] J. Provost, V. Gurev, N. Trayanova, and E. E. Konofagou. Mapping of cardiac electrical activation with electromechanical wave imaging: An in silico-in vivo reciprocity study. *Heart Rhythm.*, 8:752–759, 2011.
- [129] Z. Qu and A. Garfinkel. An advanced algorithm for solving partial differential equation in cardiac conduction. *IEEE T. Biomed. Eng.*, 46:1166–1168, 1999.
- [130] C. M. Quick, D. S. Berger, and A. Noordergraaf. Apparent arterial compliance. *Am. J. Physiol.*, 274:H1393–H1403, 1998.
- [131] R. Raamat, J. Talts, and K. Jagomägi. Application of amplitude-based and slope-based algorithms to determine beat-to-beat finger arterial compliance during hand-grip exercise. *Med. Eng. Phys.*, 30:67–74, 2008.

- [132] M. Rayner, S. Allender, P. Scarborough, and British Heart Foundation Health Promotion Research Group. Cardiovascular disease in europe. *Eur. J. Cardiovasc. Prev. Rehabil.*, 16 Suppl 2:S43–S47, 2009.
- [133] B. M. Rocha, F. Kicking, A. J. Prassl, G. Haase, E. J. Vigmond, R. Weber dos Santos, S. Zaglmayr, and G. Plank. A macro finite-element formulation for cardiac electrophysiology simulations using hybrid unstructured grids. *IEEE T. Biomed. Eng.*, 58:1055–1065, 2011.
- [134] V. L. Roger, A. S. Go, D. M. Lloyd-Jones, E. J. Benjamin, J. D. Berry, W. B. Borden, D. M. Bravata, S. Dai, E. S. Ford, C. S. Fox, H. J. Fullerton, C. Gillespie, S. M. Hailpern, J. A. Heit, V. J. Howard, B. M. Kissela, S. J. Kittner, D. T. Lackland, J. H. Lichtman, L. D. Lisabeth, D. M. Makuc, G. M. Marcus, A. Marelli, D. B. Matchar, C. S. Moy, D. Mozaffarian, M. E. Mussolino, G. Nichol, Ni. P. Paynter, E. Z. Soliman, P. D. Sorlie, N. Sotoodehnia, T. N. Turan, S. S. Virani, N. D. Wong, D. Woo, M. B. Turner, and American Heart Association Statistics Committee and Stroke Statistics Subcommittee. Executive summary: heart disease and stroke statistics–2012 update: a report from the american heart association. *Circulation*, 125:188–197, 2012.
- [135] D. Rohmer, A. Sitek, and G. T. Gullberg. Reconstruction and visualization of fiber and laminar structure in the normal human heart from ex vivo diffusion tensor magnetic resonance imaging (DTMRI) data. *Investigative Radiology*, 42:777–789, 2007.
- [136] D. Romero, R. Sebastian, B. H. Bijmens, V. Zimmerman, P. M. Boyle, E. J. Vigmond, and A. F. Frangi. Effects of the Purkinje system and cardiac geometry on biventricular pacing: a model study. *Ann. Biomed. Eng.*, 38:1388–1398, 2010.
- [137] S. Rossi, R. Ruiz-Baier, L. F. Pavarino, and A. Quarteroni. Orthotropic active strain models for the numerical simulation of cardiac biomechanics. *Int. J. Numer. Method. Biomed. Eng.*, 2012. doi: 10.1002/cnm.2473.
- [138] B. J. Roth. Electrical conductivity values used with the bidomain model of cardiac tissue. *IEEE Trans Biomed Eng*, 44:326–8, 1997.
- [139] A. J. Rowe, H. M. Finlay, and P. B. Canham. Collagen biomechanics in cerebral arteries and bifurcations assessed by polarizing microscopy. *J. Vasc. Res.*, 40:406–415, 2003.
- [140] C. F. Royse and A. G. Royse. The myocardial and vascular effects of bupivacaine, levobupivacaine, and ropivacaine using pressure volume loops. *Anesth. Analg.*, 101:679–687, 2005.
- [141] S. Rush and H. Larsen. A practical algorithm for solving dynamic membrane equations. *IEEE T. Biomed. Eng.*, 25:389–392, 1978.

- [142] G. B. Sands, D. A. Gerneke, D. A. Hooks, C. R. Green, B. H. Smaill, and I. J. LeGrice. Automated imaging of extended tissue volumes using confocal microscopy. *Microsc. Res. Tech.*, 67:227–239, 2005.
- [143] G. B. Sands, B. H. Smaill, and I. J. LeGrice. Virtual sectioning of cardiac tissue relative to fiber orientation. In *Proc. 30th Annual Int. Conf. of the IEEE Engineering in Medicine and Biology Society EMBS 2008*, pages 226–229, 2008.
- [144] T. Sano, N. Takayama, and T. Shimamoto. Directional difference of conduction velocity in the cardiac ventricular syncytium studied by microelectrodes. *Circ. Res.*, 7:262–267, 1959.
- [145] W. I. Schievink. Intracranial aneurysms. *N. Engl. J. Med.*, 336:28–40, 1997.
- [146] H. Schmid, M. P. Nash, A. A. Young, and P. J. Hunter. Myocardial material parameter estimation—a comparative study for simple shear. *J. Biomech. Eng.*, 128:742–750, 2006.
- [147] H. Schmid, P. O’Callaghan, M. P. Nash, W. Lin, I. J. LeGrice, B. H. Smaill, A. A. Young, and P. J. Hunter. Myocardial material parameter estimation: a non-homogeneous finite element study from simple shear tests. *Biomech. Model. Mechanobiol.*, 7:161–173, 2008.
- [148] H. Schmid, Y. K. Wang, J. Ashton, A. E. Ehret, S. B. S. Krittian, M. P. Nash, and P. J. Hunter. Myocardial material parameter estimation: a comparison of invariant based orthotropic constitutive equations. *Comput. Methods Biomech. Biomed. Engin.*, 12:283–295, 2009.
- [149] C. A. J. Schulze-Bauer, C. Mörth, and G. A. Holzapfel. Passive biaxial mechanical response of aged human iliac arteries. *J. Biomech. Eng.*, 125:395–406, 2003.
- [150] C. A. J. Schulze-Bauer, P. Regitnig, and G. A. Holzapfel. Mechanics of the human femoral adventitia including high-pressure response. *Am. J. Physiol. Heart Circ. Physiol.*, 282:H2427–H2440, 2002.
- [151] K. Shinmura, X. L. Tang, Y. Wang, Y. T. Xuan, S. Q. Liu, H. Takano, A. Bhatnagar, and R. Bolli. Cyclooxygenase-2 mediates the cardioprotective effects of the late phase of ischemic preconditioning in conscious rabbits. *PNAS*, 97:10197–10202, 2000.
- [152] B. Skallerud, V. Prot, and I. S. Nordrum. Modeling active muscle contraction in mitral valve leaflets during systole: a first approach. *Biomech. Model. Mechanobiol.*, 10:11–26, 2011.
- [153] J. F. H. Smith, P. B. Canham, and J. Starkey. Orientation of collagen in the tunica adventitia of the human cerebral artery measured with polarized light and the universal stage. *J. Ultrastruct. Res.*, 77:133–145, 1981.

- [154] N. P. Smith, D. P. Nickerson, E. J. Crampin, and P. J. Hunter. Multiscale computational modelling of the heart. *Acta Numerica*, 13:371–431, 2004.
- [155] H. M. Spotnitz, W. D. Spotnitz, T. S. Cottrell, D. Spiro, and E. H. Sonnenblick. Cellular basis for volume related wall thickness changes in the rat left ventricle. *J. Mol. Cell. Cardiol.*, 6:317–331, 1974.
- [156] H. J. Steiger. Pathophysiology of development and rupture of cerebral aneurysms. *Acta Neurochir. Suppl. (Wien)*, 48:1–57, 1990.
- [157] G. J. Strijkers, A. Bouts, W. M. Blankesteyn, T. H. J. M. Peeters, A. Vilanova, M. C. van Prooijen, H. M. H. F. Sanders, E. Heijman, and K. Nicolay. Diffusion tensor imaging of left ventricular remodeling in response to myocardial infarction in the mouse. *NMR Biomed.*, 22:182–190, 2009.
- [158] J. Stypmann, M. A. Engelen, A. K. Breithardt, P. Milberg, M. Rothenburger, O. A. Breithardt, G. Breithardt, L. Eckardt, and P. N. Cordula. Doppler echocardiography and tissue Doppler imaging in the healthy rabbit: differences of cardiac function during awake and anaesthetised examination. *Int. J. Cardiol.*, 115:164–170, 2007.
- [159] J. P. Sun, W. J. Stewart, X. S. Yang, R. O. Donnell, A. R. Leon, J. M. Felner, J. D. Thomas, and J. D. Merlino. Differentiation of hypertrophic cardiomyopathy and cardiac amyloidosis from other causes of ventricular wall thickening by two-dimensional strain imaging echocardiography. *Am. J. Cardiol.*, 103:411–415, 2009.
- [160] J. Sundnes, B. F. Nielsen, K. A. Mardal, X. Cai, G. T. Lines, and A. Tveito. On the computational complexity of the bidomain and the monodomain models of electrophysiology. *Ann. Biomed. Eng.*, 34:1088–1097, 2006.
- [161] L. A. Taber and R. Perucchio. Modeling heart development. *J. Elasticity*, 61:165–197, 2000.
- [162] L. A. Taber, M. Yang, and W. W. Podszus. Mechanics of ventricular torsion. *J. Biomech.*, 29:745–752, 1996.
- [163] M. Takeuchi, H. Nakai, M. Kokumai, T. Nishikage, S. Otani, and R. M. Lang. Age-related changes in left ventricular twist assessed by two-dimensional speckle-tracking imaging. *J. Am. Soc. Echocardiogr.*, 19:1077–1084, 2006.
- [164] R. L. Taylor. *FEAP – A Finite Element Analysis Program, Version 8.2 User Manual*. University of California at Berkeley, Berkeley, California, 2008.
- [165] K. H. W. J. Ten Tusscher, R. Hren, and A. V. Panfilov. Organization of ventricular fibrillation in the human heart. *Circ. Res.*, 100:e87–101, 2007.
- [166] N. A. Trayanova and J. J. Rice. Cardiac electromechanical models: from cell to organ. *Front. Physiol.*, 2:43, 2011.

- [167] W. Y. I. Tseng, J. Dou, T. G. Reese, and V. J. Wedeen. Imaging myocardial fiber disarray and intramural strain hypokinesis in hypertrophic cardiomyopathy with MRI. *J. Musculoskel. Neuron. Interact.*, 23:1–8, 2006.
- [168] T. P. Usyk, I. J. LeGrice, and A. D. McCulloch. Computational model of three-dimensional cardiac electromechanics. *Comput. Visual. Sci.*, 4:249–257, 2002.
- [169] T. P. Usyk, R. Mazhari, and A. D. McCulloch. Effect of laminar orthotropic myofiber architecture on regional stress and strain in the canine left ventricle. *J. Elasticity*, 61:143–164, 2000.
- [170] T. P. Usyk and A. D. McCulloch. Electromechanical model of cardiac resynchronization in the dilated failing heart with left bundle branch block. *J. Electrocardiol.*, 36:57–61, 2003.
- [171] T. P. Usyk, J. H. Omens, and A. D. McCulloch. Regional septal dysfunction in a three-dimensional computational model of focal myofiber disarray. *Am. J. Physiol. Heart Circ. Physiol.*, 281:H506–H514, 2001.
- [172] A. Van Der Toorn, P. Barenbrug, G. Snoep, F. H. Van Der Veen, T. Delhaas, F. W. Prinzen, J. Maessen, and T. Arts. Transmural gradients of cardiac myofiber shortening in aortic valve stenosis patients using MRI tagging. *Am. J. Physiol. Heart. Circ. Physiol.*, 283:H1609–H1615, 2002.
- [173] J. van Gijn and G. J. Rinkel. Subarachnoid haemorrhage: diagnosis, causes and management. *Brain*, 124:249–278, 2001.
- [174] F. J. Vetter and A. D. McCulloch. Three-dimensional analysis of regional cardiac function: A model of the rabbit ventricular anatomy. *Prog. Biophys. Mol. Biol.*, 69:157–183, 1998.
- [175] E. J. Vigmond, M. Hughes, G. Plank, and L. J. Leon. Computational tools for modeling electrical activity in cardiac tissue. *J. Electrocardiol.*, 36 Suppl:69–74, 2003.
- [176] L. K. Waldman and J. W. Covell. Effects of ventricular pacing on finite deformation in canine left ventricles. *Am. J. Physiol. Heart Circ. Physiol.*, 252:H1023–H1030, 1987.
- [177] H. Watanabe, S. Sugiura, H. Kafuku, and T. Hisada. Multiphysics simulation of left ventricular filling dynamics using fluid-structure interaction finite element method. *Biophysical Journal*, 87:2074 – 2085, 2004.
- [178] P. N. Watton, N. A. Hill, and M. Heil. A mathematical model for the growth of the abdominal aortic aneurysm. *Biomech. Model. Mechanobiol.*, 3:98–113, 2004.

- [179] H. Weisbecker, D. M. Pierce, P. Regitnig, and G. A. Holzapfel. Layer-specific damage experiments and modeling of human thoracic and abdominal aortas with non-atherosclerotic intimal thickening. *J. Mech. Beh. Biomed. Mat.*, in press.
- [180] J. A. Weiss, B. N. Maker, and S. Govindjee. Finite element implementation of incompressible, transversely isotropic hyperelasticity. *Comput. Meth. Appl. Mech. Eng.*, 135:107–128, 1996.
- [181] P. Whittaker, D. R. Boughner, and R. A. Kloner. Analysis of healing after myocardial infarction using polarized light microscopy. *Am. J. Pathol.*, 134:879–893, 1989.
- [182] P. Whittaker, M. E. Schwab, and P. B. Canham. The molecular organization of collagen in saccular aneurysms assessed by polarized light microscopy. *Connect. Tissue Res.*, 17:43–54, 1988.
- [183] J. R. Wilson, P. Douglas, W. F. Hickey, V. Lanoce, N. Ferraro, A. Muhammad, and N. Reichek. Experimental congestive heart failure produced by rapid ventricular pacing in the dog: cardiac effects. *Circulation*, 75:857–867, 1987.
- [184] W. Wilson, C. C. van Donkelaar, B. van Rietbergen, K. Ito, and R. Huiskes. Stresses in the local collagen network of articular cartilage: a poroviscoelastic fibril-reinforced finite element study. *J. Biomech.*, 37:357–366, 2004.
- [185] A. Y. Wong and P. M. Rautaharju. Stress distribution within the left ventricular wall approximated as a thick ellipsoidal shell. *Am. Heart. J.*, 75:649–662, 1968.
- [186] R. H. Woods. A few applications of a physical theorem to membranes in the human body in a state of tension. *J. Anat. Physiol.*, 26:362–370, 1892.
- [187] Y. Wu, S. P. Bell, K. Trombitas, C. C. Witt, S. Labeit, M. M. LeWinter, and H. Granzier. Changes in titin isoform expression in pacing-induced cardiac failure give rise to increased passive muscle stiffness. *Circulation*, 106:1384–1389, 2002.
- [188] Z. J. Yang, J. Liu, J.P. Ge, L. Chen, Z. Zhao, W. Y. Yang, and China National Diabetes and Metabolic Disorders Study Group. Prevalence of cardiovascular disease risk factor in the Chinese population: the 2007-2008 China national diabetes and metabolic disorders study. *Eur. Heart. J.*, 33:213–220, 2012.
- [189] F. C. P. Yin, R. K. Strumpf, P. H. Chew, and S. L. Zeger. Quantification of the mechanical properties of noncontracting canine myocardium under simultaneous biaxial loading. *J. Biomech.*, 20:577–589, 1987.
- [190] A. A. Young, I. J. Legrice, M. A. Young, and B. H. Smaill. Extended confocal microscopy of myocardial laminae and collagen network. *J Microsc.*, 192:139–150, 1998.

-
- [191] O. C. Zienkiewicz and R. L. Taylor. *The Finite Element Method. Solid Mechanics*, volume 2. Butterworth Heinemann, Oxford, 5th edition, 2000.
- [192] S. D. Zimmerman, W. J. Karlon, J. W. Holmes, J. H. Omens, and J. W. Covell. Structural and mechanical factors influencing infarct scar collagen organization. *Am. J. Physiol. Heart Circ. Physiol.*, 278:H194–H200, 2000.
- [193] M. A. Zulliger, P. Fridez, K. Hayashi, and N. Stergiopoulos. A strain energy function for arteries accounting for wall composition and structure. *J. Biomech.*, 37:989–1000, 2004.